Characterization of blade tip vortices on large-scale rotors

Von der Fakultät für Maschinenbau
der Gottfried Wilhelm Leibniz Universität Hannover
zur Erlangung des akademischen Grades
Doktor-Ingenieur
genehmigte Dissertation

von
Dipl.-Ing.

André Bauknecht

geboren am 31.07.1986
in Pforzheim

2016

1. Referent: Prof. Dr.-Ing. Markus Raffel
2. Referent: Prof. Dr. Friedrich Dinkelacker

Tag der Promotion: 3. Februar 2016

Abstract

THE vortices produced by helicopter rotor blades dominate the aerodynamics of the rotor wake. Their interactions with the rotor blades cause sound and structural vibrations and have detrimental effects on the aircraft performance. Current research strives to better understand and reduce the effects of these *blade-vortex interactions* (BVI). Sub-scale model rotor tests – and an increasing number of full-scale investigations – are performed to develop measures against the interaction effects. Active rotor control concepts – such as active twist actuation – have the potential to effectively reduce the sound and vibrations of helicopter rotors.

The present thesis focuses on the experimental investigation of active twist for the reduction of BVI effects on a model rotor. Results of a large-scale *smart-twisting active rotor* (STAR) test under hover conditions are described. This test investigated the effects of individual blade twist control on the blade tip vortices. The rotor blades were actuated with peak torsion amplitudes of up to 2° and harmonic frequencies of $1-5/rev$ with different phase angles. Time-resolved stereoscopic *particle image velocimetry* (PIV) and *background-oriented schlieren* (BOS) measurements were carried out to study the effects of active twist on the strength and trajectories of the tip vortices between $\psi_v = 3.56°$ and 45.74° of vortex age.

The analysis of the vortex trajectories revealed that the $1/rev$ active twist actuation mainly caused a vertical deflection of the blade tip and the corresponding vortex trajectories of up to 1.3% of the rotor radius R above and $-1\%R$ below the unactuated condition. An actuation with frequencies of $2/rev$ and $3/rev$ significantly affected the shapes of the vortex trajectories and caused negative vertical displacements of the vortices relative to the unactuated case of up to $2\%R$ within the first 35° of wake age. The $2/rev$ and $3/rev$ actuation also had the most significant effects on the vortex strength and altered the initial peak swirl velocity by up to −34 % and +31 % relative to the unactuated value. The present aerodynamic investigation reveals a high control authority of the active twist actuation on the strength and trajectories of the trailing blade tip vortices. The magnitude of the evoked changes indicates that the active twist actuation constitutes an effective measure for the mitigation of BVI-induced sound on helicopters.

The majority of available studies on BVI – including the STAR experiments – are based on sub-scale model rotor tests. It is challenging to correctly downscale the multitude of under-

lying effects contributing to BVI. Full-scale investigations with innovative, whole-field vortex visualization techniques are, consequently, required for the validation of the model test results. The present work thus also targets the advancement of optical measurement techniques for the investigation of vortices on full-scale helicopters. A series of flight tests were carried out to improve a reference-free variant of the BOS technique and demonstrate its vortex visualization capabilities for various test conditions. The goal of the main flight test was the quantitative measurement of the main rotor tip vortex system of a full-scale BO 105 helicopter under maneuvering flight. The tip vortices of the helicopter were simultaneously visualized from different perspectives by a multi-camera BOS setup consisting of ten individual cameras. Based on this data set, a three-dimensional reconstruction of the main rotor vortex system of a maneuvering helicopter was realized for the first time. The flight test results thus demonstrate the potential of the BOS measurement technique for quantitative vortex investigations on full-scale helicopters under realistic flight conditions.

Keywords: *Blade tip vortex, active twist actuation, vortex reconstruction, particle image velocimetry, background-oriented schlieren, flight test*

Kurzfassung

Die an Rotorblättern erzeugten Blattspitzenwirbel bestimmen maßgeblich die Aerodynamik im Nachlauf von Hubschrauberrotoren. Ihre Interaktionen mit den Rotorblättern erzeugen Lärm und Vibrationen und beeinträchtigen die Leistungsfähigkeit des Fluggeräts. Der Fokus der aktuellen Forschung liegt auf der Untersuchung dieser Blattspitzen-Wirbel-Interaktionen (engl.: blade-vortex interactions, BVI) und der Reduktion der dadurch verursachten Effekte. Eine Reihe von kleinskaligen Modelrotorversuchen – sowie eine zunehmende Anzahl an vollskaligen Flugversuchen – untersucht neu entwickelte Maßnahmen zur Reduzierung der Interaktionseffekte. Konzepte zur aktiven Rotorbeeinflussung – wie die aktive Blattverwindung – haben hierbei ein hohes Potenzial für die Reduzierung der Schallemission und der Vibrationen von Hubschrauberrotoren.

Die vorliegende Arbeit befasst sich mit der experimentellen Untersuchung der aktiven Blattverwindung zur Reduzierung von BVI-Effekten. Hierzu wurden Versuche mit einem großskaligen, aktiv verwundenen Rotor (engl. smart-twisting active rotor, STAR) unter Schwebeflugbedingungen durchgeführt. Als Kernpunkt des Tests sollten die Auswirkungen der individuellen Blattverwindung auf die Blattspitzenwirbel untersucht werden. Die Rotorblätter wurden mit bis zu 2° Amplitude, Frequenzen von $1-5$ pro Umlauf ($1-5/rev$) und unterschiedlichen Phasenwinkeln harmonisch tordiert. Hierbei wurden zeitaufgelöste, stereoskopische *particle image velocimetry* (PIV) und Hintergrund-orientierte Schlierenmessungen (engl. *background-oriented schlieren*, BOS) durchgeführt, um die Auswirkungen der aktiven Verwindung auf die Stärke und Trajektorien der Wirbel im Bereich von $\psi_v = 3.56°$ bis $45.74°$ zu untersuchen.

Die Analyse der Wirbeltrajektorien zeigte, dass die aktive $1/rev$ Verwindung hauptsächlich eine vertikale Verschiebung der Blattspitze und der kompletten zugehörigen Wirbelbahnen um bis zu 1.3% des Rotorradiuses R nach oben und um $-1\%R$ nach unten relativ zum unaktuierten Referenzfall verursachte. Eine Verwindung mit Frequenzen von $2-3/rev$ hatte einen erheblichen Einfluss auf die Form der Trajektorien und verursachte innerhalb der ersten 35° hinter dem Blatt eine negative vertikale Wirbelverschiebungen von bis zu $2\%R$ relativ zum Referenzfall. Die aktive Verwindung mit $2-3/rev$ hatte auch die größte Auswirkung auf die Stärke der Wirbel und veränderte die anfängliche maximale Tangentialgeschwindigkeit um bis zu $-34\,\%$ und $+31\,\%$ relativ zum unaktuierten Referenzwert. Die Ergebnisse der vorliegenden aerodynamischen Untersuchung zeigen, dass die aktive Blattverwindung einen großen Einfluss auf die Stärke und die Trajektorien der Blattspitzenwirbel aufweist. Aufgrund der Größenordnung

der hervorgerufenen Änderungen ist zu erwarten, dass die aktive Blattverwindung den BVI-induzierten Anteil des Hubschrauberlärms effektiv reduzieren kann.

Ein Großteil der in der Literatur verfügbaren Studien – inklusive der STAR Versuche – basiert auf kleinskaligen Modellrotortests. Das Herunterskalieren der verschiedenen Einflussfaktoren und Bedingungen für das Auftreten von BVI stellt jedoch eine Herausforderung dar. Aus diesem Grund werden vollskalige Vergleichsmessungen mit innovativen, das ganze Rotorwirbelfeld erfassenden Visualisierungstechniken benötigt, um die Ergebnisse der Modellversuche zu validieren. Die vorliegende Arbeit beschäftigt sich deshalb auch mit der Weiterentwicklung von optischen Messtechniken zur Untersuchung von Blattspitzenwirbeln an vollskaligen Hubschraubern. Eine referenzfreie Variante der BOS-Methode wurde in mehreren Flugversuchen weiterentwickelt und ihre Eignung für die Visualisierung von Wirbeln unter verschiedenen Messbedingungen demonstriert. Das Ziel des Hauptflugversuchs war die quantitative Vermessung des Hauptrotorwirbelsystems eines vollskaligen BO 105 Hubschraubers unter Manöverflugbedingungen. Die Wirbel des Hubschrauberrotors wurden hierbei mittels eines BOS-Aufbaus bestehend aus 10 Einzelkameras zeitgleich von verschiedenen Seiten aufgenommen und visualisiert. Basierend auf diesem Datensatz wurde zum ersten Mal eine dreidimensionale Rekonstruktion des Hauptrotorwirbelsystems eines fliegenden Hubschraubers durchgeführt. Die Ergebnisse der Flugversuche demonstrieren das Potenzial der BOS-Methode für quantitative Wirbeluntersuchungen an vollskaligen Hubschraubern unter realistischen Flugbedingungen.

Stichwörter: *Blattspitzenwirbel, aktive Blattverwindung, Wirbelrekonstruktion, Particle Image Velocimetry, Hintergrund-orientiertes Schlierenverfahren*

Acknowledgments

First and foremost I would like to thank my doctoral adviser Prof. Markus Raffel for giving me the opportunity to work in one of the most exciting scientific environments I could imagine, for enabling me to actively shape my own research, and for all the times he got me safely back to the ground when we were flying in a microlight airplane with open doors.

I also want to thank Prof. Friedrich Dinkelacker and Prof. Hans Jürgen Maier from the Gottfried Wilhelm Leibniz University Hannover, and Prof. Stefan Becker from the Friedrich-Alexander University Erlangen for their contributions as members of my dissertation committee.

I am indebted to my technical adviser Benjamin Ewers at the DLR Göttingen for his participation in most of my studies, helpful feedback, and valuable discussions. I profited from the experience and support of my colleagues Christian Wolf, Kai Richter, and Anthony Gardner from the DLR Göttingen. I thank Prof. Berend G. van der Wall for enabling my research stay at the DLR Braunschweig, and expanding my knowledge on helicopter aeromechanics. I highly appreciate the chance I got to participate in the STAR hover test and I would like to especially thank Oliver Schneider, Frauke Hoffmann, and Michael Przybilla for their help.

Many of my experiments required extra hands during their planning, execution, and evaluation. I appreciate the help I got from Christoph Merz, Markus Krebs, Johannes Braukmann, Kurt Kaufmann, Till Schwermer, Gabriel Ertz, and Detlef Hübner from the DLR Göttingen, Sebastian Soffner from the DLR Braunschweig, and Andrin Landolt from the ETH Zurich.

Special thanks go to my dear friends Oliver Wysocki, Gerrit Lauenroth, Daniela Heine, Jason Blinstrub, Roland Schuster, and Tim Wetzel at the DLR, and Désirée Braun, Robert Leicht, Anne Geppert, and Frank Nees outside work. You never failed to cheer me up, support me, and help me keep a level head when things did not turn out the way they should have.

I am deeply grateful for the continuous support and love I got from my parents, Kurt and Gabriele, and my brother Timo. They helped me become the person I am today and were always there for me.

Finally, I am indebted to my girlfriend Katie Von Holzen, who's unfailing love, support, and understanding aided me beyond words. She helped me keep up my motivation, sanity, and English grammar to the very end of writing this thesis.

Contents

List of Figures

List of Tables

Nomenclature

A, B, C	Particle tracking error constants, m^2
$\boldsymbol{A}$	Velocity gradient tensor, $1/s$
A_{pixel}	Imaged area of one pixel, m^2
a	Velocity fit parameter; empirical factor for Squire core growth
a_∞	Acceleration, m/s^2
a_n, b_n	Fit coefficients for RL vortex model and camera mapping
C	Closed curve for line integral, m
C_T	Thrust coefficient, $C_\text{T} = T/(\rho\pi\Omega^2 R^4)$
c	Blade chord length, m
D	Physical particle displacement, $D = (D_x, D_y, D_z)$, m
D_a	Aperture diameter m
d	Imaged particle displacement, $d = (d_x, d_y, d_z)$, m
d_diff	Diffraction limited particle diameter, m
d_P, d_τ	Particle and Airy disk diameter, m
$E_{95,P}$	Confidence bound of parameter P with 95% confidence level
F	Fundamental matrix
F_i, F_o	In-plane and out-of-plane loss-of-pairs
f	Shape function for convolution filter
$\text{f}, \text{f}_\text{eff}$	(Effective) focal length, m
$f_\#$	F-number, $f_\# = f/D_\text{a}$
G	Gladstone-Dale constant, m^3/kg
$I, I_\text{min}, I_\text{mean}$	Pixel intensity, minimum pixel intensity, average pixel intensity
$I_\text{threshold}$	Pixel intensity threshold
i	Counter; blade index
K	Calibration factor for density reconstruction
k	Control frequency

$L_\mathrm{m}, L_\mathrm{m,OS}$	(Oversampled) measurement resolution, m
M, m	Indices
M	Magnification factor, $M = z_0/Z_0$
M_B	Background magnification factor, $M_\mathrm{B} = Z_i/Z_B$
M_tip	Tip Mach number
M_0	Nominal magnification factor
N	Sample size
N_b	Number of blades
N_I	Number of particles in both interrogation windows
n	Vatistas swirl shape parameter; refractive index
$O_{A,B}$	Optical camera center, m
P	Parameter
$p_\mathrm{static}, p_\infty$	Local static and ambient air pressure, Pa
Q	Flow field operator, $1/\mathrm{s}^2$
q	Swirling strength
q_P	Normalized diameter for Mie scattering, $q_\mathrm{P} = \pi d_\mathrm{P}/\lambda$
R	Rotor radius, m
r	Radial coordinate, m
$r_\mathrm{c}, r_0, r_\mathrm{void}$	Radius of vortex core, vortex core at time $t = 0$, and particle void, m
$\overline{r}$	Non-dimensional radius, r/r_c, m
r'	Characteristic frequency, lines per mm
Re_v	Vortex Reynolds number, $Re_\mathrm{v} = \Gamma_\mathrm{v}/\nu$
Re_c	Chord Reynolds number, $Re_c = V_\mathrm{tip}c/\nu$
S	Area enclosed by C, m^2
$\boldsymbol{S}$	Strain tensor, s^{-1}
SF	Safety factor
St	Stokes number, $St = \tau_\mathrm{P}/\tau$
T	Rotor thrust, N
$T_\mathrm{peak}, T_\infty$	Core and ambient temperature, K
t, t'	Time, specific point in time, s
t_s	Student factor
t_0	Instant of blade quarter chord passing through measurement plane, s

Δt	Time delay, $\Delta t = t' - t$, s
U_i, U_n	Control voltage signal, maximum control voltage amplitude, V
u, v	Imaged background displacements
u, v, w	Velocity components, m/s
$\mathbf{V}$	Velocity tensor m/s
V_P	Particle velocity, m/s
V_r, V_z, V_θ	Vortex induced radial, axial, and swirl velocity, m/s
V_tip	Blade tip speed,$V_\mathrm{tip} = \Omega R$, m/s
V_0	Velocity scale, m/s
V_∞	Free-stream velocity, m/s
X, Y, Z	Coordinates in object plane, m
x, y, z	Coordinates in image plane, m
$x_\mathrm{tip}, y_\mathrm{tip}, z_\mathrm{tip}$	Blade tip position, m
$x_\mathrm{void}, y_\mathrm{void}$	Particle void center position, m
$\Delta x, \Delta y$	Apparent background displacement, m
Z_B	Distance between background and lens, m
Z_D	Distance between background and phase object, m
Z_i	Distance between image plane and lens, m
Z_S	Physical position of background screen, m
Z_0	Distance between object plane and lens, m
z_LS	Thickness of light sheet, m
z_0	Distance between lens and image plane, m

Greek letters

α	Stereoscopic camera angle, °
$\alpha_\mathrm{e}, \alpha_\mathrm{tip}$	Effective and blade tip angle of attack, °
α_L	Lamb's constant
β	Stereoscopic camera angle, °
$\Gamma, \Gamma_\mathrm{c}, \Gamma_\mathrm{v}$	Circulation, vortex circulation at r_c and at large distances, m^2/s
γ	Specific heat ratio
δ	Ratio of apparent to actual viscosity, $\delta = 1 + \nu_t/\nu$
ε	Angular deflection, $\varepsilon = (\varepsilon_x, \varepsilon_y)$, °
$\varepsilon_{xx}, \varepsilon_{yy}, \varepsilon_{xy}, \varepsilon_{yx}$	Elongational and shear strains, 1/s

$\varepsilon_\theta, \varepsilon_r$	Particle tracking errors in tangential and radial direction
ζ	Non-dimensional quantity, $\Gamma_\mathrm{v}^2 \rho_\infty / (8\pi^2 \gamma p_\infty r_\mathrm{c}^2)$
θ	Scheimpflug angle, °
ϑ	Blade torsion, °
λ, λ_{ci}	Regular and signed swirling strength, 1/s
λ_i	Non-dimensional rotor inflow velocity
λ_w	Wavelength, m
λ_2	Flow field operator, $1/\mathrm{s}^2$
μ	Dynamic viscosity, kg/(ms)
ν	Kinematic viscosity, m^2/s
ν_t	Effective turbulent value of viscosity, m^2/s
$\rho, \rho_\infty, \rho_\mathrm{P}$	Density of local air, ambient air, and the seeding particles, $\mathrm{kg/m}^3$
ρ_PS	Pseudo density
σ	Rotor solidity, $\sigma = N_b c/(\pi R)$
σ_s	Standard deviation
τ	Time scale for Stokes number, s
φ	Control phase angle, rad
Ψ	Rotor azimuth, $\Psi = \Omega t$, °
ψ	Scheimpflug angle, °
ψ_v	Vortex age, °
Ω	Rotor rotational frequency, rad/s
$\mathbf{\Omega}$	Vorticity tensor, 1/s
ω	Vorticity 1/s
ω_rot	Rotation of displacement field 1/s

Indices

AC	Area center
c	Core
max	Maximum, at position of maximum
min	Minimum, at position of minimum
v	Vortex
∞	Ambient condition

Operators

F	Convolution with the filter function f
$\mathfrak{I}$	Imaginary part of a complex number
$\|\ \|$	Absolute value
Δ	Difference

Abbreviations

$/rev$	per revolution
1D	one-dimensional
2C	two-component
2D	two-dimensional
3C	three-component
3D	three-dimensional
AFDD	AeroFlightDynamics Directorate
ATR	Active Twist Rotor
BERP	British Experimental Rotor Programme
BL	Baseline
BOS	Background-Oriented Schlieren
BVI	Blade-Vortex Interactions
CPU	Central Processing Unit
DEHS	Di-Ethyl-Hexyl-Sebacate
DLR	German Aerospace Center
DNW	German-Dutch Wind Tunnels organization
DSLR	Digital Single-Lens Reflex
FOV	Field Of View
GFRP	Glass Fiber Reinforced Plastic
GPU	Graphics Processing Unit
HART	HHC Aeroacoustic Rotor Tests
HHC	Higher Harmonic Control
HOTIS	Hover Tip Vortex Structure
IBC	Individual Blade Control
JAXA	Japan Aerospace Exploration Agency
KARI	Korea Aerospace Research Institute

LDV	Laser Doppler Velocimetry
LED	Light Emitting Diode
LLF	Large Low-speed Facility
MFC	Macro Fiber Composite
MIT	Massachusetts Institute of Technology
MTF	Modulation Transfer Function
MV	Measurement Volume
NASA	National Aeronautics and Space Administration
ONERA	Office National d'Etudes et de Recherches Aérospatiales
PDF	Probability Density Function
PIV	Particle Image Velocimetry
RANSAC	Random Sample Consensus
SPR	Stereo Pattern Recognition
SSD	Solid State Disk
STAR	Smart-Twisting Active Rotor
TAMI	Tip Air Mass Injection
TE	Trailing Edge
TPP	Tip Path Plane

1 Introduction

Helicopters possess unique operational abilities that enable them to fulfill a multitude of tasks in today's society. The combination of a high cruise speed, capability to hover, three-dimensional maneuverability, and ability to vertically land virtually everywhere makes helicopters irreplaceable for search-and-rescue missions, construction work in difficult terrain, security operations, fighting forest fires, as well as medical and personal transport. Some of these tasks require helicopters to operate close to or above densely populated areas, e.g. in the vicinity of airports and hospitals. The sound emission of the aircraft thus becomes a crucial factor that governs public acceptance of helicopters and can therefore lead to operational restrictions such as a ban on night flights. For this reason, considerable resources are invested into the reduction of helicopter sound emissions.

The main rotor constitutes the dominant source of sound on a helicopter, with additional smaller influences by the tail rotor low-order loading harmonics, and high-pitch engine and transmission sound (George 1978). The main rotor produces sound due to high-order harmonics, random loadings caused by atmospheric turbulence, and impulsive noise. The impulsive noise mainly originates from two aerodynamic phenomena: high tip Mach number effects on the advancing side of the rotor that radiate high-speed impulsive noise, and impulsive noise due to *blade-vortex interactions* (BVI) on both the advancing and retreating side of the rotor, including secondary stall and shock effects during BVI. The characteristic thumping sound during BVI dominates the overall sound emission of the helicopter, which is especially apparent for older machines, such as the two-bladed Bell UH-1. BVI noise is generated by the interaction of a rotor blade with a previously generated vortex from another blade. The most severe blade-vortex encounters occur during flight maneuvers such as descending forward flight or banked turns. During these maneuvers, the vortex filaments that are created in the forward half of the rotor disk convect close to the rotor plane. The passing vortex filament causes changes in the local blade aerodynamics and high unsteady pressure fluctuations on the interacting blade. The magnitude of these interaction effects depends primarily on the strength of the vortex, and its distance and orientation to the interacting rotor blade (Hardin & Lamkin 1986).

Over the past decades, numerous studies have been conducted to gain a better understanding of the important factors that contribute to BVI. Part of this research attempts to mitigate the effects of BVI such as sound emissions and vibrations. Passive and active measures have been investigated which reduce the vortex strength or alter the vortex trajectories. Improved blade geometries such as the BERP (Lowson 1992) or sub wing design (Brocklehurst & Pike 1994) have been shown to substantially reduce the BVI-related noise by up to 5 dB. Similar levels of noise reduction are also possible by active actuation through tip air jets (White Jr. 1980), higher harmonic blade control (Kube et al. 1996), and active trailing edge flaps (Marcolini et al. 1995). An especially promising active control concept aims at altering the shed blade tip vortices by actively twisting the rotor blades with blade-internal actuators. The potential of this concept

for the reduction of BVI-induced rotor vibrations has been demonstrated by the *active twist rotor* (ATR) project (Wilbur & Yeager 2002). The ATR project, however, did not investigate the effects of the active twist actuation on the blade tip vortices and sound emission of the rotor. Further investigations are thus required to assess the control authority of the active twist concept on the trailing tip vortices and sound generation during BVI.

The first part of the present thesis aims to investigate the effects of active twist control on the strength and positions of the tip vortices that are shed by a large-scale model rotor. This investigation was conducted within the framework of the international *smart-twisting active rotor* (STAR) project. The STAR project was initiated by an international consortium of research institutes and universities with the intent to manufacture and test an active twist model rotor under hover and BVI-relevant flight conditions. The present aerodynamic study is based on a preliminary hover test of the STAR rotor, which was carried out in the rotor preparation hall at DLR Braunschweig. Time-resolved, simultaneous, and stereoscopic *particle image velocimetry* (PIV) and *background-oriented schlieren* (BOS) measurements were conducted to study young tip vortices between 3.56° and 45.74° of wake age. The acquired measurement data thus enabled a comprehensive analysis of the actuation effects on the vortex system of the hovering rotor.

The majority of investigations on BVI – as well as the state-of-the-art vortex models – are based on experiments with fixed wings or sub-scale model rotors. The application of these model results to full-scale rotor flow critically depends on the correct scaling of the significant design and flow parameters in the experiment. The prediction of full-scale BVI is challenging due to the large number of underlying and interacting effects, such as the blade aerodynamics including the lift time history, blade aero-elasticity, fuselage-interference, atmospheric conditions, and the flight condition, performance, and trimming of the aircraft (Hardin & Lamkin 1986). The investigation of vortices on full-scale rotors, however, involves no scaling errors and thus potentially provides the information essential for the validation of sub-scale experiments and numerical simulations. To date, only a few studies are available that focus on the strength (Kindler et al. 2007) and position (Heineck et al. 2013, Klinge et al. 2006) of young vortices shed by full-scale helicopter rotors operated under steady wind tunnel or hover conditions. The localization of the entire vortex system of a full-scale helicopter – which is necessary for the assessment of blade-vortex miss-distances – has not been attempted yet due to the lack of a suitable measurement system. The development of a non-intrusive, large-scale measurement technique that can easily be applied outside the laboratory is thus required to enable full-scale vortex investigations.

The second part of the present thesis thus aims to advance the existing BOS technique for the visualization and three-dimensional localization of the complete vortex system of a full-scale helicopter under realistic flight conditions. A series of flight tests were conducted with a BO 105 and a Cougar helicopter to improve the BOS technique and demonstrate its potential for the visualization of full-scale rotor blade tip vortices outside the laboratory. In a final flight test, a multi-camera BOS setup was used to visualize and – for the first time – reconstruct the main part of the tip vortex system of a BO 105 helicopter in three-dimensional space. The two main objectives of this thesis can therefore be summarized by the following questions:

What are the effects of active twist actuation on the shed blade tip vortices?

Is it possible to acquire three-dimensional blade tip vortex positions for a full-scale helicopter under free flight conditions?

2 Blade Tip Vortices

In this chapter, the theory of and the most important literature on blade tip vortices are discussed. Section 2.1 covers the basic definition of a vortex and how vortices are generated on a *three-dimensional* (3D) airfoil. The adverse effects of vortices on an aircraft and aerodynamic vortex properties are given, followed by common vortex models used for their description, and a review of vortex decay and breakdown. Section 2.2 focuses on the vortices shed by a helicopter rotor and typical interaction phenomena such as *blade-vortex interactions* (BVI), as well as active and passive measures against them.

2.1 Basic vortex theory

Vortices are present in many natural flows such as stirred fluids, whirlpools on a water surface, dust-devils, tornadoes, and even in the atmosphere of the planet Jupiter. They also occur in technical applications, e.g. in vortex separators, cyclone combustors, on aircraft wings, and on propellers. There are a number of commonly accepted definitions for a vortex in a fluid medium that emphasize different aspects of the vortex. These definitions include:

- a region with circular flow,
- a region of high vorticity,
- a region with reduced static pressure,
- a region surrounded by closed or spiral streamlines.

Some of these definitions, however, depend on the frame of reference (i.e. are not Galilean-invariant), or are ambiguous, as e.g. shear flow also exhibits elevated levels of vorticity, and locally reduced static pressure can be caused by flow curvature. Another commonly applied definition of a vortex was proposed by Robinson (1990):

> "*A vortex exists when instantaneous streamlines mapped onto a plane normal to the vortex core exhibit a roughly circular or spiral pattern, when viewed from a reference frame moving with the center of the vortex core.*"

The application of this formulation for the identification of vortices is, however, limited, as *a priori* information about the position and orientation of the vortex is required to identify it. Other definitions based on aerodynamic formulations such as the Navier-Stokes equations are difficult to achieve, as these formulations describe the flow field at distinct spatial points and therefore cannot capture a flow structure with a large physical extent such as a vortex.

It is evident from these considerations that the term *vortex* is often used in a physically imprecise manner, and that a universal definition for it does not exist (Haller 2005). Despite this lack of an absolute definition, the available vortex detection schemes enable the identification and characterization of vortices in flow fields with sufficiently high accuracy, as will be shown throughout this work.

2.1.1 Vortex generation on a three-dimensional wing

Lift-producing wings of finite span also generate vortices at their tips. This phenomenon can be explained in three different ways (see Green 1995). A first explanation is based on the Helmholtz vortex laws and the Kutta-Joukowski law, which links the lift of an airfoil to its bound circulation. Following these principles, the tip vortices can be explained as the connections between the bound circulation of the wing and a starting vortex that forms when the wing starts to move and matches the bound wing circulation according to Kelvin's theorem. A second explanation attributes the vortex formation to the presence of a shear layer at the wing tip between the undisturbed flow and the flow over the airfoil, where vorticity is created and merged into the tip vortex. The third and most commonly adopted explanation is illustrated in Fig. 2.1 with the sketch of a finite wing. The wing exhibits almost undisturbed and *two-dimensional* (2D) flow close to its center section, as visualized by the straight streamlines. At this center section, the static pressure difference between the suction side on top and the pressure side below the airfoil reaches its maximum. Closer to the wing tips, this pressure difference decreases, together with the produced sectional lift. The span-wise pressure gradient causes the streamlines to curve inboard on the suction side and outboard on the pressure side. The outboard pressure difference forces fluid from the pressure side of the airfoil to flow around the wing tip. This swirling motion of fluid persists behind the wing and forms a wing tip vortex, as illustrated in Fig. 2.1. The difference in lateral fluid motion between the suction and pressure side causes the formation of a shear layer with increased vorticity behind the *trailing edge* (TE) of the wing, where the two flows combine again. The created vortex sheet persists in the wake of the wing, where it is af-

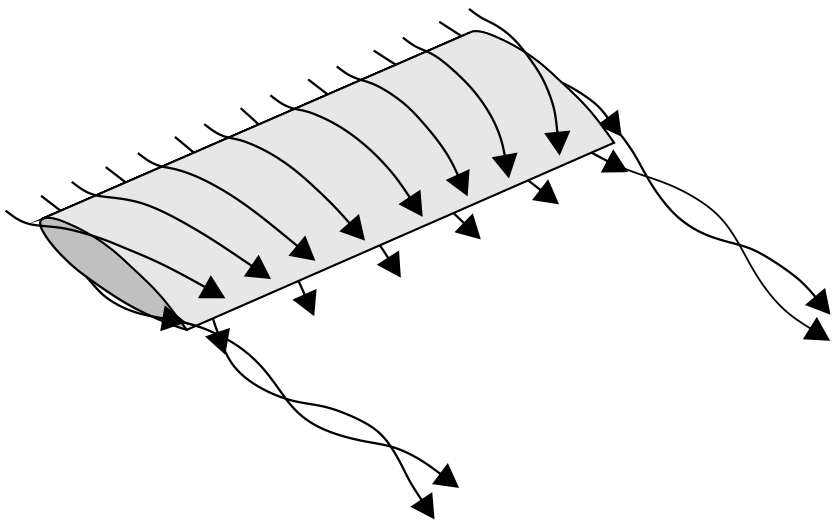

Figure 2.1: Three-dimensional flow over a finite wing and trailing tip vortices

fected by the induced velocity field around the vortex according to the Biot-Savart law. The vortex-induced velocity field – in combination with the wake of the wing – causes the vortex sheet to progressively envelop the tip vortex, what is known as the *roll-up* of the vortex.

The vortex formation phase has a great influence on the overall properties of a trailing tip vortex. The onset of vortex development occurs early on the airfoil and typically involves multiple smaller vortices merging into a single main tip vortex (Birch & Lee 1992, Bailey et al. 2006, Giuni & Green 2013). This merging is almost complete by the time the vortex reaches the TE, but it takes up to a distance of two chord lengths behind the TE before the vortex sheet is completely rolled-up and the vortex becomes fully axisymmetric (Green & Acosta 1991).

The shape and properties of a tip vortex are influenced by multiple wing and operational parameters. The geometry of the wing tip (aspect ratio, tapering, tip shape, surface roughness) and the operating conditions (wing load distribution, angle of attack α, Reynolds number Re_c computed with the chord length c) play an important role in defining the shape of the vortex (Smith & Sigl 1995, Martin & Leishman 2002, Ramasamy & Leishman 2005).

2.1.2 Adverse effects of tip vortices

Wing tip vortices have a number of adverse effects on the performance of the wing itself, but also on its environment. The induced flow field from the vortex is directed downwards on the wing and most pronounced close to the vortex position, according to the Biot-Savart law. It therefore reduces the local effective angle of attack α_e and lift of the wing. The continuous acceleration of fluid around the wing tip requires additional energy, which is called *induced drag* and decreases the efficiency of the aircraft. The trailing vortices behind the wing also pose a threat for other aircraft, as the vortex-induced velocities can reach magnitudes that are large enough to affect the stability of following aircraft. On rotorcraft, the tip vortices can interact with the fuselage, tail boom, and the rotor blades, which leads to unsteady and high frequency pressure fluctuations that cause sound emission and vibrations. A detailed description of these interaction effects will be given in Subsection 2.2.1.

2.1.3 Vortex properties

After the initial roll-up process is finished, the fully developed trailing vortex is approximately axisymmetric. It consists of an outer region and an inner part, which is referred to as the *vortex core*. The radial extend of the core – or core radius r_c – is commonly defined at the location of maximum tangential or swirl velocity V_θ (see e.g. McCormick et al. 1968 and Fig. 2.2c). Several studies have found that the flow field within the vortex core is essentially laminar, with a transitional region and a fully turbulent region surrounding the vortex core (see Devenport et al. 1996, Martin et al. 2003, Ramasamy & Leishman 2007). It is of interest to note that the high streamline curvature in the vicinity of the core prevents the generation of large scale turbulent eddies and causes the relaminarization of entrained turbulent structures (Martin et al. 2003).

From a mathematical perspective, the trailing vortex can be described as a distribution of vor-

ticity $\vec{\omega}$, which corresponds to the curl of the velocity $\mathbf{V}$, as defined e.g. by Anderson (2007):

$$\vec{\omega} = \nabla \times \mathbf{V} \tag{2.1}$$

The circulation Γ is a measure for the strength of a vortex. It is defined as the line integral around a closed curve C of the velocity field (Anderson 2007):

$$\Gamma = \oint_C \mathbf{V} ds \tag{2.2}$$

where ds is the directed line segment. According to Rossow (1999), the streamwise component of the circulation is of high importance for the study of trailing vortices. Additionally, it is the only component of the vorticity that is available from 2D *particle image velocimetry* (PIV) measurements in planes perpendicular to the vortex axis. Applying the Stokes' theorem, Eq. (2.2) can be adapted to only cover the streamwise circulation component within an area S enclosed by the curve C:

$$\Gamma = \iint_S \omega_z \, dS = \iint \left(\frac{\partial v}{\partial x} - \frac{\partial u}{\partial y} \right) dxdy \tag{2.3}$$

The definition of the circulation in Eq. (2.3) is applied in the present study. Schematic radial distributions of the vorticity and circulation of a vortex are depicted in Fig. 2.2a and b, respectively. The maximum of the streamwise vorticity at the vortex center can be used for the detection of the vortex position. For large radial distances to the vortex center, the vorticity converges to zero and the integrated vortex circulation approaches a constant value of Γ_v. For each radial position r, the tangential or swirl velocity V_θ can be expressed as (Martin et al. 2003):

$$V_\theta = \frac{\Gamma}{2\pi r} \tag{2.4}$$

which leads to the velocity profile shown in Fig. 2.2c. The core radius r_c is defined as half the distance between the two swirl velocity peaks $V_{\theta,\mathrm{max}}$, where Eq. (2.4) becomes:

$$V_{\theta,\mathrm{max}} = \frac{\Gamma_\mathrm{c}}{2\pi r_\mathrm{c}} \tag{2.5}$$

The swirling motion of the vortex evokes high centrifugal forces on the contained fluid particles and therefore a reduction of the static pressure p_static and density ρ within the vortex core, as depicted in Fig. 2.2d. The reduced core density – and the corresponding change of the refractive index of the fluid – enables the detection of trailing vortices via optical schlieren methods, as shown in Subsection 3.3.10 and Chapter 5.

The vortex shape parameters described here are applied in Chapter 3 for the analysis of blade tip vortices shed by a hovering model scale rotor. Specifically, the radial distribution and peak values of the swirl V_θ and axial velocity V_z, and core radius r_c will be analyzed, in combination with the convectional movement and meandering of the vortex positions with respect to the blade tip position.

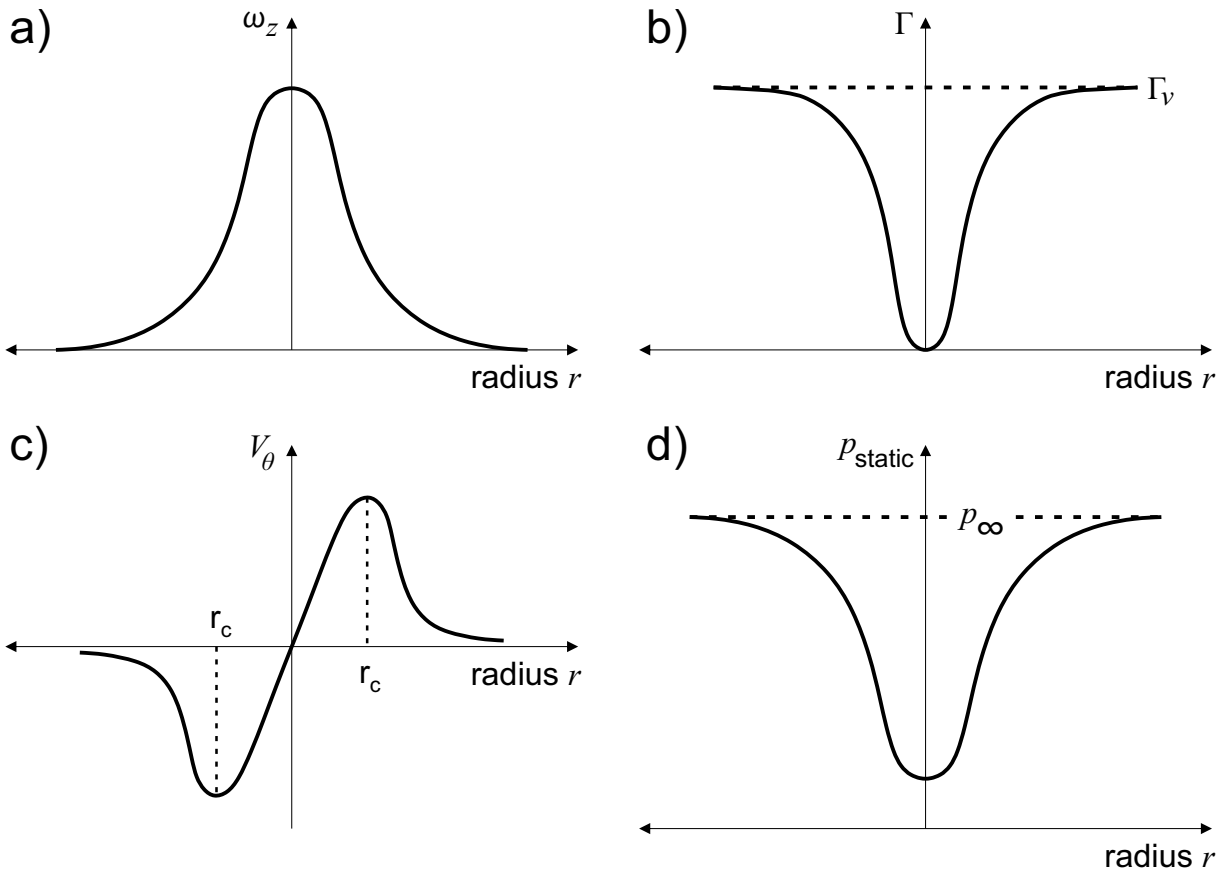

Figure 2.2: Schematic distribution of **a)** vorticity, **b)** circulation, **c)** swirl velocity, and **d)** static pressure over a vortex

2.1.4 Vortex models

Over the past centuries, various algebraic formulations and simplified solutions of the Navier-Stokes equations have been found for the radial swirl velocity distribution in a trailing vortex. The solutions of the Navier-Stokes equations comprise the potential, Batchelor, Lamb-Oseen, and Ramasamy-Leishman vortex model. The relevant algebraic formulations for the present study are the Scully or Kaufmann, Bagai-Leishman, Vatistas, and Ramasamy-Leishman models. These models for the radial swirl velocity distribution of a vortex are presented here and plotted in Fig. 2.3 for comparison. The non-dimensional radius $\bar{r} = r/r_c$ is introduced to simplify the corresponding equations.

The potential vortex model has already been specified in Eq. (2.4). The simple potential formulation does not capture the swirl velocity distribution within the core of a trailing tip vortex and has the singularity $V_\theta \to \infty$ for $r \to 0$. In the 19th century, Rankine proposed an extension of this model by introducing a solid body rotation inside the vortex core (Acheson 1990):

$$V_\theta(\bar{r}) = \begin{cases} \dfrac{\Gamma_v r_c}{2\pi}\bar{r} & \bar{r} \leq 1 \\ \dfrac{\Gamma_v}{2\pi r_c}\dfrac{1}{\bar{r}} & \bar{r} > 1 \end{cases} \tag{2.6}$$

The Rankine vortex model still features a discontinuity for $\bar{r} = 1$. In 1964, Batchelor derived a simplified solution of the Navier-Stokes equations with the assumption that the axial gradients in the vortex flow field are much smaller than the radial gradients. In cylindrical coordinates, the axial (V_z), radial (V_r), and azimuthal (V_θ) velocity components are given as:

$$V_z(\bar{r}) = V_{z,\infty} + \frac{V_0}{\left(r_\mathrm{c}/r_{\mathrm{c},0}\right)^2} e^{-\bar{r}^2} \tag{2.7}$$

$$V_r(\bar{r}) = 0 \tag{2.8}$$

$$V_\theta(\bar{r}) = qV_0 \frac{1 - e^{-\bar{r}^2}}{\bar{r}_0} \tag{2.9}$$

where $V_{z,\infty}$ is the free-stream axial velocity, V_0 is the velocity scale, q is the swirl strength as the ratio of the peak swirl velocity and core velocity, and $\bar{r}_0$ is the initial non-dimensional radius. For $V_{z,\infty}/V_0 = 0$ and infinitely large swirl number q, the Batchelor vortex reduces to the Lamb-Oseen vortex (Lamb 1932, Oseen 1911) with the azimuthal velocity distribution:

$$V_\theta(\bar{r}) = \frac{\Gamma_\mathrm{v}}{2\pi r_\mathrm{c}} \left(\frac{1 - e^{-\alpha_\mathrm{L}\bar{r}^2}}{\bar{r}} \right) \tag{2.10}$$

where $\alpha_\mathrm{L} = 1.25643$ is the Lamb's constant. The Lamb-Oseen model represents a laminar vortex that decays due to viscosity. The tip vortices of large-scale model rotors, however, operate in a turbulent or transitional flow regime, characterized by a higher vortex Reynolds number:

$$Re_\mathrm{v} = \frac{\Gamma_\mathrm{v}}{\nu} \tag{2.11}$$

where ν is the fluid's viscosity. An approximated formulation of the Reynolds number of a rotor blade tip vortex is derived by introducing the thrust coefficient C_T, rotor solidity σ, and the rotor tip speed $V_\mathrm{tip} = \Omega R$ with the rotor rotational frequency Ω and rotor radius R (Leishman 2006):

$$Re_\mathrm{v} = \frac{2\Omega R c}{\nu} \left(\frac{C_\mathrm{T}}{\sigma} \right) \tag{2.12}$$

where $C_\mathrm{T} = T/(\rho_\infty \pi \Omega^2 R^4)$ and $\sigma = N_\mathrm{b} c/(\pi R)$, with the rotor thrust T, ambient density ρ_∞, blade number N_b, and chord length c. Ramasamy & Leishman (2006a, 2007) developed a transitional vortex model based on Re_v that has been iteratively solved and approximated for a range of vortex Reynolds numbers Re_v, leading to an analytical expression with the fit coefficients a_n, b_n:

$$V_\theta(r) = \frac{\Gamma_\mathrm{v}}{2\pi r} \left[1 - \sum_{n=1}^{3} a_n \, e^{-b_n r} \right] \tag{2.13}$$

In addition to the formulations derived from the Navier-Stokes equations, selected algebraic models are also considered here. One of the most versatile algebraic models was described by

Vatistas et al. (1991):

$$V_\theta(\bar{r}) = \frac{\Gamma_v}{2\pi r_c} \frac{\bar{r}}{(1+\bar{r}^{2n})^{1/n}} \tag{2.14}$$

where n is an integer variable. For different values of n, some well-known vortex models are obtained. For $n \to \infty$, Eq. (2.14) turns into the Rankine model; for $n = 1$, the vortex model of Kaufmann (1962) or Scully & Sullivan (1972) is derived:

$$V_\theta(\bar{r}) = \frac{\Gamma_v}{2\pi r_c} \frac{\bar{r}}{(1+\bar{r}^{2})} \tag{2.15}$$

and for $n = 2$, the Bagai-Leishman model (Bagai & Leishman 1995) is given:

$$V_\theta(\bar{r}) = \frac{\Gamma_v}{2\pi r_c} \frac{\bar{r}}{(1+\bar{r}^{4})} \tag{2.16}$$

Figure 2.3 gives a comparison of the vortex models that are presented in this section. The chart shows the swirl velocity distribution over the normalized vortex radius $\bar{r}$ relative to the peak value $V_{\theta,\max}$ at $\bar{r} = 1$. The Ramasamy-Leishman model is plotted for a vortex Reynolds number of $Re_v = 131000$ to match the model rotor hover tests described in Chapter 3. The corresponding n numbers of the Vatistas model are indicated in the plot legend. The main differences between the models occur outside the vortex core, where the radial decrease in swirl velocity differs significantly.

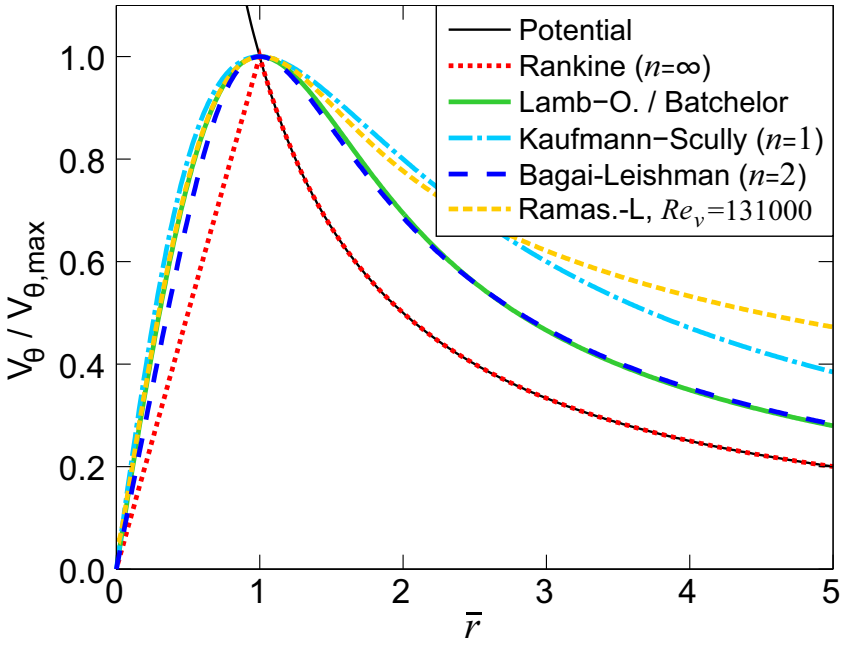

Figure 2.3: Vortex-induced swirl velocity distribution over radius for various models

2.1.5 Vortex decay and breakdown

Lifting wings continuously produce trailing tip vortices that remain coherent several chord lengths behind the wing. Their shape and strength, however, change with time due to the influence of dissipative effects and growing instabilities. The vortex diffusion is driven by viscosity, which results in an expansion of the vortex diameter and a decrease in vortex circulation. The rate of this decay depends on several factors, including the level and distribution of turbulence in the vicinity of the vortex core, which governs the transport of kinetic energy away from the vortex (see e.g. Squire 1965, Iversen 1976, Ramasamy & Leishman 2007). Formulations for the growth of the vortex core exist for different core turbulence levels. The Lamb-Oseen model features a laminar vortex core that decays due to viscosity. The vortex core growth is estimated as

$$r_c(t) = \sqrt{4\alpha_L \nu t} \tag{2.17}$$

with the time t and kinematic viscosity ν. The predicted core growth of this model was found to be unrealistically small due to its laminar formulation. Squire (1965) therefore modified the core growth rate to take into account the average effects of turbulent mixing by adding an eddy viscosity term:

$$r_c(t) = \sqrt{r_0^2 + 4\alpha_L \nu \delta t} \tag{2.18}$$

Equation (2.18) contains the core radius r_0 at the time $t = 0$ and the ratio of apparent to actual viscosity $\delta = 1 + \nu_t/\nu = 1 + a\,Re_v$, where ν_t is the effective turbulent value of viscosity and a is an empirical factor. For small values of Re_v, the model reduces to the laminar Lamb-Oseen model. The assumption of a fully laminar or turbulent vortex does not agree with flow visualizations of vortices (Martin et al. 2003, Ramasamy & Leishman 2006a), which suggest a radial transition from laminar to turbulent flow. Ramasamy & Leishman (2007) therefore modified Squire's formulation by replacing the value of ν_t with an empirical formulation including a so-called *vortex intermittency function*, which models the radial variation of the vortex turbulence level.

In general, the transitional and turbulent core growth models correlate well with experimental results from model rotor measurements for completely rolled-up vortices. For very young vortex ages below $\psi_v = 45°$ (measured as rotor azimuthal distance behind the blade), however, several studies have found a very weak growth of the core radius (Martin & Leishman 2002, McAlister et al. 2001a) or no clear trend at all (Coyne et al. 1997, Bhagwat & Leishman 2000, Mahalingam & Komerath 1997, Ramasamy et al. 2009a). According to Ramasamy & Leishman (2004), this is caused by the positive strain rates that occur during the vortex roll-up process, which are known to counter the effects of vortex diffusion.

Apart from the gradual decay of kinetic energy of the vortex, Spalart (1998) specified a second category of sudden decay due to the occurrence of a critical event that leads to the three-dimensional deformation of the vortex, followed by a breakdown to small scales and the dissipation of the kinetic energy. Lim & Cui (2005) studied this sort of vortex breakdown by visualizing vortices in a cylindrical container, generated by a rotating end wall. In particular, they observed vortex breakdown patterns that are also found for helicopter blade tip vortices, including large-scale *smooth sinuous wavetype* (Sullivan 1973), and small-scale *helical instabilities*, as

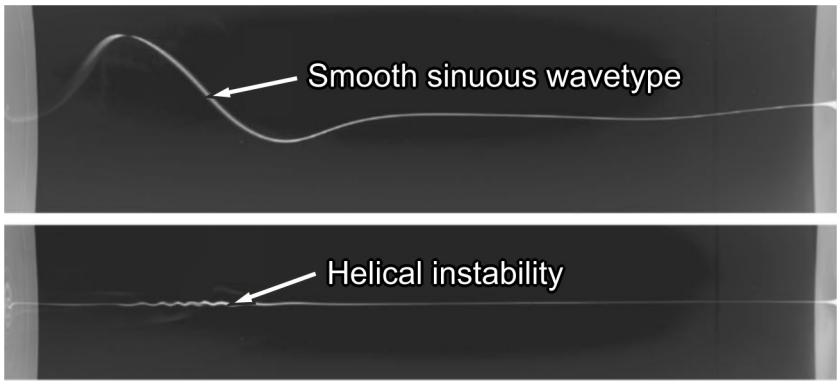

Figure 2.4: Vortex instability patterns,after Lim & Cui (2005)

depicted in Fig. 2.4. The *smooth sinuous wavetypes* are instability patterns that are commonly observed on helicopter rotors in hover flight (Sullivan 1973). They are relatively stable formations that can grow in amplitude with wake age. The *helical instabilities* or *short wavelength instabilities* were first observed by Norman & Light (1987) for highly loaded propellers or tiltrotors. Under rare conditions, they can also occur on helicopter rotors.

2.2 Rotor blade tip vortices

The flow field of a helicopter rotor and the corresponding tip vortices are highly dynamic and three-dimensional. Compared with a fixed-wing, these tip vortices possess a strong curvature and can undergo interactions with the rotor blades, helicopter fuselage, and ground. For a hovering rotor, the vortices form a helical wake below the rotor plane and predominantly convect downwards and radially inwards according to the momentum theory (Glauert 1922), as schematically illustrated in Fig. 2.5a. The graph in Fig. 2.5a depicts a side view of the vortex system of a four-bladed rotor with vortices colored by the blade they trail from. The vortex system is skewed during forward flight and the young vortices convect close to the rotor plane, as sketched in Fig. 2.5b. For descent and banking turn maneuvers, part of the vortex trajectories can even be located above the rotor plane and the distance between the vortices and the rotor blades becomes small enough for BVI to occur. BVI are of high interest for rotorcraft manufacturers due to their impact on the helicopter's sound emission and will be discussed in Subsection 2.2.1, followed by a summary of passive and active measures against BVI in Subsection 2.2.2.

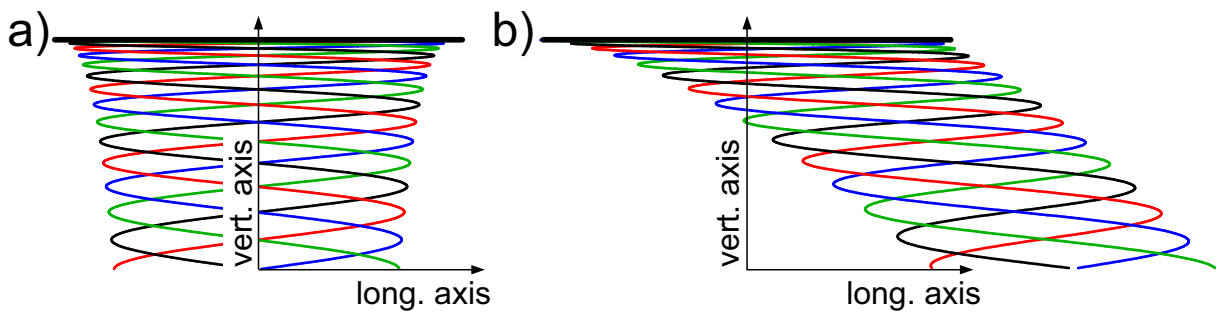

Figure 2.5: Sketches of the vortex system of **a)** a hovering rotor and **b)** a rotor in forward flight

2.2.1 Blade-vortex interactions

The sound generation of helicopters is dominated by aerodynamic phenomena that occur on the main rotor (George 1978). This comprises main rotor high-order harmonics, main rotor random loadings due to atmospheric turbulence, and impulsive noise. Especially the impulsive noise is only weakly attenuated by the atmosphere and dominates the sound immission on the ground. Impulsive noise is produced by high Mach number effects on the advancing blade side called *high-speed impulsive noise*, and by *blade-vortex interactions* and the corresponding secondary stall and shock effects. BVI occurs during various flight conditions, but the most detrimental effects occur during descent or banking maneuvers. Here, a vortex that was created at the forward edge of the rotor disk convects above the blades and traverses the rotor disk in its rear half, where the vortex encounters a rotor blade at a shallow angle and with a short miss distance. The induced velocity field of the vortex interacts with the flow around the rotor blade and causes high frequency pressure fluctuations on the blade surface that induce structural vibrations and emit impulsive noise. An example for these blade surface pressure fluctuations during BVI is given in Fig. 2.6 (van der Wall et al. 2004). The graph depicts the normalized leading edge pressure distribution of a model rotor during a 6° descent that was measured and mapped to the rotor plane. The radial streaks of alternating sign in the right half of the plane represent the BVI-induced pressure fluctuations. The magnitude of the BVI effect primarily depends on the strength and circulation distribution of the vortex, and its miss distance, interaction length, and orientation with respect to the interacting rotor blade (Hardin & Lamkin 1986).

BVI has been the subject of extensive research over the past decades, some of which will be summarized here. In 1977, Tangler tested a model rotor during descent and high-speed flight. He used a schlieren setup to visualize bow shocks on the blades and the tip vortices during BVI. Splettstoesser et al. (1984) compared sound pressure levels from a full-scale BVI flight test with data from a large-scale model rotor under similar conditions. Between 1981 and 1989, American helicopter manufacturers were funded by the NASA-AHS National Rotorcraft Noise Reduction program to investigate means of helicopter noise prediction and reduction (Childress 1991). This program included full-scale flight tests, a model rotor hover test, a main rotor-tail rotor in-

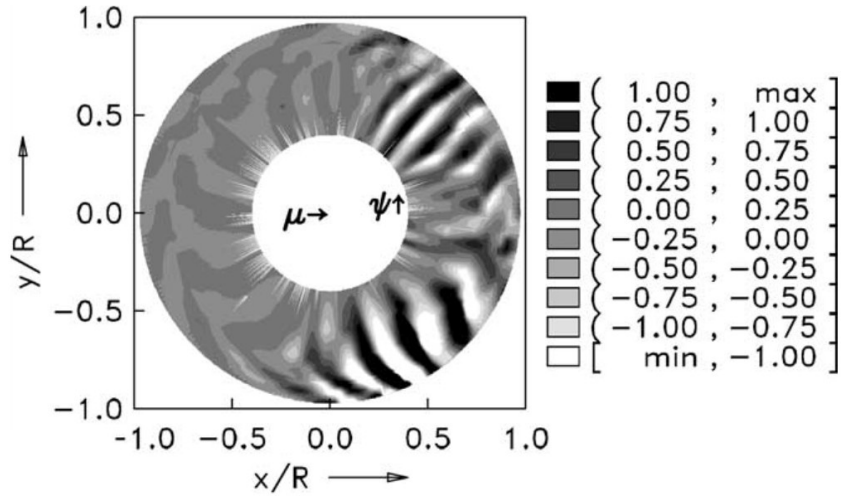

Figure 2.6: Normalized leading edge pressure distribution for a 6° descent, as measured in the HART II model rotor test, after van der Wall et al. (2004)

teraction test, and a main rotor sound test in a large-scale wind tunnel. In 1988, Caradonna et al. used a fixed 3D airfoil upstream of a model rotor to generate an interacting vortex and measured the blade surface pressure distribution during the interaction. Within the European HELINOISE project, a comprehensive wind tunnel test with an instrumented main rotor model of the BO 105 was conducted to determine the relationship between the blade pressure fluctuations and the acoustic radiation, and to investigate vortex locations during BVI (Splettstoesser et al. 1995). In 1996, Raffel et al. applied *laser Doppler velocimetry* (LDV) and PIV to a model rotor in forward flight and investigated the vortex strength and position for BVI-relevant cases. Horner et al. (1994) and a number of recent studies completely went without a rotor and used a 3D airfoil to generate a vortex upstream of a second airfoil in a wind tunnel to simulate parallel BVI (Horner et al. 1994, Klein et al. 2014, Rival et al. 2010, Peng & Gregory 2015). The results of these studies comprise velocity fields around the interacting airfoil during the vortex encounter (Horner et al. 1994, Klein et al. 2014), investigations of the vortex breakdown after the interaction and BVI-induced stall on the interacting blade (Rival et al. 2010), as well as the investigation of the influence of miss distance and sense of vortex rotation on the interaction (Peng & Gregory 2015). Ramasamy et al. (2014) and Bhagwat et al. (2015) studied the effects of orthogonal BVI with a similar dual-airfoil setup and PIV. The focus of these studies was on the interaction of the two tip vortices and the effects on the lift and circulation distribution of the interacting wing.

2.2.2 Measures against BVI

The detrimental effects of blade-vortex interactions – such as the generation of sound and vibrations, and a reduced rotor performance – have stimulated extensive research on active and passive measures that reduce the ramifications of BVI. The review paper of Yu (2000) contains an extensive overview of actuation methods to counter the effects of BVI. Here, the most important passive and active actuation methods will be introduced.

Passive measures against BVI

There are a number of helicopter design variables that can reduce the strength of aerodynamic interactions on helicopters, including the number of blades N_b, blade loading C_T/σ, tip Mach number M_tip, and shape of the blade tip (see e.g. Allongue et al. 1999, Smith & Sigl 1995, Koushik & Schmitz 2014). Allongue et al. (1999) and Bebesel et al. (1999) performed flight tests with variable rotor speed and ground microphone measurements. Allongue et al. found that a 10 % decrease in tip speed resulted in a noise reduction of up to 3 dB, whereas Bebesel et al. found a noise decrease of 0.6 – 1.1 dB due to a 2% decreased tip speed. Multiple tip geometries have been thought of and tested over the past 40 years, such as rounded, swept, tapered, parabolic, anhedral, and ogee tips, as well as tips with spoilers and sub-wings. McAlister & Takahashi (1991) and Coyne et al. (1997) investigated the influence of a rounded planform and a rounded tip cap on the vortex strength. They found a reduction in the axial velocity deficit, but only a marginal influence on the swirl velocity that became insignificant in the far field. Bebesel et al. (1999) performed a flight test with parabolic blade tips and found a noise reduction of 3.8 dB during approach. Also in 1999, Allongue et al. flight-tested a parabolic, tapered, and thin blade tip and found a noise reduction of 2.8 dB during approach.

The *British Experimental Rotor Programme* (BERP) developed a blade tip shape that reduces shock effects on the advancing side and delays blade stall on the retreating side with a combination of sweep, a thin airfoil, and a leading edge notch. The BERP blade tip achieved a reduction in BVI-related noise of up to 5 dB during descent, in combination with an increased maximum cruise speed of the helicopter (Lowson 1992). Hoad (1979) and Brocklehurst & Pike (1994) investigated the effects of a sub wing (vane) tip on a model rotor in descending forward flight. The sub wing tip produced two separate tip vortices that had a reduced impact on interacting rotor blades. BVI-induced noise was thus reduced by $4 - 5.6$ dB, while no adverse effects on the control loads or performance were reported. The test of a rectangular and swept-back parabolic-anhedral blade tip during the HELISHAPE wind tunnel test, on the other hand, did not achieve a significant noise reduction (Schultz et al. 1996). The application of a turbulence generator to the tip of a 3D airfoil caused a promising decrease in peak swirl velocity of the tip vortex of 57%, but at the cost of an 18% increase in torque (McAlister et al. 2001b).

Slotted blade tips constitute a second form of passive actuation to reduce the ramifications of BVI (Dancila & Vasilescu 2002, Vasilescu 2004, Han & Leishman 2004). This sort of actuator operates passively, as it does not require any sort of control or power input to operate, but actively influences the tip vortex by introducing jets of air at the tip side edge that intensify the vortex diffusion. The jets are generated by pressure gradient-driven flow through tubes connecting the leading edge with the tip side edge. Han & Leishman (2004) found that a slotted blade tip reduced the peak swirl velocity of the vortex by up to 60% compared to an unmodified blade, with a simultaneous enlargement of the core radius by a factor of $2 - 3$, and a $2 - 3\%$ increase in rotor power consumption. In a similar study, Vasilescu (2004) found a reduction in peak swirl velocity of 16% and 2.8 times larger core radii compared to a rounded passive tip.

The results obtained by passive modifications of the blade tips show that the strength and – to some extend – the trajectory of a trailing vortex can be modified. Typical noise reduction levels, however, have stagnated at about $3 - 5$ dB and seem to only be increasable further by simultaneously reducing the helicopter's performance or maneuverability.

Active measures against BVI

Active control concepts, on the other hand, still exhibit significant potential to achieve higher control authority over the BVI phenomenon. Even more than for the passive actuators, the gains by active actuation have to be weighed against the penalties such as additional power consumption and aircraft safety. A suitable active actuator uses little additional power to reduce the effects of BVI. There are currently two main concepts for active control of blade tip vortices. The first is based on influencing the vortex during its formation via air injection or through zero-net-mass jets. The second concept is based on the mechanical variation of the blade pitching motion, leading to a periodic modification of the span-wise lift distribution. It can be separated into active blade control from the fixed frame via the swash plate (*higher harmonic control*, HHC) and blade-individual actuation in the rotating frame (*individual blade control*, IBC).

The concept of *tip air mass injection* (TAMI) for tip vortex modification was first thought of in the 1970s. White Jr. et al. (1975, 1980) were the first researchers to investigate the application of chord- and span-wise blowing to full-scale helicopter rotors in a wind tunnel. The chord-wise

air injection resulted in spreading of the tip vortex and the span-wise blowing altered the vortex structure and displaced the tip vortex further outboard. For a BVI case, White Jr. et al. (1975) acquired sound spectra, from which they estimated a maximum noise reduction of $8 - 25$ dB. In later tests, White Jr. (1980) reported an overall noise level reduction of 7.5 dB for TAMI on a model rotor under simulated BVI conditions. The corresponding increase in power requirement was estimated as 3% of the total power for the implementation on a full-scale helicopter.

Higher harmonic control was initially developed for the reduction of blade vibrations and it was Hardin & Lamkin (1986) who first suggested its application for BVI-related noise reduction. In principle, the static swash plate control in the non-rotating frame during a certain flight state is superimposed with higher harmonic actuator controls to induce a periodic change of the blade pitch. With a typical swash plate setup, the higher harmonic actuation frequencies are limited to $N_b - 1$, N_b, and $N_b + 1$ per revolution. As an effect of this actuation, the blade lift distribution is locally modified to decrease the vortex strength and/or change the vortex trajectories at the BVI-relevant azimuthal locations. DLR, ONERA, NASA, and the US Army AFDD cooperated in a series of HHC tests that were conducted with a 4 m diameter Mach-scaled BO 105 rotor under BVI-relevant conditions in the DNW-LLF wind tunnel. In the first test of this series, Brooks et al. (1991) demonstrated the influence of HHC on the blade movement and the distribution and overall noise level below the rotor, which could be reduced by 6 dB for advancing side BVI, at the cost of increased blade vibrations. These results were confirmed by similar investigations in the *HHC Aeroacoustic Rotor Tests* (HART, Kube et al. 1996, Splettstoesser et al. 1997). During the HART I tests, Kube et al. applied microphone and flow field measurements, in combination with flow field visualization to localize the occurrence of BVI and quantify the effects of HHC on the blade tip vortices. In the follow-up project HART II (Yu et al. 2002, van der Wall et al. 2004), the database of BVI-relevant parameters was further expanded, especially with flow field data around the vortices, as obtained by PIV.

Parallel to the HHC development, multiple research groups worked on the realization of individual blade control (Ham 1983) for BVI noise reduction. Morbitzer et al. (1998) were among the first to realize an IBC concept based on actively controlled pitch links between the swash plate and the rotor blades in the rotating frame. In wind tunnel and flight tests, Morbitzer et al. demonstrated the simultaneous reduction of the blade vibrations and the overall BVI-induced noise level by up to 12 dB via multi-harmonic actuation with superimposed 2/revolution ($2/rev$) and $5/rev$ actuation frequencies. Jacklin et al. (2002) also demonstrated the application of IBC on a full-scale rotor in a wind tunnel via hydraulic pitch links, with a resulting variation in angle of attack of up to $\pm 3°$, a vibration reduction of up to 70%, and an overall BVI noise reduction of up to $6 - 8$ dB.

The development of smart materials – such as piezoelectric or magnetostrictive materials (Chopra 2000) – enabled the design of new IBC actuators that are implemented inside the rotor blades. The *active trailing edge flap* is one example of this design and based on mechanically amplified piezoelectric actuators. The higher harmonic trailing edge flap movement causes a change in blade curvature and induced blade twist, thus altering the blade lift distribution. The advantage of this concept with respect to the active pitch link design is that the flaps can be positioned only at the necessary blade location and require less actuation power and no hydraulic slip ring. The restricted installation space, however, leads to complex mechanical constructions and a corresponding mass-balancing weight penalty. Marcolini et al. (1995) conducted the first

wind tunnel test with an active trailing edge flap on a rotor. Microphone measurements detected a decrease of 4 dB in the average BVI-related noise level, with a corresponding high increase in rotor power. Schimke et al. (1997) demonstrated the applicability of an active trailing edge flap for dynamic stall flow control on an oscillating 2D airfoil in a transonic wind tunnel. They found that the maximum trailing edge flap deflection of ±5° had a comparable effect as a blade root deflection of 1°. Koratkar & Chopra (2002) designed a piezoelectric trailing edge flap and tested it on a model helicopter rotor in a wind tunnel. The flap deflection amplitude was of the order of 7° and enabled a vibration reduction of 80 – 95 % with a close-loop controller.

Piezoelectric actuators have also been applied for *active twist* blade actuation. Bernhard & Chopra (1996) and Wells & Glinka (1997) designed and numerically investigated a blade-internal actuator to solely actuate a pivoted blade tip, a so-called *flip-tip*. The separate blade tip was dynamically tested on an unloaded rotor and exhibited deflections of up to ±1.25°. Other active twist concepts are based on radially distributed twist actuators that integrally twist the entire rotor blade. In 1997, Chen & Chopra tested a Froude-scaled active twist rotor model under hover conditions, resulting in ±0.4° twist at the blade tips. In 1997, NASA, the US Army, and MIT began a collaboration in the *Active Twist Rotor* (ATR) project, with the goal of demonstrating the active twist concept on a model rotor during forward flight. The ATR rotor was tested in hover (Wilbur et al. 2001) and in a wind tunnel (Wilbur & Yeager 2002), where it demonstrated a tip twist response of 0.75° – 1.5° with a vibration reduction for certain targeted frequencies by up to 100%, at a power requirement of < 1% of the rotor power.

Concluding remarks about measures against BVI

The high control authority of the active twist actuation concept, in combination with its small power requirement, led to the creation of the *smart-twisting active rotor* (STAR) consortium, consisting of DLR, ONERA, NASA, the US Army AFDD, JAXA, Konkuk University, and KARI. The goal of this cooperation was to manufacture an active twist rotor and demonstrate its control authority over BVI effects during a wind tunnel test. In preparation for the wind tunnel entry, a hover test was conducted in the rotor preparation hall at DLR Braunschweig, as described by Hoffmann et al. (2014). The vortex characterization presented in Chapter 3 is based on this hover test and contains a detailed analysis of the effects of active twist actuation on the shed blade tip vortices.

3 STAR hover test

Active rotor control concepts – such as the ones presented in the previous chapter – have a high potential for the reduction of *blade-vortex interaction* (BVI)-induced vibrations and noise on helicopter rotors. The active twist concept showed especially promising results in previous tests (Chen & Chopra 1997, Wilbur et al. 2001, Wilbur & Yeager 2002, see Subsection 2.2.2 for details). An active twist rotor based on the design of the 41 % Mach-scaled BO 105 blades was designed and tested within the *smart-twisting active rotor* (STAR) project. The project was funded by a consortium consisting of DLR, ONERA, NASA, US Army AFDD, JAXA, Konkuk University, and KARI. Its goal was to demonstrate the control authority of an active twist rotor over BVI effects during a measurement campaign in the *large low-speed facility* (LLF) wind tunnel of the DNW. In preparation for this wind tunnel entry, a hover test was conducted in the rotor preparation hall at DLR Braunschweig. The test comprised measurements of the rotor hub forces and moments, optical and on-blade acquisition of the blade angles and deformations, on-blade pressure measurements, and a characterization of the young blade tip vortices via high-speed stereoscopic *particle image velocimetry* (PIV) and high-speed stereoscopic *background-oriented schlieren* (BOS) measurements. An overview of the test program with representative results and a preliminary PIV evaluation was given by Hoffmann et al. (2014), and some of the PIV results presented in this chapter have already been published by Bauknecht et al. (2015).

A description of the relevant measurement techniques for this study – such as PIV and the BOS method – is given in Section 3.1. The hover test setup is described in Section 3.2, followed by a description of the data processing methods (Section 3.3) that were utilized for the data analysis in this study. Results of an unactuated *baseline* (BL) case are presented in Section 4.1. A thrust variation study was conducted and is analyzed in Section 4.2. The results of the active twist actuation cases with different actuation frequencies between 1 and 5 per revolution ($1/rev - 5/rev$) are given in Section 4.3. Finally, the results of the STAR test are summarized in Section 4.4.

The temporal resolution of the PIV recordings allowed for the analysis of time-resolved vortex trajectories for all test cases. Characteristic vortex properties such as the maximum axial velocity V_z, peak swirl velocity V_θ, and the core radius r_c were computed based on individual velocity fields and individually averaged. By conducting both PIV and BOS measurements, a comparison of vortex trajectories obtained from the two measurement systems is possible. Highly resolved *laser speckle-illuminated* BOS (Meier & Roesgen 2013) allowed for the reconstruction of the density within the vortex core for multiple test cases. The combined results of the PIV and BOS measurements enabled an investigation of the effects of the active twist actuation on the blade tip vortex system of the STAR rotor under hover condition.

3.1 Measurement Techniques

A description of the measurement techniques applied for the STAR hover test is given below. As particle image velocimetry has become a standard measurement technique, it will only be explained briefly in Subsection 3.1.1. The behavior of PIV seeding particles is characterized in Subsection 3.1.2, and the basics of a high-speed stereoscopic PIV setup are covered in Subsection 3.1.3, followed by a literature review about the application of PIV to rotor flow in Subsection 3.1.4. The principles of the background-oriented schlieren method are presented in Subsection 3.1.5, and a laser-speckle illuminated variant of BOS is introduced in Subsection 3.1.6.

3.1.1 Particle image velocimetry

PIV has been used for over three decades and has become a standard measurement technique in experimental fluid dynamics. Its principles are described in detail by Adrian & Westerweel (2011) and Raffel et al. (2007) and will only be summed up briefly here. PIV is an optical, indirect, and non-intrusive method for the instantaneous measurement of *two* to *three components* (2C,3C) of the velocity in a quasi-*two-* or *three-dimensional* (2D,3D) measurement domain. Figure 3.1 depicts a standard PIV setup for a wind tunnel measurement, after Raffel et al. (2007). It consists of a pulsed light source, such as a laser, to create a thin light sheet within the flow field using light sheet optics and mirrors. The light source produces two light pulses that illuminate tracer particles within the flow at two consecutive points in time t and t' with

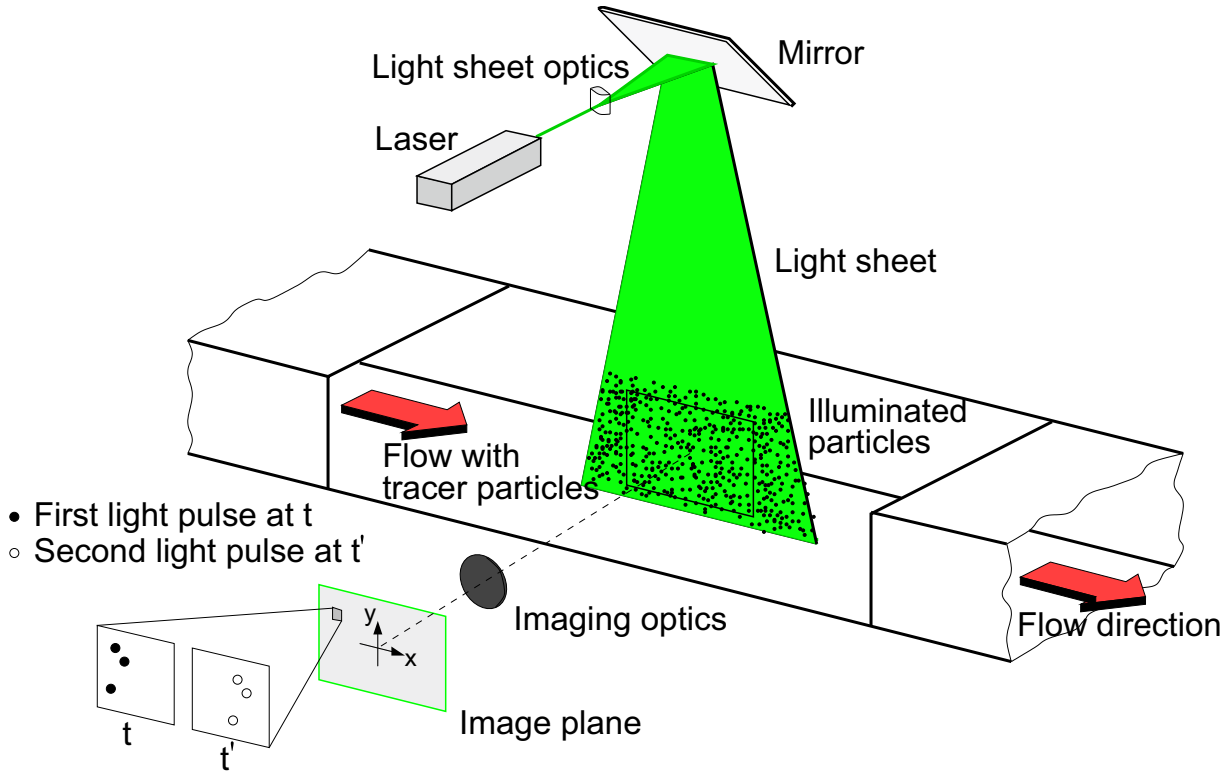

Figure 3.1: Basic PIV setup in a wind tunnel, after Raffel et al. (2007)

a well-defined time delay Δt in between. The illuminated particles are imaged by a (digital) camera with its image plane positioned parallel to the light sheet. State-of-the-art double-frame cameras capture the two particle images in two different frames, as indicated in the bottom left corner of Fig. 3.1. The recorded particle images are evaluated by splitting the image plane into smaller interrogation windows and computing the average displacement within these sub-fields via cross-correlation between the two frames. The resolution of the displacement field is determined by the size of the interrogation windows L_m, but can be increased by introducing an overlap for the interrogation windows. The velocity field V is computed from the imaged particle displacements $d = (d_x, d_y)$ and the time delay (pulse separation time) Δt as:

$$V = \frac{d}{M\Delta t} = \frac{D}{\Delta t} \tag{3.1}$$

where M is the magnification factor between the imaged displacements $d_x = x' - x$ and $d_y = y' - y$ and the physical particle displacements $D_x = X' - X$ and $D_y = Y' - Y$ in the measurement plane.

It is understood that the cross-correlation algorithms used for the PIV evaluation are of a statistical nature and represent the mean velocity of the particles within an interrogation window. To resolve high gradients in the flow field, the size of the interrogation windows has to therefore be as small as possible. The limit of this size reduction is given by a minimum number of particles that have to be present in the interrogation window in both PIV frames. The particle displacement should therefore not exceed $1/4$ of the interrogation window size (Adrian 1991), which limits the pulse separation time of the laser Δt and the accuracy of the measurement. Adaptive grid interrogation schemes, such as the multi-grid method (Scarano & Riethmuller 1999), can be applied to circumvent this restriction. The adaptive multi-grid scheme is based on the evaluation of a large particle displacement via a cascade of interrogation windows with successively decreasing size. The initial large interrogation window has to fulfill the $1/4$ rule stated by Adrian and is used to predict a coarse particle displacement that is then used to restrict the search area for a refined interrogation window of smaller size. This evaluation scheme thus combines high measurement accuracy through a large particle displacement and a high measurement resolution through the small final interrogation windows.

The mean particle displacement between two interrogation windows is evaluated by detecting a peak in the corresponding correlation map. The accuracy of this peak detection – and thus the determination of the imaged particle displacements – can reach 0.01 pixels by using subpixel correlation peak detection algorithms (Raffel et al. 2007). To achieve this subpixel accuracy, the recorded particle images have to be larger than 1 pixel to avoid the so-called *peak locking* effect. This effect refers to the tendency of a continuous distribution of particle displacements to be shifted towards integer pixel values, and is caused by the discrete size of the image sensor. Peak locking is just one of the adverse effects of inappropriate tracer particles for PIV, as discussed in the following section.

3.1.2 Seeding particle behavior

As mentioned earlier, PIV is an indirect velocity measurement technique that is based on the displacement detection of tracer particles that are added to the flow. According to Adrian (1991), a

meaningful data evaluation requires between 10 and 20 particles within each interrogation window. A high seeding density is thus necessary to decrease the interrogation window size and achieve a high spatial resolution of the velocity field. For measurements in air, this is typically achieved by employing seeding generators that either evaporate or atomize oil. The diameter of the tracer particles d_P is a crucial factor for PIV. The particles – and thus their inertia – have to be reasonably small to follow an accelerating flow with negligible lag. Raffel et al. (2007) described the velocity lag ΔV between a spherical particle with the velocity V_P and a continuously accelerating flow field with the velocity V_∞ by Eq. (3.2):

$$\Delta V = V_P - V_\infty = d_P^2 \frac{\rho_P - \rho}{18\mu} a_\infty \tag{3.2}$$

where a_∞ is the acceleration, μ the dynamic viscosity of the fluid, and ρ_P and ρ are the densities of the particle and the fluid, respectively. The tracking behavior of particles becomes especially important for the study of shock waves and high curvature flows, such as the flow field in the vicinity of a strong vortex. Here, the particle lag is integrated from the generation of the vortex to the moment the particle image is captured, leading to a reduced seeding density in the vortex core that can be too low for adequate measurements (Raffel et al. 2007).

The need for small particles to achieve a lag-free tracking of the fluid motion conflicts with the requirement for large particles to achieve an appropriate light scattering intensity and to enable the use of subpixel peak detection algorithms for a high accuracy data evaluation. Spherical particles that are much smaller than the wavelength λ_w of the illuminating light ($\ll 0.5\,\mu m$ for green laser light) scatter this incident light according to the Rayleigh model with an intensity variation proportional to d_P^6. Particles that are larger than λ_w are described by the scattering theory of Mie (van de Hulst 1957). For green laser light, the Mie scattering domain begins around particle diameters of $d_P \approx 1\,\mu m$ and describes the scattered light intensity as proportional to d_P^2. A characteristic parameter for the Mie solution is the normalized diameter:

$$q_P = \frac{\pi d_P}{\lambda_w} \tag{3.3}$$

If q_P is greater than one, the angular intensity distribution of the scattering in Fig. 3.2 (from Raffel et al. 2007) has approximately q_P local maxima over the angular range from 0° to 180°. Characteristic properties of the Mie scattering are the highly increased light intensity in the forward direction (*forward scattering*), moderate light intensity in the backward direction (*backward scattering*) and relatively small emission perpendicular to the incident light, as visible in Fig. 3.2. It is therefore advantageous to make use of the forward-scattered light in a PIV setup. The intensity distribution of Fig. 3.2 exhibits fluctuations in scattered light intensity for different observation angles. For densely seeded flow, these fluctuations are reduced by fractions of light that have been scattered by more than one particle (so-called *multi-scattering*) before reaching the image plane. This effect can increase the imaged peak intensity in a PIV recording, but simultaneously raises the background noise level, which typically results in a decreased signal-to-noise ratio (Raffel et al. 2007).

For small particle diameters, the optical camera setup can reach its physical limit, also referred to as *diffraction limited imaging*. The minimum particle image diameter d_{diff} of such a system

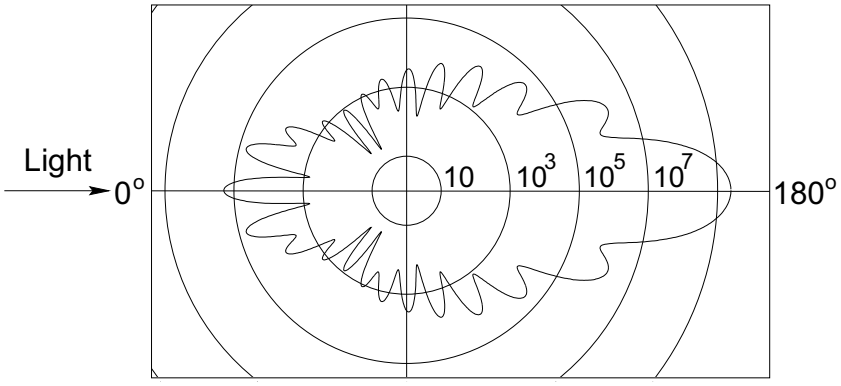

Figure 3.2: Angular intensity distribution of the Mie scattering for a 1 µm oil particle in air and incident light with $\lambda_w = 532\,\text{nm}$, after Raffel et al. (2007)

is approximated as (Adrian & Yao 1985):

$$d_{\text{diff}} = 2.44 f_{\#}(M+1)\lambda_w \tag{3.4}$$

where $f_{\#}$ is the f-number, the ratio between the focal length f and the diameter of the aperture D_a, and M is the magnification factor, which is defined as:

$$M = \frac{z_0}{Z_0} \tag{3.5}$$

with the distance between the object plane and the lens Z_0, and the distance between the lens and the image plane z_0. For larger particles, the size of the particle images increasingly depends on the geometric imaging. Neglecting lens aberrations, the particle image diameter can then be approximated by the Airy function (Adrian & Yao 1985):

$$d_\tau = \sqrt{(M d_P)^2 + d_{\text{diff}}^2} \tag{3.6}$$

The performance of a real optical system with a large aperture diameter is reduced by lens aberration effects. The contrast or image modulation constitutes a practical measure for the characterization of such a real optical system. The variation of the image modulation for different spatial frequencies is described by the *modulation transfer function* (MTF). This transfer function therefore describes the contrast reproducibility of the lens for characteristic frequencies r' that are commonly expressed as lines per mm. Based on the MTF, Raffel et al. (2007) give an approximation for the imaged particle diameter of a real optical system:

$$d_\tau \approx \sqrt{-0.64\frac{\ln[\text{MTF}(r')]}{r'^2} - \left(\frac{M}{2r'}\right)^2} \tag{3.7}$$

Typical PIV seeding contains a distribution of particle sizes, as shown for atomized *di-ethyl-hexyl-sebacate* (DEHS) particles in Fig. 3.3 (Raffel 2015). The curves in Fig. 3.3 represent the *probability density functions* (PDF) of the distribution of particle diameters (q1),

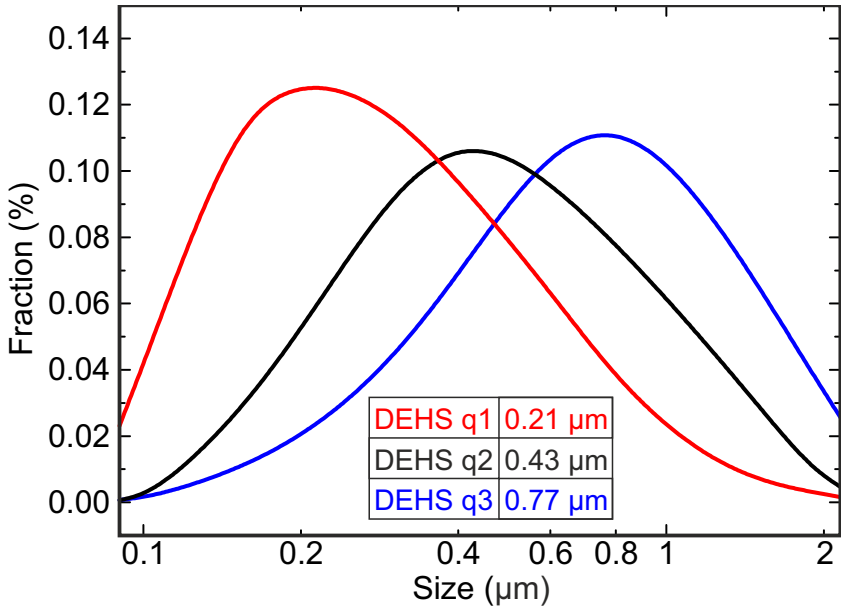

Figure 3.3: PDF of particle sizes of atomized DEHS with distribution of length (q1, red curve), area (q2, black), and volume (q3, blue), after Raffel (2015)

particle cross sections (q2), and particle volumes (q3). The maximum of the q1 distribution (d_P = 0.21 µm for DEHS) is commonly mentioned in literature. For practical PIV applications, particles of this size contribute little to the evaluated velocity field, which is dominated by the larger and brighter particles. The area-weighted distribution (q2) better represents the particle visibility in the PIV raw images, as its proportionality with d_P^2 matches the Mie solution for the intensity of particle-scattered light.

Finally, it should be noted that the concurrence of a seeding void within a vortical flow field and the statistical nature of the interrogation window-based PIV evaluation can affect the velocity output. If the interrogation window partially overlaps an area of inappropriate seeding density, the void area will not influence the corresponding correlation peak. The resulting velocity vector thus only corresponds to the mean velocity within the well-seeded part of the interrogation window and should therefore be shifted away from the void. Moving the interrogation window further into the seeding void will eventually and abruptly cause the loss of a distinct correlation peak and produce a zero correlation, i.e. a vanishing particle displacement. The velocity gradient at the edge of a seeding void is therefore increased, which partially counteracts the spatial averaging effect of the interrogation windows. This restriction of PIV should be considered when measuring velocities in a flow domain with high vorticity and inhomogeneous seeding density.

3.1.3 Stereoscopic particle image velocimetry

The velocity component perpendicular to the laser light sheet – i.e. the *out-of-plane* velocity component – has a strong influence on the imaged particle displacements ($d_x = x_i' - x_i$ and $d_y = y_i' - y_i$) for 3D flows, as illustrated in Fig. 3.4. This velocity component cannot be evaluated with a single camera and results in an uncertainty of the in-plane velocity components. The influence

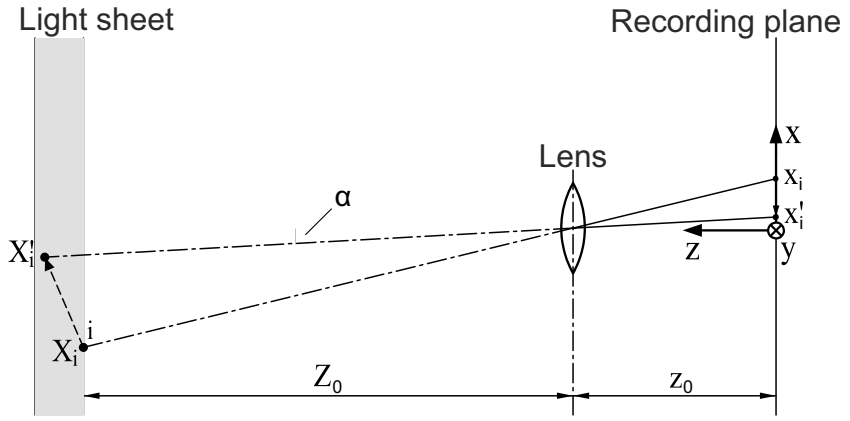

Figure 3.4: Imaging of a particle in the light sheet on the rec. plane, after Raffel et al. (2007)

of the out-of-plane component on the in-plane displacements is described by (Raffel et al. 2007):

$$d_x = x_i' - x_i = -M\,(D_x + D_z\, x_i'/z_0) \tag{3.8}$$

$$d_y = y_i' - y_i = -M\left(D_y + D_z\, y_i'/z_0\right) \tag{3.9}$$

where $D = (D_x, D_y, D_z)$ defines the particle displacement in physical space. Eqs. (3.8) and (3.9) simplify considerably for a negligible out-of-plane displacement D_z. For large out-of-plane components and highly 3D flow, it is crucial to capture D_z to prevent in-plane velocity errors in the range of $> 15\,\%$ (Raffel et al. 2007). This is typically accomplished by utilizing a stereoscopic camera setup, as depicted in Fig. 3.5. To achieve a high precision of the out-of-plane component, the opening angle between the two cameras has to be around 90°. For large setups, this requires the cameras to be mounted on separate support structures. The object plane in the light sheet is imaged with an angle of about $\alpha = 45°$ in a stereoscopic setup, which – in combination with a limited depth of field – causes part of the field of view to be out of focus. To sharply image the entire field of view, the cameras are mounted in a so-called *Scheimpflug arrangement* (Scheimpflug 1904). Following the Scheimpflug criterion, the image plane is tilted by an angle ψ with respect to the lens plane, in order for the object plane, lens plane and image plane of each camera to intersect in a common line. The half opening angles α_1 and α_2 of cameras 1 and 2, respectively, are defined in the $x - z$ plane depicted in Fig. 3.5. The half opening angles β_1 and β_2 are defined accordingly in the $y - z$ plane. With these definitions, the three velocity components u, v, w in the object plane are expressed as (Raffel et al. 2007):

$$u = \frac{u_1 \tan\alpha_2 + u_2 \tan\alpha_1}{\tan\alpha_1 + \tan\alpha_2} \tag{3.10}$$

$$v = \frac{v_1 \tan\beta_2 + v_2 \tan\beta_1}{\tan\beta_1 + \tan\beta_2} \tag{3.11}$$

$$w = \frac{u_1 - u_2}{\tan\alpha_1 + \tan\alpha_2} = \frac{v_1 - v_2}{\tan\beta_1 + \tan\beta_2} \tag{3.12}$$

It is noted that the system of Eqs. (3.10 – 3.12) contains three unknown velocities and four known input values, and thus is overdetermined and has to be solved iteratively. The evaluation of velocities from a stereoscopic PIV setup requires exact knowledge of the relative camera positions and orientations, as well as the angles between the image, lens, and object planes.

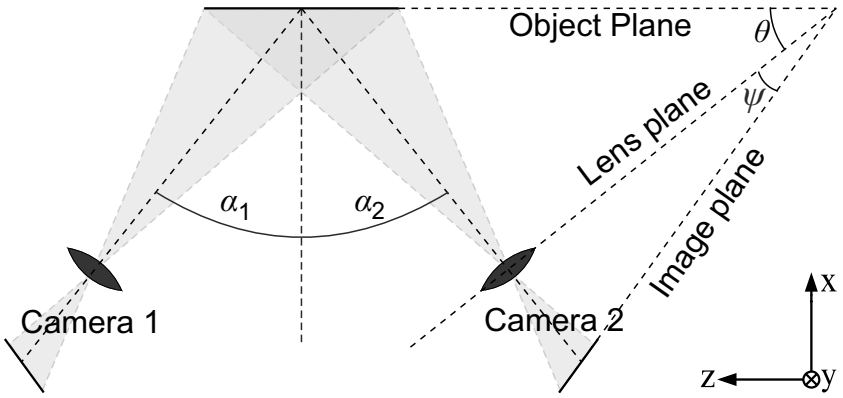

Figure 3.5: Stereoscopic PIV setup in Scheimpflug configuration, after Raffel et al. (2007)

Furthermore, the image mapping function of a stereoscopic camera is more complex than for a single camera with an orthogonal viewing angle and results in a trapezoid field of view in the object plane. It is thus necessary to calibrate the two cameras together before reconstructing the 3C velocity field. Van Oord (1997) proposed an approximate mapping function between the image (x, y) and object plane (X, Y):

$$X = \frac{\mathrm{f}\, x\, \sin\psi}{M_0 \sin\theta\,(x\, \sin\psi + \mathrm{f}\, M_0)} \tag{3.13}$$

$$Y = \frac{\mathrm{f}\, y}{x\, \sin\psi + \mathrm{f}\, M_0} \tag{3.14}$$

with the focal length f, the nominal magnification factor M_0, and the exact angles ψ and θ between the image, lens, and object planes. The formulations in Eqs. (3.13) and (3.14) do not include non-linear effects such as lens distortions and are very sensitive to inaccuracies in the input parameters. A second order image mapping approach is a more robust alternative that has frequently been employed (van Oord 1997):

$$X = a_0 + a_1 x + a_2 y + a_3 x^2 + a_4 xy + a_5 y^2 \tag{3.15}$$

$$Y = b_0 + b_1 x + b_2 y + b_3 x^2 + b_4 xy + b_5 y^2 \tag{3.16}$$

Eqs. (3.15) and (3.16) describe the camera calibration without knowledge of the exact geometry, and can also account for lens distortions and other non-linear effects. The twelve unknown parameters a_i and b_i can be determined by a least-squares method for a minimum of six point pairs for the image and object plane. This is commonly realized by imaging a 2D calibration target with structures such as dots or lines in different positions parallel to the laser light sheet, or by imaging a 3D multi-level calibration target with markers at different exactly defined heights. This calibration approach assumes that the calibration target is exactly aligned with the laser light sheet, which is not always the case or even feasible. The residual offset between target and the center of the light sheet has to be compensated, as small target misalignments cause errors in the reconstructed velocity field. This is commonly done by performing a so-called *disparity correction* or *self-calibration*. This correction is based on the cross-correlation of two mapped particle images that were simultaneously recorded by the two cameras. The corresponding disparity map is then used to compute the real position of the target within the light sheet.

3.1.4 PIV on rotors and its predecessors

The flow field around a helicopter rotor and the corresponding tip vortices is highly 3D and dynamic. Compared with a fixed-wing, the tip vortices possess a strong curvature and can undergo interactions with the rotor blades and the fuselage. Especially the blade-vortex interactions are of high interest due to their impact on the helicopter's sound emission, as already discussed in Subsection 2.2.1. An overview of the extensive research on rotor aerodynamics is given here.

A large number of experiments have been conducted over the past decades to advance our understanding of the complex flow field around (model) helicopter rotors. The first studies on helicopter blade tip vortices were conducted by whole-field flow visualization with smoke (e.g. Gray 1956, Simons et al. 1966, Landgrebe 1971) and by seeding the tip vortex with smoke (Spencer 1970). Quantitative flow investigations on rotors by conventional measurement techniques started in the 1960s. Simons et al. (1966) investigated the velocity profile of a blade tip vortex under forward flight condition via hot-wire anemometry. Boatwright (1972) measured the same velocity profile for a hovering full-scale rotor using a split-film anemometer.

Starting in the early 1970s, the conventional velocity measurement techniques were replaced by the non-invasive, optical *laser Doppler velocimetry* (LDV). Scully & Sullivan (1972) and Sullivan (1973) were among the first to apply LDV on hovering model rotors. In 1988, Thompson et al. made highly resolved measurements of the swirl velocity profile and core radius of a vortex shed from a single-bladed hovering rotor. With the ongoing development of lasers, flow visualization via laser light sheet illumination arose. This technique was applied e.g. by Leighty et al. (1991), Ghee & Elliott (1992, 1995), and Splettstoesser et al. (1995) for the detection of vortex trajectories under hover and forward flight conditions. Further improvements of the LDV technique allowed for finer resolution and the determination of a 3C velocity field around the tip vortex (McAlister et al. 1995, Boutier et al. 1996). Studies like the one published by Devenport et al. (1996) found that the accuracy of LDV was limited by a random variation of the blade tip and vortex positions, also referred to as *vortex meandering* or *aperiodicity*. Common countermeasures minimized the meandering of the rotor wake by reducing the blade number N_b to one, preventing recirculation and wall effects, and ensuring a low turbulence intensity in the rotor inflow (Leishman et al. 1996, Han et al. 1997). Various LDV studies focused on the detailed measurement of the peak values and temporal developments of the axial and swirl velocity components, as well as the core radius and circulation (Bhagwat & Leishman 1998, Martin et al. 2000b). This experimental data resulted in the formulation and improvement of the vortex models presented in Subsection 2.1.4. In 1998, a statistical aperiodicity analysis was developed for the partial compensation of the vortex meandering (Leishman 1998, Martin et al. 2000a).

The development of the particle image velocimetry (PIV) enabled a second approach to deal with the aperiodic vortex movement by instantaneously acquiring the entire flow field around the vortex. Saripalli (1995), Raffel et al. (1996), and Murashige et al. (1997) were among the first to successfully apply PIV on helicopter rotors. Studies from Raffel et al. (1998a) and Ramasamy & Leishman (2006b) compared results from simultaneous PIV and LDV measurements and promoted the validation of PIV as a reliable tool for blade tip vortex investigations. Multiple publications about PIV on rotors addressed technical aspects and the challenges involved with measuring increasingly larger rotors in simulated hover and wind tunnel tests (see e.g. Raffel et al. 1998b, Richard & Raffel 2002, Raffel et al. 2004, Kindler et al. 2009, Norman et al. 2011).

The *higher harmonic control aeroacoustic rotor tests* (HART I & II) have been described in Subsection 2.2.2 and are briefly mentioned here again, as they represent two milestones of LDV and PIV application on rotorcraft. HART I included LDV measurements for the characterization of blade tip vortices. The HART II test comprised stereoscopic PIV measurements that resulted in vortex core radius and swirl distribution data in different parts of the rotor plane (Burley et al. 2002, van der Wall & Richard 2006, Burley et al. 2006). The HART projects were succeeded by the *hover tip vortex structure* (HOTIS) test, which aimed at complementing the HART II data with comprehensive hover tip vortex data (Richard et al. 2006, van der Wall & Richard 2008). High resolution *two-* and *three-component* (2C,3C) PIV measurements were conducted on the HART rotor in the rotor preparation hall at DLR Braunschweig. The tests included an assessment of the influences of interrogation window size and overlap on the vortex parameters, which will be discussed in detail in Subsection 3.3.2. The results of the test comprised blade tip deflections, vortex trajectories, an analysis of vortex meandering, and – for the first time – the combination of several averaged velocity fields for the 3D reconstruction of a vortex segment.

Other notable applications of PIV on rotors in wind tunnel tests include tip vortex characterizations by Yamauchi et al. (1999) and Kato et al. (2003), as well as full-scale wind tunnel tests by Wadcock et al. (2011) and Yamauchi et al. (2012) with stereoscopic PIV measurements for the localization and characterization of vortices on the advancing blade side. In 2000, Heineck et al. performed PIV measurements on a hovering rotor to study the trajectories of the trailing vortices. McAlister et al. (2001a, 2003) applied stereoscopic PIV on similar rotors and investigated the temporal development of the core radius and peak swirl velocity. During these investigations, McAlister et al. did not find a clear trend for young vortices with a wake age of $\psi_v < 30°$. Johnson et al. (2010) found similar inconsistent trends for vortex ages of $\psi_v < 15°$, indicating ongoing vortex roll-up. Ramasamy et al. (2010) conducted a PIV experiment which focused on the comparison of an untwisted and a highly twisted rotor and showed the differences in circulation distribution, vortex strength, and the flow field behind the entire blade. A second experiment by Ramasamy et al. (2011) was a close-up, high resolution investigation of the vortices that focused on the swirl velocity profiles and the influence of the seeding void. Milluzzo & Leishman (2013) performed a hover test on a model rotor and focused on the tracking and characterization of vortices up to a high vortex age of $\psi_v = 420°$.

In addition to these model rotor tests, Raffel et al. (2001) and Kindler et al. (2009, 2011) performed PIV measurements on the tip vortices of a BO 105 helicopter that was bound to the ground. They investigated the swirl velocity profiles, vortex meandering, and vortex asymmetry and successfully demonstrated the first applications of PIV on a real helicopter.

The application of PIV to rotor flow continues to shed light on the complex aerodynamic mechanisms of the creation, convection, interaction, and break-down of blade tip vortices. The studies described above also illustrate some of the challenging technical aspects of flow field measurements on model rotors. The trailing vortices of rotors are among the strongest that can be artificially produced, and the associated high velocity gradients and seeding voids push modern PIV grid deformation methods to their limits. The large cycle-to-cycle variations of the blade and vortex motion necessitate elaborate aperiodicity corrections and precise azimuthal triggering of the measurements. Finally, the investigation of undisturbed vortices implies the elimination of wake recirculation and ground effects – a requirement that often conflicts with the available test facilities and safety considerations.

3.1.5 Background-oriented schlieren (BOS) technique

Schlieren-based methods have a long tradition in flow diagnostics (Tangler 1977, Merzkirch 1981, Bagai & Leishman 1993). They visualize and quantify the spatial gradient of the fluid's density ρ, which manifests as an optical distortion due to alteration of the refractive index n. This relation is generally described by the Lorentz-Lorenz equation and can be simplified for gaseous media to the Gladstone-Dale equation

$$n - 1 = G\rho \tag{3.17}$$

where the Gladstone-Dale constant G weakly depends on the wavelength of the light and can be assumed constant in the visible range. When passing through a medium with density variations, incident light rays are reproducibly refracted. For classical methods like the *Toepler schlieren photography* (Toepler 1864) or the *strobed schlieren* technique (Tangler 1977), the deflected beams are cut off using a knife edge, resulting in imaged light intensity variations proportional to the first spatial derivative of the fluid's density. The refracted rays are directly projected onto a screen for the *shadowgraph* technique (Light et al. 1999), which reduces the complexity of the optical setup and enables measurements with larger *fields of view* (FOV). For the shadowgraph technique, the imaged light intensity on the screen varies proportional to the second spatial derivative of the fluid's density. An example for the visualization of a rotor blade-tip vortex with the shadowgraph technique is given by Bagai & Leishman (1993) in Fig. 3.6.

The BOS technique is a simplified derivative of the other schlieren techniques and most closely related to *laser speckle density photography* (Debrus et al. 1972, Köpf 1972), but without the need for coherent laser illumination. The BOS method is based on the analysis of digital im-

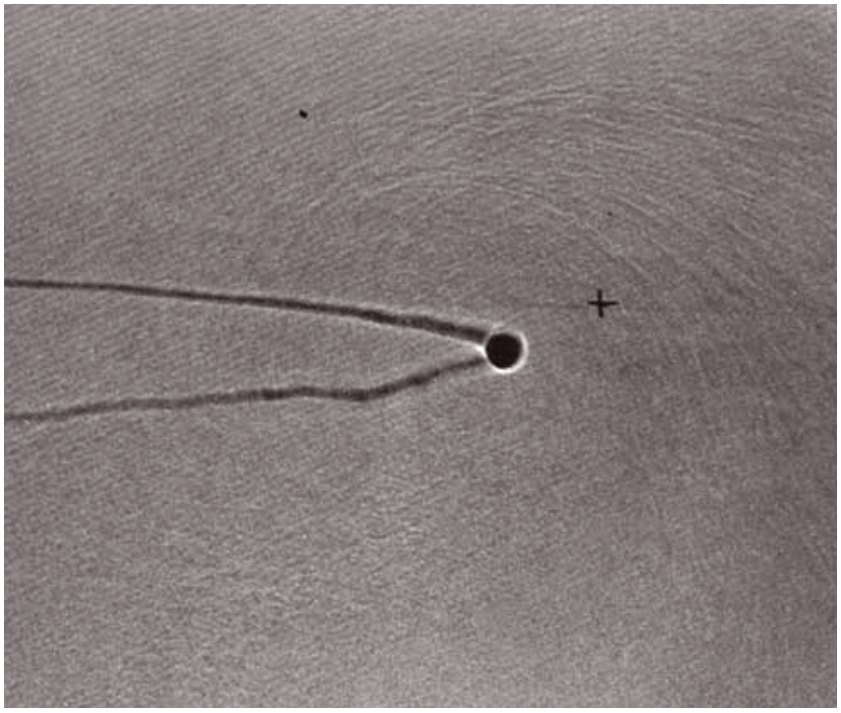

Figure 3.6: Shadowgraph of a rotor tip vortex, after Bagai & Leishman (1993)

age displacements of two-dimensional background structures that are recorded through a fluid containing spatial density gradients. It can be described as a more quantitative acquisition of a mirage or fata morgana. The BOS technique was first described by Dalziel et al. in 2000 with the term *dot pattern refractometry* as a variation of the so-called *synthetic schlieren* technique (Dalziel 1998). A publication from Raffel et al. (2000b) also focused on the principle of the BOS technique and described its application to the visualization of blade-tip vortices on a full-scale helicopter in hover flight. A patent application of Meier was also published in 2000. It included visualization results of a supersonic free jet that were recorded and also separately published by Richard et al. (2000). This article of Richard et al. (2000) also focused on the aspect of density reconstruction from BOS data. A second publication from Raffel et al. (2000a) described a reference-free and natural background variation of the conventional BOS technique with an application to a full-scale helicopter in-flight, which will be explained in Subsection 5.1.3.

The experimental setup for the BOS method requires only few components and is suitable for full-scale applications. The underlying principle of the standard BOS approach is described here according to Richard & Raffel (2001): A (digital) camera is focused on a random dot background pattern behind the measurement volume or wind tunnel test section, see Fig. 3.7. Prior to or after the acquisition of measurement images, a reference image is taken of the undisturbed background (top of Fig. 3.7). A second image is acquired during the experiment with a phase object (i.e. density gradient) located in the line-of-sight (bottom of Fig. 3.7). The corresponding refractions of the light rays evoke apparent shifts of the recorded background pattern, which are evaluated by comparison to the reference image using sectional cross-correlation algorithms as described by Raffel et al. (2007). The angular deflection ε_y of the light rays due to a variation in the refractive index n can be written after Venkatakrishnan & Meier (2004) as:

$$\tan(\varepsilon_y) = \int_0^{Z_B} \frac{1}{n}\frac{\partial n}{\partial y} dz \tag{3.18}$$

This expression yields an integral measure of the density fluctuations along the line-of-sight z. The method works best for spatially delimited density variations – such as tip vortices – within an undisturbed and homogeneous environment. With the assumption of small deflection angles, the apparent displacement Δy of the recorded background in the image plane is expressed as

$$\Delta y = Z_D M_B \varepsilon_y \tag{3.19}$$

with the background magnification factor $M_B = Z_i/Z_B$, based on the distances between the image plane and camera lens Z_i, between the density variation and background Z_D, and between the lens and background Z_B.

For the case of a rotationally symmetrical phase object or multiple camera perspectives of an unsymmetrical phase object, the 3D density field can be reconstructed from the 2D displacements Δy, as described by Richard et al. (2000) and Venkatakrishnan & Meier (2004). The reconstruction of the density field is limited to highly spatially resolved phase objects due to the spatial averaging effect of the cross-correlation evaluation and the corresponding decrease of the computed displacement magnitudes and integrated density differences. Subsection 3.3.10 contains a description of the density reconstruction carried out in the present work. The resulting density distributions of trailing vortices will be discussed in Subsection 4.2.3.

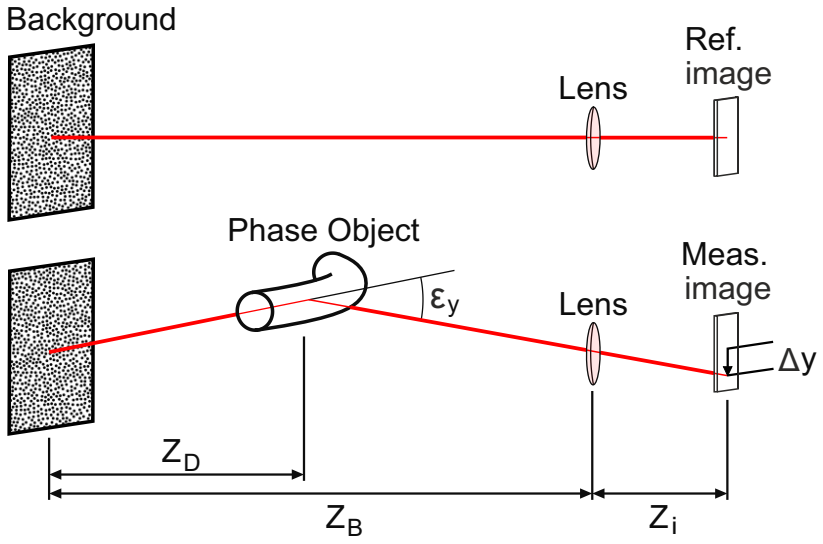

Figure 3.7: Principle of the standard BOS setup after Bauknecht et al. (2014b); top: reference, bottom: measurement image

In general, the background pattern used for the BOS measurements is to be adapted to the camera setup and should contain the highest spatial frequency that can be imaged by the camera, resulting in favorable image intensity distributions for the cross-correlation evaluation. In addition, a high contrast of the background increases the signal-to-noise ratio and allows for small exposure times. For laboratory applications, these conditions are usually met by printing a random dot pattern of adapted dot size and density onto a retro-reflective screen which is illuminated by a light source close to the optical axis of the camera for maximum light intensity.

3.1.6 Laser speckle-illuminated BOS

The *laser speckle-illuminated* BOS (LS-BOS) method is a variant of the standard BOS technique and was published by Meier & Roesgen in 2013. The principle is similar to the classical BOS method and illustrated in Fig. 3.8. In addition to the nomenclature introduced in Fig. 3.7, the physical position of the background screen Z_S is introduced and the independent position of the camera focal plane is indicated by Z_D. The LS-BOS method is comparable with earlier work of Debrus et al. (1972), Köpf (1972) and Wernekinck & Merzkirch (1987). It utilizes coherent laser light for the illumination of a bare background screen with suitable surface roughness, which is observed by a camera. Due to the spatially random phase of the back-scattered laser light, a speckle pattern is created by interference on the camera sensor's surface. The speckle pattern is constant for a stable and equalized laser and camera setup, and can thus replace the printed dot pattern on the background. Changes of the refractive index within the line-of-sight lead to displacements of the speckle pattern, which can be evaluated similar to BOS images.

The maximum achievable sensitivity of the standard BOS setup $\Delta y \rightarrow Z_i \varepsilon_y$ is reached for $Z_D \rightarrow \infty$. For the LS-BOS method, the laser illumination can be set up coaxially with the camera view, e.g. by using total reflection on a suitably tilted glass plate within the line-of-sight. Consequently, the laser light passes the phase object twice, which increases the maximum sen-

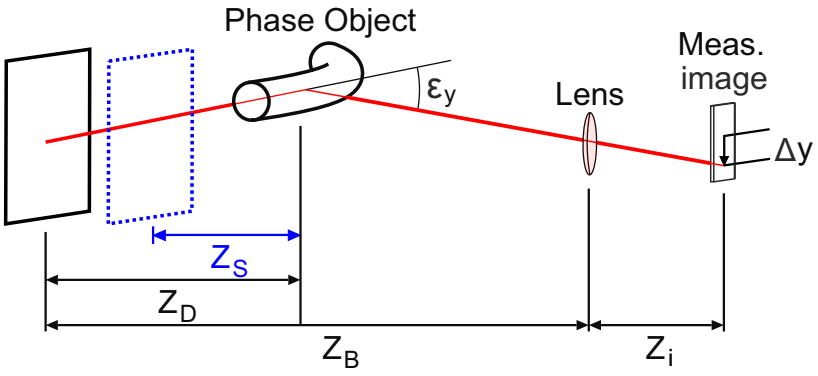

Figure 3.8: Principle of the laser speckle-illuminated BOS setup

sitivity to $\Delta y \rightarrow 2Z_i\varepsilon_y$ for $Z_D \rightarrow \infty$, as shown by Meier & Roesgen (2013). By shifting the focal plane to the position of the phase object ($Z_D = 0$), the setup is operated as a speckle interferometer, as described by Debrus et al. (1972). With this setup, the measurable displacement becomes $\Delta y = -MZ_S \tan\varepsilon_y$, which can be arbitrarily increased by moving the background screen to large distances Z_S. In addition to the advantages of the possible setup variants, the LS-BOS method features an increased light intensity, which leads to an improved signal-to-noise ratio of the measurement images and allows the usage of smaller lens aperture sizes.

3.2 STAR hover test setup

A hover test was conducted within the STAR project as part of the preparations for a planned wind-tunnel test. The preliminary hover test comprised high-speed PIV and BOS measurements to investigate the effects of the twist actuation on the blade tip vortices. The following subsections are based on the publication of Bauknecht et al. (2015) and contain a description of the rotor test stand (Subsection 3.2.1), the active twist actuation (Subsection 3.2.2), the high-speed PIV setup (Subsection 3.2.3), and the high-speed BOS setup (Subsection 3.2.4).

3.2.1 Hover test facility and rotor test rig

The hover test of the STAR rotor was conducted in the rotor preparation hall at DLR Braunschweig. The test chamber had a size of 12 m × 12 m × 8 m – compared to a rotor radius of R = 2 m – and featured a vertical traversing system for mounting the DLR rotor test rig ROTEST II (Gelhaar et al. 1993), as shown in Fig. 3.9. Besides the traversing system, the room contained only one other big structure; the support for a camera that recorded the blade tip positions. The components of the PIV and BOS setups were positioned close to the ground to minimize their effect on the rotor flow. The test rig was attached to the vertical traversing system by a horizontal beam, and also loosely connected to the floor via two support struts with a limited clearance. These struts change the characteristic frequency of the test stand in case of a ground resonance during rotor run up and prevent a resonance catastrophe. The ROTEST II test rig consists of a main rotor drive system that is powered by a 160 kW hydraulic motor, a swash plate actuation

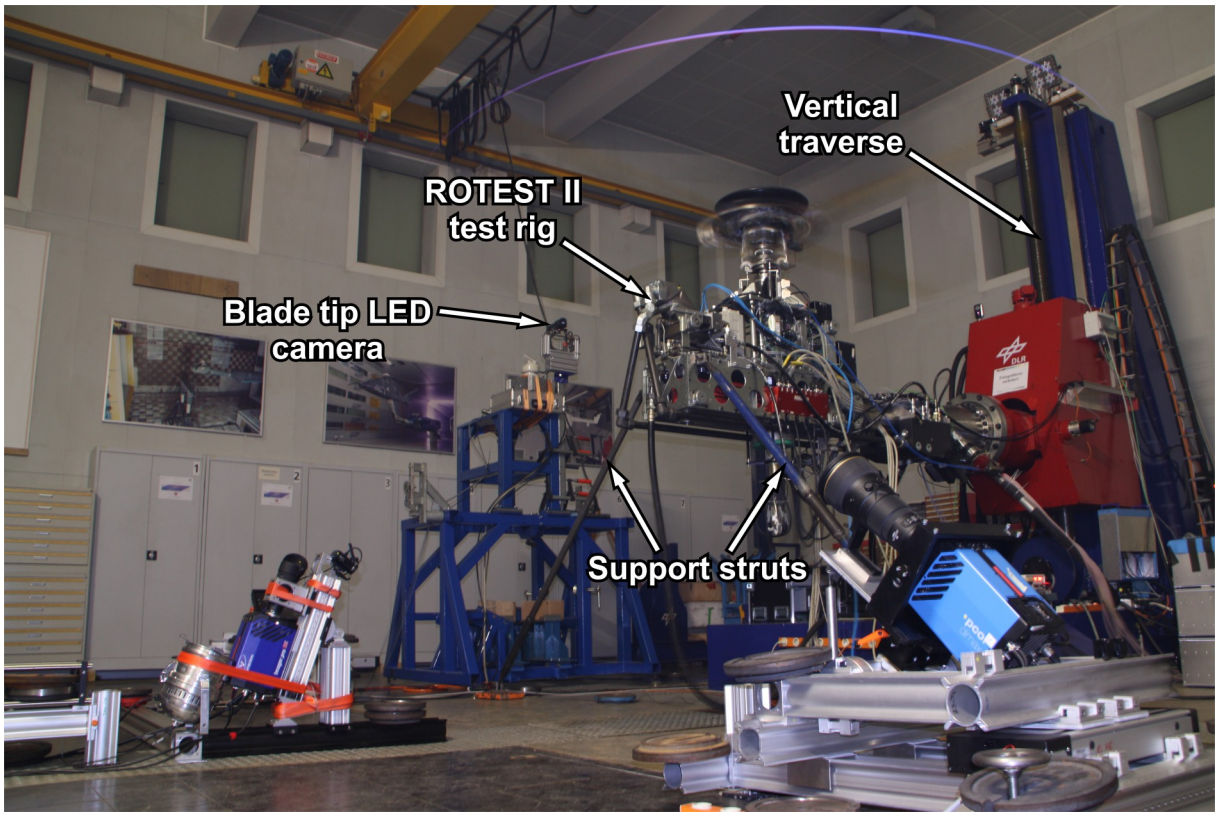

Figure 3.9: STAR hover test facility with ROTEST II test rig

system, a six-component rotor balance, and a data acquisition and triggering system for the rotating frame. The test rig also featured two slip rings: one for the power supply and signal transmission for sensors that were implemented into the blades, and a high-voltage slip ring for the transmission of high-voltage control signals for the twist actuators. A transputer-based TEDAS II computer recorded the rotor balance and sensor data with a sampling rate of $128/rev$ ($\approx$ 2.22 kHz). An azimuth encoder on the rotor shaft triggered the acquisition system with a $1/rev$ reference signal and ensured that the data recording was synchronized with the rotor rotation.

During the hover experiment, the test rig with the STAR rotor blades was horizontally centered in the rotor hall with a minimum tip distance of $2\,R = 4$ m to the walls. The rotor hub was placed at a height of $1.38\,R = 2.76$ m above the ground without inclination of the rotor tip path plane. The rotor was thus operated within a recirculating flow field and in moderate ground effect. The rotor speed was a nominal 1041 rpm ($\Omega = 109$ rad/s), with a tip speed $V_{\text{tip}} = 218$ m/s, and a corresponding tip Mach number of $M_{\text{tip}} = 0.63$. A nominal rotor thrust of $T = 3580$ N had been planned for the STAR wind tunnel test. The thrust was reduced to $T = 2450$ N for the hover test, due to an increasing unsteadiness of the flow and the rotor dynamics above this level. The reduced nominal thrust corresponded to a thrust coefficient of $C_{\text{T}} = T/(\rho_\infty \pi \Omega^2 R^4) = 0.0035$ and a blade loading of $C_{\text{T}}/\sigma = 0.045$, with the rotor solidity $\sigma = N_{\text{b}} c/(\pi R)$ and the number of blades N_{b}. The reduced thrust level ensured a meaningful analysis of the impact of active twist actuation on the trajectories and properties of the blade tip vortices, and on the blade tip motion.

Two optical systems were applied to independently measure the blade (tip) deformations. The tip deformation was acquired with the previously mentioned single camera system from the

DLR at an azimuthal position of $\Psi = 270°$ by tracking two *light emitting diodes* (LEDs) embedded in the blade tip caps. The blade deformation along the span was measured at $\Psi = 180°$ by a dual camera *stereo pattern recognition* (SPR) system. The SPR study was conducted by the *German-Dutch wind tunnels organization* (DNW) after the PIV and BOS measurements to prevent mutual disturbance. A description of both systems is given by Hoffmann et al. (2014).

3.2.2 Active twist actuation

The STAR active twist blades were designed and manufactured based on a 41 % scaled geometry of the BO 105 rotor blades, which was operated at the full-scale Mach number and 41 % of the full-scale Reynolds number. Conclusive descriptions of the manufacturing, build-up, and previous testing of the STAR rotor blades are given by Wierach et al. (2007), and Hoffmann et al. (2009, 2014). Five rotor blades including one back-up blade were produced, as shown in Fig. 3.10. The blades had a radius of $R = 2\,\mathrm{m}$ and a chord length of $c = 0.121\,\mathrm{m}$. The four-bladed STAR model rotor was fully articulated, had no pre-cone, and was operated with a clockwise sense of rotation. The blades were designed to have a linear pre-twist of $-8°/R$ that started at a radial position of $r = 0.44\,\mathrm{m}$. The real pre-twist differed from the design value due to manufacturing complications, resulting in each blade having a different pre-twist in the range of $-10.3°/R$ and $-11.3°/R$. Twelve piezoceramic *macro fiber composite* (MFC) actuators (Riemenschneider et al. 2007) were integrated both into the upper and lower blade skin to generate the active blade twist. The actuators worked in a fiber direction of ±45° towards the spanwise direction depending on the lower and upper side. The span-wise distribution of the actuators is illustrated in Fig. 3.10 by the marked outermost actuator of blade 4.

Figure 3.11 shows a cut along the chord-wise direction of blade 3. The blades were manufactured in two parts and glued together via an adhesive film. The inner part of the blade consists of a foam core, a *glass fiber reinforced plastic* (GFRP) C-spar, sensor and actuator cables, and two weights made from tungsten and bronze to balance the blade. The outer part is made up of two GFRP layers and the actuators on the lower and upper surface. Potentiometers were integrated into the lead-lag and flap hinges and the attachment of each blade at $r = 0.0375\,R$ to measure the blade angles. In addition to these external sensors, the set of active twist blades was equipped with 14 strain gages to measure the flap-bending, lead lag, and torsion moments, 24

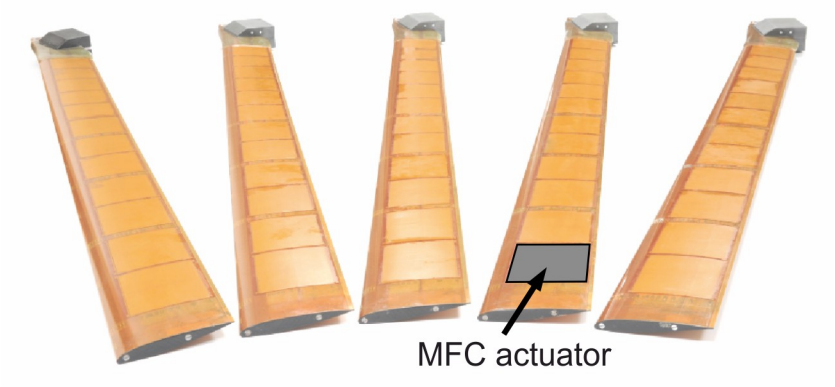

Figure 3.10: STAR active twist rotor blades with MFC actuators, after Hoffmann et al. (2014)

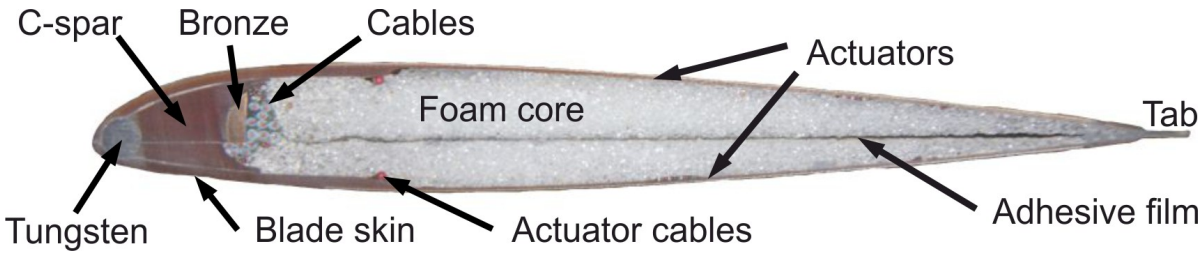

Figure 3.11: Sectional view of a STAR active twist rotor, after Hoffmann et al. (2014)

strain gages for measuring the blade deformation and 186 pressure transducers. Most of these sensors were integrated in blades 1 and 3, whereas blades 2 and 4 had less sensors and multiple dummy sensors and cables instead to compensate for the corresponding structural and dynamic differences. This measure in harmonizing all blades was not entirely effective (Riemenschneider et al. 2013). Therefore, blades with a similar stiffness and axis position – such as blades 1 and 3, or blades 2 and 4 – were assembled across from each other on the rotor. The differences between the four blades resulted in an increased aperiodicity of the blade tip and vortex positions, which was of the same order of magnitude as the jitter introduced by the recirculation in the hover chamber. The aperiodicity of the acquired flow data was counteracted during the PIV evaluation by averaging over a suitable number of measurement cycles, and transferring the vortex positions into the blade tip frame of reference.

The data acquisition of the optical measurement systems (SPR, tip LED, PIV, and BOS) was triggered at certain phase angles of the active twist actuation. The phase of the active twist control signal was changed in increments of 45° to investigate a complete cycle of the blade deformation, while keeping the azimuthal position of the optical setup constant. This was done to circumvent azimuthally shifting the entire optical measurement setup, which would have been more time-consuming. The current approach thus was a compromise between a high azimuthal measurement resolution and the number of configurations that could be tested in the hover test.

The MFC twist actuators had a specified voltage range between −500 V and +1500 V, which was generated by three Trek PZD2000A amplifiers per blade. A Matlab/Simulink-code running on a real time dSPACE system adjusted the control voltage relative to the $1/rev$ trigger signal of the data acquisition system. The actuators on the upper and lower blade skin were controlled in phase and with the same control signal for all four blades, to ensure that each blade experienced the same control law at the same rotor azimuth. Several short circuits occurred within the twist actuators throughout the hover test campaign. These short circuits were caused by cracks in the piezoceramics of the MFC actuators that increased in number with operational time. The short circuits had not occurred for the prototype active twist blades and were counteracted by lowering the upper voltage limit to +600 V and regular repairs of the actuators during the test runs. Despite these measures, the actuator performance still deteriorated over time. It was therefore decided that a wind tunnel entry with the damaged blades was not reasonable within the STAR project. In spite of the diminishing actuator performance and the rotor downtime, the majority of the planned measurement conditions could be tested during the hover test, resulting in a comprehensive set of measurement data for the active twist actuation.

The control voltage for the actuators was set as a phase-shifted cosine signal for the excitation of higher-harmonic blade torsion oscillation. The maximum control amplitude was set to

$U_n = 600\,\mathrm{V}$ without voltage offset. Hoffmann et al. (2014) defined the control voltage signal $U_i(\Psi)$ over the rotor azimuth Ψ for the i-th blade by Eq. (3.20):

$$U_i(\Psi) = U_{k,i}(\Psi)\,\cos(k\Psi - \varphi_i - \varphi_k) \tag{3.20}$$

with $\varphi_i = (i-1) \times 90°$, the control phase φ_k, and the control frequency k as a multiple integer of the rotational frequency, reaching values of 0 to 5. With this definition, a positive voltage amplitude corresponds to a nose-down moment. Figure 3.12 gives a visual representation of the azimuthal variation of the active twist control voltage signal described in Eq. (3.20). The four subfigures show individual 3D views of the rotor plane with the marked azimuth positions of $\Psi = 0°$ at the rear end and $\Psi = 180°$ at the front end of the rotor, where the PIV FOV is sketched as a gray area. The colored bands represent the variation of the control voltage signal over the azimuth between $-600\,\mathrm{V}$ (blue color) and $+600\,\mathrm{V}$ (red color). The subfigures in the top row correspond to actuation frequencies of $1/rev$ and $3/rev$ with phase angles of $\varphi_{1,3} = 0°$, while the bottom row depicts the voltage signal for $5/rev$ actuation with phase angles of $\varphi_5 = 0°$ and $\varphi_5 = 90°$, respectively.

The active twist actuation primarily affects the blade torsion ϑ, especially for an excitation close to the characteristic torsion mode of the blade. As a secondary effect, the twist actuation also excites a blade flapping motion through aerodynamic and structural coupling (Hoffmann et al. 2014). Both blade deformations exhibit a phase delay with respect to the actuation signal. This hysteresis effect is caused by the inertia of the blades and increases with actuation frequency. A discussion of the measured blade deformations and phase delays of the STAR rotor, as obtained by SPR, and the expected effects on the rotor aerodynamics is given in Subsection 4.3.1.

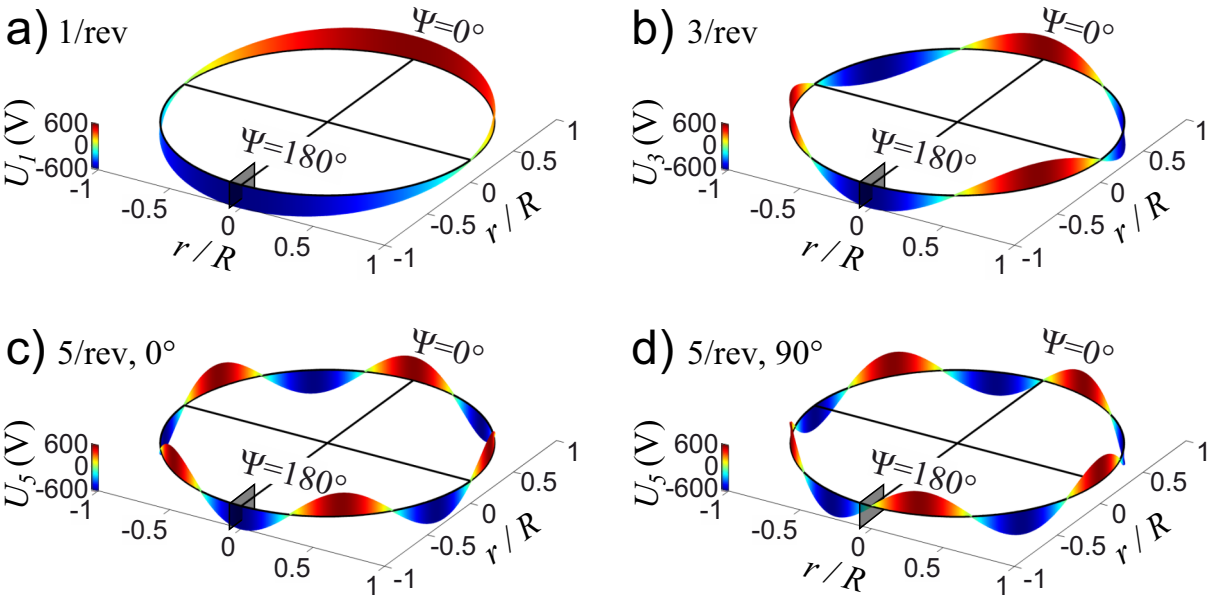

Figure 3.12: Azimuthal variation of active twist control voltage for **a)** $1/rev$, **b)** $3/rev$, and $5/rev$ actuation with phase angles **c)** 0° and **d)** 90°

3.2.3 High-speed PIV setup

Stereoscopic high-speed PIV measurements were conducted as part of the hover test program of the STAR project. Figure 3.13 shows a picture of the entire optical test setup during a measurement run. The focus of both the BOS and PIV system was on the blade tip vortices in the near-field behind the blade tips at a rotor azimuth of $\Psi = 180°$, as indicated in Fig. 3.13. Optimal optical access was gained by moving the measurement position to the forward rotor position, which was possible due to the assumed rotational symmetry of the flow field.

Cameras

The PIV system consisted of two high-speed double frame cameras and a dual cavity high-speed laser. The two PCO Dimax cameras were equipped with Nikon Nikkor lenses with a focal length of f = 400 mm and a maximum aperture of $f/2.8$. The lenses contained band-pass filters with a narrow bandwidth around the 527 nm green laser light to diminish the background noise due to the BOS illumination. Cameras and lenses were rigidly mounted in adapters that fulfilled the Scheimpflug condition, and placed at a height of 0.6 m above the ground with a distance of 5.15 m between the two cameras, as shown for PIV camera 2 to the right of Fig. 3.13. The inclination of the cameras and the lenses were 46° and 39° with respect to the horizontal, respectively, resulting in an opening angle of 102° between the cameras. The position of the

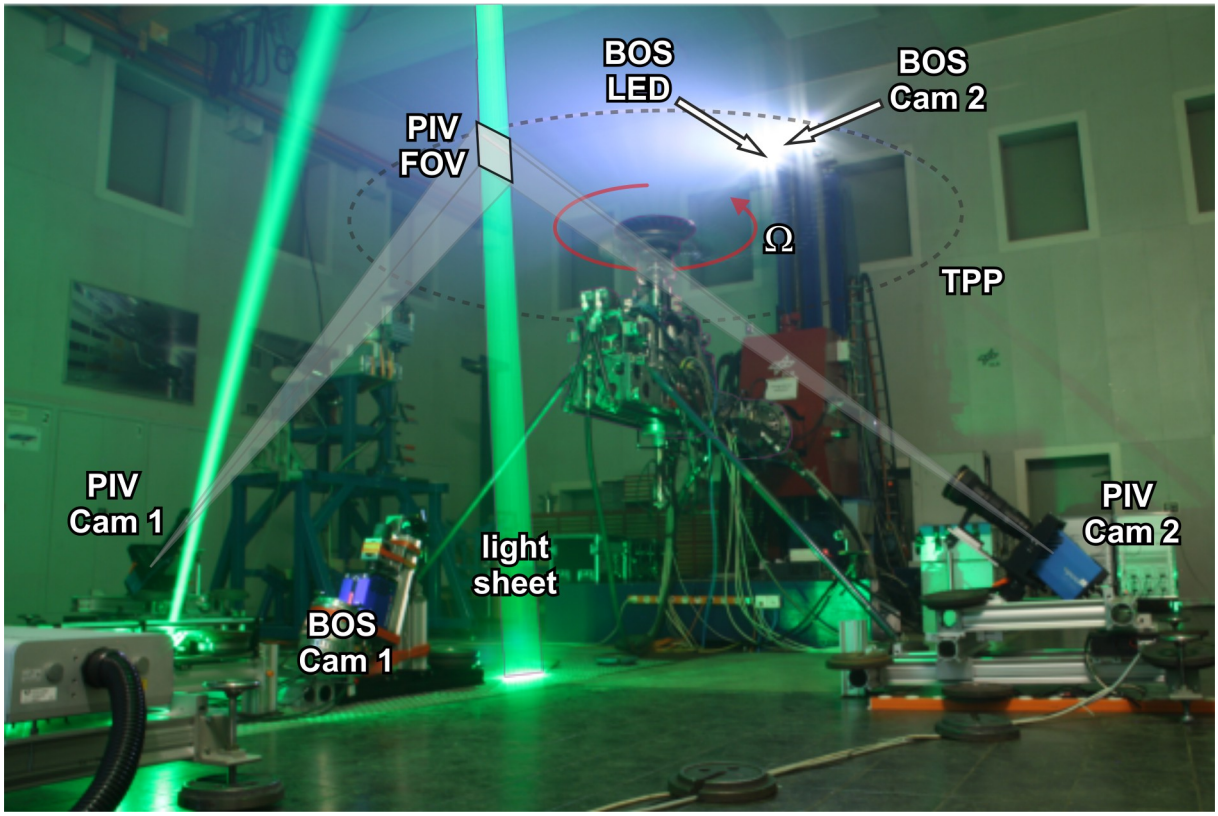

Figure 3.13: STAR hover test setup with marked positions of the PIV and BOS cameras, the PIV FOV, and the *tip path plane* (TPP), after Bauknecht et al. (2015)

PIV FOV is sketched in Fig. 3.13. It was located in the longitudinal symmetry plane of the test stand at $\Psi = 180°$ and at a radial position of $0.96\,R$ to $1.01\,R$. The vertical position of the PIV measurement domain was adjusted for one third of the image height to be located above the nominally loaded blade tips. The native resolution of the PCO Dimax cameras of $2016 \times 2016\,\text{pixels}^2$ had to be reduced to $1152 \times 820\,\text{pixels}^2$ to achieve double-frame recording rates of up to 2.22 kHz. In total, the combined PIV FOV had a width of 94 mm, height of 83 mm, and corresponding scales of 12.2 pixels/mm in the radial and 9.9 pixels/mm in the vertical direction.

The ratio between the length of the PIV interrogation window L_m and the vortex core radius r_c is an important parameter for velocity measurements of vortex flow fields. It has to be below a critical value of 0.2 to resolve quantitative vortex parameters such as the swirl velocity and the core radius (Grant 1997). For an estimated core radius of $r_\text{c} = 0.05c$ (van der Wall & Richard 2006) and a fine interrogation window size of $16 \times 16\,\text{pixels}^2$, a measurement resolution of $L_\text{m}/r_\text{c} = 0.24$ is determined, which compares well with similar rotor blade tip measurements, as listed by van der Wall & Richard (2006). An overlap of the interrogation windows effectively increases the resolution of PIV, as shown by Richard & van der Wall (2006). The overlap of 75 % in the present study thus leads to an oversampling resolution of $L_\text{m,OS}/r_\text{c} = 0.06$ – i.e. 33 vectors within the vortex core – which is well below the critical value of 0.2.

Camera calibration

As already mentioned in Subsection 3.1.3, the camera calibration is essential for a stereoscopic PIV setup. The two PIV cameras of the present setup were calibrated *in-situ* by a two-sided, two-level calibration target, as shown in Fig. 3.14. The target was positioned on a rigid but mobile structure that allowed accurate placement of the target within the PIV FOV for the acquisition of calibration images, and could be removed for the measurements. The laser light

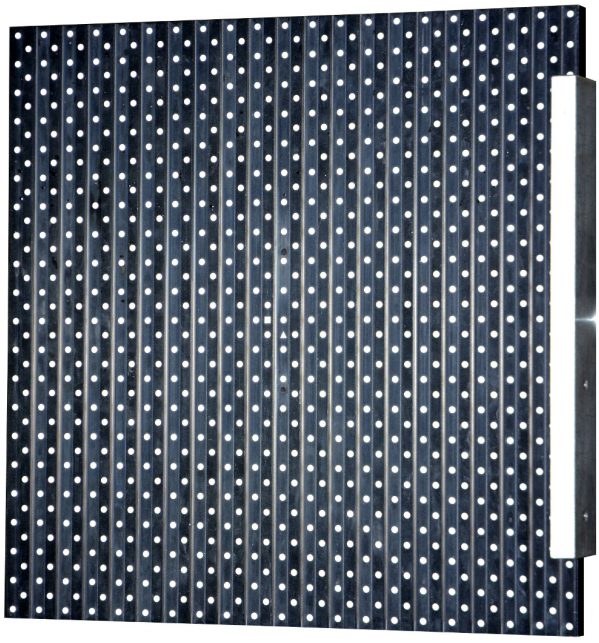

Figure 3.14: Picture of one side of the 3D calibration target for PIV

sheet was regularly checked for alignment with the center line of the test stand, and used to exactly position and center the calibration target on the measurement plane. A third order polynomial fit was used as a camera mapping function. Since both sides of the target were imaged by the cameras, the calibration levels on the target were located up to 7.5 mm outside the center of the light sheet. The consequent vertical mismatch of the two camera images was of the same order of magnitude in physical space and about 60 pixels within the image plane. The mismatch was corrected by performing a self-calibration with the raw particle images of each measurement run, as described in Subsection 3.1.3.

Laser

A Litron LDY 300 Nd:YLF high-speed laser was used to generate a PIV light sheet. The laser has two separate cavities and generates two sequential laser pulses with a length of 150 ns and a frequency-dependent pulse energy of 20 – 30 mJ. Figure 3.15 shows the optical setup of the laser and the light sheet optics in front of the rotor test stand. The laser head was mounted on a rigid and weighted aluminum structure, while the corresponding power supply unit was placed outside the rotor hall to allow manual operation during the rotor tests. The path of the generated laser pulses is marked with a green line in Fig. 3.15. The two light pulses generated within the laser head were axially aligned with the light sheet optics by three mirrors. A set of a biconcave lens (f = −100 mm), two cylindrical lenses (f = +200 mm), and a biconvex lens (f = +500 mm) created a light sheet that was redirected by a mirror behind the optics and a second mirror on the ceiling above the forward rotor blade tip position (see Fig. 3.16b). The light sheet illuminated the measurement region from above to capture the forward-scattered light with the ground-based PIV cameras and thus achieve an increased particle visibility. Within the PIV FOV, the light sheet had a thickness of approximately z_{LS} = 2.5 mm and a length of 300 mm, which was

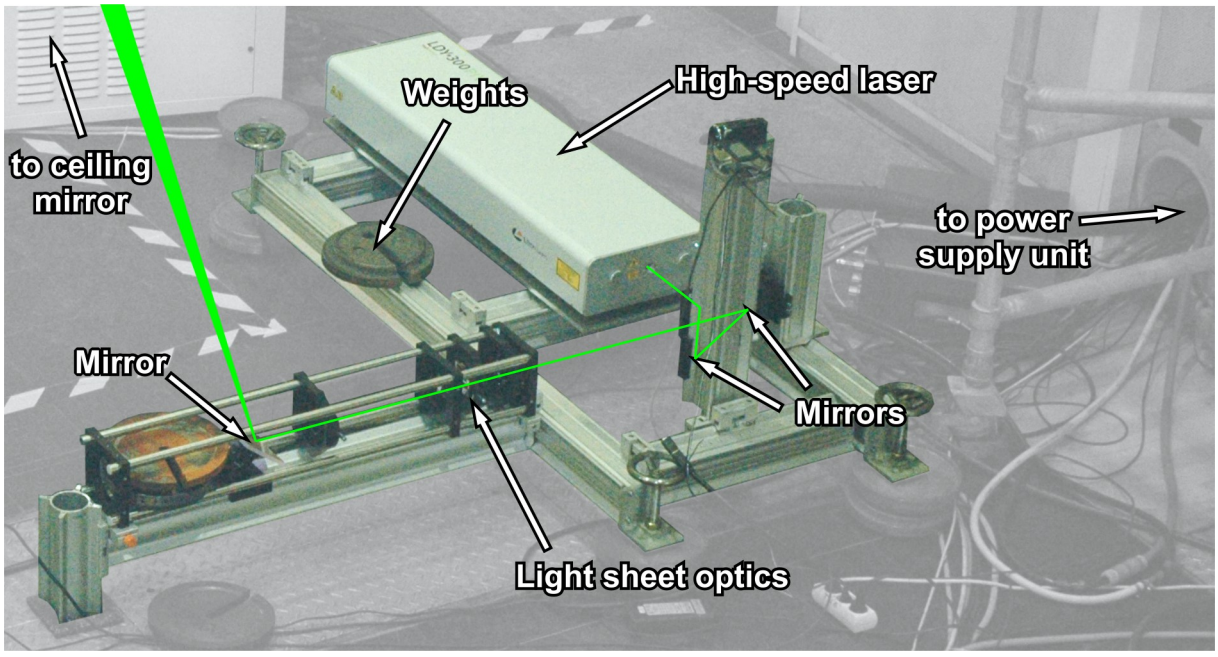

Figure 3.15: Picture of the PIV laser setup with sketched light path

restricted by the length of the mirror on the ceiling. Note that the two cylindrical lenses were positioned with a short distance of 5 mm in between and had the same orientation to emulate the effect of an unavailable, single cylindrical lens with a shorter focal length.

Seeding

A PIVTec PIVpart45 seeding generator with 45 Laskin nozzles was used to fill the rotor hall with a dense and homogeneous aerosol of DEHS particles. The particle size distribution of the particle generator is depicted in Fig. 3.3. According to the area-weighted size distribution, the particles had a mean visible diameter of about $d_P = 0.43\,\mu m$ during the present measurements*.

Recording

The commercial PIV software Davis 8.1.4 was used for the operation of the PIV and BOS systems, including the time-resolved acquisition of speckle and particle images. For each test case, 10 – 20 full revolutions of the rotor were captured with 124 images per revolution. The size of the PIV FOV enabled the investigation of the formation and convection of young tip vortices for vortex ages of $\psi_v = 3.56° - 45.74°$, as measured from the passage of the quarter chord line. The image acquisition was triggered by an azimuth-locked rotor encoder signal at a rate of $128/rev$ ($\Delta\Psi = 2.8125°$) or 2.22 kHz. The time delay between the two PIV image acquisition times was set to 29.4 µs, which corresponded to a blade rotation of $\Delta\Psi = 0.18°$.

3.2.4 High-speed BOS setup

Density-based vortex information – such as the vortex position and core density – was acquired by a dual-camera high-speed BOS system parallel to the PIV measurements. The present BOS camera assembly is comparable with a BOS wind tunnel setup of Heineck et al. (2010) for measuring the blade tip vortices of a helicopter model in forward flight. One of the STAR BOS cameras was located on the floor at the $\Psi = 180°$ position of the rotor (*camera 1* in Fig. 3.16d), while the second camera was positioned on top of the vertical traversing system at the $\Psi = 0°$ rotor position (*camera 2* in Fig. 3.16a). Both cameras were set up with an overlapping FOV close to the PIV measurement domain and focused on retro-reflective background screens that were attached to the wall for camera 2 (Fig. 3.16c) and to a crane below the ceiling for camera 1 (Fig. 3.16b). The overlap of the cameras allowed for a reconstruction of the vortex convectional motion, which was compared with the vortex trajectories determined by the PIV system. The distances between the cameras and the backgrounds (Z_B), and the measurement domain and the backgrounds (Z_D) are given in Table 3.1 and illustrated in Fig. 3.17. The camera setups had similar distance ratios of $Z_D/Z_B \approx 0.53$ for camera 1 and $Z_D/Z_B \approx 0.42$ for camera 2, and therefore similar geometrical amplification factors for their sensitivity. At the beginning of

*Average diameter according to the probability density function (PDF) of the distribution of length: 0.21 µm. Average diameter according to the PDF of the distribution of volume: 0.77 µm.

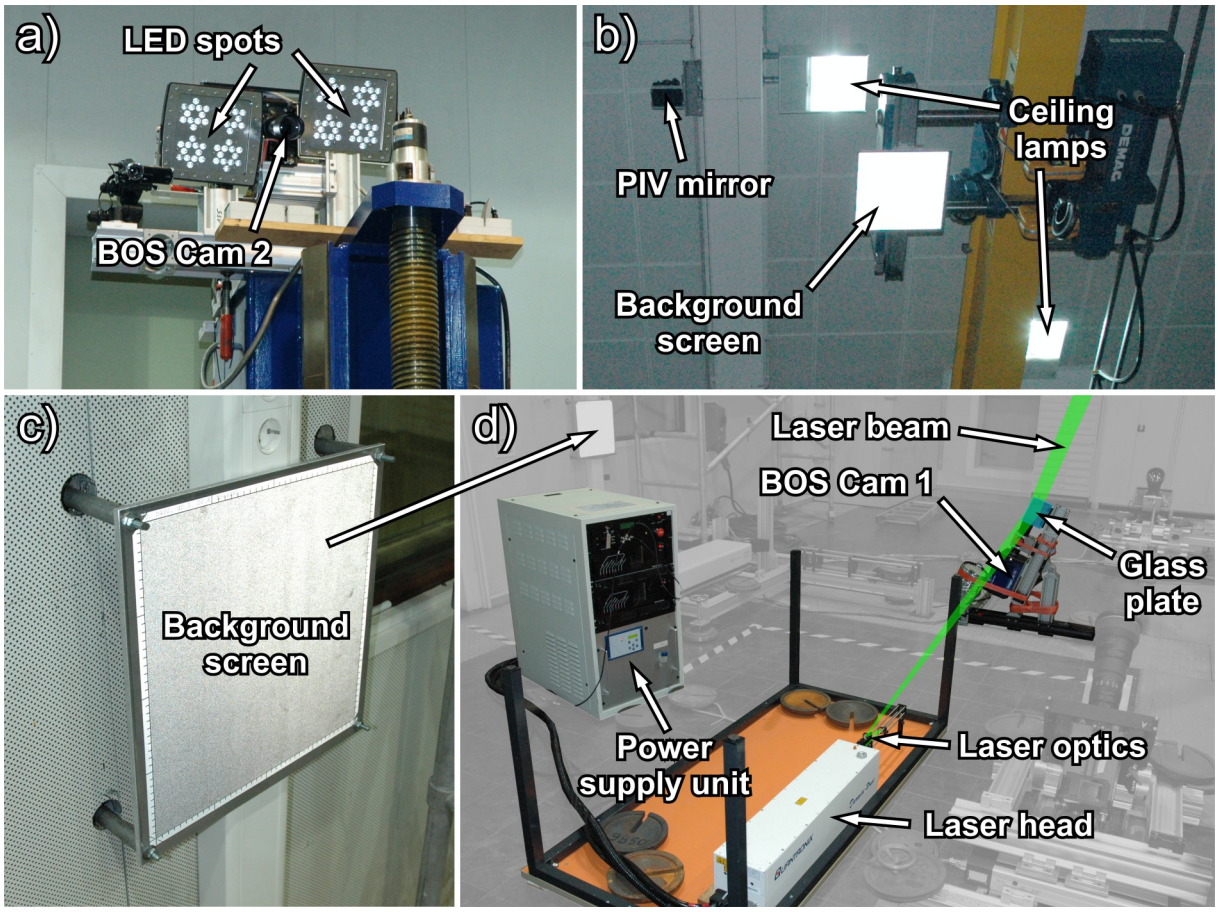

Figure 3.16: Pictures of **a)** BOS camera 2, **b)** the PIV mirror and LS-BOS background, **c)** the BOS background, and **d)** the LS-BOS setup

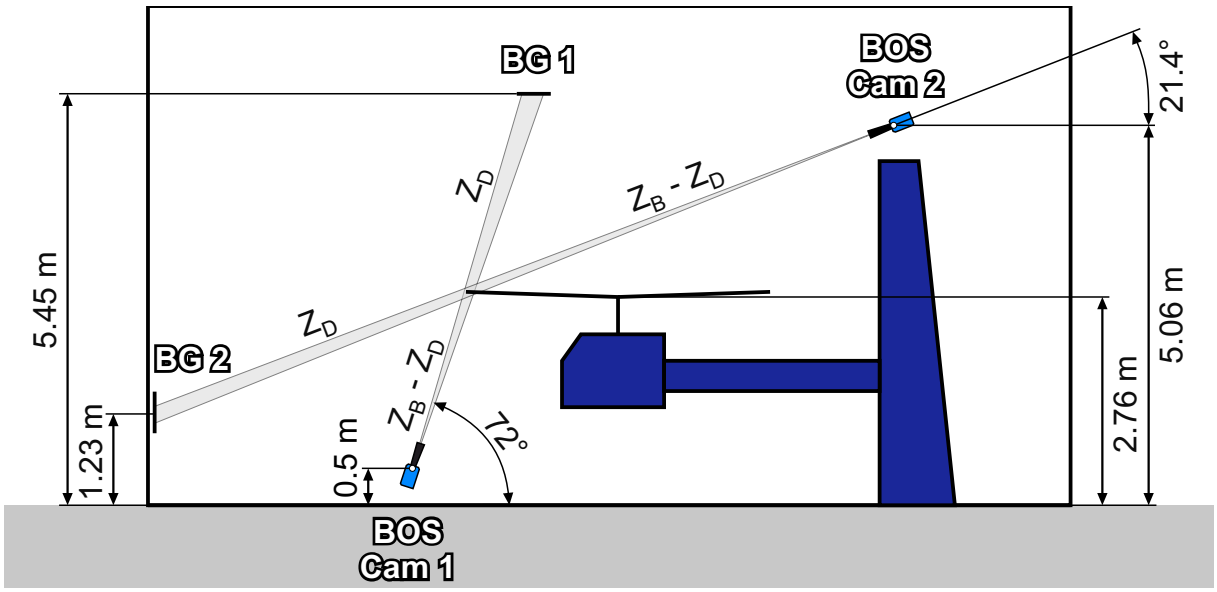

Figure 3.17: Schematic side-view of the STAR rotor test hall including the positions of the BOS cameras and background screens (BG)

the hover tests, both cameras were operated in a classical BOS configuration with the illumination realized by LED spots that were positioned next to the cameras. The setup of camera 1 was modified during the measurement campaign to test an LS-BOS system, as described in Subsection 3.1.6. The laser illumination reduced the effective exposure time and the corresponding image blur significantly and allowed for the reconstruction of density profiles of the vortices. The results presented in this work were all acquired with the modified LS-BOS setup for camera 1.

Table 3.1: STAR BOS camera distances and settings

	Z_B (m)	Z_D (m)	f_{eff} (mm)	$f_\#$	FOV (mm^2)
BOS Cam 1	5.2	2.77	360	22	77.5×108
BOS Cam 2	10.5	4.45	1000	16	70.5×94.5

Cameras

The BOS system consisted of two PCO Dimax cameras that were operated in single-shutter mode and controlled by the same computer system as the PIV cameras. The resolution of the cameras was reduced to 1200×1600 pixels^2 to achieve a frame rate of 2.22 kHz. The bottom camera 1 was equipped with a Nikon Nikkor lens with a focal length of f = 180 mm and a focal length doubler, resulting in an effective focal length of about f_{eff} = 360 mm. Due to the laser illumination, camera 1 received enough light for the aperture to be closed to $f/22$ to increase the depth of field. The camera exposure time was set to 100 µs, although the actual image recording time was fixed to a 200 ns time frame by the pulsed laser. The upper camera 2 was equipped with a Walimex lens with a focal length of f = 500 mm which was also combined with a focal length doubler to realize an effective focal length of f_{eff} = 1000 mm. The lens aperture was set to $f/16$ as a compromise between a large depth of field and adequate imaged background intensity. Unlike the short-term illumination of camera 1, camera 2 was conventionally illuminated over the entire exposure time of 100 µs. The length of this time interval corresponded to a blade rotation of $\Delta\Psi = 0.62°$ and was necessary to assure adequate contrast of the recorded background pattern. The corresponding vortex motion was below 10 %ΩR or < 2 mm and led to a blurred vortex image for camera 2. To compensate for the changing vortex position during the camera exposure, camera 2 was triggered 50 µs before camera 1 and only used for the localization of the vortices and not for the density reconstruction.

Background patterns

Two background screens were mounted inside the rotor test hall for the conventional BOS setup. A picture of the background screen for camera 2 is shown in Fig. 3.16c. It shows an aluminum plate with a size of $450 \times 450 \times 10$ mm^3 that was rigidly mounted on the concrete wall below a sound-absorbing layer via threaded rods and hollow steel cylinders to prevent it from moving during the test runs. A self-adhesive foil with a retro-reflective surface was printed with a randomized pattern of black dots with a diameter of 0.3 mm and applied to the aluminum plate.

The background screen for camera 1 had the same dimensions, a pattern with a dot diameter of 0.4 mm, and was fixed to the counterweight of a crane that was installed below the ceiling, as shown in Fig. 3.16b. The final layout of the LS-BOS setup of camera 1 did not use the printed dot pattern, as the background pattern was generated through laser speckles.

Illumination

The illumination system for camera 2 consisted of two Treble-Light POWER LED 20000 high-power LED spots, installed on both sides of the camera, as shown in Fig. 3.16a. The original spots had a light output of 20000 lm and a light cone with an opening angle of 9°. Instead of the continuous operation with their nominal power of 168 W, the spots were pulsed with three times the nominal power level and a duty cycle of about 30 %. The pulsed operation was achieved by a multi-channel solid-state switching device and a McPower MRGN-900 power supply unit.

The illumination for camera 1 was realized with a Quantronix Darwin Duo 527-100-M Nd:YLF laser. The provisional LS-BOS setup is shown in Fig. 3.16d. It comprises the power supply unit, laser head, beam optics consisting of a biconcave lens and redirecting mirrors, and a glass plate that was installed in front of the camera lens. The glass plate was used as a semi-transparent mirror to realize on-axis illumination for the camera. The laser light thus passed the phase object twice, which effectively doubled the sensitivity of the setup. Compared to the standard BOS setup, the recorded light intensity of the LS-BOS setup increased by more than a factor of ten by using only one cavity of the dual-pulse high-speed laser with a pulse energy of about 30 mJ.

3.2.5 Test sequence

The BOS measurements were performed with a short time delay with respect to the acquisition of PIV data to minimize mutual interference. The temporal setup of the PIV, BOS and LS-BOS systems is illustrated in Fig. 3.18. Each line in Fig. 3.18 represents the timing of one component of the setups over a time interval of just above one image cycle of 450.3 µs. The first line shows the $128/rev$ output signal of the azimuth encoder on the rotor shaft. The PIV laser was programmed to fire a 150 ns pulse with the rotor trigger (t_{PIV}) and another $\Delta t = 29.4\,\mu\mathrm{s}$ later (t'_{PIV}). Note that the laser pulse widths in Fig. 3.18 are not plotted to scale for reasons of visibility. The first PIV frame was simultaneously recorded by both PIV cameras around the first laser pulse. The image information was transferred to a buffer chip and the image sensor was illuminated again by the second laser pulse (frame 2). The read-out of the buffer and the image sensor required almost the entire remaining time of the image cycle, as the sensor resolution was maximized with respect to this duration. The slowest parts of the BOS setup were the pulsed LED spots due to the capacitive and inductive components in their electronic circuits. The spots were thus activated with the $128/rev$ trigger to build up their full output around $t = 40\,\mu\mathrm{s}$, when the exposure of the upper BOS camera 2 was started. Both the LED spots and the BOS camera 2 remained active for 100 µs, after which the light output of the spot slowly decayed. In the middle of the exposure time of BOS camera 2 – at $t_{\mathrm{BOS}} = 90\,\mu\mathrm{s}$ – the LS-BOS laser fired a 200 ns pulse to illuminate LS-BOS camera 1. For a minimized interference of the LED spots, the LS-BOS camera 1 was activated 40 µs after BOS camera 2 at $t = 80\,\mu\mathrm{s}$ and remained active for 100 µs.

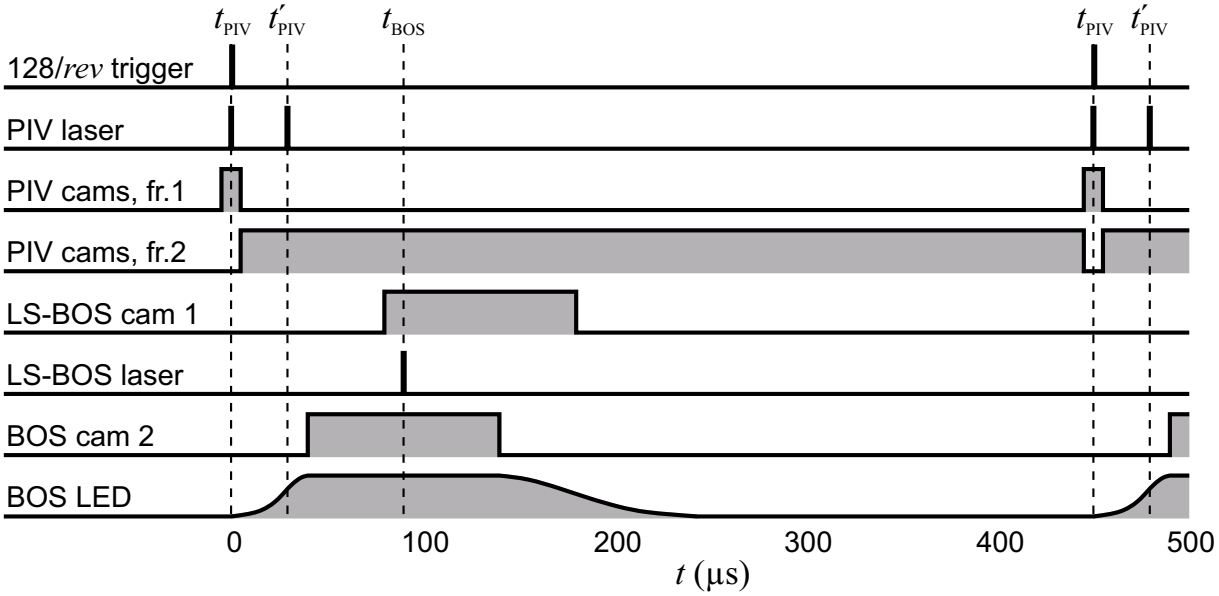

Figure 3.18: Trigger sequence for a single image cycle of the PIV and BOS systems

3.2.6 Measurement procedure and test cases

Before each test sequence, the PIV system was calibrated as described in Subsection 3.2.3, the rotor preparation hall was seeded with particles, particle images for the self-calibration were recorded with the PIV cameras, and undisturbed reference images were acquired by the BOS and LS-BOS systems. For safety reasons, the doors of the rotor hall were locked before the start-up of the test stand and the measurement systems could only be remotely controlled during the measurement runs. The model rotor was then brought up to its nominal frequency of 1041 rpm and thrust of 2450 N and trimmed for zero moments, as well as lateral and longitudinal forces. Each test sequence was preceded by a measurement of the unactuated baseline case, before the actuated test cases were investigated. Rotor loads and deformation data were acquired at the beginning of each new test condition, followed by simultaneous measurements of the PIV and BOS systems, according to the acquisition scheme shown in Fig. 3.18. A total of 124 sets of measurement images per blade revolution were acquired by the two optical flow measurement systems with the 128/*rev* image clock. Four trigger signals at the end of each rotor cycle were skipped to prevent influencing the next rotor cycle. The images of 10 – 20 rotor revolutions were stored in the internal camera buffers, before the data was checked for anomalies and transferred to a *solid state disk* (SSD) storage. A typical recording sequence with 10 cycles was completed in 2 – 3 minutes, and the majority of this time was required for the data transfer from the cameras to the computer. The next measurement point was already set up while completing the data storage. The different test cases studied during the hover test are briefly described below.

Baseline case

The BL case represents the operation of the rotor without active twist actuation at the nominal test conditions of $T = 2450\,\text{N}$ and $\Omega = 109\,\text{rad/s}$. This measurement point serves as a reference for the effects of the active twist actuation and will be analyzed in detail in Section 4.1.

Thrust variation case

The measurement program for the hover test included unactuated rotor measurements with a thrust variation of $500-3580\,\mathrm{N}$ ($C_\mathrm{T}/\sigma = 0.009-0.066$) at the nominal rotor speed. The lowest thrust setting was omitted here, as the small vortex strength did not allow for an automated vortex detection. The measurements at the highest thrust setting could not be completed due to a structural failure of the tip cap of one blade, resulting in the premature abortion of the hover test. Results corresponding to $T = 1000-3004\,\mathrm{N}$ ($C_\mathrm{T}/\sigma = 0.019-0.056$) are analyzed in Section 4.2.

Actuated case: active twist control

The main part of the STAR hover test addressed the effects of the active twist actuation on the blade deformations and tip vortices. Five different actuation frequencies ($1/rev - 5/rev$) with eight different actuation phase angles each were studied during the hover test. 10×124 sets of measurement images were acquired for every actuation frequency and phase angle, resulting in about 330000 raw images for the actuated test cases alone. The detailed aerodynamic analysis of this flow field data is described in Section 4.3. The effects of the actuation on the blade deformations were already discussed by Hoffmann et al. (2014) and are reinterpreted in Subsection 4.3.1 with respect to their influence on the blade aerodynamics.

3.3 Data Processing

The amount of raw data acquired during the hover test required a multiple step data processing and reduction strategy that will be described in this section. The initial analysis step was the evaluation of the raw BOS and PIV images, which is described in Subsection 3.3.1. A study of the effects of the interrogation window size and overlap on the data analysis is presented in Subsection 3.3.2. An automated algorithm for the extraction of the position and shape of the seeding particle void from the raw PIV particle images is presented in Subsection 3.3.3. The raw PIV images also allowed for the extraction of the blade tip position, as described in Subsection 3.3.4. The determinations of the position and velocity distribution of the blade tip vortices from the evaluated PIV velocity fields are illustrated in Subsections 3.3.5 and 3.3.6, respectively. The applied individual averaging technique is explained in Subsection 3.3.7, followed by an analysis of the accuracy of the PIV measurements in Subsection 3.3.8. Finally, the algorithms applied for the 3D reconstruction of the vortex positions and the derivation of a density distribution from the acquired BOS data are described in Subsections 3.3.10 and 3.3.11. The contents of Section 3.3 are, in part, based on a paper published by Bauknecht et al. in 2015.

3.3.1 Evaluation of PIV and BOS raw data

The recorded particle images were evaluated with the commercial PIV software Davis 8.2.0, as shown in Fig. 3.19. The entire evaluation of the recorded particle images was carried out on

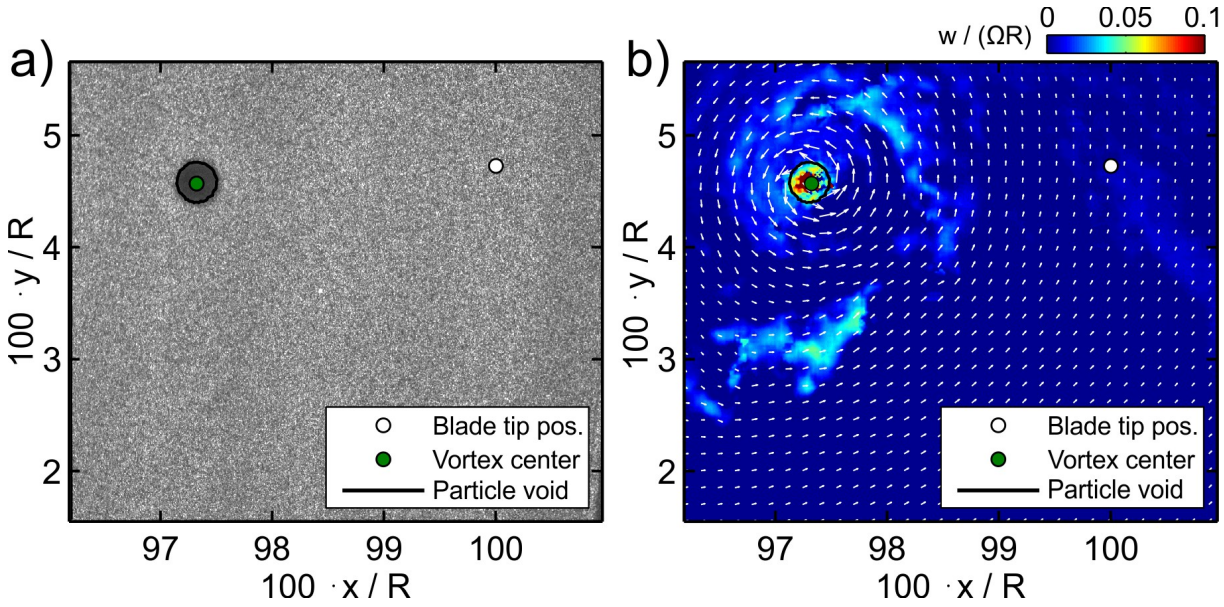

Figure 3.19: a) Particle image and **b)** velocity field for BL case and $\psi_v = 28.87°$ with vortex center, void outline, and blade tip TE position, after Bauknecht et al. (2015)

the *central processing units* (CPUs) of a highly parallelized computer. The raw PIV images – as depicted in Fig. 3.19a – were preprocessed with a sliding background subtraction with a filter length of 5 pixels. The particle images of both cameras were evaluated using a multi-grid stereoscopic cross-correlation algorithm with an initial round and Gaussian-weighted interrogation window of 96×96 pixels^2 dimension. The window size was refined down to an interrogation window of 16×16 pixels^2 with a window overlap of 75 %. For the last iteration step, the shape of the interrogation window was adapted to the local seeding density and flow gradients, according to Wieneke & Pfeiffer (2010). Spurious vectors that deviated by more than 2 standard deviations from neighboring vectors were removed from the fine vector field and replaced by interpolated vectors. Typically, less than 1 % of the vectors were treated that way. This post-processing was found to be effective for well-seeded regions outside the core. The area within the seeding void was filtered out in a later processing step, as explained in Subsections 3.3.3 and 3.3.6. Figure 3.19b depicts a fine velocity field for an unactuated test case and a wake age of $\psi_v = 28.87°$, as measured from the quarter chord line. The graph features a contour plot of the out-of-plane velocity component w and every eighth vector of the in-plane velocities u, v. The analysis of quantitative vortex parameters was carried out based on these weakly filtered, high resolution 2D3C vector fields. Van der Wall & Richard (2006) found that a smoothed and coarse vector field enabled a more robust detection of the vortex positions than a fine and scattered vector field. The fine vector fields were therefore post-processed with Gaussian smoothing and a median filter, and interpolated onto a coarse grid with a vector distance of 16 pixels.

3.3.2 PIV interrogation window size and overlap study

In 2006, Richard & van der Wall analyzed the influence of the size and overlap of the interrogation windows on the characterization of vortices via a single stereoscopic recording of a blade tip vortex, as shown in Fig. 3.20. The subplot in Fig. 3.20a depicts the normalized peak swirl veloc-

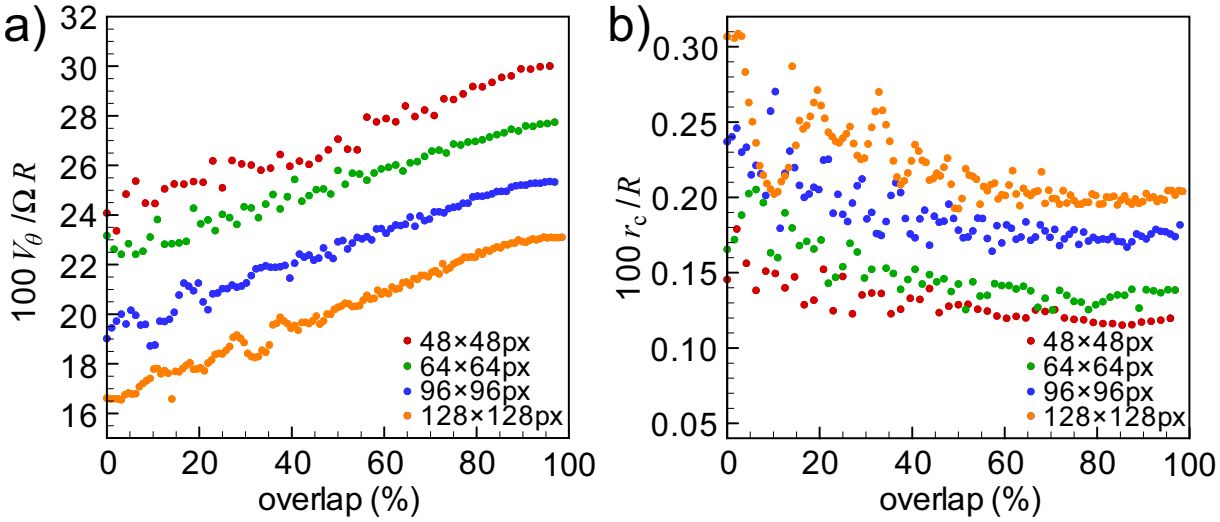

Figure 3.20: Influence of the interrogation window size and overlap on **a)** peak swirl velocity and **b)** core radius, after Richard & van der Wall (2006)

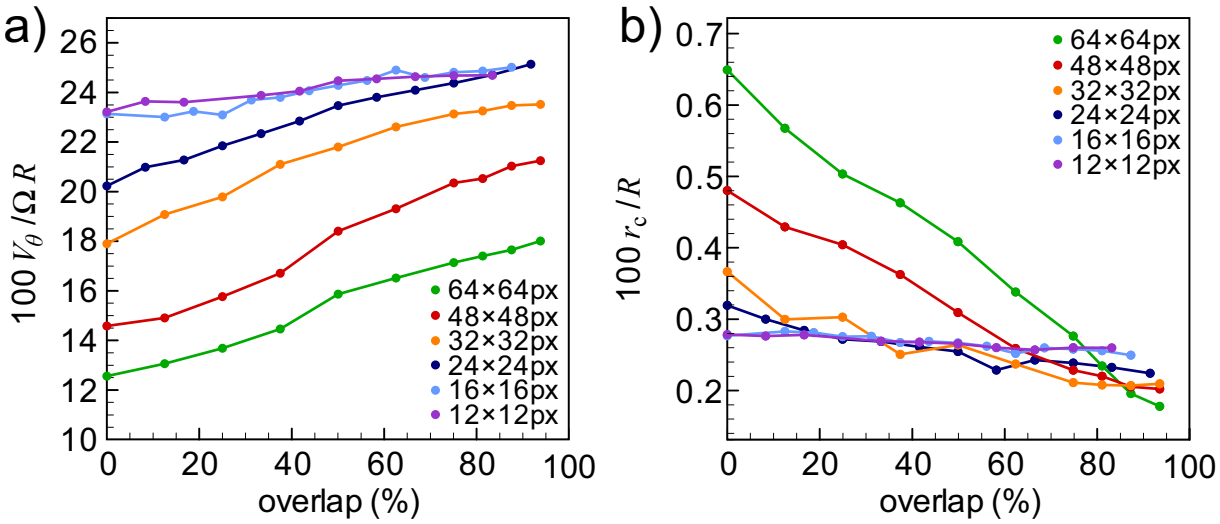

Figure 3.21: Results of the current study on the influence of the interrogation window size and overlap on **a)** peak swirl velocity and **b)** core radius

ity 100 $V_\theta/\Omega R$ in a horizontal cut through the vortex core and Fig. 3.20b gives the corresponding normalized core radius 100 r_c/R over the interrogation window overlap in percent. The plot colors represent different square interrogation window sizes between 48 pixels and 128 pixels. The detected peak velocity increases with higher overlap and smaller interrogation window size. The graphs representing the core radius exhibit a high fluctuation for low overlaps, and smaller and more stable values for high overlaps above 70 %. The detected core radius values also diminish with decreasing window size. All graphs exhibit a convergence towards fixed values for increasing overlaps. No convergence is detected, however, for the decreasing window size, which shows that the interrogation windows were still too large to resolve the peak swirl velocity.

An analysis similar to the studies of Richard & van der Wall (2006) was conducted in the present work, as shown in Fig. 3.21. It is based on a single stereoscopic measurement image of a vortex at a wake age of $\psi_v = 23.24°$. Unlike the previous study, the present analysis of

vortex parameters was carried out by averaging the velocity profiles in 72 radial cuts through the vortex center with varying cut angles. Two previously studied square interrogation window sizes (64 and 48 pixels) and various smaller window sizes down to 12 pixels were examined. Their influence on the normalized swirl velocity and core radius are depicted in Fig. 3.21. The graphs for the peak swirl velocity show a similar trend to the data from Richard & van der Wall (2006) for window sizes between 24 and 64 pixels (see Fig. 3.21a). The two smallest window sizes of 16 and 12 pixels show a stagnation at a high peak swirl velocity level with a reduced influence of the window overlap. Figure 3.21b exhibits a similar stagnation of the core radius for small window sizes, and a decreasing influence of the window overlap with decreasing window size. The stagnation in both subfigures can be interpreted as a convergence towards the real values of the core parameters and illustrates that a further reduction of the interrogation window size is likely to have no positive effect on the returned core parameters. Interrogation windows below 12 pixels no longer contain enough particles for an accurate and stable velocity measurement, and even a window size of 12 pixels resulted in an increased number of spurious vectors. It is found that window overlaps above 75 % only weakly affect the obtained results and furthermore cause a significant increase in computation time. The present PIV evaluations were thus carried out with an interrogation window size of 16×16 pixels^2 and an overlap of 75 %.

3.3.3 Particle void detection

The velocity information obtained from poorly seeded areas within the vortex core is not based on physical particle displacements and therefore has to be filtered out. In the present work, this was achieved by detecting the position and extent of the seeding void in the particle images. The four raw images from both cameras at a single measurement instant were mapped to the light sheet plane and merged with a local minimum filter, as shown in Fig. 3.22a. The resulting image contained the average particle void information of all four included image frames in the form of merged pixel intensity I over image coordinates x and y. The image was exported from the Davis software and imported in Matlab for further analysis. An area of $0.2c \times 0.2c$ was extracted around the vortex center position, as labeled with *subframe* in Fig. 3.22a. The

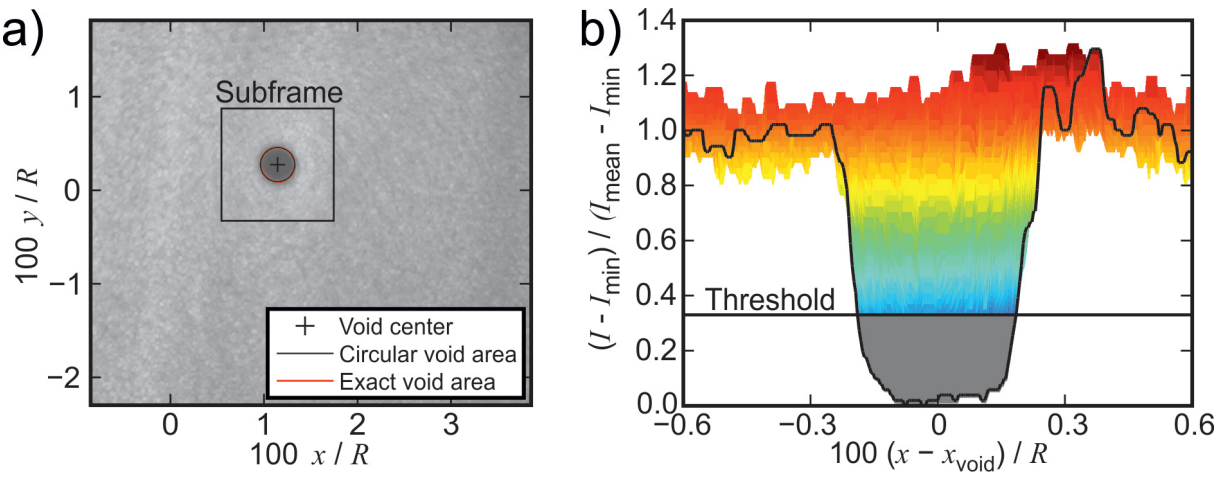

Figure 3.22: Pictures of **a)** merged particle image with seeding void, and **b)** normalized image intensity distribution within a subframe of **a)**, including an intensity threshold

detection of the vortex center position will be described in Subsection 3.3.5. The void center position x_{void}, y_{void} was obtained as the local minimum of the highly spline-smoothed subframe, whereas a weakly filtered version of the subframe was used to compute the void area, as shown in Fig. 3.22b. The absolute minimum intensity level I_{min} and average intensity I_{mean} outside the subframe were computed and a threshold was calculated as:

$$I_{\text{threshold}} = \frac{1}{3}\left(I_{\text{mean}} - I_{\text{min}}\right) + I_{\text{min}} \tag{3.21}$$

Figure 3.22b shows the normalized intensity distribution in the upper half of the subframe area. The horizontal cut through the void center is marked with a black curve and a black horizontal line indicates the threshold level. Image intensities below this threshold are colored gray and were regarded as insufficient for a stable and physically meaningful result in the cross-correlation evaluation. A simple, circular estimate for the void area was derived by counting the number of pixels with intensities below the threshold $I_{\text{threshold}}$, multiplying this number with the imaged area of one pixel A_{pixel}, and computing the radius of a circle with the same overall area:

$$r_{\text{void,circ}} = \sqrt{\frac{I_{\text{threshold}}\, A_{\text{pixel}}}{\pi}} \tag{3.22}$$

The black circle in Fig. 3.22a represents the detected circular void area for this particle image. The exact void outline was determined in a polar coordinate system in an area of $r \leq 2r_{\text{void,circ}}$ around the detected vortex center position (see Subsection 3.3.5). The radial positions r_{void}, where the intensity levels were closest to the threshold value, were determined for each azimuthal angle around the vortex center. The exact void outline is marked by a red line in Fig 3.22a and shows a high overlap with the circular void estimate. The shape of the void exhibited noticeable deviations from a circular shape for very young vortex ages and some actuated test cases. An example for the application of the void detection is given in Fig. 3.23. It depicts

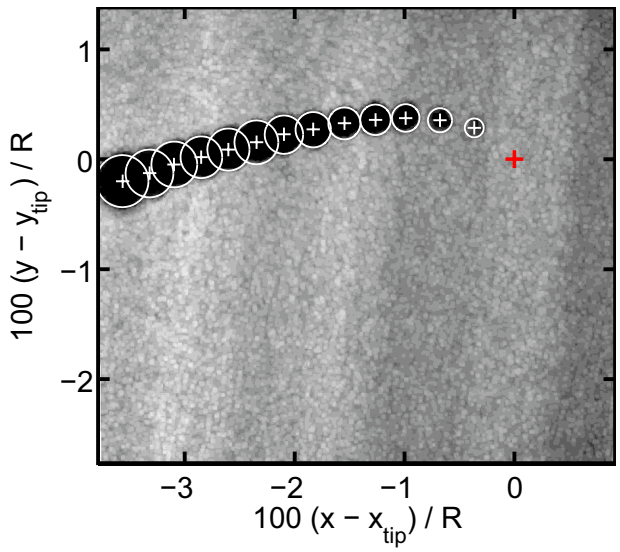

Figure 3.23: Combined view of a series of particle images with detected particle void outlines (circles), center positions (white plus signs), and blade tip TE (red plus sign)

a combined view of a series of instantaneous particle images with the merged particle seeding voids. The detected vortex positions (white plus signs) and circular vortex outlines (white circles) are plotted relative to the position of the blade tip TE, which is indicated by a red plus sign.

3.3.4 Blade tip detection

The vortex and blade tip positions exhibited aperiodic scattering during the hover experiment. Exact knowledge of the relative positions of the blade tips and the vortices is crucial to separate the blade scattering from the aerodynamic effects. The SPR measurements, however, were performed in a second hover campaign after the aerodynamic tests and the blade tip LED camera only captured the blade deformations at the $\Psi = 270°$ position. The lack of instantaneous data at the $\Psi = 180°$ position could be resolved for three of the four blades by analyzing the PIV particle images that contained the blade tip*. An example for such an image is given in Fig. 3.24. It depicts the first image frame of camera 1 that was recorded at a wake age of $\psi_v = 0.74°$ and blurred *a posteriori*. The gray area represents the intersection of the blade with the light sheet plane. The blade areas above and below this intersection region are located in front and behind the light sheet, respectively. The laser light is illustrated by green color. It also illuminates the region above the blade section, which is not visible from the camera position close to the ground. The PIV FOV is illuminated by the laser light from above with an angle of 5.5° to the rotor axis. Therefore, the shadow of the blade – marked by the light green line – is also tilted and intersects the projected tip side edge at a shallow angle. The intersection point of these two lines represents the blade pressure side tip position within the light sheet, and is marked by a blue plus in Fig. 3.24.

The positions of the tip side edge and light sheet edge were detected by an automatic Matlab routine. Horizontal cuts through these lines were averaged in groups of 10 and smoothed. Points on the edges were detected for each averaged horizontal cut by finding the maxima of their smoothed horizontal gradients. Two separate lines were fitted with a least-squares algorithm to the upper and lower group of points. The line fit parameters were used as starting values for a second least-squares fit of a sectionally defined line pair function to all detected points. The intersection point of the two lines was then determined as the blade pressure side tip position.

The position of the tip *trailing edge* (TE) was derived from the pressure side tip location by estimating the blade tip pitch and lead lag angles from the LED camera measurements at the $\Psi = 270°$ position. The mean blade angles were phase-shifted where necessary to match the deformations at the PIV position. With the known blade tip geometry, the TE position could be approximated, as shown by the red plus sign in Fig. 3.24. The TE tip position is typically located below the rotor blade section due to the finite blade tip angle of attack. The influence of a substantial error of $\pm 10\,\%c$ in the lead lag estimation resulted in an inaccuracy of the vertical TE position of $\pm 1.6\,\%c$. A deviation of the blade tip pitch angle of $\pm 0.5°$ caused the vertical TE position to scatter by $\pm 0.5\,\%c$. The TE tip localization was therefore considered to return sufficiently accurate results for the normalization of the vortex positions in the present study.

*The blade tip detection from the PIV images was realized after the experiments. The first blade of each PIV image sequence had not been recorded and could therefore not be analyzed.

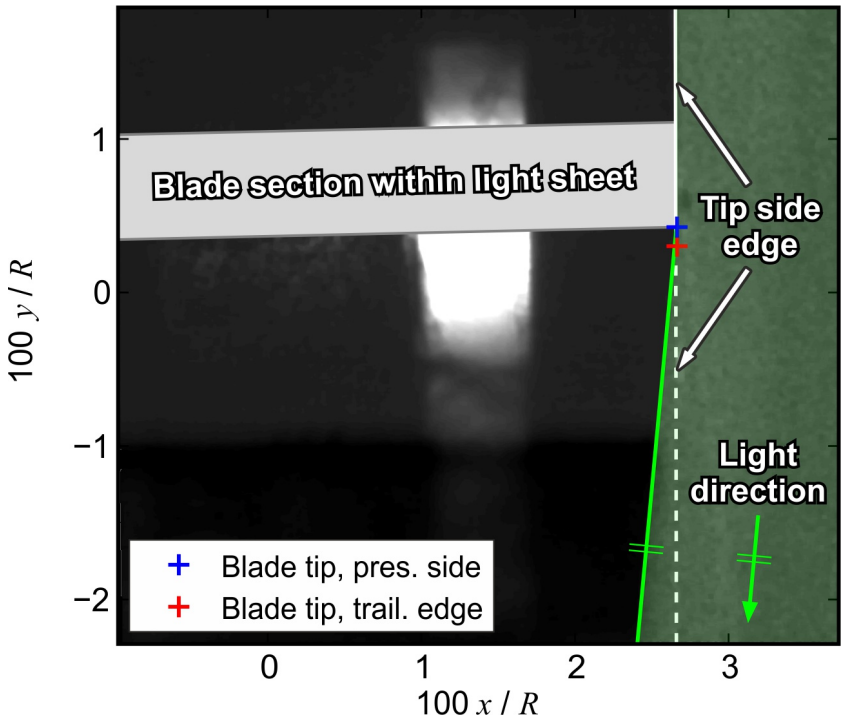

Figure 3.24: Processed PIV particle image with intersecting blade tip and indicated tip side edge, blade section within the light sheet, and laser-illuminated area

3.3.5 Vortex detection in PIV flow fields

Common identification schemes for vortex positions are based on flow field operators. These operators are based on the flow field gradients that become large in the vicinity of the vortex center. Four of the most commonly used operators were applied in this work and will be described here. All four operators are derived from the velocity gradient tensor $\boldsymbol{A} = \boldsymbol{S} + \boldsymbol{\Omega}$, where $\boldsymbol{S}$ is the strain tensor and $\boldsymbol{\Omega}$ the vorticity tensor (Lugt 1996). The gradient tensor $\boldsymbol{A}$ is defined for a 2D measurement field with the coordinates x, y and the in-plane velocity components u, v as:

$$\boldsymbol{A} = \begin{bmatrix} \dfrac{\partial u}{\partial x} & \left(\dfrac{\partial v}{\partial x} + \dfrac{\partial u}{\partial y}\right) / 2 \\ \left(\dfrac{\partial u}{\partial y} + \dfrac{\partial v}{\partial x}\right) / 2 & \dfrac{\partial v}{\partial y} \end{bmatrix} + \begin{bmatrix} 0 & \left(\dfrac{\partial v}{\partial x} - \dfrac{\partial u}{\partial y}\right) / 2 \\ \left(\dfrac{\partial u}{\partial y} - \dfrac{\partial v}{\partial x}\right) / 2 & 0 \end{bmatrix} \tag{3.23}$$

$$= \begin{bmatrix} \varepsilon_{xx} & \varepsilon_{xy} \\ \varepsilon_{yx} & \varepsilon_{yy} \end{bmatrix} + \begin{bmatrix} 0 & -\omega_z \\ \omega_z & 0 \end{bmatrix} = \boldsymbol{S} + \boldsymbol{\Omega}$$

The first matrix contains the elongational ($\varepsilon_{xx}, \varepsilon_{yy}$) and shear strains ($\varepsilon_{xy}, \varepsilon_{yx}$). The second matrix contains one of the flow field operators used in the present study, the out-of-plane component of the vorticity ω_z. The other vortex criteria used in the present work are based on the invariance of the velocity gradient tensor $\boldsymbol{A}$ in a vortex center (van der Wall & Richard 2006). This invariance is found for a positive determinant of $\boldsymbol{A}$, in combination with a complex Eigenvalue λ_2 (Jeong & Hussain 1995) of the characteristic equation, which is achieved by a negative second invariant

Q (Zhou et al. 1999). With the definitions of the determinant and trace of A,

$$\det\boldsymbol{A} = \frac{\partial u}{\partial x}\frac{\partial v}{\partial y} - \frac{\partial u}{\partial y}\frac{\partial v}{\partial x} \tag{3.24}$$

$$\mathrm{tr}\boldsymbol{A} = \frac{\partial u}{\partial x} + \frac{\partial v}{\partial y} \tag{3.25}$$

the expression for Q and $\lambda_{1,2}$ are derived as:

$$Q = (\mathrm{tr}\boldsymbol{A})^2/4 - \det\boldsymbol{A} < 0 \tag{3.26}$$

$$\lambda_{1,2} = \mathrm{tr}\boldsymbol{A}/2 \pm \sqrt{Q} \tag{3.27}$$

where Q constitutes a measure of the dominance of vorticity over the strain, and therefore does not detect shear or boundary layers. The points in the flow field that are described by the complex eigenvalues λ_2 exhibit common features of vortices such as spiral and closed stream lines and potentially also a pressure minimum. The vorticity ω_z, Q, and λ_2 take on a value of $\omega_z^2 = |Q| = |\lambda_2|$ in the center of an ideal vortex (van der Wall & Richard 2006). In addition to these operators, Zhou et al. (1999) proposed the swirling strength λ_{ci} as a flow operator for the detection of vortices, which is the imaginary part $\Im$ of the complex eigenvalue of the velocity gradient tensor A. It is analogous to enstrophy, frame-independent, and only detects regions of high vorticity with simultaneous spiraling motion (Zhou et al. 1999). The signed swirling strength $\lambda = \lambda_{ci}\,\omega_z/|\omega_z|$ is a derivative of the swirling strength λ_{ci} that introduces the sense of the flow rotation (Roussinova & Balachandar 2012). This leads to the final definitions of the flow field operators ω_z, Q, λ_2, and λ that were used for the vortex detection in the present work:

$$\omega_z = \left(\frac{\partial u}{\partial y} - \frac{\partial v}{\partial x}\right) \Big/ 2 \tag{3.28}$$

$$Q = \left(\frac{\partial u}{\partial x} + \frac{\partial v}{\partial y}\right)^2 \Big/ 4 + \frac{\partial v}{\partial x}\frac{\partial u}{\partial y} - \frac{\partial u}{\partial x}\frac{\partial v}{\partial y} \tag{3.29}$$

$$\lambda_2 = \left(\left(\frac{\partial u}{\partial x}\right)^2 + \left(\frac{\partial v}{\partial y}\right)^2\right) \Big/ 2 + \frac{\partial v}{\partial x}\frac{\partial u}{\partial y} \tag{3.30}$$

$$\lambda = \frac{\omega_z}{|\omega_z|} \max\left[\Im\left\{\left(\frac{\partial u}{\partial x} + \frac{\partial v}{\partial y}\right) \Big/ 2 + \sqrt{Q}\right\}, \Im\left\{\left(\frac{\partial u}{\partial x} + \frac{\partial v}{\partial y}\right) \Big/ 2 - \sqrt{Q}\right\}\right] \tag{3.31}$$

The tip vortices shed by a helicopter rotor are typically well-defined and can be localized by identifying the peak values of one of the operators described in Eqs. (3.28 – 3.31). This, however, is only true as long as the blade tips are adequately loaded, the vortex roll-up process is finished, and the vortex has not begun to decay or become unstable. Some of the young vortices in the present work exhibited distortion effects due to the unfinished roll-up process and the active twist actuation of the blades, as depicted in Fig. 3.25a. The subfigure shows a 3D surface plot of the out-of-plane vorticity component ω_z that features a double-peak in the vicinity of the vortex center. The vorticity operator was computed based on the coarse and smoothed velocity field with a distance of 16 pixels between the vectors. The above mentioned global peak detection algorithms proved to be unstable for this sort of non-axisymmetric vortices and had to be modified. An improvement of the vortex detection method was achieved by processing the

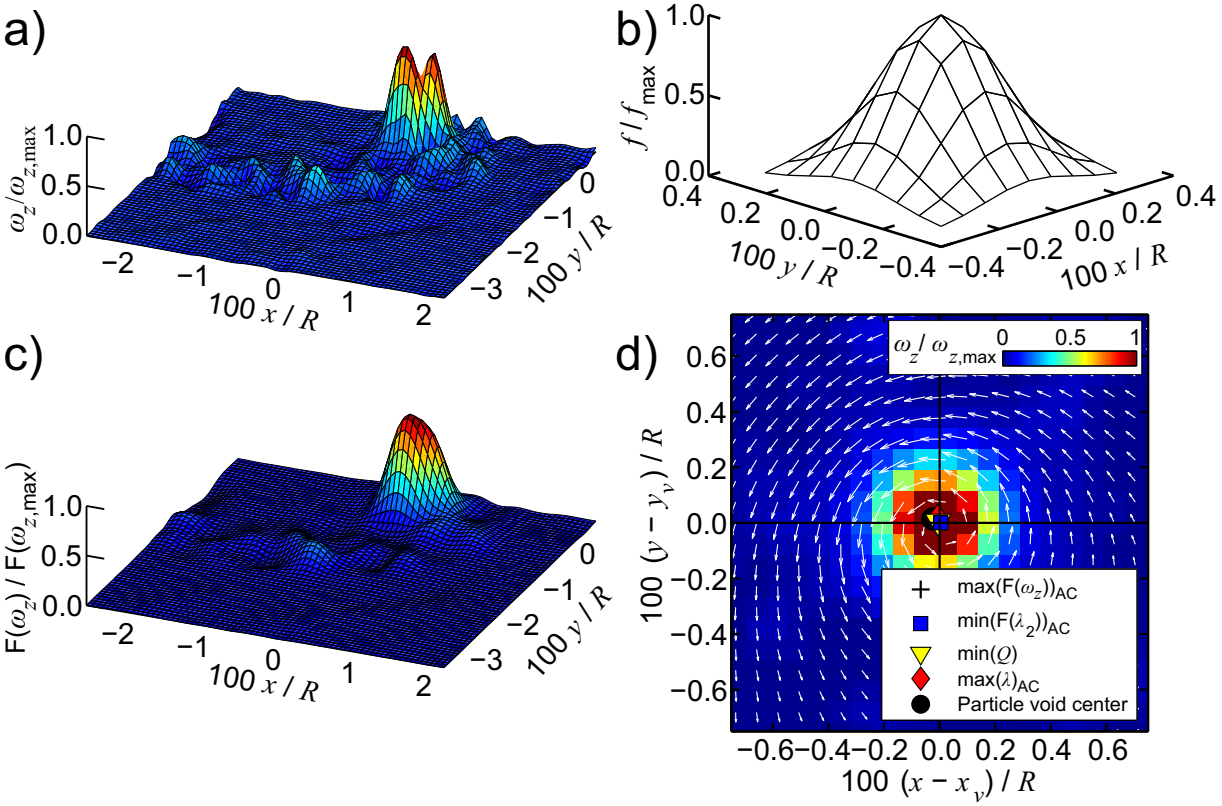

Figure 3.25: Plots of **a)** vorticity, **b)** shape function for convolution filter, **c)** convolution-filtered vorticity, and **d)** vortex detail with center positions, after Bauknecht et al. (2015)

vorticity and swirling strength operators with a norm shape function convolution filter, as described by van der Wall & Richard (2006). The 2D Gaussian-distributed curve f that was used for the convolution filtering is visualized in Fig. 3.25b and of the form:

$$f = \frac{1}{\sqrt{2\pi}} \exp\left(-\frac{x^2+y^2}{r_c^2}\right) \tag{3.32}$$

The formulation of f was adapted to fit the expected peak value of the operator and the vortex core radius. The convolution of the vorticity or swirling strength field with f amplifies the peak corresponding to the blade tip vortex (see Fig. 3.25c) and suppresses secondary peaks that are e.g. caused by the vortex sheet behind the blade. The final peak position was based on the area center of operator values above a threshold of 80 % of the peak values. Figure 3.25d shows a comparison of vortex positions that were detected by the flow field operators specified in Eqs. (3.28 – 3.31). It depicts a detail of the filtered vorticity field corresponding to Fig. 3.25c that is centered on the vortex position x_v, y_v, as detected by the convolution-filtered area center of the vorticity field $\max(F(\omega_z))_{AC}$. The other flow field operators exhibit only minor deviations from the vorticity-based center position for this particular measurement image, but showed increased scattering for some highly-actuated test cases. The method based on the convolution-filtered vorticity field featured the highest accuracy and stability for a majority of the test measurement cases and was thus selected as the standard vortex detection scheme here. For the few measurement images where this method produced unphysical results, the vortex position found by one of the other operators was selected instead.

The vorticity-based vortex detection algorithm automatically localized the vortices in continuous image series behind each blade passage. The vortex locations were assembled into time-resolved vortex trajectories, and approximated by fifth order polynomial curves. The polynomial estimates were analytically derived to determine the instantaneous vortex convection rates for each measurement instant. The in-plane vortex convection velocity and the mean out-of-plane velocity outside the vortex were subtracted from the fine velocity fields that were used for the detailed analysis of the vortex parameters. This global approach used a larger number of detected vortex positions and was therefore found to be more reliable than the determination of the vortex convection rate as the residual velocity at the vortex center of the instantaneous images.

3.3.6 Evaluation of axial and swirl velocity

The velocity fields that were created by the cross-correlation with the 16×16 pixels^2 interrogation windows were analyzed in a second part of the PIV evaluation. An example velocity field for the BL case and a vortex age of $\psi_v = 17.6°$ is shown in Fig. 3.26a. Only every fourth vector is plotted for reasons of clarity, which illustrates the high spatial resolution of the fine evaluation grid. Figure 3.26b depicts the derived out-of-plane vorticity component, normalized with the rotor rotational frequency Ω. Figure 3.26b shows the vortex center as a global maximum of vorticity, which is surrounded by the rolling-up shear layer that was created in the wake of the blade and contains moderate levels of vorticity. The velocity field around the previously determined vortex locations was evaluated to determine the swirl (tangential) velocity V_θ profiles, axial velocities V_z, and the core radii r_c for each instantaneous velocity field. The initial step of this analysis was the subtraction of the vortex convectional velocity from the raw velocity fields. The out-of-plane component was determined from the mean velocity in the region outside the blade wake in the measurement images, while the in-plane convection was derived from the previously determined vortex trajectories, as explained in Subsection 3.3.5. This velocity

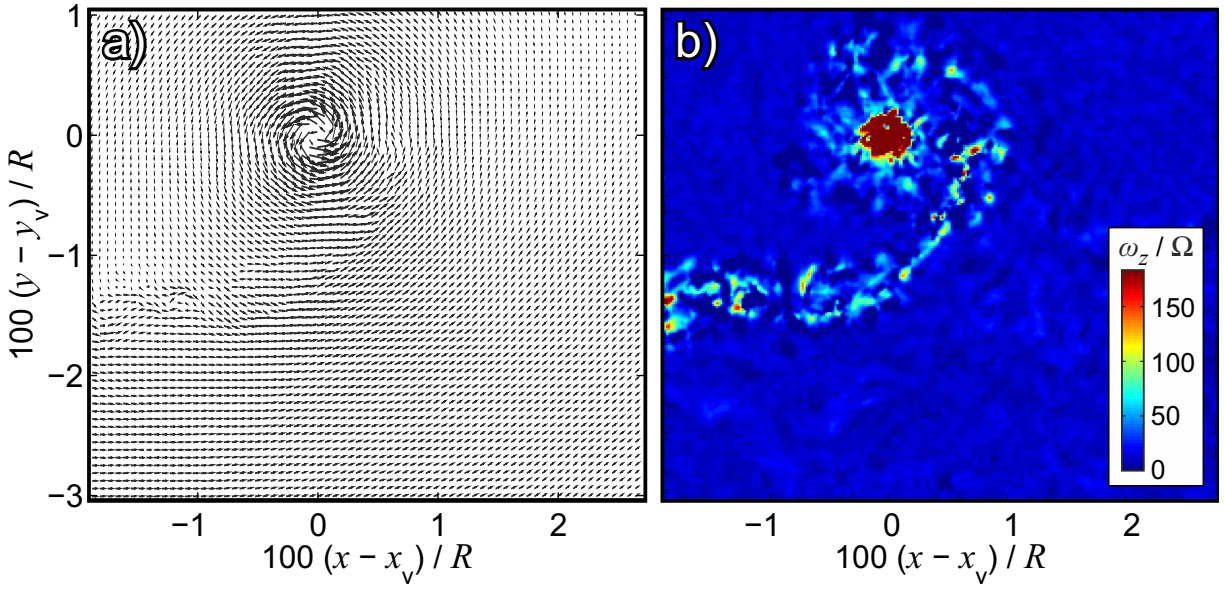

Figure 3.26: Instantaneous data at $\psi_v = 17.6°$ of **a)** fine velocity field for the BL case (every fourth vector shown), and **b)** corresponding vorticity field

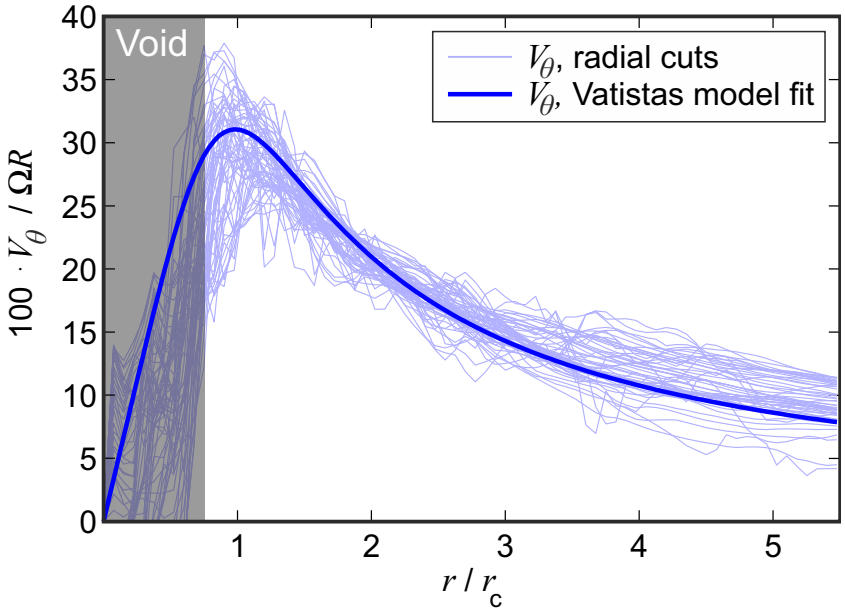

Figure 3.27: Radial cuts of the instantaneous swirl velocity profile of the BL case at $\psi_v = 28.87°$, including a Vatistas model fit, and the particle void

subtraction was performed to study the velocity components in the vortex frame of reference. The velocities in a region with a radius of $r = 0.2c$ around the vortex center were interpolated onto a polar grid with comparable radial spacing as the Cartesian grid and an azimuthal spacing of 5°. The polar velocity vectors were decomposed into radial (V_r) and azimuthal (V_θ) components. Typical radial distributions of the swirl velocity are depicted in Fig. 3.27 for a vortex age of $\psi_v = 28.87°$. The light blue curves represent radial cuts through the instantaneous swirl velocity field around the vortex. The extent of the seeding void is illustrated by a transparent gray box with $r_{void,circ} = 0.75r_c$. Values within the void are not based on real seeding particles and therefore ignored in the further evaluation. The individual cuts exhibit scattering and have to be averaged azimuthally to perform a meaningful analysis of the vortex flow field. A simple average, however, was found to underestimate the peak swirl velocities, which strongly contribute to the sound generation during BVI. The radial $V_\theta(r)$ profiles for each individual azimuthal cut were therefore sorted by their peak velocity value and the Vatistas vortex model (Vatistas et al. 1991) was fitted to the highest 10 % of the curves to obtain a high level swirl velocity profile, which represented a stable measure for the peak swirl velocities of the vortex. The Vatistas vortex model is described in Eq. (2.14) and was applied here with an integer factor of $n = 2$, which Bhagwat & Leishman (2002) found to be a good match for rotor blade tip vortices. The model fit to the tangential velocity profiles is depicted in Fig. 3.27 as a thick blue curve. The global maximum of the Vatistas model curve and its radial position represent the peak swirl velocity of the high level profile $V_{\theta,max}$, and the corresponding core radius r_c, respectively.

In addition to the peak swirl velocity and the core radius, the axial velocity distribution was studied. This out-of-plane component peaks within the vortex core, where the acquisition of reliable PIV data is not possible due to the lack of seeding particles. The determination of the peak axial velocity component V_z is further complicated by out-of-plane loss-of-pairs within the vortex core. The innermost part of the axial velocity profile was thus estimated by computing a spline interpolation based on the valid outer data points for 72 individual radial cuts through

the vortex core. The final peak value of V_z was determined as the median of the local peak values of all radial velocity distributions $V_z(r)$. Although the final value of V_z was only based on valid data points, the applied interpolation had a relatively high margin of error and can only be regarded as an approximation of the real peak value.

3.3.7 Individual averaging

If a simple average is calculated for a series of flow fields around meandering vortices, the resulting velocity profile is smoothed out and features a diminished peak swirl velocity. This bias is commonly compensated for by aligning the vortex centers of the velocity fields before the averaging, which is referred to as *conditional averaging* (Vogt et al. 1996, Leishman 1998). This averaging scheme returned reduced peak velocity amplitudes compared to the instantaneous profiles in the present evaluation. The reason for this was that the azimuthal location of the maximum swirl velocity around the vortex center varied between individual velocity fields of the same vortex age. These vortex asymmetries were non-systematic and did not originate from a shallow or non-perpendicular intersection angle between the vortex and the light sheet, as this intersection angle was quantified by the BOS measurements to be close to 90°. The variations were thus attributed to the unfinished roll-up process and cycle-to-cycle variations of the inflow and blade movements. To preserve the values of r_c and V_θ, these parameters were determined for each individual velocity field and averaged consecutively. This process has been used by other researchers such as Ramasamy et al. (2011) and is referred to as *individual averaging*.

3.3.8 PIV measurement accuracy

It is essential to determine the uncertainty involved with quantitative PIV measurements. The accuracy of PIV is reduced by various sources of error, and the relevant sources are discussed in this section. The estimation for these error sources is based on the works of Raffel et al. (2007) and Lazar et al. (2010), which give an overview on the error analysis for PIV systems. The factors that influence the velocity output of a PIV system can be sorted into four categories:

- particle tracking errors,
- errors in frame separation time Δt,
- errors in particle displacement detection d, and
- statistical errors

The first three of these categories describe the accuracy of a single and instantaneous result. The fourth category discusses the uncertainties involved with the mean statistics of a finite sample size N. The effect of the uncertainties of specific parameters P on the velocities is described by 95 % confidence bounds $E_{95,P}$. The concept of confidence bounds is explained e.g. by Bendat & Piersol (1986) and will not be derived here. The impact of the uncertainty of a parameter P on the measured velocities V is described by its sensitivity $\partial V/\partial P$. The total confidence level of

the velocities $E_{95,V}$ is defined for several independent parameters P_m with $m = 1...M$ as:

$$E_{95,V} = \sqrt{\sum_{m=1}^{M} \left(\frac{\partial V}{\partial P_m} E_{95,P_m} \right)^2} \tag{3.33}$$

The present confidence bounds will be referred to the peak swirl velocity V_θ, which simultaneously represents the largest and most significant velocity in the current flow field.

Particle tracking errors

Some common aspects of the particle tracking behavior have already been discussed in Subsection 3.1.2. This universal description is complemented here with a quantitative analysis of the tracking errors in the flow field of a tip vortex. The strong radial velocity gradients in the vicinity of a vortex cause deviations between the stream lines of the flow field and the particle tracks. Birch & Martin (2013) proposed an analytical description of this effect that is based on the incompressible Batchelor vortex:

$$\frac{V_\theta(\bar{r})}{V_{\theta,\max}} = \left(1 + \frac{1}{2\alpha_\mathrm{L}} \right) \frac{1 - e^{-\alpha_\mathrm{L} \bar{r}^2}}{\bar{r}} \tag{3.34}$$

where $\alpha_\mathrm{L} = 1.25643$, and $\bar{r} = r/r_\mathrm{c}$. The tracking error due to the tangential velocity of the particles $V_{\theta,P}$ is expressed as:

$$\frac{V_\theta(\bar{r})}{V_{\theta,P}} - 1 = A\, e^{-B\bar{r}^2} \tag{3.35}$$

with the error amplitude A, the constant $B = C r_\mathrm{c}/V_{\theta,\max}$, and $C = 18\nu\rho_\infty/(\rho_\mathrm{P} d_\mathrm{P}^2)$. An estimation for the peak value of the error amplitude A is given by Eq. (3.36):

$$A = 2\,(\alpha_\mathrm{L} + 0.5)^2 \left(\frac{V_{\theta,\max}}{C r_\mathrm{c}} \right)^2 \tag{3.36}$$

Table 3.2 lists the experimentally determined values for V_θ and r_c, the corresponding values for A and B, and the particle diameter d_P for two vortex ages $\psi_\mathrm{v} = 3.56°$ and $\psi_\mathrm{v} = 45.74°$.

The centrifugal forces inside the vortex cause the particles to radially deviate from the correct paths. An estimation of this error is computed based on the Stokes number $St = \tau_\mathrm{P}/\tau$, which is defined as the ratio between the time scales of a particle τ_P and the surrounding fluid τ. The values of St are also given in Table 3.2 for the two vortex ages. The characteristic time scale τ_P can be interpreted as a response time of the spherical particle to a change in the local flow velocity. The local time scale of the fluid τ describes the large scale fluid motion with $\tau = r/V_\theta$.

Table 3.2: Particle tracking errors due to tangential and radial velocity

ψ_v (deg)	$V_{\theta,\max}$ (m/s)	r_c (mm)	d_P (µm)	A (%)	B	St	ε_θ (%)	ε_r (%)
3.56	76.3	3.63	0.5	0.1079	75.62	0.0928	0.11	1.60
45.74	65.4	4.84	0.5	0.0446	117.63	0.0596	0.04	1.03

The Stokes number is estimated by Eq. (3.37):

$$St = 2\sqrt{2A}\left(1 - \frac{\rho_\infty}{\rho_P}\right) \tag{3.37}$$

A particle that is in near equilibrium with the fluid is described by a Stokes number of $St << 1$. Based on Eq. (3.37) and the assumptions that $A << 1$ and $dV_r/d\bar{r} \approx 0$, Birch & Martin (2013) estimated the maximum radial tracking error relative to a case with $V_r = 0$:

$$\varepsilon_r = \frac{V_{r,\max}}{V_{\theta,\max}} = \frac{St}{5.8} \tag{3.38}$$

This peak error is independent of the value of B and occurs at $\bar{r} = 0.6618$. The maximum tracking errors in the tangential ($\varepsilon_\theta = |V_{\theta,P} - V_\theta|/V_\theta$) and radial direction ($\varepsilon_r/V_{\theta,\max}$) are given in Table 3.2. The maximum tracking errors occur for the youngest detected vortex age and are of the order of 0.11 $\%V_{\theta,\max}$ in the tangential and 1.6 $\%V_{\theta,\max}$ in the radial direction. These deviations – and especially the low particle lag in the tangential component – prove that the imaged particles in the present study had a sufficiently good tracking behavior for the investigation of the vortex flow field.

Errors in frame separation time

The frame separation time Δt is a critical factor for the accurate determination of the velocity from the particle displacements. Its uncertainty is governed by the response times and precisions of the hardware components. The triggering of the high-speed PIV system was controlled by a high-speed controller from Lavision (Lavision manual 2010). It has a temporal accuracy of 1 ns for the trigger outputs and a delayed response to external input signals of up to 5 ns. The jitter of the input signal only affects the vortex age of the measurement and is negligible for the present test setup. The second source of error is the accuracy of the pulse separation time of the Litron high-speed laser. This time delay was checked with a photo diode and an oscilloscope, and found to differ from the commanded time delay of 30 µs by 600 ns. The pulse separation time used in the PIV evaluation was thus corrected as $\Delta t = 29.4$ µs. The measurement accuracy of the photo diode setup was estimated as 10 ns, resulting in an uncertainty of 20 ns between the two laser pulses. The total uncertainty of the time delay amounts to:

$$E_{0.95,V,timing} = \frac{\partial V}{\partial \Delta t} E_{0.95,\Delta t} = \frac{22\,\text{ns}}{29.4\,\mu\text{s}} V = 7.5 \times 10^{-4}\, V \tag{3.39}$$

This number is negligible compared with the other sources of error. The magnitude of the frame separation time also affects the movement of the vortex core between the two image frames. The current delay of $\Delta t = 29.4\,\mu s$ corresponds to a blade rotation of $\Delta\Psi = 0.18°$, which is within the range of available results from literature (van der Wall & Richard 2006). Martin et al. (2000b) suggested that the vortex core movement should be restricted to below 1 % of the core radius:

$$\Delta t \frac{\Omega R \lambda_i}{c} < 0.1\,\% \tag{3.40}$$

where λ_i is the non-dimensional inflow velocity and a minimum core radius of $r_c = 5\,\%c$ is assumed. The frame separation time in the present test resulted in a value of 0.26 %, which slightly exceeded the criterion of Eq. (3.40).

Errors in particle displacement detection

The accuracy of the particle displacement detection is the dominant factor for the overall PIV uncertainty. It is influenced by the accuracy of the camera calibration procedure, which was described in Subsection 3.2.3. The calibration returned a deviation of 0.055 pixels between the polynomial fit functions and the marks on the calibration target. This deviation is converted to physical units with the averaged camera magnification of 11.04 pixels/mm, and compared with a distance between the calibration points of 15 mm:

$$\frac{\sqrt{2}\ 0.055\,\text{pixels}}{11.04\,\text{pixels/mm} \times 15\,\text{mm}} = 4.7 \times 10^{-4} \tag{3.41}$$

The calibration is furthermore influenced by the target inaccuracy of ±0.02 mm per target length of 300 mm, according to the manufacturer (Lavision manual 2009):

$$\frac{0.02\,\text{mm}}{300\,\text{mm}} = 9.43 \times 10^{-5} \tag{3.42}$$

Both factors influence the uncertainty of the determination of the length scales Δs, and thus the calculated velocities. The combined confidence bound for the camera calibration thus becomes:

$$E_{0.95,V,cal} = \frac{\partial V}{\partial \Delta s} E_{0.95,\Delta s} = \sqrt{(4.6 \times 10^{-4})^2 + (9.43 \times 10^{-5})^2}\, V = 4.8 \times 10^{-4}\, V \tag{3.43}$$

After the self-calibration, a maximum deviation of the calibration plane from the light sheet of less than 0.25° and $\Delta z = 0.7$ pixels = 0.06 mm was detected. The corresponding magnification error of the cameras was found to be negligible compared to the other sources of error.

Keane & Adrian (1992) described a measure for the detection probability of a particle displacement based on the number of particles N_P contained in an interrogation window. The effective number of detected particle pairs in both corresponding interrogation windows N_I is commonly reduced by in-plane loss-of-pairs F_i and out-of-plane loss-of-pairs F_o. In a perfect measurement environment, both loss factors become 1, while for a real PIV measurement, they are re-

duced. The particle images that were recorded during the present hover test contained about $7-15$ particles per 16×16 pixels^2 interrogation window. An effective particle number of about $N_I = 6$ is obtained for example values of $F_i = F_o = 0.75$, which results in a detection probability of about 95 %. The out-of-plane loss-of-pairs is described by Eq. (3.44):

$$\Delta t < \frac{z_{\mathrm{LS}}}{4\ |w_{\max}|} \tag{3.44}$$

where z_{LS} is the light sheet thickness and $w_{\max}$ is the maximum out-of-plane component of the velocity. For the present frame separation time $\Delta t = 29.4\,\mu$s and a light sheet thickness of $z_{\mathrm{LS}} = 2.5$ mm, the requirement of an out-of-plane loss coefficient of $F_o = 0.75$ restrains the out-of-plane velocity w to values below $0.1\Omega R$. This criterion is fulfilled by the flow field outside the vortex core. The peak out-of-plane velocity is found in the center of the youngest vortices measured during the STAR hover test. It takes on values of up to $0.25\Omega R$ and decays away from the vortex axis. Loss coefficients of $F_o < 0.75$ only occur within the particle seeding void, which is entirely removed from the final evaluation. For young vortex ages $\psi_{\mathrm{v}} < 10°$, the region around the peak swirl velocity is also affected by moderate out-of-plane particle losses with loss coefficients of between $F_o = 0.75$ and $F_o = 0.9$. The results of a Monte Carlo based measurement error estimation by Raffel et al. (2007) are applied to estimate the influence of the out-of-plane particle loss and the in-plane sources of error on the confidence bound of the evaluated velocities. It is understood that the particle simulation results described by Raffel et al. (2007) cannot directly be applied to the current measurement conditions. They can, however, help to identify the main sources of error and – with an additional safety factor of $SF = 2$ – provide a conservative estimate for the present test setup. Accordingly, the reduction of the effective particle number through out-of-plane loss-of-pairs causes an estimated uncertainty of the order of $SF \times 0.02\ V_{\theta,\max}$ (Raffel et al. 2007, p. 171).

The results of this Monte Carlo simulation are further applied for an estimation of the in-plane uncertainties of the present PIV measurements. The uncertainty due to random errors is determined as $SF \times 6.0 \times 10^{-3}$, and the influence of a 5 % white background noise level reduces the accuracy by $SF \times 2.0 \times 10^{-3}$. Moderate peak locking effects contribute to an uncertainty of $SF \times 1.6 \times 10^{-3}$, and the image shifting causes an uncertainty of $SF \times 4.0 \times 10^{-4}$. Flow field gradients that are not properly resolved by the spatial averaging within the finite interrogation windows constitute the largest source of errors here. For a maximum, non-dimensional, in-plane gradient of 0.135 pixels/pixels* in the region around the core radius, the uncertainty was approximated after Raffel et al. (2007, p. 175) as $SF \times 1.01 \times 10^{-2}$. Together with the calibration and out-of-plane uncertainties, the combined confidence bound for the particle displacements becomes:

$$E_{0.95,V,ps} = \sum \left(\frac{\partial V}{\partial \Delta s}\, E_{0.95,\Delta s} \right)^2 = 0.045\ V_{\theta,\max} \tag{3.45}$$

This value of $4.5\ \%\ V_{\theta,\max}$ demonstrates that the determination of the particle displacements constitutes the largest source of uncertainty for the present PIV setup. It is noted that this uncertainty is only valid for the first detected vortex and rapidly decreases with wake age and with distance to the vortex center.

*Change in vector length between two neighboring vectors devided by a distance of 4 pixels in between

Statistical errors

The discussion of measurement accuracy in the previous paragraphs was focused on single, instantaneous measurement images. In the present study, the vortex parameters were extracted from these instantaneous images and individually averaged for each vortex age. As mentioned before, the number of measurement images per test case had to be restricted to $N = 40$ to cover all test conditions within the measurement campaign. A statistical analysis based on a finite sample size causes sampling errors, i.e. only an infinite sample size will return mean results equivalent to the initially unknown true value. Again, 95 % confidence intervals are applied to estimate the sampling uncertainty. Assuming a normally distributed variation of the individual measurement values around the mean, the confidence interval for the averaging of the peak swirl velocity is defined after Bendat & Piersol (1986):

$$E_{95,V,mean} = t_s \frac{\sigma_s}{\sqrt{N-1}} V_{\theta,\max} \tag{3.46}$$

with the standard deviation σ_s and the student factor t_s. A standard deviation of $\sigma_{s,\theta} = 8.5\,\mathrm{m/s}$ is calculated for the peak swirl velocity. A tabulated student factor of $t_s = 2.021$ is retrieved from literature (Bendat & Piersol 1986) for a confidence level of 95 % and the sample size $N = 40$. With these values, Eq. (3.46) returns a confidence bound of $E_{95,V,mean} = 0.036\,V_{\theta,\max}$. Equation (3.46) can also be applied to assess the uncertainty of the detected vortex trajectories, with a standard deviation of $\sigma_{s,xy} = 4.8\,\mathrm{mm}$. For the vertical coordinate of the vortex trajectory y/c, the confidence bound is determined with $E_{95,y,mean} = 1.55\,\mathrm{mm} = 0.0128\,y/c$. Note that the sample size of the BL case was $N = 120$ per vortex age, which yields confidence bounds of $E_{95,V,mean} = 0.021\,V_{\theta,\max}$ for the peak swirl velocity and $E_{95,y,mean} = 0.88\,\mathrm{mm} = 0.0073\,y/c$ for the vertical vortex positions.

Combined PIV uncertainty

During the PIV evaluation with the commercial software Davis, 90 – 96 % of the evaluated vectors were determined by the highest peak in the correlation map, depending on the vortex age and the maximum velocities. This quota was mainly affected by the size of the unmasked particle seeding void. The number of correlated particle pairs outside the particle void was sufficient to obtain accurate velocity values.

The total confidence bound of the PIV evaluation is computed based on Eq. (3.33), taking into account the uncertainties due to the frame separation time, the particle tracking error, the particle shift detection, and the sampling error. The total confidence bound for the velocities is determined as $5.79\,\% V_{\theta,\max}$. As shown in the paragraphs above, this value is mainly influenced by the uncertainties due to the in-plane gradients, the out-of-plane loss-of-pairs, and the sampling errors. The stated magnitude of the confidence bound thus only describes the youngest vortex age and decreases with wake age and distance to the vortex axis. The error estimation for the present rotor test therefore shows that the PIV measurements return repeatable and accurate results that are adequate for the analysis of the tip vortices and the effects of the active twist actuation thereon.

3.3.9 Evaluation of BOS raw data

The evaluation of the BOS recordings is described in the following subsections. The recorded displacement images of the BOS cameras were evaluated with the commercial PIV software Davis 8.2.3. The evaluation is based on series of measurement images containing the blade tip vortices, and undisturbed reference images that were acquired before each test run. An average reference image was obtained by calculating the mean of 100 undisturbed images to reduce the influence of sensor noise. Each measurement image of a test sequence was paired with the averaged reference image. A correlation-based shift and rotation correction ensured that small camera vibrations and the corresponding global image shifts did not affect the resulting displacement map. The raw images were filtered by subtracting a sliding background with a filter length of 8 pixels. The image shifts between the mapped image pairs were evaluated using a multi-grid direct cross-correlation algorithm that was executed on four *graphics processing units* (GPUs). The highly parallelized processing on the GPUs was significantly faster than an evaluation on CPUs and enabled the evaluation of one measurement image per second. The initial square interrogation windows had a size of $32 \times 32\,\text{pixels}^2$ and an overlap of 50 %, and were refined down to round windows of $8 \times 8\,\text{pixels}^2$ with an overlap of 75 % and no post-processing. The small interrogation windows were required to achieve a fine resolution of the vortex and to avoid averaging effects of the displacement field. Figure 3.28 depicts an evaluated displacement field from camera 1 at an average vortex age of $\psi_v = 4.7°$. Every 8th vector is shown in horizontal x and vertical y direction. The background color corresponds to the vertical displacement v and illustrates the position of the tip vortex.

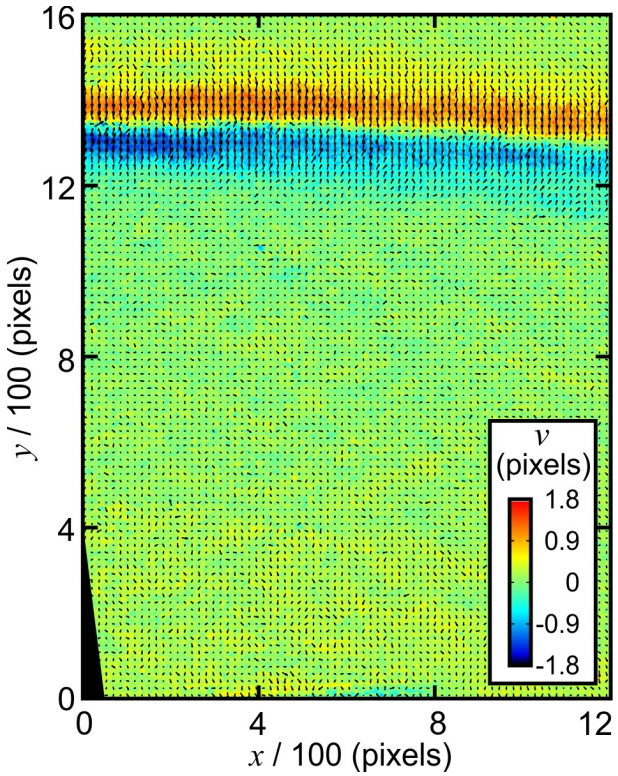

Figure 3.28: Evaluated displacement field from a LS-BOS image of camera 1

3.3.10 Reconstruction of vortex positions from BOS data

The two BOS cameras enabled the reconstruction of the vortex positions in a measurement domain close to the PIV FOV. The positions of the BOS cameras are depicted in Fig. 3.17 in Subsection 3.2.4. The lower BOS camera 1 was positioned on the symmetry plane of the rotor test stand, whereas the upper BOS camera 2 could only be positioned with an offset of 0.29 m to the symmetry plane. The FOVs of the two BOS cameras had an overlap of 17 mm in the azimuthal direction of the rotor due to the positions of the cameras and backgrounds. The reconstruction of vortex trajectories was therefore restricted to a 2D plane parallel to the PIV light sheet with a distance of 38 mm at $\Psi \approx 181°$. The reconstructions of the vortex trajectories – as well as the density reconstructions in the following subsection – were carried out within the scope of a master thesis of Braukmann (2015). This master thesis contains a comprehensive description of the BOS data evaluation, which will therefore only be briefly outlined here.

Both BOS cameras depicted the blade tip close to the upper edge of the FOV, as shown in Fig. 3.29. The tip vortex originated from this tip position and convected downwards in the recorded image sequences of both cameras. Depending on the measurement case, the vortex was captured up to the 15th or 20th picture of the image sequence, and the vortex analysis was thus restricted to images 1 – 15 behind each passing blade, corresponding to vortex ages of between $\psi_v = 2.6° - 45.2°$. Figure 3.29 also shows the intersection lines of the vertical reconstruction plane, which were used for the calculation of vortex trajectories. The 2D displacement fields of both cameras were analyzed with custom routines in the commercial software MATLAB. Residual global image displacements with respect to the reference image were compensated

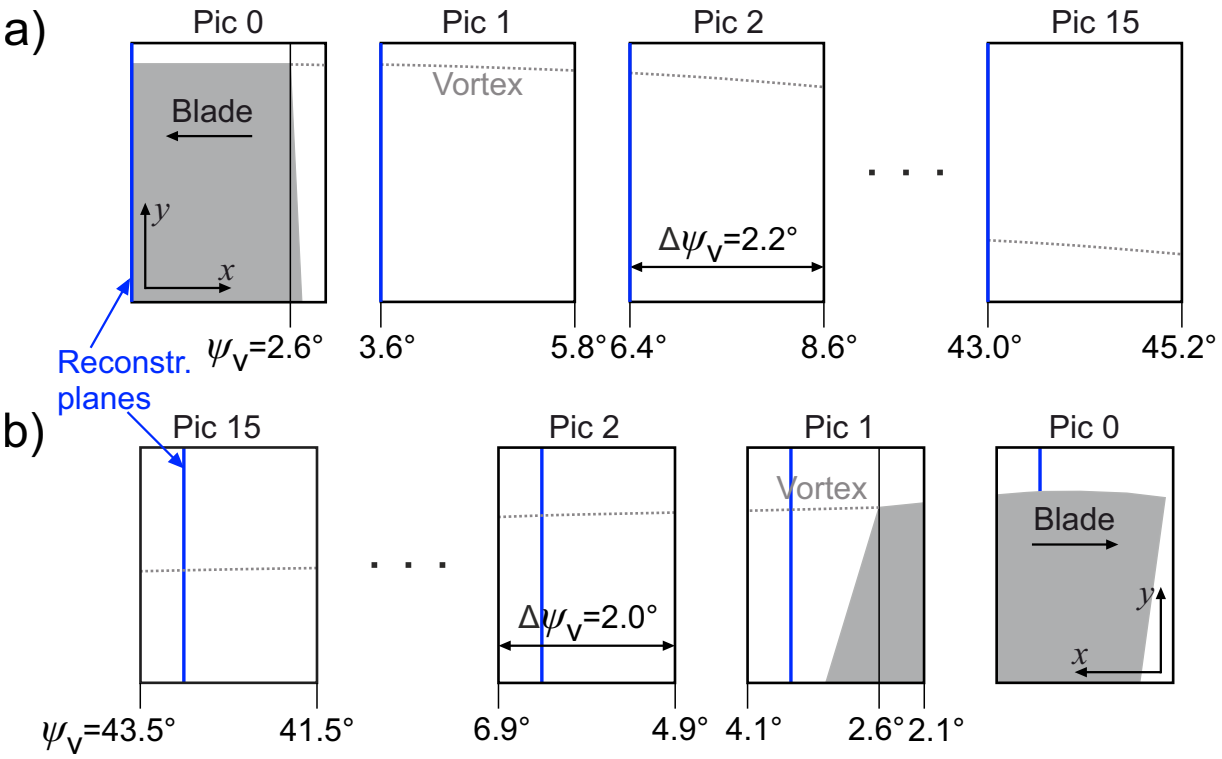

Figure 3.29: Image sequences for **a)** the lower BOS camera 1, and **b)** the upper BOS camera 2, including blue vortex reconstruction planes, after Braukmann (2015)

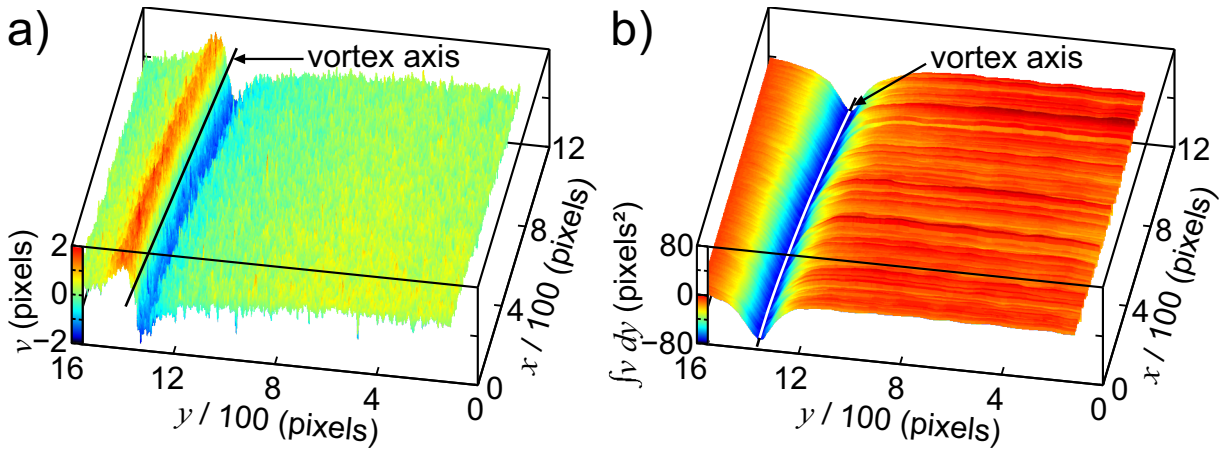

Figure 3.30: Plots of **a)** vert. displacement field v, and **b)** corresponding cumulatively integrated scalar $\int v\,dy$ over horizontal x- and vertical y-axis, after Braukmann (2015)

by subtracting the median of the displacement field from each evaluated measurement image. This procedure guaranteed negligible displacement magnitudes outside the vortex. Figure 3.30a shows an example displacement field of an unactuated measurement case at an average wake age of $\psi_v = 4.1°$ in the center of the image. It depicts the vertical image displacements v over the horizontal x- and vertical y-axis. The field contains a segment of the trailing blade tip vortex, which has an almost horizontal orientation and is located close to the upper edge of the FOV. The displacement gradient is positive above and negative below the marked vortex axis, with peak displacements of ±1.5 pixels. Figure 3.30b depicts the cumulatively integrated vertical image displacements. This value is computed by solving the integral

$$\int_{y}^{y_{max}} v(x,y)\,dy \tag{3.47}$$

for each position x, y of the vertical displacement field v. The integral value takes on a minimum value of around $-70\,\text{pixels}^2$ at the marked vortex axis in Fig. 3.30b. This minimum position was used to detect a vortex position for each vertical line in the displacement field. Vortex positions that deviated by more than two standard deviations from the average vertical position were treated as outliers and vortex line segments containing at least 90% invalid vortex points were sorted out completely. The detected 2D vortex positions of both cameras were sampled at the intersection lines between a vertical plane in physical space and both camera sensor planes. The two corresponding *one-dimensional* (1D) data sets of both BOS cameras were used as the input for a vortex reconstruction within the vertical plane in physical space.

Exact knowledge of the camera positions and orientations with respect to each other is required for a reconstruction of the vortex positions. The camera positions and angles are depicted in Fig. 3.17 and were acquired during the test campaign using a laser distance meter. The magnification factors of the two camera systems were determined by imaging calibration plates with a regular dot pattern that were placed close to the BOS backgrounds and within the measurement domain, which was defined as the combined FOV of both cameras. The precision of this preliminary calibration, however, did not suffice to determine the vortex positions with an accuracy of less than 5 mm and was therefore iteratively optimized. The details of this optimization are

given by Braukmann (2015), and adapted from an iterative camera optimization described in Subsection 5.4.3 after Bauknecht et al. (2014d). The quality of the calibration was determined by projecting corresponding 2D image positions into the combined measurement volume by means of a stereo photogrammetry approach (Mikhail et al. 2001) and computing the minimum miss distance of corresponding line pairs. The iterative routine moved camera 2 by less than 2 mm and 0.1° and improved the maximum miss distance between corresponding line pairs of both cameras from 3.8 mm to 0.3 mm. In a last step, corresponding vortex points on the blue intersection lines of both cameras in Fig 3.29 were reconstructed as time-resolved vortex trajectories within the BOS reconstruction plane and plotted with respect to the likewise determined blade tip TE positions. The results of this reconstruction process are shown in Subsection 4.1.3.

3.3.11 Density reconstruction

The acquired BOS displacement fields of camera 1 were also used for the reconstruction of the density distribution around the trailing tip vortices, as described by Braukmann (2015). The computation was restricted to camera 1 as it required a density calibration that was only carried out for the optical setup of camera 1. The determination of density is based on the proportionality between the recorded apparent background displacements and the integrated density gradients along the camera's line of sight, as described in Eqs. (3.17 – 3.19). The vertical displacement field was processed and cumulatively integrated according to the previous subsection, as shown in Fig. 3.30b. The integrated displacement field in Fig. 3.30b was consequently split into blocks with a horizontal width of 30 pixels and horizontally averaged to obtain a sub-sampled data set. The vortex position y_v was determined for each vertical cut through the vortex as described in Subsection 3.3.10. For each individual vertical line segment, the integrated vertical displacements between y_{max} and the vortex position y_v were mirrored and centered at y_v, padded with zeros, and recombined as shown in Fig. 3.31a. The resulting field represents the density variation between the vortex center and the undisturbed density in the measurement hall. The mirroring was applied to enforce a rotational symmetry of the resulting field and to minimize the influence of the density fluctuations within the wake of the blade, as visible in the lower part of Fig. 3.28. The corresponding symmetrical data fields at the same wake age behind all four

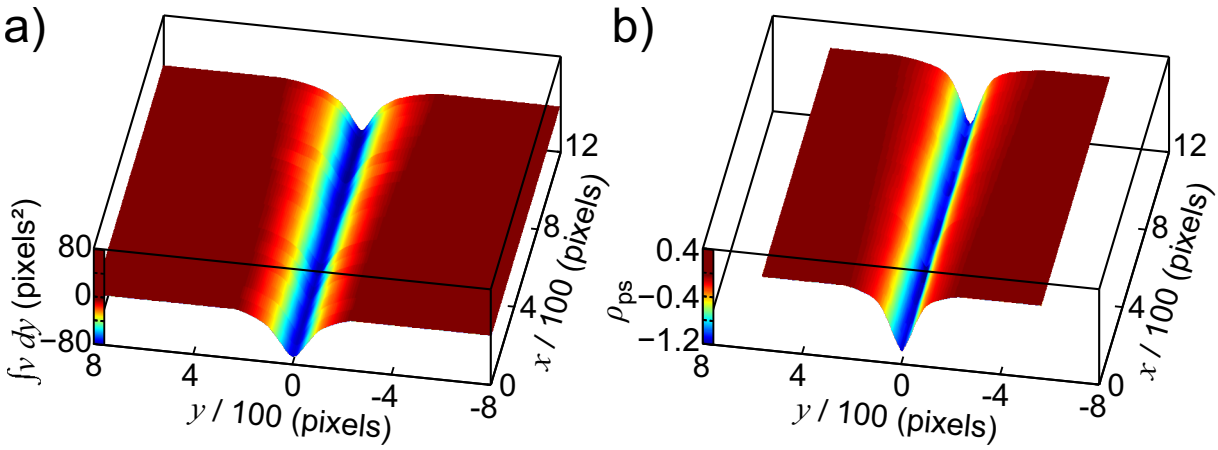

Figure 3.31: Plots of **a)** cumulatively integrated, centered, and mirrored vertical displacement field, and **b)** reconstructed pseudo-density ρ_{PS}, after Braukmann (2015)

blades of a single rotor revolution were phase-averaged to reduce the fluctuations within the data as well as the computational cost of the density reconstruction process. The reconstruction was conducted by applying a filtered back-projection algorithm to the symmetrical data field. The reconstruction process is based on the assumptions that the vortex is rotationally symmetrical and its projection onto the 2D camera sensor can be described by a Radon transformation. The density field can therefore be computed via an inverse Radon transformation or the presently used filtered back-projection, as shown in Fig. 3.31b. The result of the filtered back-projection is a non-dimensional scalar distribution that resembles the density deficit around the vortex and will be called a *pseudo density* (ρ_{PS}) here. It is possible to determine the exact scale of ρ_{PS} by measuring all factors in Eqs. (3.17 – 3.19), which describe the exact relation between the recorded apparent image displacements and the density distribution. This approach, however, is prone to measurement errors and not easy to implement for an imperfect measurement environment. Instead, the pseudo density distribution was correctly scaled here by conducting a reference experiment with the same optical setup and a known density distribution to determine a calibration factor K for the density scale. This factor is defined as the peak density deficit of a known density distribution $\rho_{peak} - \rho_\infty$, divided by the non-dimensional pseudo and ambient density:

$$K = \frac{\rho_{peak} - \rho_\infty}{\rho_{PS}\,\rho_\infty} \tag{3.48}$$

The reference experiment for the determination of K is illustrated in Fig. 3.32a. It shows a BOS displacement image featuring the airflow from a hot air gun that was positioned in the measurement volume. The hot air gun was connected to a settling chamber that reduced to a metal tube with an interior diameter of 12.9 mm and an outer diameter of 14.8 mm, marked as a hot air nozzle in Fig. 3.32a. A constant flow of hot air emerged from the tube and quickly expanded in the vertical image direction. Only the marked axisymmetric region in Fig. 3.32a featured flow with a comparable position, dimension, and shape as the trailing tip vortex. The core temperature of the air flow was determined by a temperature sensor as $T_{peak} = 410\,\mathrm{K}$ ($\pm 5\,\mathrm{K}$), compared to an ambient temperature of $T_\infty = 298\,\mathrm{K}$. With the assumption of isobaric conditions at an ambient pressure of 1009 hPa, the ambient density in the room was determined as $\rho_\infty = 1.18\,\mathrm{kg/m^3}$ and the core density as $\rho_{peak} = 0.86\,\mathrm{kg/m^3}$. These values were used to

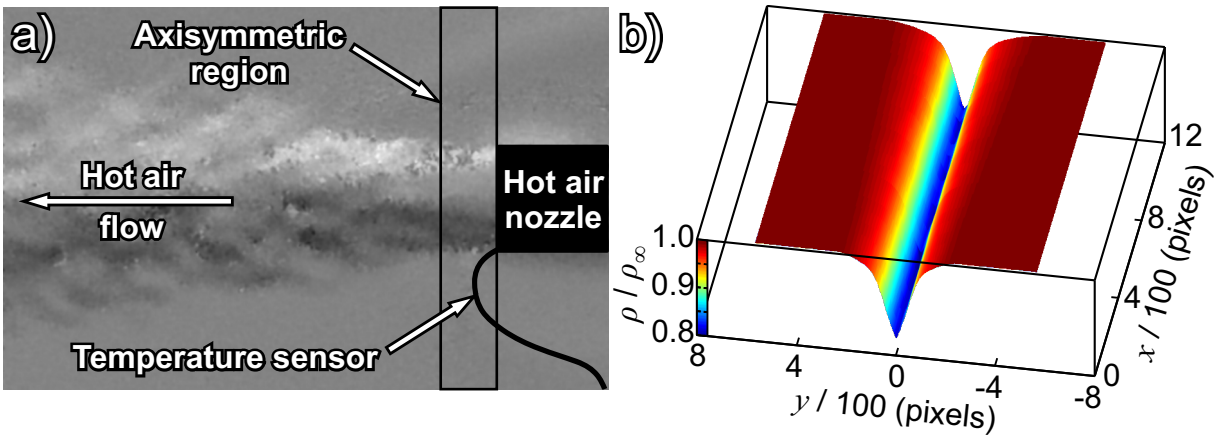

Figure 3.32: Depictions of **a)** the hot air reference experiment, and **b)** the correctly scaled reconstructed density field, after Braukmann (2015)

compute the setup-dependent calibration factor K with an accuracy of ±4.5%. The correction of the reconstructed pseudo density in Fig. 3.31b was then computed as

$$\frac{\rho}{\rho_\infty} = \rho_{\mathrm{PS}} \times K + 1 \tag{3.49}$$

The resulting vortex density field is plotted as a reduced density relative to the ambient density in Fig. 3.32b. Density profiles were extracted in cuts across the vortex axis from the reconstructed density field and fitted with a vortex density model. Bagai & Leishman (1993) derived an approximate solution for the reduced density of the Scully vortex:

$$\frac{\rho}{\rho_\infty} = \left(1 - \frac{\gamma - 1}{1 + r/r_\mathrm{c}}\zeta\right)^{\frac{1}{\gamma-1}} \tag{3.50}$$

The formulation is based on the assumptions of inviscid and isentropic flow and contains the specific heat ratio γ and a non-dimensional quantity $\zeta = \Gamma_\mathrm{v}^2 \rho_\infty / (8\pi^2 \gamma p_\infty r_\mathrm{c}^2)$. In the present case, ζ and r_c were used as fit parameters to approximate the measured density distributions across the vortex core. A discussion of the reconstructed density distributions for various levels of blade loading is given in Subsection 4.2.2.

4 STAR results and discussion

Representative *particle image velocimetry* (PIV) and *background-oriented schlieren* (BOS) results of the *smart-twisting active rotor* (STAR) hover test are presented within this chapter. The results of the unactuated *baseline* (BL) case are presented in Section 4.1, followed by an analysis of the thrust variation study in Section 4.2, and the active twist actuation in Section 4.3.

4.1 Baseline case

Results of the unactuated BL measurements are presented in this section. The same nominal test conditions of $T = 2450\,\mathrm{N}$ and $\Omega = 109\,\mathrm{rad/s}$ were applied for the unactuated measurements and the active twist actuation cases. The BL test case therefore serves as a reference for the effects of the active twist actuation and is characterized in detail here.

4.1.1 Baseline case: time-resolved velocity and vorticity fields

Figure 4.1 depicts a series of vorticity contour plots and velocity vector fields to illustrate the basic flow characteristics of the unactuated BL case. The subfigures Fig. 4.1a-f show the instantaneous flow field for vortex ages of $\psi_\mathrm{v} = 3.56° - 31.68°$ relative to the quarter chord line or $\psi_\mathrm{v} = 0.96° - 29.08°$ relative to the blade *trailing edge* (TE). Every second recorded image of the corresponding time series is depicted, with a vortex age difference between the plots of $\Delta\psi_\mathrm{v} = 5.625°$. The vorticity contours corresponding to values between $\omega_z/\Omega = -50$ and $+150$ are plotted, together with every fourth vector of the in-plane velocity field. The position of the blade tip TE is marked by a red plus and the detected circular seeding void is indicated by a white circle. Figure 4.1a contains two masked-out regions with artifacts due to the illuminated blade close to the light sheet in both camera *fields of view* (FOVs).

For the earliest vortex age in Fig. 4.1a, the forming tip vortex is indicated by a global maximum in vorticity. Its outline is non-axisymmetric and it contains the highest vorticity magnitude of the time series. Inboard of the vortex, a sheet of moderate vorticity indicates the shear layer behind the blade. The vortex roll-up is evident in Fig. 4.1b, where the vorticity sheet starts to convect with the flow field. Its outboard part is affected by the vortex-induced velocity, while the influence of the rotor downwash dominates further inboard. The imaged part of the vorticity sheet thus starts to convect downwards in a spiraling motion around the tip vortex, while part of it merges with the vortex core. Simultaneously, the vortex starts to convect radially inwards, above the vorticity sheet. In the following subplots in Fig. 4.1c-f, the vorticity magnitude of the tip vortex further decays and its shape becomes increasingly axisymmetric. Due to the

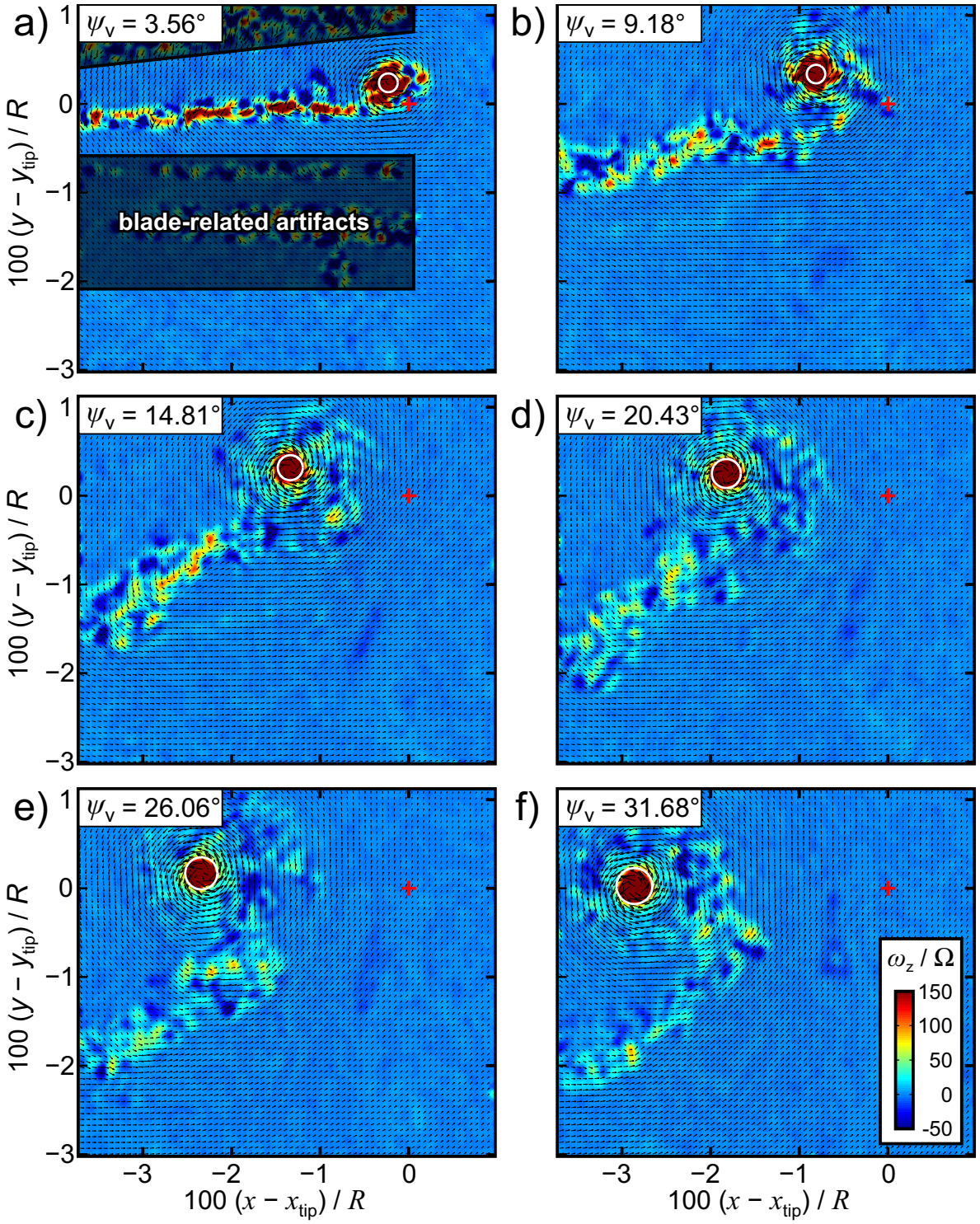

Figure 4.1: Temporal development of BL tip vortex and vorticity sheet for $\psi_v = 3.56° - 31.68°$ with vorticity contour, velocity field, seeding void (white circle), blade tip TE (red plus), and blade-related artifacts. Every second frame and fourth vector is shown.

initial asymmetry and the ongoing roll-up process, it is expected that the derived form factors of the tip vortex deviate from the theoretical vortex development models in literature (see e.g. Ramasamy & Leishman 2006a) for young vortex ages below $\psi_v \approx 15°$. Concurrently with the

vortex development depicted in Fig. 4.1c-f, the particle void increases in diameter and covers a significant part of the vortex core. The vorticity in the wake sheet further decays and continues to merge with the tip vortex. One especially accentuated part in the middle of the imaged vorticity sheet is maintained for a longer time than the rest of the sheet and is visible e.g. as a band of elevated vorticity on the left side of Fig. 4.1c. The structure decays into discrete spots of elevated vorticity in the following time steps, and can be traced throughout the remainder of the roll-up process.

The high temporal and spatial resolution of the PIV system allowed for the spatial combination of instantaneous velocity and vorticity fields. Figure 4.2 depicts *three-dimensional* (3D) vorticity data based on a sequence of 13 instantaneous velocity fields corresponding to the same BL case as shown in Fig. 4.1. The image sequence contains an extended range of vortex ages of $\psi_v = 3.56° - 37.31°$, with an azimuthal increment of $\Delta\Psi = 2.81°$ between the images. The data corresponds to a total measurement time of 5.4 ms, which is plotted with respect to the passing of the quarter chord through the measurement plane at t_0. Five example planes are depicted parallel to each other along the vortex age axis. For reasons of clarity, the parallel layout neglects the angular offset between the image planes, and only every third image plane is depicted. Each of the five depicted planes contains a down-sampled in-plane velocity field with every eighth vector shown, and the weakly smoothed out-of-plane vorticity component ω_z, which is normalized with the rotor rotational frequency Ω and colored according to the legend in the top right corner of the graph. Figure 4.2 further contains interpolated isosurfaces of the vorticity at six discrete levels between $\omega_z/\Omega = 25$ and 150.

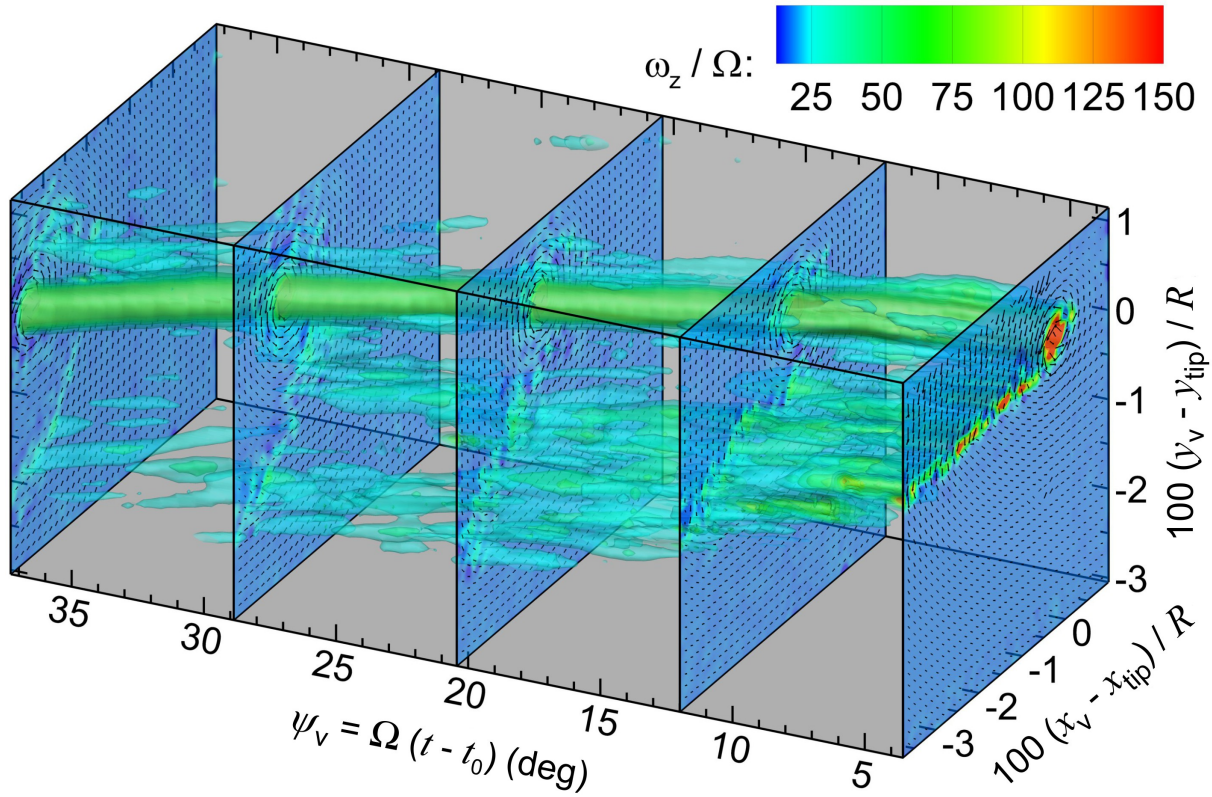

Figure 4.2: Temporal development of BL tip vortex and vorticity sheet behind the blade. Only selected vorticity isosurfaces, contour planes, and velocity vectors are shown.

The most dominant flow feature in Fig. 4.2 is the blade tip vortex, which appears as a semitransparent green cylinder that stretches over the entire measurement domain. As explained earlier, the vortex has a predominant radial convection towards the rotor hub at negative x values, and travels close to the rotor plane. The vorticity isosurfaces also visualize the sheet of vorticity that is created in the shear layer behind the rotor blade. As previously discussed, the vorticity magnitude within the sheet quickly decays, while part of the vorticity sheet rolls up around the tip vortex. This roll-up process is almost complete at the maximum visible vortex age of $\psi_v = 37.31°$, where the vorticity in the outboard blade wake is largely diffused, or spiraling around the tip vortex. The diameter of the tip vortex, as represented by the isosurfaces in Fig. 4.2, appears to slowly decrease over the observation period. This effect is caused by the constant vorticity levels of the isosurfaces and the diffusion of the vorticity with time. The graph therefore does not show that the vortex diameter – which is represented by the radial location of the peak swirl velocity – slowly increases after the initial vortex roll-up phase. The peak swirl velocity V_θ simultaneously decreases, which is indicated by the decrease in vector length from the first to the last measurement plane. The temporal development of the vortex parameters will be discussed in detail in Subsection 4.1.4.

The plot in Fig. 4.2 illustrates the visualization capabilities of a PIV system with both a high spatial and temporal resolution. The computation of a 3D vorticity field in the present work is not the first of its kind, see e.g. Richard et al. (2006) and Percin et al. (2014). Richard et al. performed a quantitative analysis of a measurement domain $3.44° - 7.04°$ behind a hovering blade based on 65 phase-averaged PIV images. Compared with the reconstruction by Richard et al. (2006), the present evaluation aimed at the investigation of a large azimuthal flow domain. It was solely based on 13 unaveraged and instantaneous PIV images and therefore required a fraction of the measurement time and processing of the previous study. The evaluation presented in Fig. 4.2 therefore constitutes an effective measure for the study of tip vortex-related flow phenomena such as *blade-vortex interactions* (BVI).

4.1.2 Baseline case: vortex trajectories from PIV

Figure 4.3 depicts the normalized vortex trajectories from two different measurement runs under nominal conditions without actuation, after Bauknecht et al. (2015). The 80 individual and time-resolved vortex trajectories are depicted as light blue curves on top of the blade contour marked in gray. This contour marks the average intersection area between the laser light sheet and the rotor blades. The vortex positions are plotted relative to their corresponding blade tip TE positions. The axes of the graph are normalized with one percent of the rotor radius and centered on the combined blade tip position, which is marked by a red plus in the graph. A dark blue line with blue dots represents the mean vortex trajectory. The dots indicate the averaged data points at vortex ages of $\psi_v = 3.56° - 34.49°$. Note that vortex positions outside an interval of two standard deviations around the average curve and trajectories consisting of at least $1/3$ of those scattered positions were considered to be outliers and are thus not included in this average curve. A light blue band of one standard deviation around the mean indicates the scattering of the curves. The band combines the vertical and horizontal standard deviations in one representative value. The individual trajectories all exhibit a similar trend with a dominant radial convection towards the rotor hub, located to the left of the graph. Superimposed is a

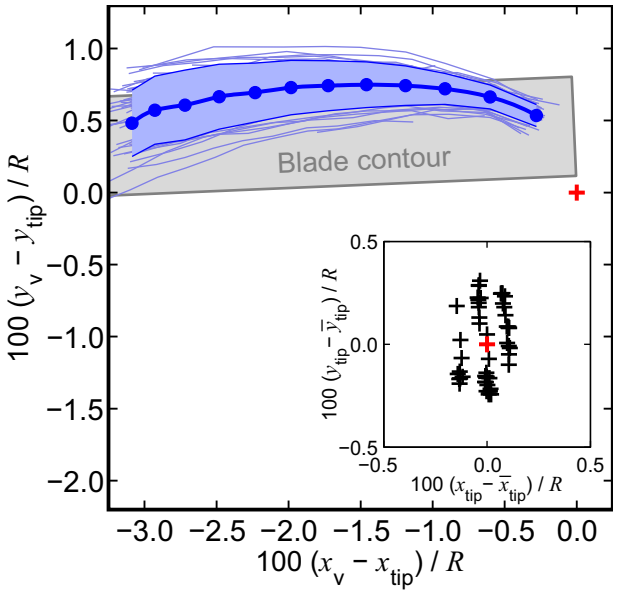

Figure 4.3: Vortex trajectories of BL case relative to detected blade tip TE position with inset of blade tip scattering, after Bauknecht et al. (2015)

slight upward convection close to the blade tip that turns into a downward convection as the vortices are affected by the rotor downwash. This convectional pattern occurs due to the pre-twisted blades that reduce the local lift, and therefore the downwash, close to the blade tip (van der Wall & Richard 2008). The turning points of the individual trajectories are found between $\psi_v = 10° - 20°$. The present data thus compares well with results from van der Wall & Richard (2008), who reported a turning point at a wake age of $\psi_v = 15°$ for a hovering rotor with similar test conditions and pre-twist.

The scattering of the vortex trajectories that has been observed in the current BL measurements is a characteristic feature of rotors that are operated in recirculating flow in ground effect. The aperiodicity of the blade tip TE position is presented in the inset of Fig. 4.3 and illustrates the cycle-to-cycle and blade-to-blade variations. The inset shows an enlarged view of the individual blade tip TE positions with respect to the mean position that is marked by a red plus sign. The vertical tip scattering has a standard deviation of ±0.17 %R, while the horizontal scattering is predominantly caused by the inhomogeneous blade radii and otherwise negligible. The detected blade-to-blade variations in the radial direction are of the order of ±2 mm or ±0.1 %R. The standard deviation of the absolute vortex positions at the youngest measured wake age of $\psi_v = 3.56°$ is 0.19 %R in the vertical and 0.07 %R in the radial direction, and comparable with the blade tip scattering. The vortex aperiodicity decreases when plotted in the blade tip-normalized frame of reference in Fig. 4.3, and takes on values of 0.05 %R in both the horizontal and vertical direction. The amplitude of the vortex aperiodicity in the normalized frame of reference increases with wake age and amounts to standard deviations of 0.13 %R in the horizontal and 0.17 %R in the vertical direction at $\psi_v = 34.49°$. The determined normalized aperiodicity values thus show that the initial vortex scattering is mainly induced by the unsteadiness of the blade tip position, while for older vortex ages of around $\psi_v = 34.49°$, the cycle-to-cycle variations in the flow field dominate the vortex scattering.

4.1.3 Baseline case: vortex trajectories from BOS

In addition to the PIV-based vortex positions, vortex trajectories were reconstructed based on images acquired by the two BOS cameras, as described in Subsection 3.3.10. Figure 4.4 depicts BOS-based vortex trajectories for an unactuated test case similar to Fig. 4.3 with a blade loading of $C_T/\sigma = 0.044$ close to the BL case. The positions correspond to a plane parallel to the PIV light sheet with a distance of 38 mm from the PIV light sheet at $\Psi \approx 181°$. In contrast to Fig. 4.3, only one mean tip position was determined for the set of 40 individual vortex trajectories. The vortex trajectories, therefore, are not normalized with each individual blade tip position, but instead plotted in a common frame of reference that includes the aperiodicity due to blade-to-blade variations. The red plus sign representing the mean tip TE position and the gray intersection area of the blade with the PIV light sheet in Fig. 4.4 are added as a reference for the trajectories. For better comparison with the PIV-based trajectories, the plot axes are normalized with the mean TE position and expressed as a percentage of the rotor radius R. It is noted that the blade tip and contour were reconstructed from a pair of BOS recordings by manually selecting the TE position in the unsharp images of the rotor blade tip. Their positions therefore have an increased uncertainty compared to the reconstructed tip positions from the PIV images.

Figure 4.4 shows 40 individual vortex curves as light blue lines corresponding to a range of vortex ages between $\psi_v = 3.6°$ and 43.0°. The corresponding average vortex convection is indicated by a solid and dark blue curve with markers indicating the individual measurement points. The trajectories exhibit a similar trend as obtained by the PIV analysis, with a predominant convection towards the rotor hub in combination with an initial uplift and a subsequent vertical redirection. The BOS trajectories feature a slightly lower vertical acceleration as for the PIV data in Fig. 4.3, possibly due to the decreased blade loading compared to the BL case. The curves also exhibit a radial offset of about $-0.2\%R$, which could by connected to the inaccurate tip localization in the BOS data. Overall, the two PIV and BOS data sets show a reasonably good overlap considering the slightly different test conditions and measurement planes.

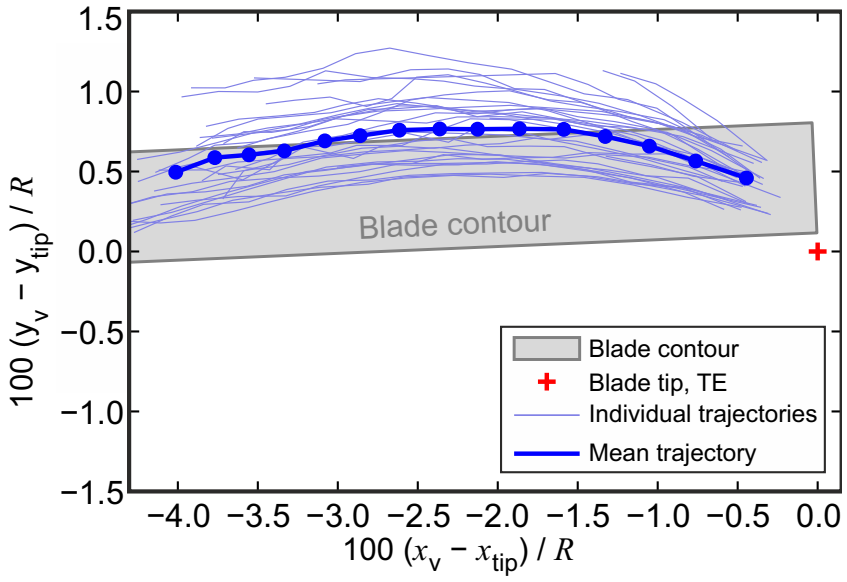

Figure 4.4: BL vortex trajectories reconstructed from two BOS cameras with added blade tip position for reference, after Braukmann (2015)

4.1.4 Baseline case: vortex characterization from PIV

The instantaneous velocity fields around the detected vortex center positions of a BL test case were extracted and corrected for the vortex convectional velocity. The peak swirl velocity $V_{\theta,\max}$ and the core radius r_c were then extracted from a Vatistas model fit to the swirl velocity profiles, as described in Subsection 3.3.6, and individually averaged. The peak axial velocity component $V_{z,\max}$ was estimated according to the evaluation described in Subsection 3.3.6. Figure 4.5a depicts the temporal development of $V_{\theta,\max}$ (blue curve) and $V_{z,\max}$ (red curve) for an individually averaged sequence of 80 test sequences of the BL case, after Bauknecht et al. (2015). Figure 4.5b shows the corresponding core radius r_c and void radius. The two velocity components are normalized with the blade tip speed ΩR, while the core and void radius are normalized with the chord length c. All curves are plotted over a range of vortex ages of $\psi_v = 3.56° - 37.31°$ relative to the passage of the quarter chord. The passage of the blade tip TE through the measurement plane is also indicated in both subplots of Fig. 4.5 by black vertical lines. The dots in the graph represent the individually averaged peak velocity values or radii, and the colored bands around them indicate the aperiodicity by one standard deviation. The peak values of $V_{\theta,\max} = 0.35\, V_{tip}$ and $V_{z,\max} = 0.24\, V_{tip}$ are both found for the youngest vortex age of $\psi_v = 3.56°$ and compare well with previous measurements of van der Wall & Richard (2008). A substantial decrease of 18 % $V_{\theta,\max}$ and 30 % of $V_{z,\max}$ occurs within the first 37.3° of vortex age. The reduction rate of $V_{\theta,\max}$ in the comparable HOTIS test was substantially higher with 34 % during the initial 37.3° of vortex age. The temporal development is approximated by an arbitrary curve fit with $V_{\theta,z} \propto \psi^{-a}$ with the fit coefficient $a = 0.07$ for $V_{\theta,\max}$ and $a = 0.16$ for $V_{z,\max}$. The curve fits are added as solid lines in Fig. 4.5a to illustrate the general trend of the data. The standard deviation for the peak swirl velocity is of the order of 2.5 $\%V_{tip}$ and illustrates the significant cycle-to-cycle variations of the unactuated rotor. The standard deviation of $V_{z,\max}$ is of the order of 5 $\%V_{tip}$ and mainly affected by the increased measurement uncertainty within the particle void.

The core development for the present BL case is plotted as a series of blue dots in Fig. 4.5b for the same range of vortex ages of $\psi_v = 3.56° - 37.31°$ as plotted in Fig. 4.5a. Studies by various researchers (Oseen 1911, Lamb 1932, Squire 1965) have found that the temporal development

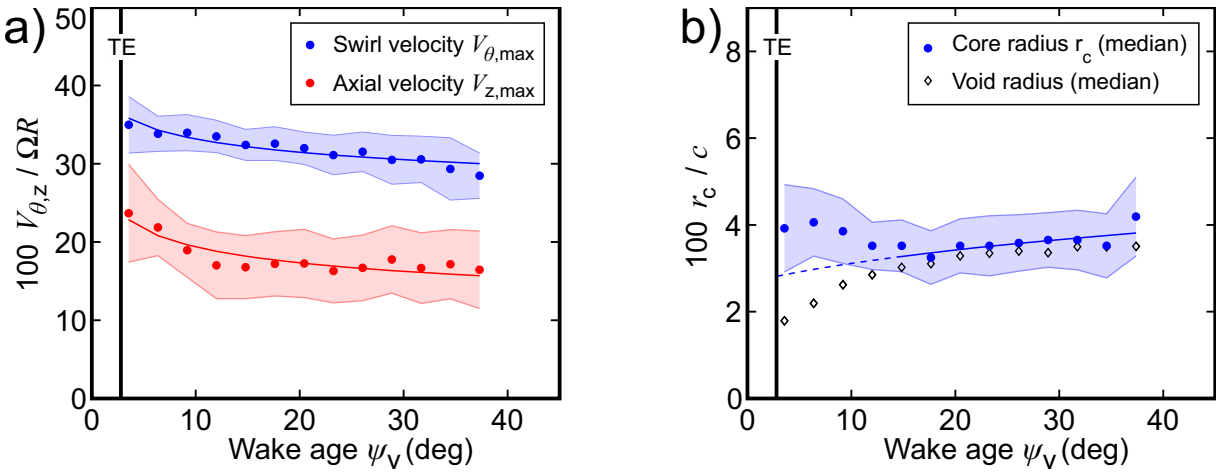

Figure 4.5: Plots of **a)** peak swirl and axial velocities over vortex age for BL case, and **b)** core radius with standard deviations and simple model fits, after Bauknecht et al. (2015)

of the core radius of a trailing blade tip vortex can be approximated by a square root function, as e.g. described in Eqs. (2.17) and (2.18). A corresponding fit function is plotted in Fig. 4.5b as a blue line. The fit curve compares well with the data points above a vortex age of about $\psi_v = 15°$. Below this value, the measured core radius does not follow the fit curve and initially decreases by 19 % from 4 %c to 3.25 %c. The deviation from theory mainly originates from the previously discussed unfinished vortex roll-up, with additional minor influences due to the radial particle tracking errors and high flow field gradients close to the core boundary. The influence of the vorticity sheet on the young tip vortex has already been described in Fig. 4.2 and could explain the shift of the core radius to larger values. Several studies reported similar deviations of the core radius from the vortex models for young vortex ages. The core radius measurements performed by Coyne et al. (1997) with a *laser Doppler velocimetry* (LDV) system exhibit no clear trend below a vortex age of 20° for a one-bladed rotor and below 60° for a two-bladed rotor. The results obtained by Bhagwat & Leishman (2000) show a reversed growth trend for vortex ages below 30°. Ramasamy et al. (2009b) also discovered a reduction of the core radius by up to 30 % for vortex ages between $\psi_v = 0° - 30°$. They attributed this trend to the positive strain rates during the unfinished vortex roll-up and the corresponding counteraction of the vortex diffusion. It is noted that the initial decrease of the core radius is found for the majority of the present measurement conditions, except for some highly actuated active twist test cases. In addition to the core radius, Fig. 4.5b also depicts the temporal development of the void radius by black diamond signs. The seeding void radius quickly expands from 1.8 %c to 3.1 %c for young vortex ages below $\psi_v = 14.81°$. Thereafter, the growth rate decreases and the seeding void radius follows the core radius development with only a marginal offset. The largest void radius is reached at the oldest observed wake age of $\psi_v = 37.31°$ with a value of 3.5 %c.

4.1.5 Baseline case: vortex characterization from BOS

The density field around the unactuated tip vortex was analyzed in a second part of the BL vortex characterization. A reconstruction of the density was carried out by Braukmann (2015) based on the detected vortex positions in the displacement images of the lower BOS camera 1, and according to the processing schemes described in Subsection 3.3.11. The results of the BL density analysis are plotted in Fig. 4.6. The left subplot in Fig. 4.6a shows the temporal development of the minimum density in the vortex core ρ_{min} relative to the ambient density ρ_∞ over a range of vortex ages between $\psi_v = 3.6°$ and 45°, including a fit curve as a guide to the eye. The corresponding decay of the peak swirl velocity $V_{\theta,max}$ is given for reference and plotted over a second vertical axis on the right border of Fig. 4.6a. The minimum core density of $\rho_{min}/\rho_\infty = 0.894$ is found at the first detected vortex age of $\psi_v = 3.6°$. The density deficit quickly recovers to $\rho_{min}/\rho_\infty = 0.946$ at $\psi_v = 22.9°$, followed by a moderate increase to $\rho_{min}/\rho_\infty = 0.955$ at $\psi_v = 45°$. The corresponding temporal development of $V_{\theta,max}$ exhibits a continuous decrease in the rate of change with wake age without a distinct switching point in time.

The reconstructed density profiles across the vortex core also enabled the determination of the vortex size from the BOS data. The core radius r_c was obtained as the half width at half height of the instantaneous density distributions. This measure constitutes an appropriate estimation for the core radius, as it corresponds exactly to the radial distance of the peak swirl velocity from the vortex axis for the Vatistas vortex model with $n = 2$. Figure 4.6b depicts the temporal

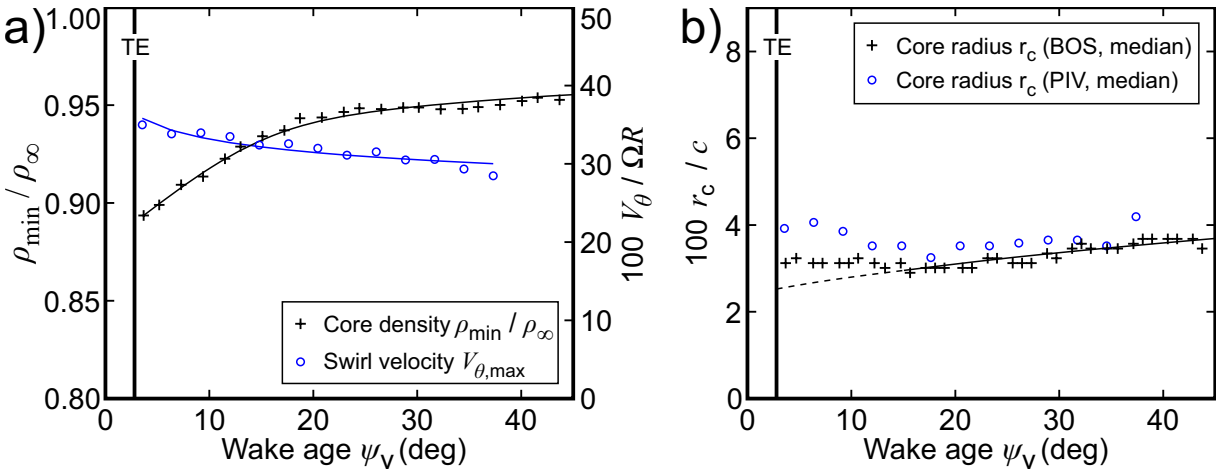

Figure 4.6: Plots of **a)** peak swirl velocity and density, and **b)** core radius of the BL case over vortex age, after Bauknecht et al. (2015) and Braukmann (2015)

development of the median core radius r_c relative to the blade chord c, as determined from PIV and BOS data. A square root trend curve represents the characteristic core development with time, as expected by common vortex models. The velocity-based core radius exceeds the density-based core radius by about $0.35\%c$ on average and by up to $0.9\%c$ during the vortex roll-up. Compared to the PIV data set, the density-based core radius exhibits a similar but less pronounced deviation from the characteristic square root trend during the initial roll-up phase, and both data sets locate the end of the roll-up phase at about $\psi_v = 15°$. Overall, the velocity- and density-based core radii exhibit qualitatively similar trends with only a small offset. The combined density and velocity data sets for the unactuated BL test case constitute a proper reference data base for the investigation of the actuator-induced effects on the blade tip vortices.

4.2 Thrust variation case

The second phase of the hover test aimed at determining a performance diagram for the unactuated BL rotor. A thrust sweep was conducted at a nominal blade frequency of $\Omega = 109\,\text{rad/s}$ with thrust and blade loading settings, as specified in Table 4.1. The corresponding blade tip angles that were measured with *stereo pattern recognition* (SPR) at the $\Psi = 270°$ position are also included in Table 4.1.

Table 4.1: Rotor settings for the thrust sweep

Thrust T (N)	1000	1356	1897	2450	3004
Blade loading C_T/σ	0.019	0.025	0.035	0.045	0.056
Tip angle α_{tip} (deg)	3.44	4.24	5.25	6.28	7.23

4.2.1 Thrust variation case: vortex trajectories from PIV

Figure 4.7 shows the average vortex trajectories for blade loadings of $C_T/\sigma = 0.019 - 0.045$. The layout of the plot is consistent with Fig. 4.3, where the vortex trajectories are all plotted relative to their corresponding blade tip TE positions. The vortex trajectories for thrust levels above the nominal condition exhibited highly increased cycle-to-cycle variations compared to the other test cases. This aperiodicity originated from the recirculation in the rotor test hall and the inhomogeneous inflow conditions of the rotor, and necessitated the previously mentioned reduction of the nominal thrust level to 2450 N instead of the planned value of 3580 N for the wind tunnel test. The increased aperiodicity above the present nominal thrust level rendered the mean vortex trajectories meaningless. The blade loading of $C_T/\sigma = 0.056$ featured cycle-to-cycle variations with more than twice the amplitude of the baseline case and is therefore not shown in Fig. 4.7. The phase-averaged vortex positions of the other thrust levels are plotted as colored markers in Fig. 4.7, together with polynomial curve fits as a guide to the eye. The background of the chart contains gray blade contours with edge colors according to the different blade loadings. These contours represent the mean intersection area between the PIV measurement plane and the rotor blades. The blade tip TE position is marked by a red plus sign and located outside this intersection area for blade tip angles above $\alpha_{tip} \approx 4.5°$.

The depicted vortex trajectories exhibit a general trend of a predominantly radial convection, similar to the BL case shown in Fig. 4.3. The peak height of the trajectories above the TE tip increases with blade loading and stagnates for the nominal thrust case. At the same time, the blade tip pitch angle and absolute vertical blade tip position increase as well. The initial location of the vortex trajectories above the tip TE suggests that the vortices form further upstream on the blades. Finally, Fig. 4.3 depicts a variation of the convection velocity for the different blade loadings. The mean convection velocity is of the order of 2.4 % V_{tip} for the lowest blade loading of $C_T/\sigma = 0.019$, and increases to 5.9 % V_{tip} for the nominal thrust level.

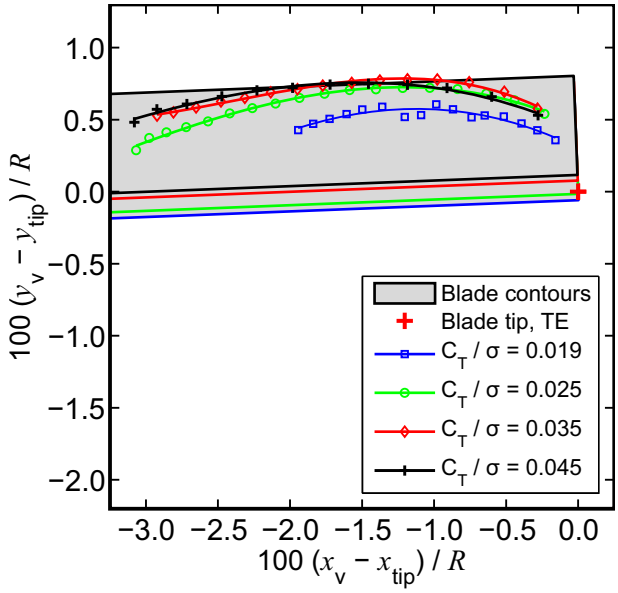

Figure 4.7: Vortex trajectories for different blade loadings C_T/σ, normalized with the blade tip TE positions, after Bauknecht et al. (2015)

4.2.2 Thrust variation case: vortex strength from PIV

The variation of $V_{\theta,\max}$ and r_c with blade loading are shown in Fig. 4.8. The two subfigures depict data from the STAR hover test (red and blue markers), and from other studies (black markers), as listed by Martin & Leishman (2002). The peak swirl velocities of the present thrust variation study were sampled at a vortex age of $\psi_v = 6.37°$ relative to the quarter chord line or 3.77° relative to the TE, see Fig. 4.8a. Data corresponding to the second-youngest vortex age is plotted here for comparison with results in the literature that were sampled around $5° - 10°$ of wake age. A steady increase is found for $V_{\theta,\max}$ with blade loading. Only the reduced value for the highest blade loading of $C_T/\sigma = 0.056$ does not follow this trend. As discussed before, the aperiodicity increases significantly for this thrust level, and the swirl velocity fields feature an increased asymmetry. These influences, in combination with the large particle displacements due to the selected image separation time, led to an underestimation of $V_{\theta,\max}$ for this elevated thrust level, which is marked by a hollow symbol in Fig. 4.8a. Apart from the highest thrust level, the present results correlate well with results from the similar HOTIS test (van der Wall & Richard 2008). The increase of $V_{\theta,\max}$ over blade loading is steeper for the STAR and HOTIS data sets than for the other results from literature. The overall agreement, however, is still acceptable, as the scales, blade pre-twists, and test conditions vary between these experiments.

Figure 4.8b depicts the normalized core radius over blade loading. The STAR data is plotted for two different wake ages of $\psi_v = 6.37°$ (red markers) for the unfinished vortex roll-up and for $\psi_v = 14.81°$ (blue markers) to the end of the roll-up process. Both data sets are of comparable value and trend, with an increase of the core radius with blade loading. The core radii from the HOTIS measurements also show an increase with blade loading above a value of $C_T/\sigma = 0.04$, but remain on a constant level for smaller blade loadings. Apart from the HOTIS and STAR measurements, there is a lack of publicly available thrust sweep data including the core radius, as well as general results for blade loadings below $C_T/\sigma = 0.05$. The other plotted data sets in Fig. 4.8b constitute singular measurement points that are difficult to compare with the present results. It is noted that any comparison of initial core radii over blade loadings is complicated by the influence of the vortex roll-up and the different sampling vortex ages of the evaluated studies.

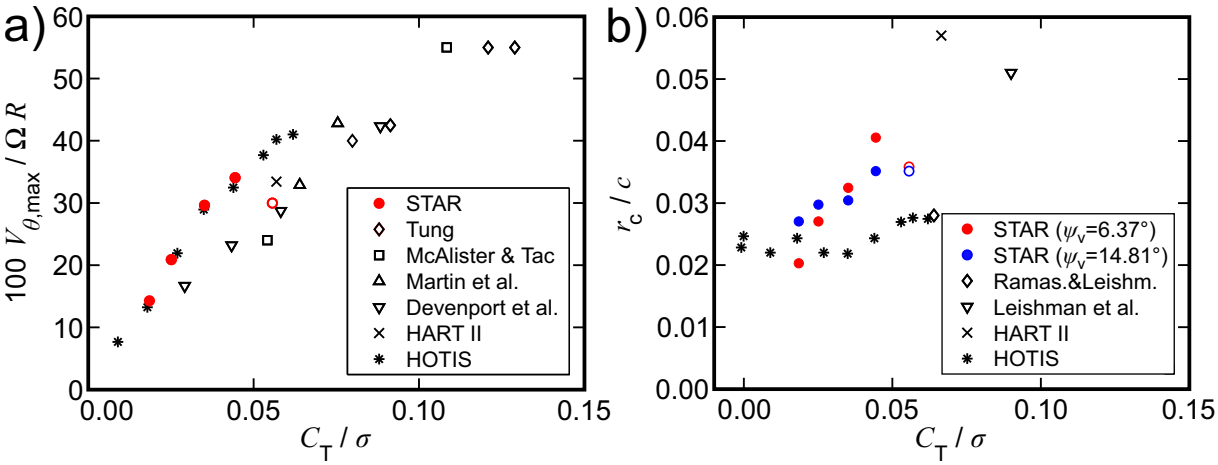

Figure 4.8: Plots of **a)** initial peak swirl velocity, and **b)** core radius over blade loading, compared with literature values from Martin & Leishman (2002)

4.2.3 Thrust variation case: vortex strength from BOS

An additional analysis of the effects of the thrust variation on the vortex strength was conducted based on the reconstructed density fields around the vortex. Figure 4.9 (after Braukmann 2015) shows average density distributions across the vortex for vortex ages of $\psi_v = 7.51°$ (Fig. 4.9a) and $\psi_v = 32.83°$ (Fig. 4.9b), and different blade loadings between $C_T/\sigma = 0.025$ and 0.065. The reduced density values ρ/ρ_∞ are plotted with a vertical offset of 0.03 between individual data sets for reasons of clarity. The solid lines represent best fits of a vortex density model from Bagai & Leishman (1993) to the data, as specified in Eq. (3.50). All curves in Fig. 4.9 depict a similar qualitative trend with a peak density reduction at the vortex center and an asymptotic density recovery to the ambient level for increasing distance to the vortex axis. The minimum core density of $\rho_{min}/\rho_\infty = 0.831$ is obtained for the highest blade loading of $C_T/\sigma = 0.065$ at a vortex age of $\psi_v = 7.51°$, as shown in Fig. 4.9a. The core density continuously increases with dropping blade loading to a value of $\rho_{min}/\rho_\infty = 0.974$ for $C_T/\sigma = 0.025$. A comparison of the two subplots in Fig. 4.9 shows that the density deficit reduces with time, as expected e.g. from the decay in vortex strength in Fig. 4.5.

The temporal development of the density field around the vortex is illustrated more clearly in Fig. 4.10. The subplot in Fig. 4.10a depicts the minimum core density over the vortex age for different blade loadings $C_T/\sigma = 0.025 - 0.065$, including fitted spline curves. The curves in Fig. 4.10a exhibit a qualitatively similar trend of a continuous density recovery, which is divided into an initial phase with a steep recovery and a subsequent phase with a moderate and asymptotic density increase. The transitional point between the two phases depends on the blade loading and increases from about $\psi_v = 10°$ for $C_T/\sigma = 0.025$ to $\psi_v = 30°$ for the highest depicted blade loading of $C_T/\sigma = 0.065$. The density recovery is not complete at these vortex ages and the remaining density deficit also scales with the blade loading.

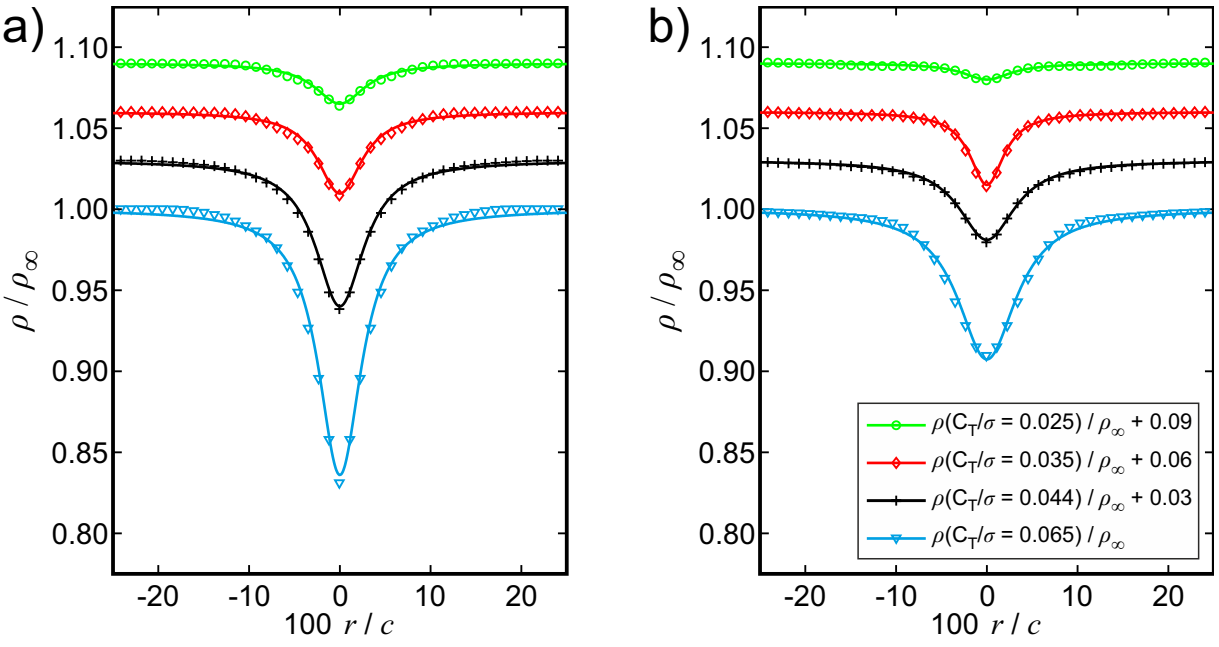

Figure 4.9: Vortex density profiles at **a)** $\psi_v = 7.51°$, and **b)** $\psi_v = 32.83°$ for different blade loadings C_T/σ, with an offset of 0.03 between the curves, after Braukmann (2015)

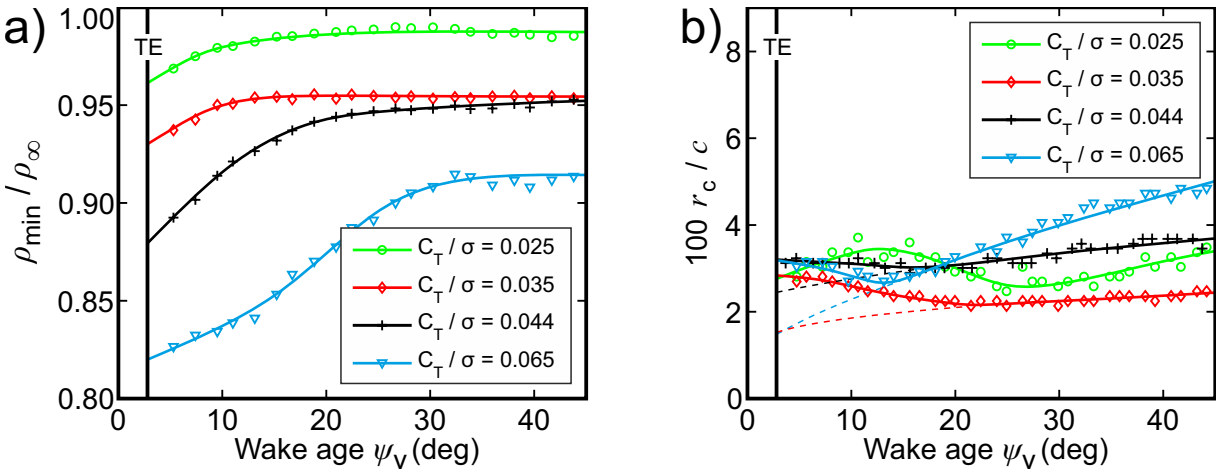

Figure 4.10: Temporal development of **a)** vortex core density, and **b)** core radius over wake age for different blade loadings, after Braukmann (2015)

The subplot in Fig. 4.10b depicts the core radius and fitted spline curves over the same range of blade loadings as in Fig. 4.10a. The data points for the lowest blade loading of $C_T/\sigma = 0.025$ exhibit an increased variation with vortex age compared to the other curves and no meaningful trend for young vortex ages below $\psi_v = 25°$, possibly due to the flat density distribution of the corresponding curves in Fig. 4.9. The curves corresponding to higher blade loadings exhibit an initial reduction in core radius due to the vortex roll-up, followed by a characteristic growth of r_c proportional to the square root of the wake age, as indicated by the dashed lines. The core growth and the consequent core radii at increased vortex ages depict a dependency on the blade loading. At a vortex age of $\psi_v = 45°$, a core radius of $r_c = 2.44\%c$ is obtained for a blade loading of $C_T/\sigma = 0.035$, compared to a maximum core radius of $r_c = 5.01\%c$ for $C_T/\sigma = 0.065$.

The results obtained from the reconstructed vortex density reproduce the trends for the initial vortex strength in Fig. 4.8a. The initial development of the density-based core radius suggests that the core radii in Fig. 4.8b might be sampled at a wake age that is too early and may contain effects of the unfinished vortex roll-up. The growth of the core radius with increasing blade loading that was found in the PIV data is confirmed by the density measurements.

4.2.4 Summary

In summary, the thrust variation study demonstrates the influence of the blade loading on the vortex trajectories and core parameters. The examined vortex trajectories show qualitatively similar trends, as well as an increasing vertical offset and vortex convection velocity with blade loading. The peak swirl velocity exhibits a variation with blade loading that compares well with results from the similar HOTIS test. The core density of the vortex depicts a comparable proportionality with the blade loading. The core radius shows a stronger dependency on blade loading than the HOTIS results, but matches the range of results found in literature. This dependency is found for core radii based on the velocity and density evaluation. The magnitude of the changes due to the variation of the blade loading serves as a comparison for the effects of the active twist actuation, which will be discussed in the following section.

4.3 Active twist actuation

The active twist actuation has a direct effect on the blade twist distribution and the blade flap deformation via a coupled motion. The aerodynamic effects are indirect, as they are caused by the deformation of the blades. The blade deformations are consequently outlined first in Subsection 4.3.1, followed by a discussion of the effects of the active twist actuation on the strength (Subsection 4.3.3) and positions (Subsection 4.3.2) of the blade tip vortices, as well as an analysis of 3D vorticity fields in Subsection 4.3.5. Preliminary PIV results based on instantaneous velocity fields for the $1/rev$ and $3/rev$ actuation frequencies have already been published in a STAR overview paper by Hoffmann et al. (2014). Part of the final PIV results presented within this section have also recently been published by Bauknecht et al. (2015).

4.3.1 Active twist actuation: blade deformation

The blade response to the active twist actuation was measured in a separate test campaign after the aerodynamic examination. SPR and blade tip *light emitting diode* (LED) measurements were conducted by researchers from the DNW and the DLR Braunschweig, respectively. The results of this second hover test were published by Hoffmann et al. (2014) and are summarized here. An additional interpretation of the blade deformations is given with respect to their impact on the blade aerodynamics and a prediction of the vortex strength is derived.

The twist actuation was applied to the trimmed rotor with BL conditions of $T = 2450\,\mathrm{N}$ and $\Omega = 109\,\mathrm{rad/s}$. The higher-harmonic blade control caused a harmonic change in the elastic torsion and flap bending with a certain phase delay. A direct correlation between the blade torsion and the blade tip angle can be assumed, as the effects of the elastic torsion outweigh other unsteady effects. The blade tip angle therefore oscillated harmonically around the unactuated BL condition. The control angles of the rotor were not readjusted during the active twist control, to measure the actuation-induced changes of the rotor loads and moments. The present evaluation is based on a series of active twist test cases with sinusoidal actuation with frequencies of $1/rev - 5/rev$ and a control amplitude of $U = 600\,\mathrm{V}$. The active twist control phase was varied in increments of 45° to capture one complete period of the higher-harmonic blade motion.

Blade tip deformations from SPR measurements are shown in Fig. 4.11, after Hoffmann et al. (2014). The subplots depict the twist deformation amplitudes (Fig. 4.11a), vertical tip displacements (Fig. 4.11b), as well as the corresponding phase delays (Fig. 4.11c,d) of all four rotor blades over the actuation frequency k. The inhomogeneous blade properties cause some discrepancies between the individual curves of the four rotor blades in all subplots of Fig. 4.11, but do not affect the overall consistent trends. The blade tip response in twist in Fig. 4.11a reaches its peak between the actuation frequencies $2/rev$ and $3/rev$, and decreases to negligible amplitudes for a frequency of $5/rev$. This is due to the natural torsion frequency of the blades of about $3.5/rev$ and an amplification of the torsion close to this frequency. Simultaneously, the corresponding phase delay in twist increases with actuation frequency, as depicted in Fig. 4.11c. The amplitude distribution of the flapping motion is shown in Fig. 4.11b and peaks at the $1/rev$ frequency, which is close to the first flap mode of the rotor blades at $1.03/rev$. The corresponding phase delay in Fig. 4.11d peaks for the $4/rev$ actuation frequency with a phase angle of 360°.

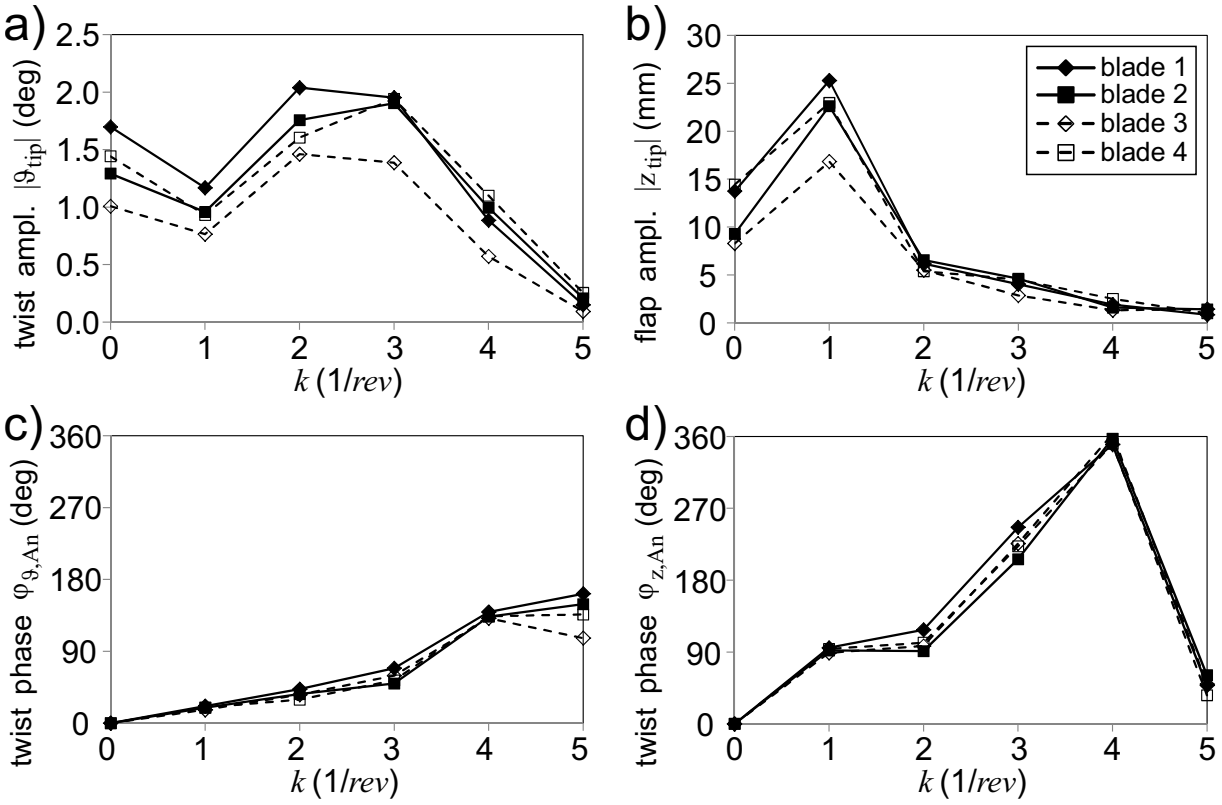

Figure 4.11: Graphs of **a,b)** blade twist and flap deflection amplitude, and **c,d)** corresponding phase angles over control frequency for U_n = 600 V, after Hoffmann et al. (2014)

The local pitch angle at the blade tip influences the blade aerodynamics, including the tip vortices. The strength of the blade tip vortices, however, is also affected by the local lift and circulation distribution close to the tip, and the effective angle of attack α_e at the blade tip with respect to the oncoming flow field. In the present study, the actuator-induced changes of the effective angle of attack at the blade tip $\Delta\alpha_e$ are used as a simplified predictor for the vortex strength. The effective tip angle is influenced by the blade twist and the vertical blade tip flapping motion; both, therefore, have to be considered for the prediction of the vortex strength. Depending on the actuation frequency, the vertical blade motion evokes changes of α_e of up to 0.7° in amplitude. This effect is proportional to the vertical tip velocity, which runs −90° ahead of the tip flapping oscillation. The resulting actuator-induced changes of the effective angle of attack $\Delta\alpha_{e,total}$ relative to the BL tip angle are computed here as the superposition of the tip torsion angle $\Delta\alpha_{e,tors}$ and the induced angle due to the vertical flapping motion of the blade tip $\Delta\alpha_{e,flap}$.

Figure 4.12 depicts the corresponding changes of α_e at the forward rotor position Ψ = 180° for actuation frequencies between $1/rev$ (Fig. 4.12a) and $5/rev$ (Fig. 4.12e). The curves in Fig. 4.12 consider the phase delays of flapping and torsion, and the −90° offset for the peak velocity of the vertical blade motion. The square markers in Fig. 4.12 indicate the tip torsion measured by SPR with 45° increments. The markers in Fig. 4.12a and b have a phase offset of 10° due to an issue with the triggering system. The thick blue lines represent the mean change due to the tip torsion of all four blades $\Delta\alpha_{e,tors,k}$, with the corresponding standard deviation marked by light blue bands. The red dashed lines represent the flap-induced change of the effective angle of attack $\Delta\alpha_{e,flap,k}$ and the solid black lines the total change $\Delta\alpha_{e,total,k}$ as the sum of the other curves.

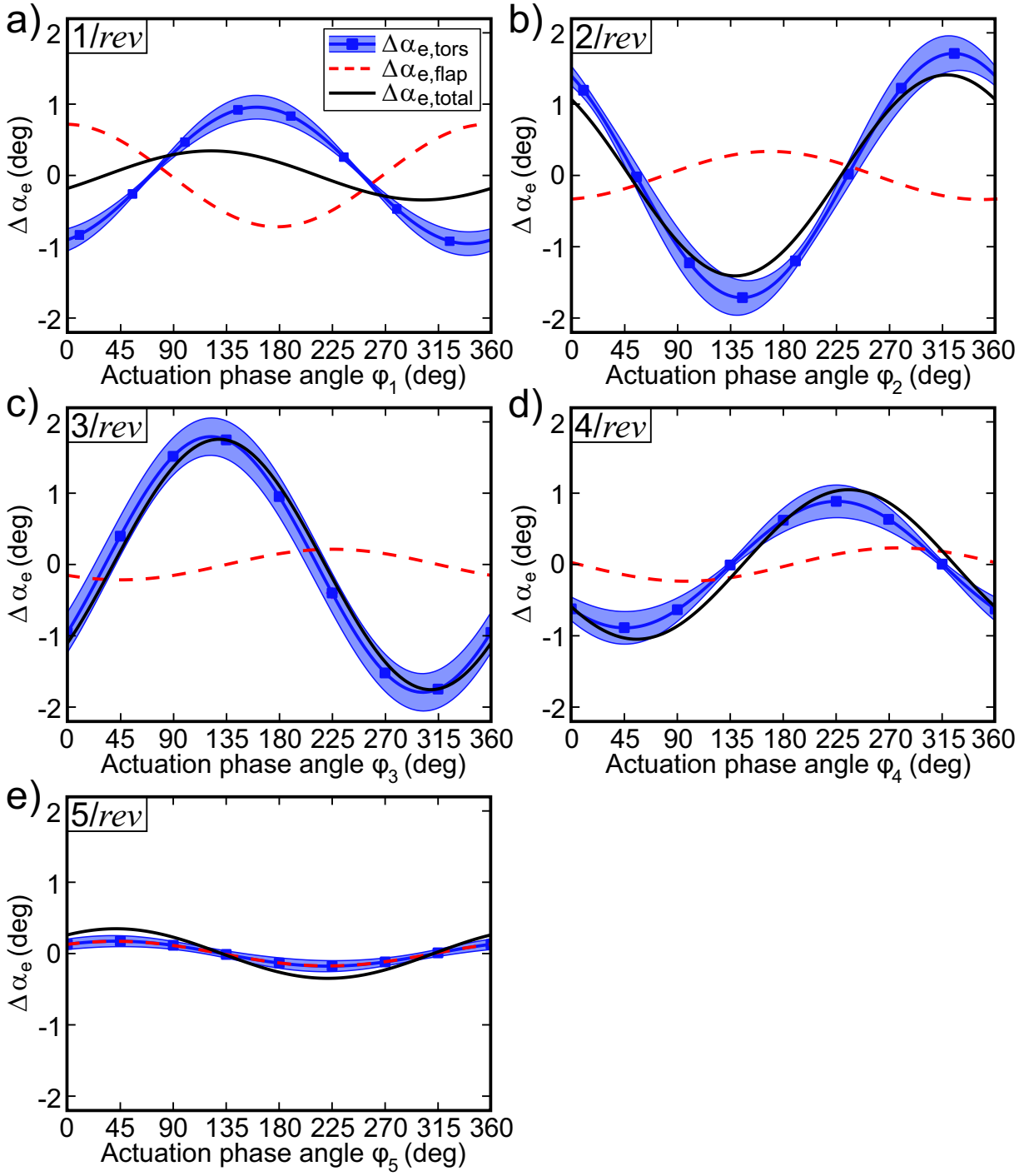

Figure 4.12: Change in effective blade tip angle at $\Psi = 180°$ rotor azimuth due to torsion- and flap-induced blade motion, plotted over actuation phase angle φ_k for actuation frequency of **a)** $1/rev$ to **e)** $5/rev$

Figure 4.12a shows moderate torsion angles of around $|\Delta\alpha_{e,tors,1}| = 1°$ for the $1/rev$ actuation frequency, with a corresponding phase delay in torsion response of 19°. The proximity of the actuation to the first flap mode of the rotor blades at $1.03/rev$ leads to large blade tip deflections of $17 - 25$ mm with a phase delay in flap response of about 92°. The corresponding peak vertical velocity of the blade tip is of the order of 2.7 m/s or 1.2 %ΩR, and results in a harmonic

change of the effective angle of attack with an amplitude of $|\Delta\alpha_{\mathrm{e,flap,1}}| = 0.7°$. The flap- and torsion-induced curves are almost anti-cyclic and partly cancel each other out, as indicated by the reduced amplitude of $|\Delta\alpha_{\mathrm{e,total,1}}| = 0.34°$ for the black curve. Based on the SPR results, the $1/rev$ actuation is thus expected to have a small effect on the vortex strength and cause a moderate vertical offset of the vortex trajectories due to the blade flapping motion.

The torsion amplitudes of the $2/rev$ and $3/rev$ actuation in Fig. 4.12b and c are both of the order of $|\Delta\alpha_{\mathrm{e,tors,23}}| = 1.8°$, but with different phase angles for the peak positions. The maximum variations between the torsion-induced changes of the individual blades are of the order of 0.5° in amplitude and 20° in phase delay. The vertical blade tip deflections of 7 mm for the $2/rev$ actuation and 5 mm for the $3/rev$ actuation result in small flap-induced amplitudes of $|\Delta\alpha_{\mathrm{e,flap,2}}| = 0.35°$ and $|\Delta\alpha_{\mathrm{e,flap,3}}| = 0.2°$, respectively. The flap-induced changes therefore have no significant effect on the total effective angles of attack of $|\Delta\alpha_{\mathrm{e,total,2}}| = 1.41°$ and $|\Delta\alpha_{\mathrm{e,total,3}}| = 1.76°$. The $2/rev$ and $3/rev$ actuation frequencies are therefore expected to have a strong effect on the vortex strength, and a moderate effect on the initial vertical vortex locations.

Figure 4.12d corresponds to the $4/rev$ actuation frequency and shows a comparable torsion amplitude as for the $1/rev$ actuation. A moderate flap-induced effect occurs with almost the same phase angle as the harmonic torsion, leading to an increased total change of the effective angle of attack of about $\Delta\alpha_{\mathrm{e,total,4}} = 1.05°$, which is expected to be visible in the vortex strength. Finally, the curves for the $5/rev$ actuation in Fig. 4.12e depict a negligible variation of the effective angle of attack over the phase angle φ_5 with peak amplitudes of $|\Delta\alpha_{\mathrm{e,tors,5}}| = |\Delta\alpha_{\mathrm{e,flap,5}}| = 0.17°$ and a total peak value of $|\Delta\alpha_{\mathrm{e,total,5}}| = 0.35°$. Accordingly, the $5/rev$ actuation is expected to have no significant effect on the strength and positions of the tip vortices.

4.3.2 Active twist actuation: vortex trajectories

Figure 4.13 depicts the impact of the active twist actuation on the vortex convection. The response to the actuation frequencies $1/rev - 5/rev$ is shown in the subplots Fig. 4.13a-f. Each subplot features the average vortex trajectories of the unactuated BL case (black curve), and for the active twist actuation with a certain frequency k and various phase angles φ_k (colored curves). Note that vortex positions outside an interval of two standard deviations around the average curve and trajectories consisting of at least 1/3 of those scattered positions were considered to be outliers and are thus not included in this evaluation. The vortex trajectories in Fig. 4.13a and Fig. 4.13c-f correspond to the actuation frequencies $1/rev - 5/rev$ and are plotted with respect to the corresponding individual blade tip TE positions x_{tip},y_{tip}, which are marked by red plus signs. The average intersection area between the rotor blades and the PIV measurement plane is indicated by a gray area in the background of these subplots. The blade tip TE is located vertically below the intersection area due to the pitch angle of the blade. Figure 4.13b shows the same $1/rev$ data as Fig. 4.13a, but in the fixed frame of reference of the BL blade tip TE position. Minor differences between the curves in Fig. 4.13a and Fig. 4.13b result from the previously described outlier detection routine, which affected different data points in the two frames of reference. The blade tip TE positions corresponding to the individual actuated vortex trajectories are plotted as colored plus signs on the right side of the graph, whereas the BL TE position is marked by a black plus sign. Figure 4.13b thus illustrates the effects of the relatively large vertical flapping motion of the blade tip on the vortex trajectories for the $1/rev$ actuation

frequency. The plot axes of all six subplots are normalized with one percent of the rotor radius. One count in the subplots thus corresponds to a physical length of 20 mm. The actuation phase angle was varied between $\varphi_{3-5} = 0°$ and 315° for the $3/rev - 5/rev$ actuation. For the $1/rev$ and $2/rev$ actuation frequencies, a phase offset due to an issue with the triggering system introduced a shift of the investigated phase angles to the range of $\varphi_{1-2} = 10° - 325°$.

Actuation with 1/*rev*

The subplots in Figs. 4.13a,b illustrate the effects of the $1/rev$ active twist actuation on the vortex convection for different phase angles φ_1. The vortex trajectory for the phase angle $\varphi_1 = 235°$ is located outside the PIV field of view and therefore not depicted here. The trajectories corresponding to $\varphi_1 = 280°$ and 325° are also located close to the upper boundary of the field of view – which is apparent in Fig. 4.13b – and therefore cut off at a vortex age of 9.2°. The maximum visible vortex age for the other trajectories ranges between $\psi_v = 31.7°$ and 37.3° due to the different convection velocities. The majority of the vortex trajectories exhibit relatively small deviations of less than 0.4 %*R* from the BL trajectory in Fig. 4.13a. Only the curve corresponding to a phase angle of $\varphi_1 = 100°$ deviates from the BL case by more than 0.5 %*R*, as it has the steepest ascent above the tip path plane of all visible curves.

This picture changes noticeably in the absolute frame of reference of Fig. 4.13b. The effects of the twist actuation on the absolute vortex trajectories are dominated by the vertical displacement of the blade tip. The maximum deviations from the BL TE position are found for $\varphi_1 = 100°$ with −1.01 %*R* and for $\varphi_1 = 280°$ with +0.61 %*R*. In addition to this automatically determined data, the tip position corresponding to the not depicted $\varphi_1 = 235°$ trajectory was also estimated from the measurement images. This estimated tip TE position is depicted in Fig. 4.13b as a light blue plus sign in brackets. It is located approximately 1.3 %*R* above the BL tip position, which increases the total actuator-induced, vertical blade tip variation to about 2.3 %*R*. This blade tip displacement also affects the initial vortex positions and therefore the whole vortex trajectories. The shape of the $\varphi_1 = 100°$ curve still differs from the other trajectories in Fig. 4.13b, but it does not exhibit a large or growing deviation to the BL curve, as visible in Fig. 4.13a. The trajectories for $\varphi_1 = 145°$ and 55° feature an almost constant offset to the BL trajectory of about 1 %*R*, which simultaneously constitutes the largest actuator-induced displacement for the $1/rev$ actuation. The alteration of the young vortex trajectories by the $1/rev$ actuation is thus dominated by the blade tip deflection and only weakly affected by the variation of the tip angle.

Actuation with 2/*rev*

The effect of the $2/rev$ actuation on the vortex convection is shown in Fig. 4.13c. The evaluation is based on a phase angle sweep excluding the $\varphi_2 = 100°$ and 145° angles due to reoccurring actuator faults and the tight test schedule*. As for the $1/rev$ actuation, the majority of the vortex trajectories are located within a region of ±0.5 %*R* around the black BL curve. The curve for $\varphi_2 = 325°$ is located up to 0.65 %*R* below the BL trajectory. A maximum deviation of more than

*A malfunction of the active twist actuators occurred during the test of the $2/rev$ actuation, which led to an interruption of the hover test for three weeks and thus disrupted the test schedule.

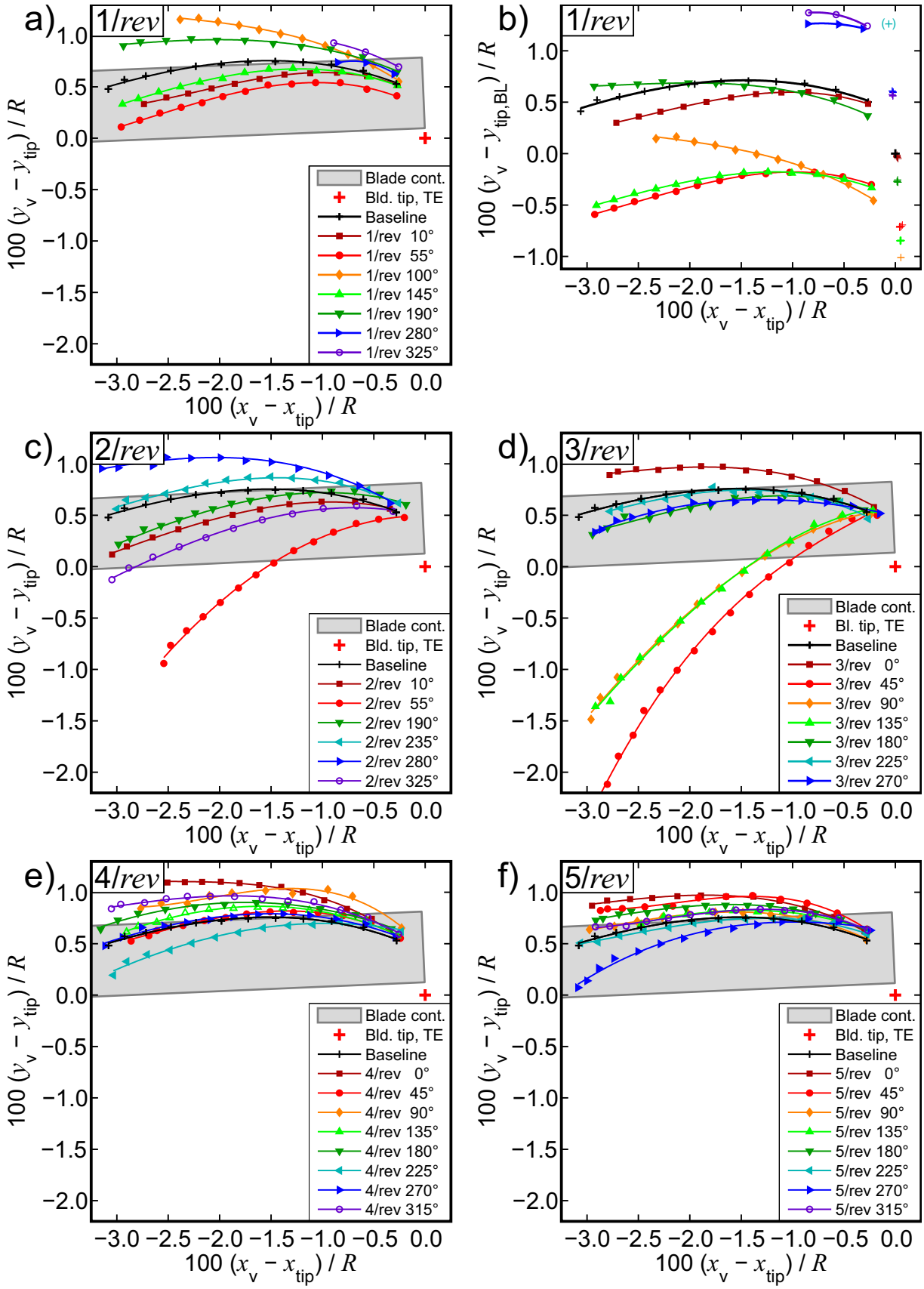

Figure 4.13: Vortex trajectories for BL case and **a)** $1/rev$ to **e)** $5/rev$ actuation with different phase angles φ_k, normalized with each individual blade tip TE position

1.4 %R below the BL curve is achieved for a phase angle of $\varphi_2 = 55°$. The vertical scattering of the blade tip TE positions due to the actuation is of the order of 0.38 %R relative to the BL tip position; much lower as for the $1/rev$ actuation. The moderate effect of the $2/rev$ actuation on the blade tip deflection only weakly modifies the trajectories, and the peak deviation of the $\varphi_2 = 55°$ curve from the BL case still reaches 1.2 %R in the absolute frame of reference.

Actuation with 3/*rev*

The most articulated effects of the active twist actuation on the vortex convection were observed for the $3/rev$ actuation frequency, as illustrated in Fig. 4.13d. The vortex positions for a phase angle of $\varphi_3 = 315°$ are located above the PIV field of view and therefore not accessible for this evaluation. The maximum visible vortex age of the other vortex trajectories varies between $\psi_v = 34.5°$ and 45.7°. The curves corresponding to the phase angles $\varphi_3 = 180° - 360°$ resemble the outline of the black BL trajectory and deviate from it by less than 0.3 %R at the maximum visible vortex age. A second group of trajectories, corresponding to the phase angles $\varphi_3 = 45° - 135°$, is located below the BL trajectory. These curves exhibit a significantly increased vertical convection velocity for the entire range of observed vortex ages. The trajectories thus resemble the trailing vortex system of an untwisted rotor with increased sectional lift in the outboard part of the blade, see e.g. Milluzzo & Leishman (2013). The largest vertical deviation from the BL trajectory is found for a phase angle of $\varphi_3 = 45°$ and takes on a value of 2 %R for the maximum visible vortex age of the BL curve of 34.49°. The vertical distance of the actuated vortex to the lower rotor blade surface increases to about 2.1 %R within the first 45° of wake age. The miss distance to the following rotor blade – which is an important factor for the strength of BVI – is estimated to be of the order of 5 %R, based on an extrapolation of the measured convection rates. The basic layout of the curves in Fig. 4.13d is not significantly affected by the vertical blade tip position, which scatters by up to +0.7 %R and −0.2 %R around the BL location (not shown here). The range of vertical blade tip movement of 0.9 %R for the $3/rev$ actuation is significantly smaller than the 2.3 %R of the $1/rev$ actuation, which is in accordance with the blade tip deformation measurements shown in Fig. 4.11b.

It is interesting to note that the effect of the $3/rev$ actuation on the vortex trajectories highly depends on the actuation phase angle, as it is negligible for phase angles outside the effective $\varphi_3 = 45° - 135°$ range. The effective modification of the vortices is thus restricted to three equally spaced azimuthal ranges with a combined extend of about one third of the rotor circumference. In a potential application of active twist to reduce BVI effects, the $3/rev$ actuation could be applied to simultaneously modify the BVI-relevant vortex trajectories that are created around the $\Psi = 135°$ and 225° azimuthal positions on the advancing and retreating blade side.

Actuation with 4/*rev* and 5/*rev*

Finally, the results for the $4/rev$ and $5/rev$ actuation frequencies are depicted in the subplots in Fig. 4.13e,f. Both graphs feature the trajectories of all eight actuation phase angles. The curves are all similar to the BL trajectory with a comparable convection velocity and general trend. For both actuation frequencies, the majority of curves vertically deviate by less than ±0.35 %R

from the BL case. Only the $\varphi_4 = 0°$ trajectory for the $4/rev$ actuation frequency has a larger and positive offset of 0.6 $\%R$ from the BL case, which is reached at a vortex age of $\psi_v = 34.5°$. The other noteworthy measurement case is the $\varphi_5 = 270°$ phase angle for the $5/rev$ frequency, which is located within the general band of scattering around the BL case, but features a different trend with a slightly increased vertical convection rate. The vertical blade tip variation from the BL case is similarly small with maximum deviations of $-0.17\ \%R$ to $+0.37\ \%R$ for the $4/rev$ frequency, and $-0.1\ \%R$ to $+0.44\ \%R$ for $5/rev$. The small blade tip flapping amplitudes correlate well with the SPR measurements in Fig. 4.11b. All in all, the changes in vortex trajectory are negligible for the higher actuation frequencies of $4/rev$ and $5/rev$. For the $4/rev$ actuation frequency, the measured changes are smaller than the predicted effects in Fig. 4.12d. The reason for this over-prediction is not apparent and could not be determined from the present data set. The displacement amplitudes of the $5/rev$ actuation from the BL trajectory are in accordance with the predicted changes in Fig. 4.12e.

Comparison of vortex displacements at a single vortex age

A comparison of the effects of the five different actuation frequencies on the vertical vortex displacement is given in Fig. 4.14. The depicted data points correspond to a single vortex age of $\psi_v = 28.87°$. This vortex age represents the maximum wake age at which a majority of the detected vortices were still visible in all the subplots of Fig. 4.13. The plot depicts the vertical deviation between the normalized and actuated vortex positions $(y_v - y_{tip})_k$ and the normalized BL position $(y_v - y_{tip})_{BL}$ at the same wake age $\psi_v = 28.87°$ as a percentage of the rotor radius, plotted over the actuation phase angle φ_k. The BL position is marked by a black horizontal line. The average vertical distances between the actuated trajectories and the BL case are indicated by markers according to the plot legend. The error bars mark an interval of one standard deviation around the actuated vortex positions to illustrate the corresponding level of aperiodicity. Neighboring markers of the same actuation frequency are connected by a colored line, whereas missing values are indicated by a dashed line. The data points in Fig. 4.14 underline the findings from Fig. 4.13. The vertical vortex locations for the actuation frequencies

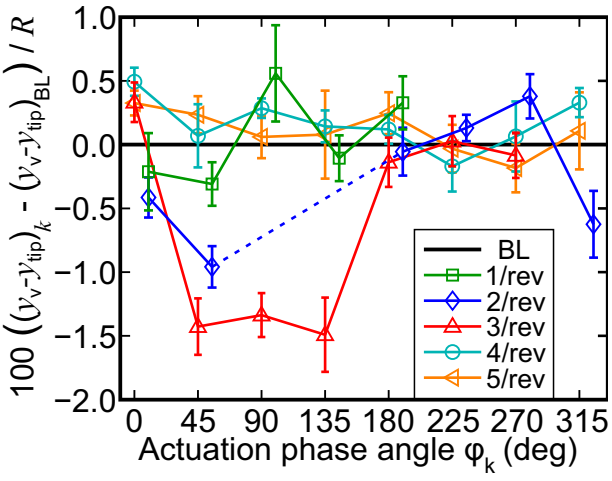

Figure 4.14: Vertical vortex displacement relative to BL case at $\psi_v = 28.87°$, plotted over phase angle φ_k for $1 - 5/rev$ actuation

$k = 1, 4, 5$ are located within a band of $\pm 0.5\,\%R$ around the BL value. Only the $1/rev$ actuation with a phase angle of $\varphi_1 = 100°$ reaches a value of $0.56\,\%R$ above the BL trajectory, where simultaneously the highest aperiodicity of $\pm 0.38\,\%R$ occurs. The peak displacement for the $2/rev$ frequency is of the order of $1\,\%R$ below the BL case. The highest displacements of about $1.4 - 1.5\,\%R$ below the BL trajectory are again obtained for the $3/rev$ actuation frequency with the phase angles $\varphi_3 = 45° - 135°$. While Fig. 4.14 contains only information from Fig. 4.13, it facilitates the comparison of the vertical vortex displacements at a fixed wake age, which is not obvious in Fig. 4.13 due to the varying vortex convection velocities.

4.3.3 Active twist actuation: vortex strength

The influence of the active twist actuation on the peak vortex strength was studied in a second part of the data evaluation. The initial peak swirl velocity $V_{\theta,\max}$ was used as a measure for the vortex strength. It was determined from the velocity fields corresponding to the earliest wake age of $\psi_v = 3.56°$ by individually averaging the peak values of the fitted Vatistas vortex model, as described in Subsections 3.3.6 – 3.3.7. Figure 4.15 shows the variation of $V_{\theta,\max}$ from the BL value $V_{\theta,\max,BL}$ for actuation frequencies of $1/rev$ (Fig. 4.15a) to $5/rev$ (Fig. 4.15e) and various actuation phase angles φ_k. The peak swirl velocity of the BL case is indicated by a black horizontal line in each subplot of Fig. 4.15. The individually averaged values of $V_{\theta,\max}$ are plotted as colored markers over actuation phase angle, corresponding to the legends in Fig. 4.13. The standard deviation of the averaged velocity values is represented by vertical bars. As mentioned above, the velocity values for some phase angles are not available here because the corresponding vortices left the FOV of the PIV cameras or could not be measured due to issues with the actuators during the test campaign. In addition to the velocity data, the average variation of the effective blade tip angle is added to the graphs as dashed sinusoidal curves. These curves correspond to the black solid lines in Fig. 4.12 and are used for a comparison of the PIV results with a simple prediction of the vortex strength. The dashed lines are centered on the BL value and have the same, arbitrary scale for all five subplots.

Actuation with 1/*rev*

Figure 4.15a depicts the initial peak swirl velocity of the $1/rev$ actuation relative to the BL velocity. The average velocity magnitude for the phase angles $\varphi_1 = 100°$ and $325°$ is located close to the BL level. An average increase of $+12\,\%$ with respect to the BL case is obtained for $\varphi_1 = 190°$. The other phase angles exhibit a moderate decrease in $V_{\theta,\max}$ of around $-16\,\%$. The smallest average swirl velocity of $V_{\theta,\max} = 0.26\,\Omega R$ is found for $\varphi_1 = 55°$ and $145°$ with an average reduction of $-18\,\%$ compared to the BL case. The typical aperiodicity of the velocity values is of the order of $\pm 10\,\%$ to $\pm 20\,\%$ for most phase angles. A larger level of scattering of $\pm 33\,\%$ is observed for the phase angle $\varphi_1 = 190°$. A comparison between the effective tip angle prediction and the peak swirl velocities only shows a weak correlation. The scattering of $V_{\theta,\max}$ is random and incoherent, and does not exhibit the expected harmonic trend. From the SPR results in Fig. 4.12, no significant alteration is expected for the swirl velocities. This is due to the flap-induced vertical blade tip motion, which reduces the impact of the actuation on the effective tip angle by up to $65\,\%$. Consequently, no clear correlation is found between

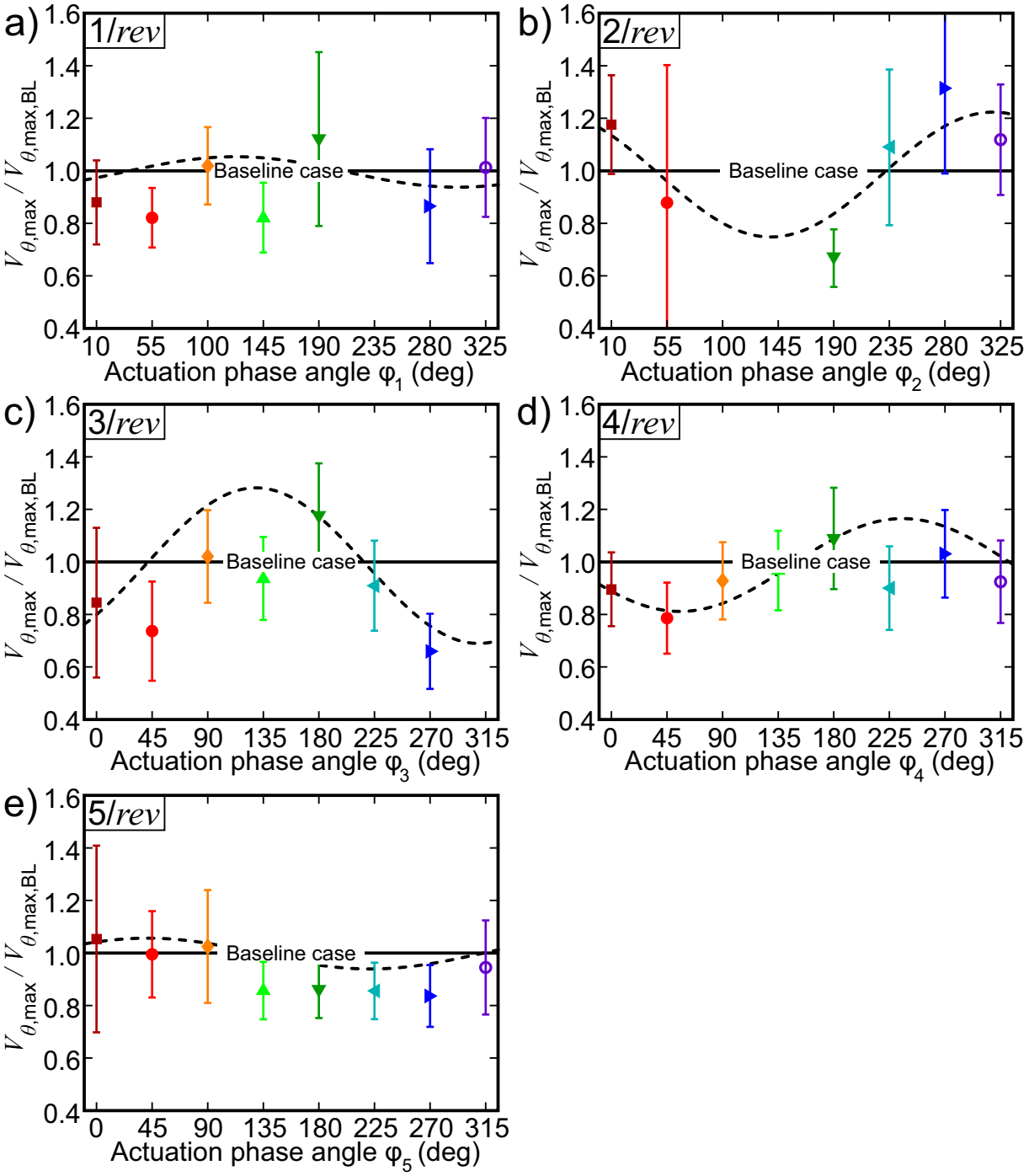

Figure 4.15: Initial peak swirl velocity relative to BL case for **a)** $1/rev$ to **e)** $5/rev$ actuation with different phase angles φ_k and dashed prediction models from Fig. 4.12

the predicted and measured vortex strength over φ_1. A second factor that possibly contributed to these deviations is the fact that for some actuation phase angles, the initial vortex roll-up was not completely finished at a vortex age of $\psi_v = 3.56°$. The corresponding swirl velocities were partly reduced by elliptical vortex outlines or two smaller vortex cores in the process of merging. Naturally, these complex conditions cannot be described by a simple correlation with the effective angle of attack. As the excitation of flap motion is much less pronounced for the other actuation frequencies, the $1/rev$ actuation can be regarded as an exceptional test case.

Actuation with 2/*rev*

Based on the SPR results in Fig. 4.12, an increased impact of the active twist actuation on the vortex strength is expected for the $2/rev$ actuation frequency due to the reduced flapping motion and a closer proximity to the natural torsion frequency of the blades. This increased effect is indeed observed in Fig. 4.15b, with measured peak deviations of up to ±60 % relative to the BL peak swirl velocity, and average deviations of about half the size. An average increase with respect to the BL condition is observed for actuation phase angles of $\varphi_2 = 10°$, and $\varphi_2 = 235° - 325°$. The average swirl velocity exceeds the unactuated test case by up to +31 % for a phase angle of $\varphi_2 = 280°$. This data point illustrates that the active twist actuation does not necessarily accomplish a decrease in vortex strength on the entire rotor, but instead causes a redistribution of the trailing vortex strength over the rotor azimuth. The highest average reduction of the peak swirl velocity of −33 % relative to the BL condition is determined for the test condition with a phase angle of $\varphi_2 = 190°$. As the minimum effective pitch angle – represented by the dashed curve in Fig. 4.15b – coincides with the unmeasured phase angles $\varphi_2 = 100° - 145°$, the peak reduction in swirl velocity could be even higher than the minimum of −33 % that was measured here. The observed scattering in the range of ±11 % to ±46 % is comparable with the $1/rev$ actuation case, and indicates a significant level of aperiodicity. Despite the scattering, the average velocity values exhibit a good correlation with the effective pitch angle curve, and the measured deviations from the BL velocity level even exceed the prediction. The results for the $2/rev$ actuation frequency thus show a significant control authority of the active twist actuation over the strength of the trailing blade tip vortices.

Actuation with 3/*rev*

Figure 4.15c shows the influence of the $3/rev$ active twist actuation on the initial peak swirl velocity $V_{\theta,\max}$ for different phase angles φ_3. The resulting individual peak swirl velocities deviate from the BL value by up to −48 % and +38 %. The $3/rev$ actuation with a phase angle of $\varphi_3 = 180°$ causes the highest average increase of the $3/rev$ actuation with +18 % compared to the unactuated case. The values for $\varphi_3 = 90°$ and 135° are located close to the BL case. The other phase angles exhibit a mean reduction in initial peak swirl velocity of −10 % or more. A peak reduction of the average velocities of −34 % compared to the BL value is found for $\varphi_3 = 270°$ with $V_{\theta,\max} = 0.22\,\Omega R$. This reduction in initial vortex strength is about twice as pronounced as for the $1/rev$ actuation, as expected from the excitation of natural blade frequencies, shown in Fig. 4.12. The aperiodicity of the $3/rev$ measurements is slightly reduced compared to the $1/rev$ and $2/rev$ actuation frequencies. The scattering amplitude around the average velocities takes on values of around ±15 % for the majority of the actuation phase angles, and an absolute maximum of ±28 % for $\varphi_3 = 0°$. A vortex strength prediction based on the effective angle of attack of the blade tip is again added as a dashed curve in Fig. 4.15c. Its amplitude is comparable to the $2/rev$ case, but it features a phase offset of close to 180°. The average values for the initial swirl velocity show a good correlation with the vortex strength prediction. An increased deviation occurs for the $\varphi_3 = 135°$ phase angle, which returns the same swirl velocity as for the unactuated case, but was expected to feature the highest increase in vortex strength according to the effective pitch angle prediction. It is yet unclear if this deviation can be attributed to a measurement issue or to the simplified assumptions that the prediction model is

based on. The results for the $3/rev$ actuation frequency illustrate a high control authority of the active twist actuation on the vortex strength, which is comparable with the $2/rev$ results.

Actuation with 4/*rev*

A moderate impact on the vortex strength is observed for the $4/rev$ actuation frequency, which is shown in Fig. 4.15d. The predicted control authority for the $4/rev$ frequency is slightly smaller than for the $2/rev$ actuation, whereas the observed variations are comparable with the $1/rev$ actuation case. The measured swirl velocities scatter in a region between $-35\,\%$ and $+28\,\%$ relative to the BL value. The variation of the average values is restricted to a range between $+8\,\%$ for $\varphi_4 = 180°$ and $-22\,\%$ for $\varphi_4 = 45°$. The aperiodicity of the individual swirl velocity values is of the order of $\pm 15\,\%$ for the majority of phase angles, and thus comparable to the $3/rev$ case. The highest level of aperiodic scattering of $\pm 19\,\%$ is obtained for a phase angle of $\varphi_4 = 180°$. The average swirl velocities exhibit a high overlap with the dashed curve representing the effective pitch angle variation. The peak deviation from the prediction occurs for $\varphi_4 = 225°$ with a reduction of $-10\,\%$ instead of the predicted increase in vortex strength. It is interesting to note that the value for the $\varphi_4 = 225°$ phase angle was reproducible, as it was measured twice on different test days with the same results. In general, the $4/rev$ actuation attains only a moderate control authority over the strength of the shed vortices, which is comparable to the $1/rev$ test case.

Actuation with 5/*rev*

The highest control frequency of $5/rev$ is situated relatively far away from the natural torsion frequency of the blades, and thus expected to have no significant effect on the strength of the trailing vortices. A small variation of the average swirl velocities is observed over the actuation phase angle in Fig. 4.15e. The average swirl velocities corresponding to the phase angles $\varphi_5 = 0° - 90°$ and $315°$ deviate from the BL level by $5\,\%$ or less. The other phase angles feature a reduced average swirl velocity of about $-14\,\%$ with a peak reduction of $-16\,\%$ relative to the BL case for a phase angle of $\varphi_5 = 270°$. The aperiodicity of the swirl velocity is of the order of $\pm 15\,\%$ for the majority of the measured phase angles. Only the scattering for the phase angle $\varphi_5 = 0°$ takes on a significantly increased value of $\pm 36\,\%$. This scattering simultaneously governs the total actuator-induced scattering of the individual measurement values of between $-30\,\%$ and $+41\,\%$ around the BL level. Overall, the $5/rev$ actuation only evokes small changes of the vortex strength, as expected from the SPR results.

Concluding remarks

With the assumption of a linear dependency between α_e and the vortex strength, the actuation is thought to induce a sinusoidal oscillation of the peak swirl velocity around the BL value. The obtained PIV results for all five actuation frequencies, however, exhibit a global tendency towards smaller velocity amplitudes. In other words, the correlation between the prediction model and the actuated velocity data could be improved by adding a negative offset to the dashed model curves. This offset, as well as reproducible deviations between the PIV data and

the model, illustrate that the impact of the twist actuation on the trailing vortex geometry is too complex to be described by a single blade parameter alone. Nevertheless, the comparison of the PIV results with the effective blade tip angle α_e shows that the simple model has an adequate overlap with the data and captures the main features of the higher harmonic vortex strength variation. The results presented in Fig. 4.15 thus demonstrate the control authority of the active twist actuation over the strength of the shed vortices on a hovering rotor.

4.3.4 Active twist actuation: swirl velocity and core size for 3/*rev*

The effect of the active twist actuation on the initial peak swirl velocity $V_\theta(\psi_v = 3.56°)$ has been shown in Fig. 4.15 in the previous subsection. While the initial vortex strength describes the impact of the actuation on the young vortices, the effects on older vortex ages should also be investigated, as the twist actuation also affects the temporal development of the swirl velocity. Figure 4.16 depicts this temporal development of the peak swirl velocity $V_\theta(\psi_v)$ and the core radius $r_c(\psi_v)$ for the BL case and the $3/rev$ actuation frequency with different control phase angles. The individually averaged data points are plotted over a range of wake ages between the marked passage of the blade tip TE at $\psi_v = 2.6°$ and a maximum age of 50°. Spline curves are fitted to the data points as a guide to the eye. The peak swirl velocity is plotted as a percentage of the blade tip speed $V_{tip} = \Omega R$ in Fig. 4.16a, and the core radius is visualized as a percentage of the blade chord length c in Fig. 4.16b. The individual data points and fitted curves are color-coded corresponding to the plot styles in Figs. 4.13 and 4.15, and labeled in Fig. 4.16b.

The black BL curves in Fig. 4.16 feature a characteristic decrease of V_θ with time, and an initial decrease in core radius due to the vortex roll-up, followed by a slow increase due to the radial diffusion of the vortex. The relative values of the initial swirl velocities for the actuated test cases correspond to the data depicted in Fig. 4.15c. The majority of the actuated test cases in Fig. 4.16a resemble the BL curve with a phase angle-dependent velocity offset and small variations of the rate of decay. The swirl velocity curves corresponding to the phase angles $\varphi_3 = 180°$ and 225° have an increased slope compared to the BL case. The shape of the orange

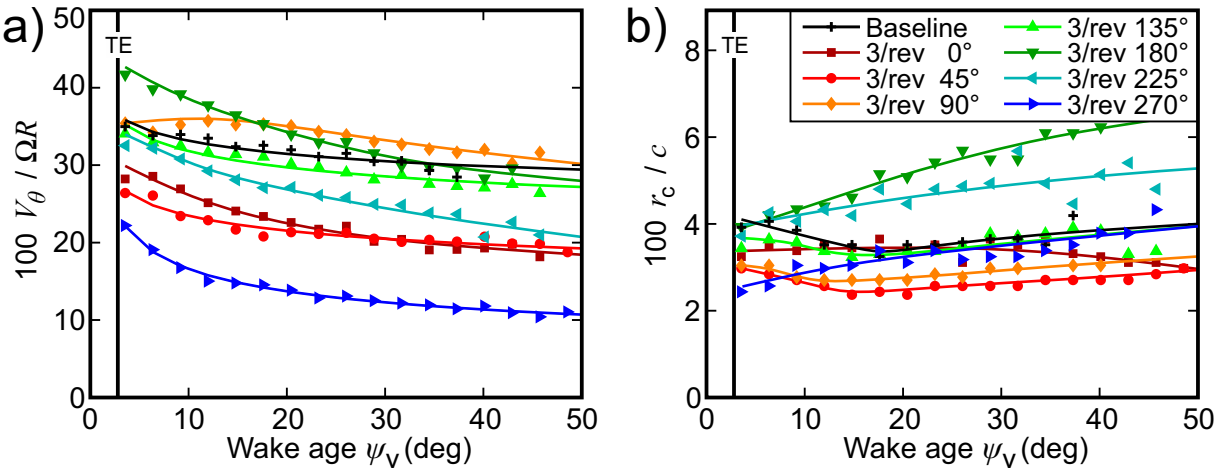

Figure 4.16: Temporal development of **a)** the peak swirl velocity, and **b)** the corresponding core radii for $3/rev$ actuation with different phase angles φ_3 and the BL case

curve representing a phase angle of $\varphi_3 = 90°$ does not show the characteristic decrease in swirl velocity of the other curves for vortex ages up to $\psi_v = 15°$, and instead features a slight initial growth in vortex strength. Similar but less pronounced effects are also found for the youngest detected vortex age of other swirl velocity curves. These deviations from the expected monotonous decrease in vortex strength might be explained by the unfinished vortex roll-up, which is also visible in the elevated initial core radii of some curves in Fig. 4.16b. The initially shrinking core radius with a consequent core expansion has already been discussed for the BL case in Subsection 4.1.4. Effects of the vortex roll-up are also observed for the $3/rev$ actuated test cases with phase angles of $\varphi_3 = 45° - 135°$ and for small wake ages up to $\psi_v = 15°$. After the initial vortex roll-up, a majority of the actuated curves in Fig. 4.16b exhibit a steady growth of the core radius r_c with time. At an advanced vortex age of $\psi_v = 37.31°$, the BL fit function takes on a value of 3.8 $\%c$, compared to a minimum actuated core radius of 2.7 $\%c$ for $\varphi_3 = 45°$, and a maximum actuated core radius of 6.1 $\%c$ for $\varphi_3 = 180°$.

The swirl velocities at an advanced vortex age of $\psi_v = 37.31°$ are compared to the BL case in Fig. 4.16a to better understand the impact of the active twist actuation on the trailing vortex strength after the completion of the initial vortex roll-up. The general variation of the vortex strength at this increased wake age is similar to the initial changes in Fig. 4.15c, but with an offset to smaller velocities. A peak reduction in vortex strength of about −60 % compared to the BL value at $\psi_v = 37.31°$ is found for a phase angle of $\varphi_3 = 270°$. The swirl velocities of the $\varphi_3 = 0°$ and 45° phase angles also show an increased reduction of about −31 % relative to the BL case. Only the vortex trajectory for the phase angle $\varphi_3 = 90°$ is still located noticeably above the BL curve at the advanced vortex age of $\psi_v = 37.31°$ with an 11 % increased swirl velocity. The changes in swirl velocity at the advanced wake age thus illustrate that the effect of the $3/rev$ active twist actuation on the trailing vortex strength is even more pronounced when investigating the fully rolled-up tip vortex. The shift towards smaller velocities for older wake ages, however, is not found for the $2/rev$ actuation frequency (not shown here). Despite minor changes, the variation of the peak swirl velocity by the $2/rev$ actuation at a vortex age of $\psi_v = 37.31°$ still closely resembles the velocity distribution plotted in Fig. 4.15b. This finding underlines the potential of the active twist actuation with a $3/rev$ actuation frequency for affecting the vortex strength in the far-field of the blade wake.

4.3.5 Active twist actuation: 3D vorticity fields for 2/rev and 3/rev

Reconstructions of the 3D vorticity fields behind the rotor blade were carried out based on individual, time-resolved image sequences. The reconstructions for two example measurement cases are shown in Fig. 4.17, similar to the BL result presented in Fig. 4.2. The upper subplot in Fig. 4.17a corresponds to the $3/rev$ actuation frequency with a phase angle of $\varphi_3 = 45°$. This measurement case was shown in the previous subsections to feature the largest vertical vortex displacement and one of the smallest vortex strengths of the tested measurement conditions. The lower subplot in Fig. 4.17b shows data corresponding to the $2/rev$ actuation frequency with a phase angle of $\varphi_2 = 280°$. This test case features a vortex trajectory that is located close to and above the BL condition and has the highest recorded vortex strength of the hover test. Both subplots have the same scale and depict data between a vortex age of $\psi_v = 3.56°$ and the maximum visible vortex age of $\psi_v = 45.74°$ for the upper graph and $\psi_v = 37.31°$ for the lower graph, cor-

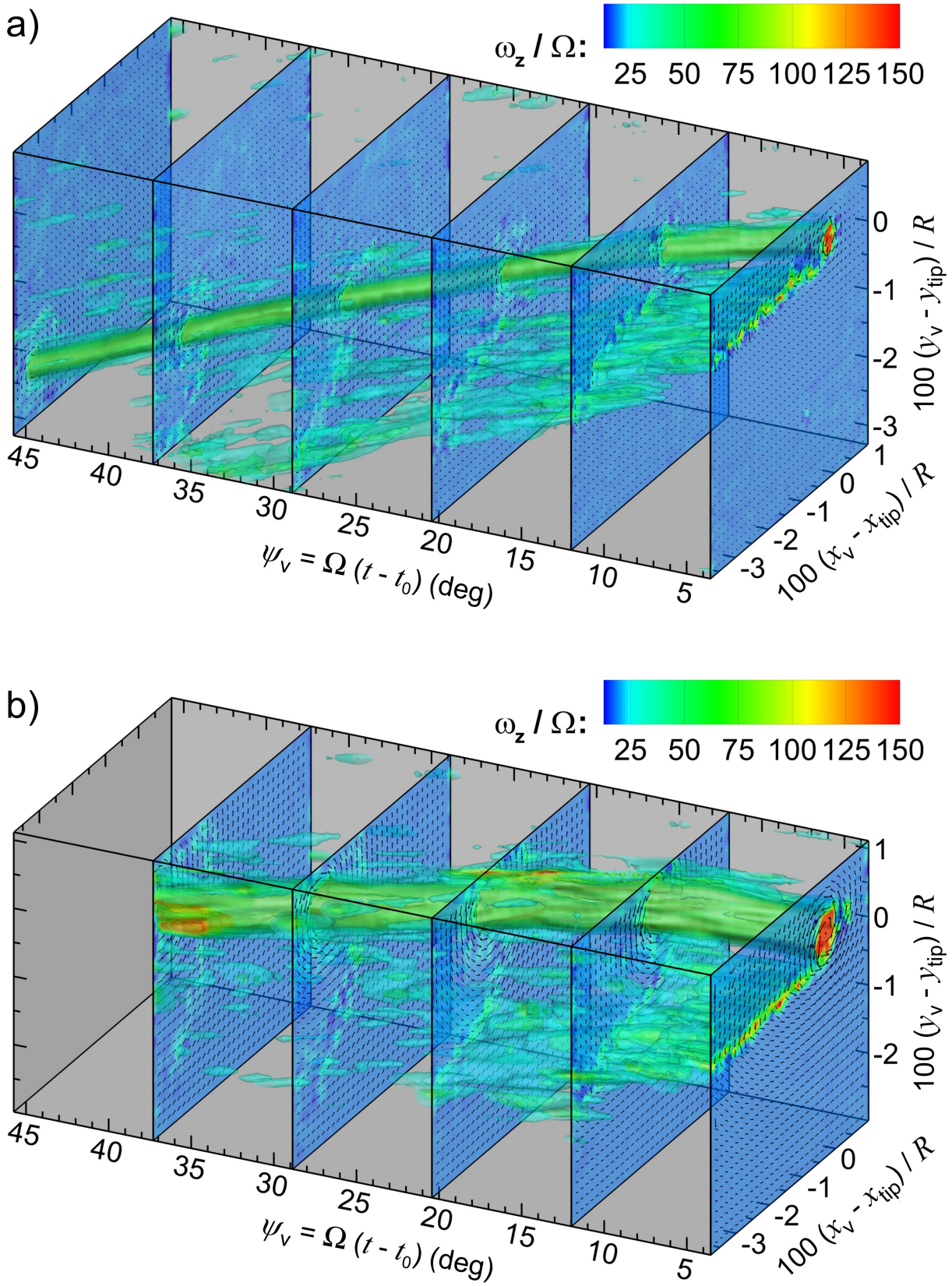

Figure 4.17: Temporal development of actuated tip vortices and vorticity sheet behind the blade for **a)** max. vortex displacement and small vortex strength ($3/rev$, $\varphi_3 = 45°$), and **b)** no vertical displacement and max. vortex strength ($2/rev$, $\varphi_2 = 280°$)

responding to 16 and 13 instantaneous velocity fields, respectively. Note that minor differences in the plotted range of the in-plane axes are caused by the normalization with different blade tip positions. The depicted range of vortex ages corresponds to a total measurement time of 7.3 ms, relative to the passing of the quarter chord through the measurement plane at t_0. Both subplots of Fig. 4.17 show every third image plane in a parallel layout that neglects the angular offset between the image planes for reasons of clarity. These example planes depict down-sampled in-plane velocity fields with every eighth vector shown, as well as the weakly smoothed out-of-plane vorticity component ω_z, which is normalized with the rotor rotational frequency Ω and colored according to the legend in the top right corner of the graph. The volumetric vorticity distribution is visualized by isosurfaces at six discrete levels between $\omega_z/\Omega = 25$ and 150.

The volumetric isosurfaces in both subplots of Fig. 4.17 visualize the blade tip vortex as a semi-transparent green tube that stretches over the entire measurement domain. The large vertical convection for the $3/rev$ case is apparent in Fig. 4.17a, especially when compared to the negligible vertical convection of the $2/rev$ vortex in Fig. 4.17b. Despite the significant difference between the two vortex trajectories, the convection velocities of the two vortices are of comparable magnitude. The vortex in Fig. 4.17b thus reaches the border of the PIV field of view before the diagonally convecting upper vortex. The second noticeable deviation between the two subplots is the difference in vortex strength and the magnitude of the corresponding swirl velocity field around the vortex. The in-plane velocity vectors in Fig. 4.17a are visibly shorter than the ones in Fig. 4.17b, despite having the same scale. According to Fig. 4.15, the average values for the peak swirl velocity of the two test cases differ from each other by a factor of 2, whereas the changes in the surrounding flow field appear to be even higher. The differences between the velocity fields of the two measurement conditions peak close to the blade tip, where a significant variation of the local lift distribution, and consequently the vortex- and lift-induced velocity field occurs.

The phase-averaged core radii for the two measurement conditions also differ from each other by a factor of about 2, which is accurately reproduced by the isosurfaces in the instantaneous data sets in Fig. 4.17. As already mentioned in Subsection 4.1.1, the growth of the core diameter with time is not captured by the constant vorticity levels of the isosurfaces. Instead, the vortex expansion and the diffusion-related decrease in vorticity magnitude lead to the appearance of a constant core diameter over time. The vorticity isosurfaces also visualize the sheet of vorticity that is created in the shear layer behind the rotor blade. The vorticity sheet subsequently rolls up around the tip vortex, as described in Subsection 4.1.1. The vortex-induced rotation of the vorticity sheet around the vortex core is comparable for the two different test cases, despite the different swirl velocity magnitudes. The vorticity sheet in the lower subfigure of Fig. 4.17 features an increased initial vorticity level compared to the upper graph. The vorticity sheet in Fig. 4.17b, however, appears to have a relatively higher diffusion rate, as it dissolves more quickly than the vortex sheet in Fig. 4.17a. The 3D vorticity plots in Fig. 4.17 enable a qualitative description of the actuator-induced changes in the flow field behind the rotor blade. The information obtained from the time-resolved data sets completes the quantitative analysis of the PIV data that has been presented in the previous subsections.

4.4 Summary of the STAR hover test

Aerodynamic results of a comprehensive hover test of the STAR active twist blades have been presented within this chapter. The goal of the measurements was to study the effects of the active twist actuation on the rotor and the trailing blade tip vortices. To investigate the impact of the actuation, first an unactuated baseline test case was closely examined. This baseline examination contained an analysis of the characteristic vortex convection and roll-up of the vorticity sheet around the vortex core. The key properties of the velocity field behind the rotor blade were qualitatively described based on a series of instantaneous velocity and vorticity fields, as well as a combined 3D vorticity field. The aperiodicity in the detected vortex trajectories was analyzed and an average baseline trajectory was computed. The velocity field around the detected vortex positions was closely examined by studying the temporal development of the axial and swirl velocity, as well as the core and void radii.

A thrust variation study was performed as part of the hover test. The effect of the blade loading variation on the vortex trajectories was examined and revealed a moderate impact on the vertical position of the trajectories and a significant alteration of the vortex convection velocity. The initial peak swirl velocities exhibited a good correlation with the results of the highly comparable HOTIS test and also compared reasonably well with other literature results. The detected core radii showed a steady trend over blade loading and some variation from the HOTIS results.

Test cases corresponding to higher harmonic actuation with frequencies of $1/rev$ to $5/rev$ and varying actuation phase angles were evaluated in the main part of the present study to gain a comprehensive overview of the active twist effects on the blade tip vortices. The previously evaluated, actuator-induced blade deformations were interpreted with respect to their impact on the blade aerodynamics. The effective angle of attack at the blade tip was derived to obtain a simple prediction of the shed vortex strength. The analysis of the detected vortex trajectories revealed that the $1/rev$ active twist actuation mainly affected the vertical blade deformation and led to a vertical displacement of the blade tips and the corresponding vortex trajectories of up to $1.3\,\%R$ above and $-1.01\,\%R$ below the BL condition. Apart from these constant vertical offsets, the $1/rev$ actuation only caused small variations of the vortex trajectories with peak changes of up to $\pm 0.5\,\%R$ around the BL curve at a maximum detected vortex age of about 35° behind the blade. An increase of the miss distance between a trailing vortex and a rotor blade during BVI is therefore difficult to realize with a $1/rev$ active twist frequency. The active twist actuation with frequencies of $2/rev$ and $3/rev$ significantly affected the shapes of the vortex trajectories and had a moderate effect on the vertical blade displacement. The actuation caused negative vertical displacements of the tip vortices relative to the BL case of up to $1.4\,\%R$ for the $2/rev$ frequency and up to $2\,\%R$ for $3/rev$. Based on the peak displacement for the $3/rev$ actuation, a potential miss distance of $5\,\%R$ is estimated between the actuated vortex and the following rotor blade. No significant effects on the vortex trajectories were obtained for the $4/rev$ and $5/rev$ actuation frequency, with typical vertical deviations below $\pm 0.35\,\%R$ and a maximum displacement of $0.6\,\%R$ above the BL case for the $4/rev$ frequency.

The impact of the active twist actuation on the vortex strength was evaluated based on the initial peak swirl velocities, and compared with vortex strength predictions based on the effective angle of attack at the blade tip. The peak swirl velocities for the $1/rev$ actuation frequency and various actuation phase angles exhibited moderate scattering relative to the baseline swirl

velocity with peak deviations between −18 % and +12 % of the BL value. A larger effect of the actuation on the vortex strength was found for the $2/rev$ actuation frequency. The harmonic variation of the initial peak swirl velocity over the actuation phase angle correlated well with the prediction model and featured average variations in swirl velocity from the BL case between −33 % and +31 % of the BL value. The general consistency of these relations was confirmed for older vortex ages such as $\psi_v = 37.31°$ for the $2/rev$ actuation frequency. The active twist actuation with a frequency of $3/rev$ exhibited a similarly high control authority over the vortex strength as the $2/rev$ actuation, as well as a good correlation between the prediction model and the measurement data. The average swirl velocities varied between −34 % and +18 % around the baseline value. The −34 % reduction compared to the unactuated test case was obtained for a phase angle of $\varphi_3 = 270°$ and constitutes the overall peak reduction in vortex strength for the current tests. The trends for the initial swirl velocity and the $3/rev$ actuation frequency were found to underestimate the actuation effects on older vortices. An increased reduction in swirl velocity with peak values up to −60 % below the BL case was measured at an advanced vortex age of $\psi_v = 37.31°$. The inconsistent trends for the swirl velocity over wake age originated from the unfinished vortex roll-up at the initial vortex age and different levels of vortex diffusion. This finding also underlines the necessity to investigate the actuation effects on the vortex strength at older vortex ages close to a possible blade-vortex encounter. Finally, smaller amounts of swirl velocity variation were observed for the $4/rev$ and $5/rev$ actuation frequency with peak variations between −22 % and +8 % around the BL velocity and adequate correlations between the swirl velocities and the prediction model.

The range of effects of the active twist actuation on the trailing blade tip vortices was illustrated by two combined 3D vorticity fields behind the blade tip. The two measurement cases corresponded to a maximum vortex displacement relative to the baseline case in combination with a large reduction in vortex strength, and a minimum vortex displacement in combination with the maximum detected vortex strength. The two measurement cases were qualitatively analyzed and illustrated the entire spectrum of actuation effects on the tip vortices.

The present PIV and BOS investigations allowed for a detailed study of the effects of the active twist actuation on the blade tip vortices. The results revealed a high control authority of the actuators – especially for the $2/rev$ and $3/rev$ actuation frequencies – on the shape and vertical offset of the vortex trajectories, and the vortex strength. The outcome of the STAR hover tests, therefore, serves as a proof of functionality of the active twist concept. Judging by the magnitude of the evoked changes, the active twist actuation is expected to constitute an effective measure for the reduction of noise and vibrations generated by blade-vortex interactions.

5 Localization of blade tip vortices on a full-scale helicopter

In the past years, considerable effort has been put into understanding the effects of *blade-vortex interactions* (BVI), such as the generation of sound and vibrations (Splettstoesser et al. 1997, van der Wall et al. 2004, Kutz et al. 2013). As already discussed in Chapter 3, the magnitude of the BVI effects primarily depends on the strength of the vortex and its distance and orientation to the interacting rotor blade (see Hardin & Lamkin 1986 for details). A number of sub-scale experimental (Splettstoesser et al. 1997, van der Wall et al. 2004) and numerical studies (Lim & Strawn 2008, van der Wall 2012, Kutz et al. 2013) have been conducted to examine the vortex strength and trajectories of helicopter models. In general, these studies return qualitatively converging results for the positions and orientations of the blade tip vortices. In detail, however, the results still exhibit significant scattering and a strong dependency on respective boundary and experimental conditions.

An important aspect of these small-scale experiments is that phenomena such as the BVI effect are very challenging to study on sub-scale models. For the BVI case, this is due to the multitude of underlying and interacting physical effects such as blade aerodynamics including the lift time history, blade aero-elasticity, fuselage-interference, atmospheric conditions, and overall aircraft performance and trimming (Hardin & Lamkin 1986), which cannot easily be reproduced at lab-scale model dimensions. As a consequence, some recent studies have focused on the blade tip vortices of full-scale helicopter rotors, where scaling effects are not an issue (Wadcock et al. 2011, Heineck et al. 2013, Bauknecht et al. 2014a, Raffel et al. 2014). So far, however, there is still a lack of quantitative experimental data; available studies only focus on the reconstruction of blade tip vortices on a small part of a full-scale helicopter (Klinge et al. 2006, Heineck et al. 2013) or the visualization of blade tip vortices on a full-scale helicopter during maneuvering flight (Bauknecht et al. 2014c, Bauknecht et al. 2014a, Raffel et al. 2014).

Within this chapter, results from a range of full-scale flight tests are presented. After a short introduction of the measurement techniques applied for the flight tests in Section 5.1, a series of preliminary flight tests are described in Section 5.2. The preliminary tests aimed at exploring the potential of the *background-oriented schlieren* (BOS) method and advancing the technique for the full-scale and outdoor visualization of helicopter rotor vortex systems under realistic flight conditions. In a main flight test (discussed in Subsections 5.3.1 – 5.5.3), a multi-camera BOS system consisting of 10 individual cameras and a natural background was used to visualize and – for the first time – to reconstruct the main part of the rotor blade tip vortex system of a full-scale helicopter in *three-dimensional* (3D) space.

5.1 Measurement techniques

The measurement techniques applied in the full-scale flight tests are explained here and put in context with related measurement or visualization techniques. A summary of full-scale vortex visualization techniques is given in Subsection 5.1.1. The basic principle of the BOS method is explained in Subsection 3.1.5, including an analysis of natural backgrounds. The reference-free BOS method – a variant of the classical BOS technique – is described in Subsection 5.1.3.

5.1.1 Large-scale vortex visualization techniques

Flow visualization is an important tool in advancing our understanding of normally invisible flow phenomena such as vortices. In the past, various visualization techniques have been developed and applied to study the vortices shed by helicopter rotor blade tips. A natural visualization of rotor blade tip vortices – as shown in Fig. 5.1 – is caused by natural condensation of water caused by the low pressure within the vortex core (Fradenburgh 1990, Felker et al. 1986). Other methods rely on the introduction of artificial seeding particles such as smoke into the rotor flow field (Landgrebe 1972, Ghee & Elliott 1995) or exclusively into the vortex core (Gray 1956, Spencer 1970). The whole-field smoke visualization is based on the generation of a particle void in proximity of the vortex center due to the centrifugal forces acting on the seeding particles (see Subsection 3.1.2). For the core seeding, small tracer particles are directly injected into the vortex center region, where they remain for a sufficiently long time due to the moderate diffusion in the laminar vortex core. The smoke method can be improved by laser light sheet illumination, which allows the flow visualization in a sectional plane of the flow field (Leighty et al. 1991, Ghee & Elliott 1992). For a vortex localization based on the flow velocities, the particle field can furthermore be probed with *laser Doppler velocimetry* (LDV, see e.g. Sullivan 1973) or *particle image velocimetry* (PIV, see e.g. Raffel et al. 1998a). PIV, for example, has already been applied for full-scale flight tests on fixed- and rotary-wing aircraft (Raffel et

Figure 5.1: Natural condensation on a Cougar helicopter, after Leishman (2006)

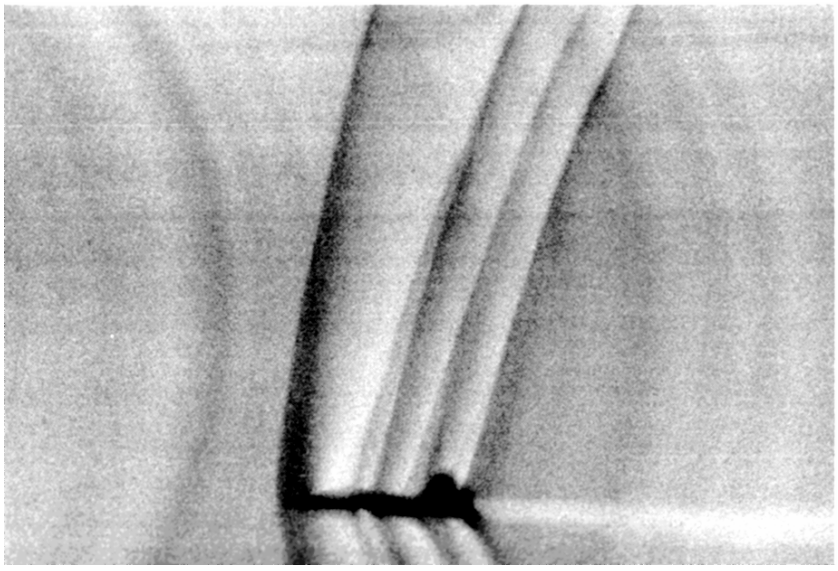

Figure 5.2: Full-scale schlieren image of T-38 aircraft, after Weinstein (1994)

al. 2001, Politz et al. 2010, Kindler et al. 2011). The drawback of these techniques is that they heavily rely on seeding particles or on very specific atmospheric conditions and that vortex visualization is limited to young vortex ages or a small part of the flow field. Their application for comprehensive and large-scale flight tests is therefore limited.

Besides the visualization based on tracer particles, vortices can also be detected based on the reduced density within the vortex core, as shown in Subsection 3.3.10. The basic measurement techniques, such as the classical *schlieren methods* (Toepler 1864, Tangler 1977), *shadowgraph technique* (Light et al. 1999, Bagai & Leishman 1993), and BOS (Dalziel et al. 2000, Raffel et al. 2000b), have already been explained in Subsection 3.1.5. Application of the classical schlieren techniques to outdoor environments and large scale measurements is usually limited by the size of the necessary high-quality optics. However, there are certain exceptions, as for example shown in Fig. 5.2 by Weinstein (1994), who visualized shock waves around a T-38 jet plane flying at an altitude of 13700 ft at a Mach number of 1.1 using natural illumination by the sun and a telescope with a slit mask. Regarding the large-scale application of the shadowgraph technique, the publication by Norman & Light (1987) is to be mentioned. Norman & Light herein describe the visualization of blade tip vortices from a 0.16-scale Sikorsky S-76 rotor using a shadowgraph setup with large retro-reflective background screens. A review of schlieren applications in outdoor environments is given by Settles (1999), including the visualization of heat plumes, jet exhaust gases, thermal boundary layers as well as aerodynamic and explosion-driven shock waves in front of natural backgrounds.

5.1.2 Natural background BOS

Recently, considerable effort has been put into refining the BOS method for out-of-laboratory use (see e.g. background studies by Hargather & Settles 2010 or the Colored-BOS technique by Leopold 2007). As scalability is one of the main advantages of the BOS method, it is especially well-suited for full-scale flight testing. The application of large artificial background patterns

for this sort of full-scale experiments has been demonstrated by Bauknecht et al. (2014a) and Raffel et al. (2014). The large background screens required for this approach are, however, impracticable and expensive, especially for multi-camera setups. As an alternative, natural backgrounds can be utilized for BOS, as shown by Hargather & Settles (2010) and Kindler et al. (2007). The necessity of using readily available background structures has been understood by researchers from the very start of outdoor BOS testing, as can be seen by the publication of Raffel et al. (2000b). In this early BOS paper, Raffel et al. visualized blade tip vortices of a full-scale helicopter in hover flight by recording a pattern of white paint spots on concrete ground using a camera inside a high building.

Natural background structures such as scree or short grass also provide appropriate conditions for BOS measurements, combined with minimal preparation and low cost. Suitable natural backgrounds for BOS must fulfill several requirements including adequate contrast and structure size. The background also should not change between the acquisition of the reference and measurement images. As a consequence, changes in illumination – e.g. by a relocation of clouds and shadows – have to be avoided and vegetated areas should not be used in case of wind gusts. Furthermore, the background must be large enough to cover the entire region of interest. Thus, large-scale stepped or sloped terrains have been used as natural backgrounds for BOS measurements in the past (see e.g. Bauknecht et al. 2014d).

A comparison of typical natural background structures encountered by Bauknecht et al. (2014b) during outdoor BOS measurements is shown in Fig. 5.3. In the corresponding paper, Bauknecht et al. introduced a quality indicator for assessing the suitability of natural structures for application as BOS backgrounds. The quality indicator was adapted from a measure introduced by Kindler et al. (2007), which is based on the autocorrelation of an image of a natural structure. To prevent a bias of the results by autocorrelation of the image noise, the new method is based on the displacement field of two measurement images of the same natural structure. As residual misalignments of the two images should not distort the result, the quality indicator is based on the rotation ($\omega_{\mathrm{rot}} = \partial v/\partial x - \partial u/\partial y$) of the in-plane displacements u, v, which is constant for rigid body motions. Therefore, the inverse of the variance of the rotation is a robust index of the noise contained in the BOS measurements of different background structures and interrogation window sizes.

Figure 5.3: Selection of natural backgrounds with increasing structure sizes from left to right, after Bauknecht et al. (2014b)

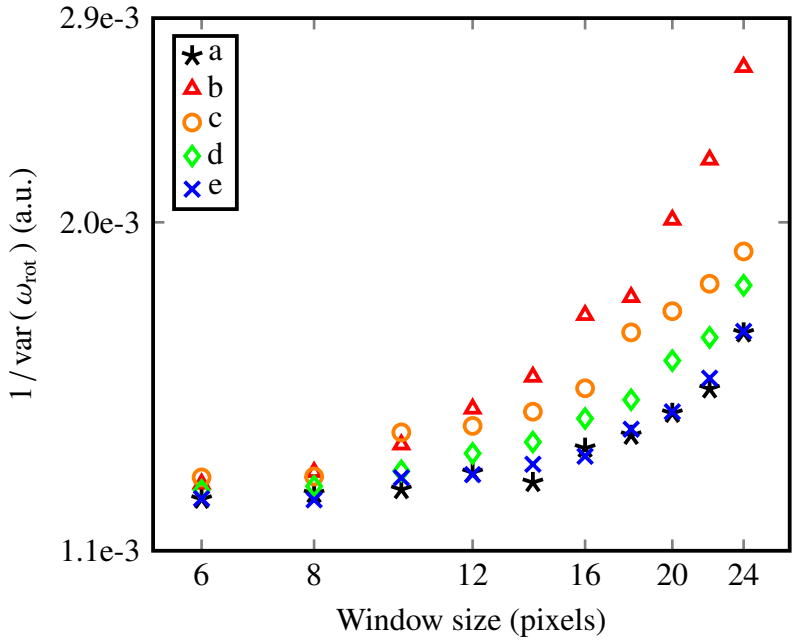

Figure 5.4: Quality indicator plotted for the five different natural backgrounds of Fig. 5.3 as a function of the interrogation window size, after Bauknecht et al. (2014b)

An assessment of the suitability of the natural backgrounds depicted in Fig. 5.3 based on the new quality indicator is given in Fig. 5.4. The diagram shows plots of the quality indicator for the five different natural backgrounds over a realistic range of interrogation window sizes used for outdoor BOS measurements. For the optical setup in Bauknecht et al. (2014b), best results are expected for the fine scree background (Fig. 5.3b), whereas solid rock formations (Fig. 5.3e) and very fine grass structures (Fig. 5.3a) are less suitable. While this trend is consistent for similar optical layouts, it is not universal and cannot be applied to other setups of different magnification. With a higher magnification, the grass structures (Fig. 5.3a) can for instance become a very suitable background. The same holds true for large rock formations imaged with a decreased magnification. Overall, Fig. 5.3 shows that large interrogation window sizes generally improve the quality of the measurements, however, at the cost of a reduced measurement resolution and increased spatial averaging. Therefore, smaller interrogation window sizes at the edge of detectability may be necessary to maintain a high spatial measurement resolution.

5.1.3 Reference-free BOS

The classical BOS method is well suited for applications in relatively steady environments such as wind tunnels and laboratories. For unsteady and outdoor measurements, however, acquisition of an undisturbed reference image with the same lighting and background topology is not always possible. For this reason, Raffel et al. proposed a reference-free BOS setup suitable for highly unsteady measurement environments such as large-scale flight tests and inflight measurements (Raffel & Meier 2000, Raffel et al. 2000a, Kindler et al. 2007, Raffel et al. 2013). The reference-free BOS method is applicable when the observed density variation has a limited extent and does not cover the whole field of view, therefore leaving some parts of the image almost free

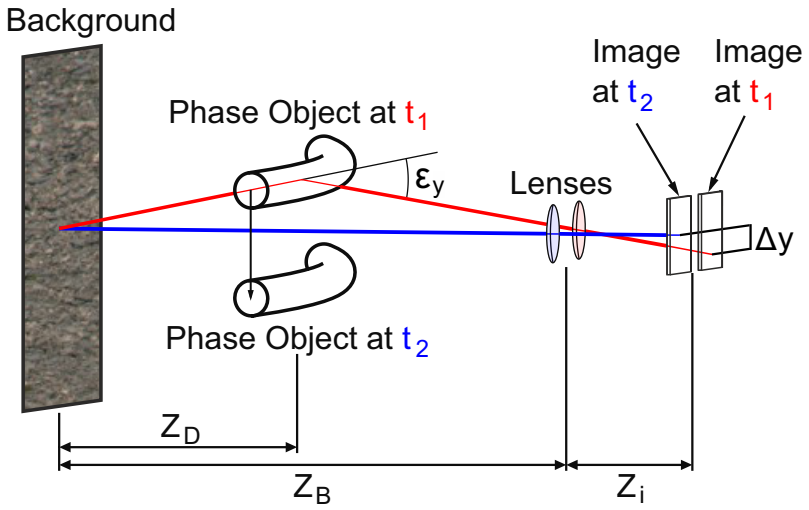

Figure 5.5: Principle of the reference-free BOS setup, after Bauknecht et al. (2014b)

of distortions. These mostly undisturbed parts are used as a reference for another measurement image, which has the density variations in front of a different part of the common background. This spatial separation of the imaged phase objects can be achieved with two different setups: the *stereoscopic configuration* and the *paraxial configuration*.

The *stereoscopic configuration* uses two cameras that simultaneously record images of the same background from different perspectives. By properly setting up the cameras, the density structure is located in front of different parts of the common background. After mapping and cross-correlation of the two images, a combined result image is created that features the overlaid two perspective views of the density variation. As the background is imaged from different angles, its planarity must be ensured. This setup is suitable for highly unsteady backgrounds and does not require an unsteady density field. The separation of the two cameras, however, renders this setup less feasible for the investigation of moving objects such as a helicopter in forward flight.

The *paraxial configuration* can be realized if the phase object moves relative to the background with time. This is e.g. the case for the vortices of a helicopter which convect with the rotor downwash. The principle of the camera layout is shown in Fig. 5.5. Two cameras are paraxially mounted and record the same background at two consecutive points in time t_1 and t_2. The distance between the cameras has to be small in comparison to the background distance Z_B for the alignment error to be negligible. The time delay $\Delta t = t_2 - t_1$ is selected as a compromise between two opposing requirements: the delay has to be short enough to ensure that the same part of the background is recorded – especially if the cameras are moved in between the recordings – but long enough for the density object to be recorded in front of different parts of the background in the two measurement images. For a properly adjusted time delay, the recorded background behind the density object in the first frame is almost free of distortions in the second frame and vice versa. The almost undistorted parts of the images serve as reference images for the cross-correlation evaluation of the two measurement images. The resulting displacement field features the density variation at both image acquisition times, but with a different sign. The two paraxial cameras are a workaround for a presently unavailable *monoscopic configuration* that combines a high spatial resolution and short interframing times in a single camera.

Just as the standard BOS method, the reference-free BOS technique only returns a *two-dimensional* (2D) projection of the 3D refractive-index field onto the image plane. For the reconstruction of the vortex system in physical space, two or more calibrated camera locations are necessary, as will be discussed in Subsection 5.4.5. An integrative reconstruction of the density field from the image displacements is not possible for the reference-free BOS method because the parts of the images that act as a reference for the other frame are not completely undistorted. The paraxial setup, however, allows for a simple implementation for out-of-the-lab experiments and even enables an airborne operation of the measurement system, as described by Raffel et al. (2013) and demonstrated in Subsection 5.4.1.

5.2 Preliminary flight tests

Between 2011 and 2013, a series of flight tests was carried out to explore and demonstrate the potential of the reference-free BOS method for flow investigations on full-scale helicopters and to optimize the standard BOS method for the quantitative vortex localization described in Sections 5.3 – 5.5. A brief overview of the most important preliminary flight tests, their objectives, and some characteristic results is given here.

5.2.1 Reference-free BOS hover test in ground effect

A ground-based vortex visualization experiment with a reference-free BOS setup was conducted on the apron in front of a hangar at DLR Braunschweig, see Bauknecht et al. (2014a). The test helicopter – an MBB BO 105 described in detail in Subsection 5.3.2 – was operated in hover, landing, and take-off flight conditions close to the ground in front of the hangar, as depicted in Fig. 5.6a. The hangar wall was covered with a 12 m × 6.3 m background screen consisting of retro-reflective foil with a printed random dot pattern, as shown in Fig. 5.6b in a close-up view. On the opposite side of the apron, a dual-camera system was installed on top of a car on a rigid support, see Fig. 5.6a and c. The reference-free BOS setup consisted of two Nikon D3X *digital single-lens reflex* (DSLR) cameras that each had a resolution of 24.5 Mpx. The cameras were equipped with lenses with a focal length of 135 mm and imaged the entire background screen from a distance of 46 m and at a height of 2.25 m above the ground. The background pattern was illuminated by camera flash units and recorded with an exposure time of 1 ms with an aperture of $f/16$ and an ISO value of 100. The inter-framing time was set to 32 ms between the cameras, corresponding to a rotor rotation of 80°.

Detailed results of the hovering test have already been published by Bauknecht et al. (2014a). A typical result of the investigation is shown in Fig. 5.7. The photograph depicts the forward part of the fuselage and the rotor of the BO 105 in hovering flight and is overlaid with the result from the cross-correlation analysis of the two measurement images. The two 2D projections of the vortex system corresponding to the two image acquisition times are visible in the image background as black and white lines and can be distinguished by the sign of the displacement, as mentioned in Subsection 5.1.3. The main features of the flow field are marked in the image by the numbers (1) – (5). The engine exhaust gases are visible as an area with an increased noise

Figure 5.6: Photographs of the reference-free BOS hover test with **a)** test overview, **b)** artificial background pattern, and **c)** dual-camera setup, after Bauknecht et al. (2014a)

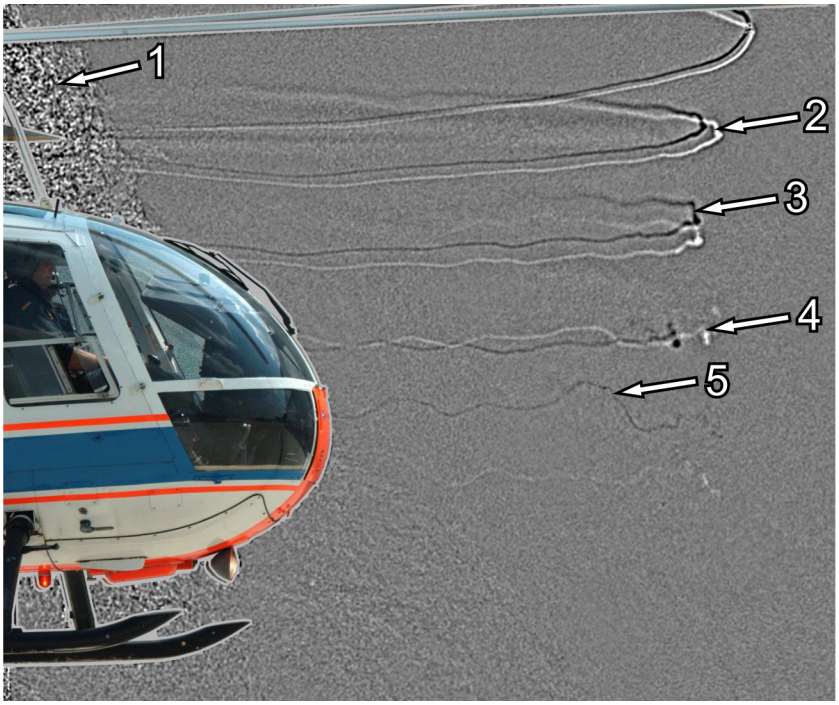

Figure 5.7: Photograph of the BO 105 in hover with overlaid BOS result depicting vortices up to $\psi_v = 450°$ and vortex instability effects, after Bauknecht et al. (2014a).

level (1). Two depictions of a vortex shed by a single rotor blade are indicated by (2) at a vortex age of about $\psi_v = 100°$ and by (3) at a vortex age of $\psi_v = 180°$. A slight contraction of the wake occurs up to a vortex age of $\psi_v = 270°$, indicated by (4), which is followed by a moderate expansion due to the influence of the ground effect. Starting from a vortex age of $\psi_v = 180°$, the onset of vortex instability effects is observed, with a maximum articulation around a vortex age of $\psi_v = 450°$, denoted by (5). Shortly after this point, the advanced diffusion of the vortices renders them undetectable by the BOS method.

5.2.2 Reference-free BOS maneuvering flight test

In 2013, a flight test with an AS532UL Cougar helicopter was conducted in cooperation with the Swiss Air Force, as described in detail by Bauknecht et al. (2014b). The goal of the test was the visualization of the helicopter's blade tip vortices during unsteady and high-speed maneuvering flight out of the ground effect. The test took place in the Swiss Alps near Schilthorn Mountain. Naturally illuminated structures such as scree-covered slopes were used for a background, as depicted in Fig. 5.3 and marked in Fig. 5.8a with a red dashed line. Measurement images were acquired with the reference-free dual-camera system shown in Fig. 5.8b. The system consisted of two Nikon D3X cameras with lenses with a focal length of 500 mm, and was positioned at distances of 500 – 700 m from the background. The camera support allowed for the pivoting of the camera setup to follow the maneuvering helicopter. The time delay between the two cameras was set to 16 ms, which corresponded to an angular increment of the rotor of about 26° and allowed for the spatial separation of the projected vortex systems in the evaluated measurement images. The investigated flight maneuvers included high-speed turns, forward flight, accelerating slow forward flight, and flare.

Figure 5.9 shows two raw photographs (Fig. 5.9a,b) and the corresponding displacement field of the cross-correlation evaluation (Fig. 5.9c) of the Cougar helicopter in accelerating forward flight with an instantaneous velocity of 35 knots (18 m/s) at a distance of 240 m from the cameras. The pictures of the helicopter fuselage and rotor blades are overlaid on the displacement field and indicate the movement of the helicopter in between the two image acquisition times. The two noisy plumes (1) underneath the helicopter are caused by the hot exhaust gases from the engines, which prevent the detection of vortices. One of the rotor blades is marked with (2) in both raw photographs. The corresponding tip vortices are labeled with (3) in the displacement image. The maximum visible vortex age of $\psi_v = 360°$ is found at the forward blade position labeled with (4). Around this position, the onset of vortex disturbance effects is observed, before the signal amplitude drops to the background noise level.

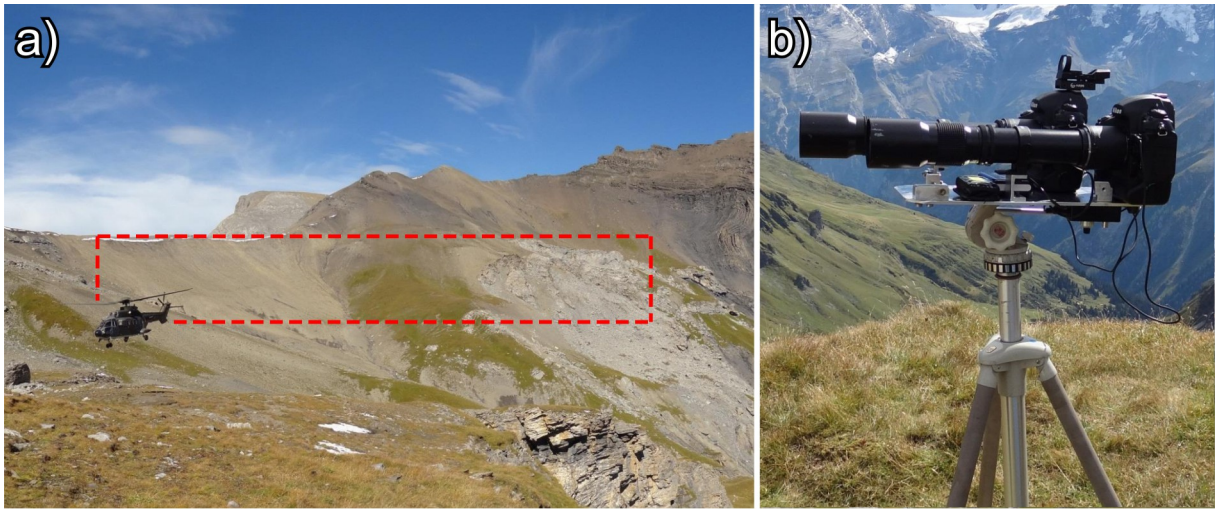

Figure 5.8: Photographs of **a)** the flight test region (with marked backgrounds) and the Cougar helicopter, and **b)** the reference-free BOS setup, after Bauknecht et al. (2014b)

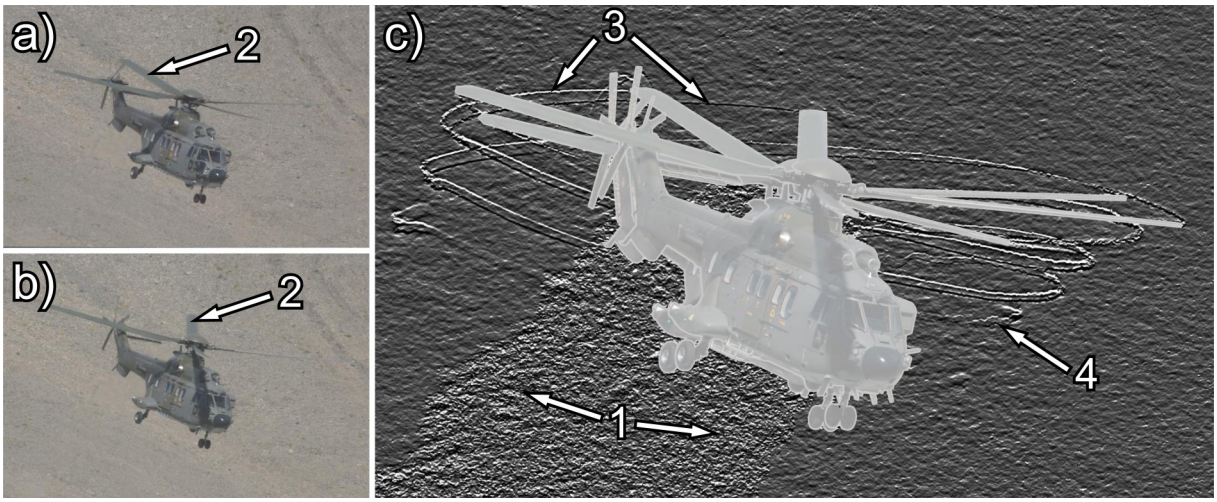

Figure 5.9: Result from the reference-free BOS maneuvering flight test, after Bauknecht et al. (2014b). Depictions of **a**,**b)** the time-displaced raw images, and **c)** the corresponding displacement gradient field around the Cougar helicopter.

5.2.3 Airborne reference-free BOS inflight test

The versatility of the reference-free BOS method and the possibility to circumvent the operational restrictions imposed on the helicopter by a ground-based measurement system were demonstrated by another flight test in 2013, see Bauknecht et al. (2014a) for details. For this test, the dual-camera system described in the previous subsection was operated aboard a microlight airplane flying above a BO 105 helicopter, as schematically illustrated in Fig. 5.10. The two cameras were sequentially triggered with short interframing times of $5 - 16$ ms, corresponding to an angular increment of the rotor of about $13° - 41°$. The helicopter was operated $200 - 300$ m above natural backgrounds such as fields and meadows with the airplane flying $100 - 200$ m above and to the side of it. The helicopter performed forward flight, curve flight, and accelerating forward flight maneuvers at speeds of $65 - 100$ knots.

Figure 5.11 shows the result of a processed pair of measurement photographs of the BO 105 in accelerating forward flight. The structure of the natural background is overlaid in the bottom left corner of the image. The photographs were acquired with a time delay of 8 ms and an exposure time of $1/1600$ s. The movement of the aircraft and cameras during the interframing time resulted in a shift of 90 pixels between the two images, which was corrected before the final processing. The helicopter, rotor blades, and vortices are depicted twice in the result image due to the combined evaluation of two raw images. The two vortex systems are distinguished by their color in the plot: white lines correspond to the earlier image (1) and black lines to the later image (2). Aside from the vortices, the most distinct feature in the image is the strongly decorrelated area due to the engine exhaust, denoted by (3). The combination of the flight velocity and the rotor downwash causes the formation of a helically skewed vortex system. Despite the inconsistent vortex visibility within the image, vortices up to a vortex age of $\psi_v = 270°$ are detected around the location marked with (4). At the right lateral edge of the rotor disk, the rotor wake starts to roll-up, which causes the vortices to roll-up and merge into a single and accentuated vortex, labeled with (5). A disturbance of the vortex filaments is observed on the retreating blade side, denoted by (6). The cause for this flow feature is not apparent, as the

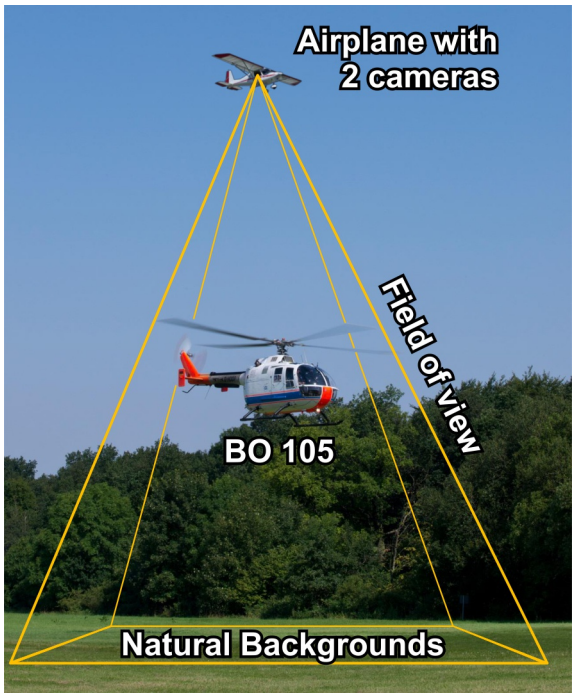

Figure 5.10: Schematic inflight BOS setup with observer airplane and helicopter flying at a reduced altitude above the natural background, after Bauknecht et al. (2014a)

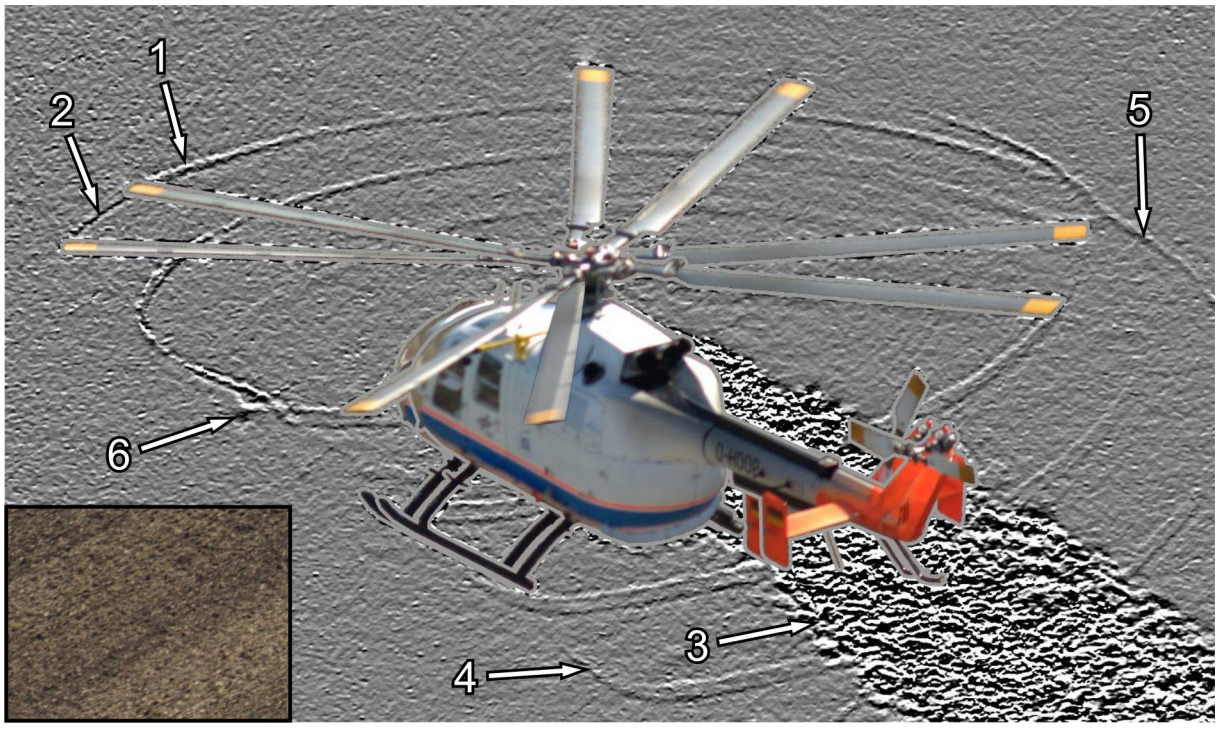

Figure 5.11: Photograph of the BO 105 in accelerating forward flight with vortex system acquired during reference-free inflight BOS test, after Bauknecht et al. (2014a)

rotor blades were not instrumented. The location however suggests that it originates from an interaction of the adjacent rotor blade with the vortex shed by the blade 90° ahead.

5.2.4 Concluding remarks about the preliminary flight tests

The application of the reference-free BOS method during the preliminary flight tests enabled the visualization and study of helicopter blade tip vortices under realistic flight conditions with unprecedented quality. The 2D projections of the vortex system acquired by the paraxial camera setups, however, only allowed for the qualitative study of the aerodynamic effects in the rotor wake. Consequently, the advancement of the BOS measurement technique for quantitative vortex localization was targeted in a multi-camera 3D BOS experiment that is described in the following section. The results and experience gained in the preliminary flight tests with regard to natural background structures, natural illumination, vortex obstructions by the fuselage and the engine exhaust gases, sensitivity of the setup, and operation of the test helicopter contributed to the design and execution of this main flight test campaign.

5.3 3D BOS flight test

This section contains a detailed description of the main 3D BOS flight test, including specifications of the measurement setup in Subsection 5.3.1, test helicopter in Subsection 5.3.2 and flight conditions in Subsection 5.3.3.

5.3.1 Measurement setup

A large-scale multi-camera BOS experiment was conducted in 2013 to quantitatively determine the locations of the blade tip vortices in the wake of a full-scale helicopter. An open-pit chalk mine of the company Fels-Werke GmbH in the Harz Mountains in Germany was chosen as a test site, see Fig. 5.12. For a natural background, the location featured a large slope with a curved layout that had a height of 45 m, width of about 200 m, and inclination of 45°. The top half of the slope was mainly covered with scree and small rocks and the bottom part featured rocks of varying size, as visible in Fig. 5.12b and in detail in the background of Fig. 5.13a. The slope was enclosed on both sides by steep cliffs that were covered with unsuitable background structures for BOS, such as trees and low-contrast solid rock. The bottom level of the pit was covered by a shallow lake, which did not affect the BOS measurements, e.g. through thermal distortions.

A BO 105 helicopter – described in detail in Subsection 5.3.2 – was flown into the quarry to serve as a measurement object. The full-scale helicopter is depicted within the measurement volume in the lower right corner of Fig. 5.12. A system of ten DSLR cameras was used to acquire background-focused schlieren images of the helicopter during maneuvering flight. The overlapping *field of view* (FOV) of the cameras led to an approximately cylindrical shape of the measurement volume, which had a diameter of 17 m, a height of 11 m, and was situated 7 – 18 m above the solid ground next to the lake. The cameras were set up on the north-east side of the quarry opposite the background slope on two different plateaus of the stepped sidewall with a vertical separation of 14 m. Five of the ten cameras were set up in an approximately semicircular layout on the lower level (indicated by C1 – C5 in Fig. 5.12). The cameras were positioned 1.8 m above the ground level with distances to the measurement volume around $(Z_B - Z_D) = 110$ m

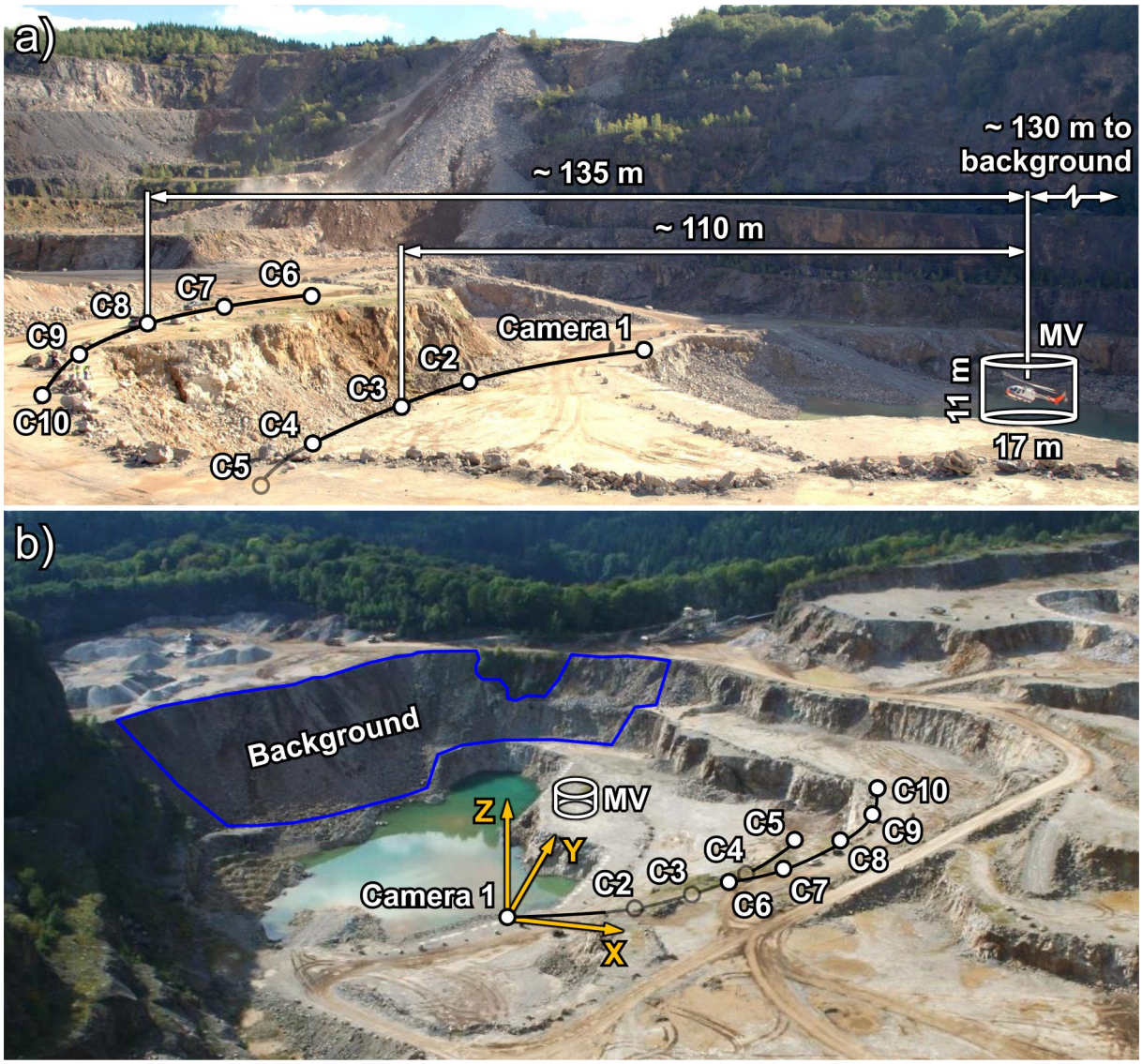

Figure 5.12: Photographs of the multi-camera BOS setup viewed **a)** from the ground, and **b)** from above with indicated camera positions, coordinate system, *measurement volume* (MV), and natural background, after Bauknecht et al. (2014d)

and inclination angles of +3° to +4°, see Table 5.1 for details. The other five cameras (C6 – C10) were set up 1.8 m above the upper floor level with distances to the measurement volume around $(Z_B - Z_D) = 135$ m and inclination angles of −2° to −3°. The distance to the background varied between cameras in the range of $Z_B = 230 - 300$ m. The camera setup covered a horizontal angle of 83° and a vertical angle of 7° between the outermost cameras. The horizontal angles of the individual cameras are given relative to camera 1 in Table 5.1.

A coordinate system was introduced for the camera calibration and vortex reconstruction carried out in the following sections. It is centered at the position of camera 1, as shown in Fig. 5.12. The Y axis corresponds to the horizontal component of the orientation vector of camera 1. The Z axis is oriented along the positive vertical direction. The X axis is defined orthogonal to the other axes to complete the Cartesian coordinate system. The camera positions within this coordinate system are also given in Table 5.1. The exact positions of individual cameras were

Table 5.1: 3D BOS camera orientations and settings

Camera	**1**	**2**	**3**	**4**	**5**	**6**	**7**	**8**	**9**	**10**
Position X (m)	0.0	54.0	80.2	97.4	117	80.2	102	117	127	130
Position Y (m)	0.0	19.1	35.3	58.5	84.6	-5.8	15.1	39.0	64.5	91.6
Position Z (m)	0.0	-0.2	1.5	-0.1	0.7	14.1	14.0	13.9	13.7	13.7
Hor. angle (°)	0.0	31.6	47.5	63.1	78.5	35.3	47.7	58.7	71.1	82.9
Inclination (°)	3.7	4.0	2.9	3.8	3.1	-2.7	-2.9	-2.3	-2.9	-2.8
Observer Dist. (m)	109	105	108	110	119	140	138	136	134	131
Focal length f (mm)	150	165	150	165	165	195	195	185	180	180
Rel. aperture $f/$	11	8	8	8	5.6	8	8	8	8	5.6
Exposure time (s)	1/1000									
ISO	400									

chosen to optimize the covered background, resulting in an unevenly distributed camera setup. This can be seen e.g. for camera 1 in Fig. 5.12, which had an increased distance to the other cameras to avoid coverage of a vegetated area in the background.

A single camera of the multi-camera system is shown in Fig. 5.13b. The camera system consisted of Nikon D7100 cameras with 24 Mpx image sensors and Nikkor 55 – 300 mm zoom lenses. The cameras were positioned on tripods at a height of 1.8 m above the ground and connected to a cable-based remote triggering system to ensure simultaneous image acquisition. The cameras had an inherent, random time delay between the trigger input and the image recording. The jitter of this delay was reduced to about 0.7 ms by taking into account the mean delay for each camera in combination with the application of the mirror lockup function. The zoom lenses were adjusted to provide a similar resolution of about 0.34 px/mm within the measurement volume, requiring focal lengths f of between 150 mm and 195 mm, as specified in Table 5.1. All cameras were set to an ISO value of 400 and an exposure time of 1 ms. The aperture sizes of the camera lenses were adapted to the natural illumination of the corresponding background and varied between $f/5.6$ and $f/11$, see Table 5.1. During the measurements, sunny and windless weather conditions were present with an ambient temperature of about 15°C and wind velocities of less than 1 m/s.

In the evaluation process of the BOS images, it was found that the main part of the natural background of the bottom row cameras 1 – 5 was appropriately illuminated, largely 2D, and therefore well suited for the BOS evaluation. An increased background noise level with a reduced vortex visibility was found for the upper level cameras 6 – 10. This is mainly caused by the different illumination angle in the lower part of the slope in combination with larger and more 3D rock formations. The consequently increased shadowing effects caused an increased noise level, especially for cameras 8 – 10. As the additional information gained by cameras 8 – 10 was limited, they were neglected for the reconstructions carried out in this study.

Figure 5.13: Photographs of **a)** the BO 105 in front of the natural background, and **b)** one of the ten measurement cameras

5.3.2 BO 105 helicopter

The 3D BOS flight tests – as well as the majority of the preliminary flight tests – were conducted with an MBB BO 105 helicopter from DLR Braunschweig, as shown in Fig. 5.13a. The BO 105 is a twin-engine, multi-purpose helicopter with a four-bladed ($N_b = 4$) hingeless rotor. The rotor blades have square blade tips, a radius of $R = 4.92$ m, and a chord length of $c = 0.27$ m, which leads to a rotor solidity of $\sigma = N_b c/(\pi R) = 0.07$. Under normal flight conditions, the blades rotate at an angular velocity of $\Omega = 44.4$ rad/s, which corresponds to a hover tip Mach number of $M_{tip} = 0.64$. During the test runs, the helicopter was manned with two pilots and a radio operator and had an initial take-off weight of about 2300 kg. In order to fly unsteady maneuvers, the helicopter had to generate thrust in the range of $T = 23 - 28$ kN, corresponding to a thrust coefficient of $C_T = T/(\rho_\infty \pi \Omega^2 R^4) = 0.005 - 0.006$ and a blade loading of $C_T/\sigma = 0.07 - 0.09$.

5.3.3 Flight conditions

For the flight tests, the BO 105 was operated within the open-pit mine at an elevation of 400 m (1310 ft) above sea level and approximately 1 – 1.5 rotor diameters above the ground. The challenging topology of the quarry with steep slopes to all sides and large steps in the terrain restricted the flight maneuvers to slow flight speeds. It was therefore decided to put the focus of the experiments on hovering flight and unsteady swinging maneuvers to simulate higher loads characteristic for unsteady free-flight conditions. The unsteady maneuvers included accelerations along the vertical axis of the helicopter (ascent / descent, see Fig. 5.14a-e) and swinging motions along the longitudinal axis of the helicopter in combination with a variation of the pitch angle (see Fig. 5.14f-j). The data set used for the final vortex reconstruction corresponded to an ascending hovering flight with an instantaneous rate of climb of about 1 m/s. For the positioning of the helicopter, lines were sprayed on the ground as a guide for the pilot and observers were employed at different camera positions to relay position information back to the pilots via voice radio. With these measures, the helicopter was operated primarily within the measurement volume during the test runs, while performing maneuvers with translational motions of

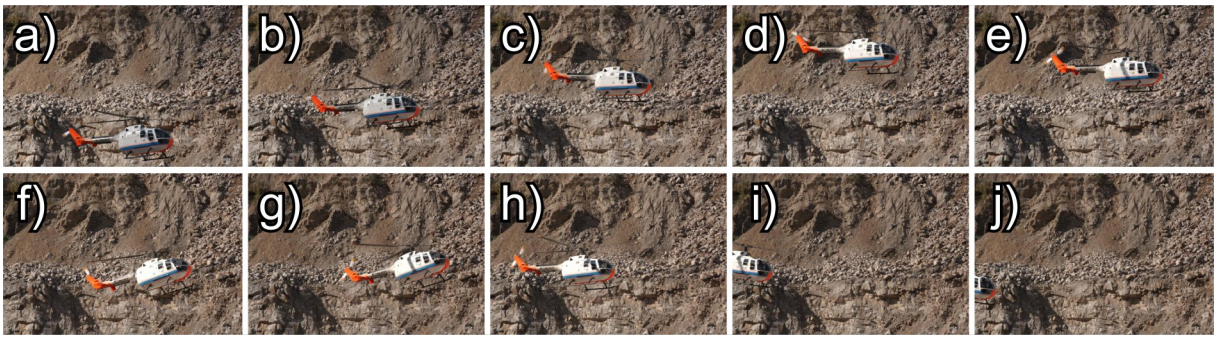

Figure 5.14: Photographs of the BO 105 **a)-e)** during ascent/descent, and **f)-j)** during a swinging motion along the longitudinal axis

up 10 m and fuselage pitch angles of up to 30°. Finally, the safety of the aircraft was ensured by watering the area underneath the measurement volume prior to the tests to prevent dust from being blown up. An emergency landing zone was kept clear as the surrounding steep slopes and the lake on the bottom of the pit limited the escape routes in case of an engine failure.

5.3.4 Concluding remarks about the 3D BOS flight test setup

The 3D BOS flight tests were conducted on a single day at the end of September 2013. Prior to the test day, the camera positions, measurement volume, and suitable natural backgrounds had been laid out with the initial measurement volume located above the lake. Because of a last-minute change in the permission for off-field landings by the communal administration – due to the apparent nesting of bats in a wall of the active quarry – the setup had to be changed on the day before the flight test. Consequently, the measurement region was shifted to its final location above the solid ground with a decreased clearance and maneuverability of the helicopter. During the planning phase of the flight test in the summer of 2013, the natural illumination intensity on the natural background had been found to be sufficient for the BOS measurements. Due to the changed course of the sun at the end of September and the north-east facing natural background, however, adequate natural illumination was restricted to a short period of about 3 hours in the morning of the test day.

5.4 BOS data analysis

The process of reconstructing the 3D locations of the helicopter blade tip vortices requires multiple processing steps, as described in this section. For each raw measurement image, the projections of the vortices are visualized (Subsection 5.4.1), semi-automatically discretized, and paired with the corresponding projections in other measurement images (Subsection 5.4.2). Based on an interative camera calibration (Subsection 5.4.3), the 3D vortex locations are found by means of a stereo photogrammetry method (Subsection 5.4.5).

5.4.1 Vortex visualization using the BOS technique

The present main flight tests were conducted with ten individual standard BOS camera setups. As explained earlier, the BOS method requires the acquisition of undisturbed reference images without the helicopter directly before or after each test run, see Fig. 5.15a for an example. The reference images have to be acquired as close to the measurement images (Fig. 5.15b) as possible, in the current case $< 5-10$ minutes apart. This time frame was found to be sufficiently small to minimize changes in the background such as the movement of shadows or drying of wet surfaces. In an initial processing step, both the reference and measurement images were converted to grayscale based on luminance-preservation as the natural backgrounds were too monotonous to apply a color-BOS scheme, see Leopold (2007) for details. During acquisition of the measurement images, it could not be ruled out entirely that the cameras were moved by interaction of an observer or by gravitational settlement of the camera mounts. Therefore, the measurement images were mapped onto the reference images using the normalized direct linear transformation algorithm given by Hartley & Zisserman (2003), based on the image displacements in the corners of the images as determined by cross-correlation. A sectional cross-correlation of the mapped image pairs was carried out with commercial PIV software (Davis 8.1, LaVision). A multi-grid evaluation scheme with interrogation window sizes between 96×96 pixels^2 and 16×16 pixels^2 with an overlap of 75% was applied that resolved the small displacements u and v by the vortices in the horizontal and vertical directions, respectively. In the resulting displacement map, blade tip vortices are indicated by the vectors pointing towards regions of low density, i.e. the vortex cores. Bauknecht et al. (2014b) found in an earlier study that the spatial gradients of the displacement field $\partial u/\partial x$ and $\partial v/\partial y$ normal to the main vortex orientations serve as robust vortex indicators that emphasize the vortices due to their high spatial gradients compared to the gradual changes in the surrounding flow field. Typical vortex-induced peak-to-peak displacements in the order of $\Delta v = 0.15 - 1.5$ pixels were discovered for the present 3D BOS flight test.

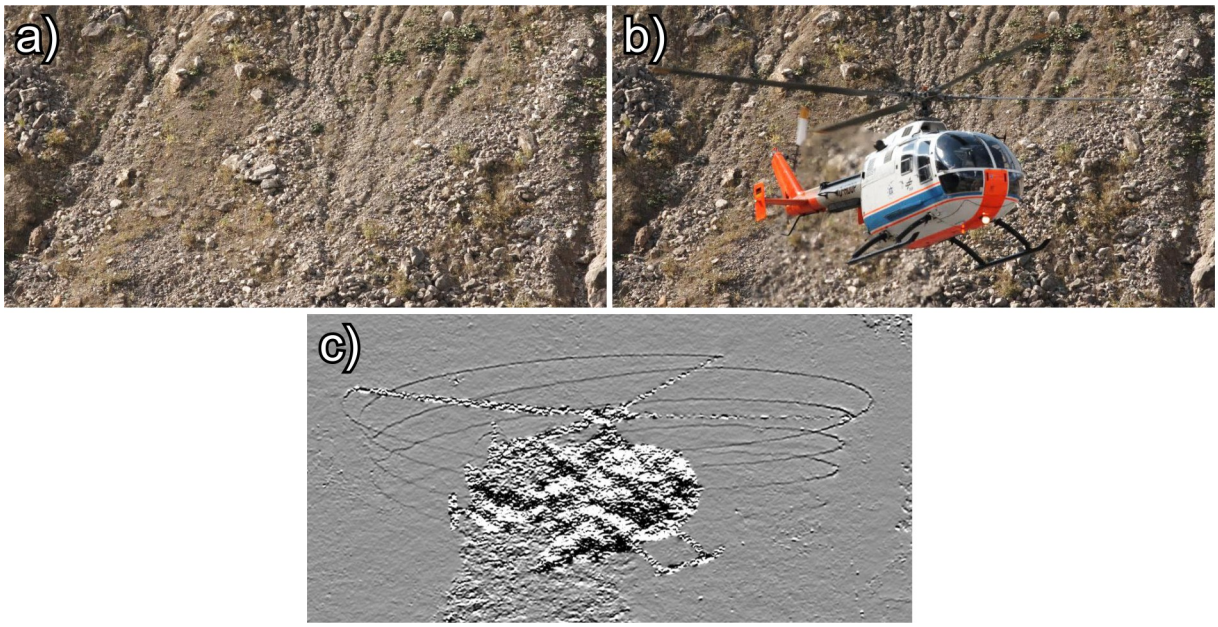

Figure 5.15: Cutouts of example **a)** reference-, and **b)** measurement pictures, with **c)** corresponding vertical displacement gradient field, after Bauknecht et al. (2014d)

An example result for the vortex visualization is given in Fig. 5.15c as the result of the sectional cross-correlation between a reference image (Fig. 5.15a) and a measurement image (Fig. 5.15b) featuring the BO 105 during an ascending flight maneuver. The evaluated image depicts the unfiltered vertical gradient $\partial v/\partial y$ of the vertical displacement component v. The 2D projection of the vortex system is visible in the form of dark and helically curved lines in front of the gray and weakly distorted background. Strongly de-correlated regions appear at the image positions where the helicopter is located. The noisy area below and behind the helicopter marks the trajectories of the exhaust gases from the two engines.

5.4.2 Discretization and pairing of vortex segments

As a second step in the processing of the raw images, the positions of the 2D blade tip vortices were detected in all camera planes. This discretization process is crucial for ongoing data processing as it transforms the scalar displacement information shown e.g. in Fig. 5.15c into quantitative, in-plane vortex positions, as given in Fig. 5.16. A semi-automatic procedure was used for the vortex extraction, as the signal-to-noise ratio was not high and consistent enough in the entire displacement field for a fully automated algorithm, and interruptions of the vortex filaments were caused by the rotor blades, exhaust gases, helicopter fuselage, and background noise. Starting from user-selected points on the vortex filaments, discrete points on the vortex filaments were computed by step-wise cross-correlation between cuts orthogonal to the main vortex axis in combination with a polynomial predictor. The algorithm advanced until the end of the selected line segment was found or until a horizontal turning point was reached, as marked by white dots in Fig. 5.16. The step size of the computation scheme was automatically adapted to fit the curvature of the lines and small undetectable segments in the vortex signal were skipped. The resulting set of vortex segments was manually completed in regions with large adapted step sizes and weak signal-to-noise ratio. The discrete points on each vortex filament were used for a spline curve fit computed by a least-squares procedure. The splines were labeled by their position relative to the helicopter fuselage and coded by the blade from which they originated, as

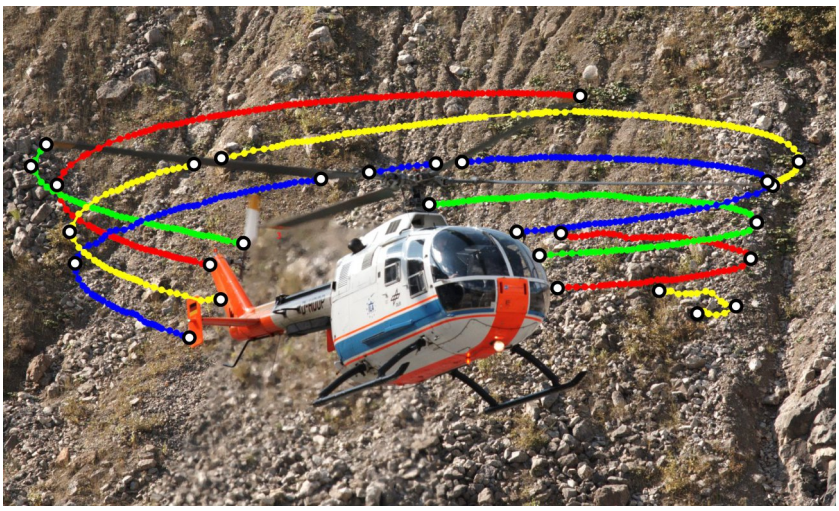

Figure 5.16: Photograph of BO 105 with individually detected 2D vortex segments color-coded by blade and end points marked by white dots

indicated by the different colors in Fig. 5.16. The labeling was necessary to ensure that – for a given point on a 3D vortex filament – the corresponding 2D points on the correct projected vortex segments in all camera image planes were selected during the point-pairing process.

5.4.3 Iterative camera calibration

The quality of the calibration of the camera system is crucial for experiments that deal with tomography, holography, or 3D reconstructions. In a laboratory experiment, the extrinsic camera parameters (see Hartley & Zisserman, 2003 for details) are typically estimated using a 2D or 3D calibration target with a known geometry and position that is imaged by all cameras of the measurement setup, see e.g. Raffel et al. (2007) and Heineck et al. (2013). The application of a calibration target covering the entire measurement volume (i.e. the overlapping FOV of all cameras) of a full-scale experiment outside the laboratory can pose a significant challenge. In the present flight tests, the measurement volume was located up to 18 m above the ground and had dimensions of 17 m × 11 m, necessitating a different approach for the camera calibration.

Before the test runs, a helium balloon with a diameter of 1 m was positioned within the measurement volume, as shown in Fig. 5.17a. The cameras were aligned with the helium balloon and their lens magnifications adjusted to cover approximately the same FOV. The distances and angles between the cameras and the balloon were measured by a laser distance meter with an accuracy of ± 0.5 m. An initial extrinsic camera calibration was calculated based on these geometric measurements and the set values of the camera focal lengths. The balloon was imaged by all cameras and the camera plane coordinates of the balloon center were determined. The camera orientations were corrected by the differences between their principle points and the projected balloon center. For the present camera setup, lens distortion effects were found to be negligible due to the small (*cropped*) camera sensor and a centered object of interest that covered less than 70% of the image width.

The initial camera calibration was not accurate enough for the reconstruction of small phase objects such as the blade tip vortices with a diameter of less than 0.05 m. Therefore, the initial

Figure 5.17: Photographs of **a)** a large helium balloon, and **b)** the BO 105 with selected marker positions for the camera calibration

camera calibration was iteratively optimized based on prominent points on the helicopter fuselage, which acted as an *in-situ* calibration target. For each camera, a total number of 44 points from five different measurement images were manually selected, as shown by white markers in Fig. 5.17b for one measurement image of camera 2. Despite the lack of precise marker points and the reduced sharpness of the helicopter image due to the background-focused cameras, the manual selection had an uncertainty of below ± 2 pixels, or ± 6 mm in the physical domain.

The optimization of the camera calibration was carried out by iteratively varying the positions, orientations and effective focal lengths of all cameras relative to a single fixed master camera, e.g. camera 1. Each camera was paired with the master camera and the points on the helicopter fuselage visible in both cameras were reconstructed in 3D object-space using a triangulation-based stereo photogrammetry technique by Mikhail et al. (2001), which is described in detail in Subsection 5.4.5. The reconstruction can briefly be explained for a 2D representation of a 3D point in the camera image plane that is back-projected as a line through the camera optics and into the 3D measurement volume using the pinhole camera model together with the camera's position and orientation. For an optimal camera calibration, the 3D coordinates of the sought object-space point are found by intersecting the back-projected lines from a pair of cameras. In practice, however, pairs of lines typically do not perfectly intersect in 3D space. Therefore, the nearest points on the master camera lines with respect to the other camera's lines were chosen as intersection points and the miss distances between the line pairs were averaged and used as a quality indicator for the convergence of the iterative scheme. For the final and converged camera calibration, the cameras were shifted by less than 0.8 m and the reconstructed calibration points typically scattered by less than ± 0.03 m. The positions, horizontal orientations and focal lengths of the final camera setup are also given in Table 5.1 in Subsection 5.3.1.

5.4.4 Epipolar geometry

The 3D reconstruction of solid objects via photogrammetry requires discrete markers or prominent points on its surface to be imaged and identified in two or more camera images. The application of the corresponding reconstruction algorithms to invisible and continuous objects such as blade tip vortices implies that corresponding points on the vortex lines can be identified clearly in the images of all cameras. This issue is described as *correspondence problem* by Meyn & Bennett (1993) and can be solved by application of the *epipolar geometry* method, as described by Hartley & Zisserman (2003). The epipolar geometry method is based on the pinhole camera model and imposes geometric constraints on pairs of camera images, as shown in Fig. 5.18. In the illustration, two cameras (A,B) are depicted including their optical centers O_A and O_B and image planes (blue rectangles). An object-space point X (e.g. a point on a 3D vortex segment) and its projections X_A and X_B onto the two image planes are sketched. Following the idea behind the epipolar geometry, the point X and its projections X_A and X_B define an epipolar plane that intersects the image planes of both cameras. If only the epipolar plane, X_A, and O_A are known, the line through these two points can be mapped as an epipolar line in the image plane of camera B (see red line in Fig. 5.18). The point X_B corresponding to X_A must be located on this epipolar line. The point X_B can be determined by identifying the vortex filament X is located on in both camera planes and intersecting it with the epipolar line. The constraint

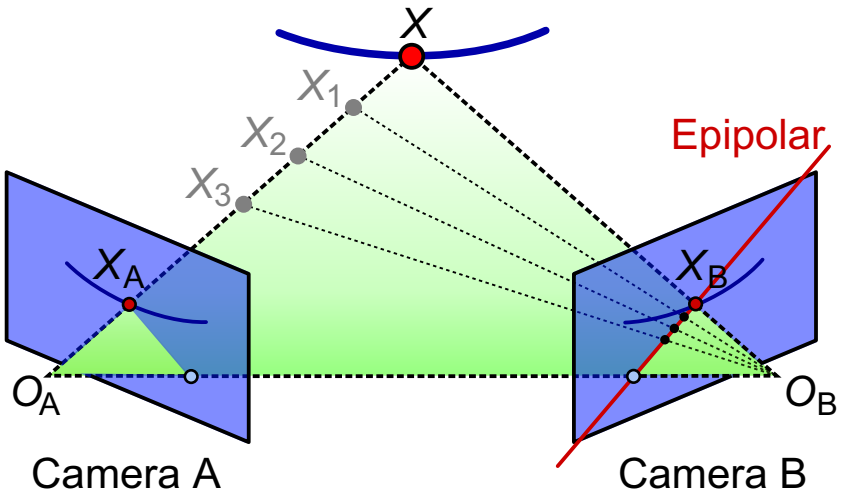

Figure 5.18: Epipolar geometry with projected camera plane points X_A and X_B of the 3D point X, and the corresponding red epipolar line, after Heineck et al. (2013)

imposed by epipolar geometry is written as

$$\begin{bmatrix} x_A & y_A & 1 \end{bmatrix} \times F \times \begin{bmatrix} x_B \\ y_B \\ 1 \end{bmatrix} = 0 \tag{5.1}$$

where (x_A, y_A) and (x_B, y_B) are the coordinates of corresponding points in the images A and B, and F is the 3×3 fundamental matrix. At least seven corresponding point pairs in the two images are necessary to estimate this fundamental matrix. During the present evaluation, two different methods were applied for the estimation of F, both based on point pairs on the fuselage of the helicopter, as shown in Fig. 5.17b. These methods are the *normalized eight-point algorithm* by Hartley (1997) and the *random sample consensus* (RANSAC) method by Fischler & Bolles (1981), which used 44 point pairs here. The fundamental matrices were estimated for all possible camera combinations in the multi-camera setup. The fuselage points from one camera image were projected as epipolar lines in the other corresponding camera image as a check of the precision of the estimated fundamental matrices. Differences between the epipolar lines and the respective fuselage points of less than 1.5 pixels were found.

Discrete points with a distance of between 5 and 10 pixels were extracted from the previously determined 2D spline representations of the vortex segments of a selected master camera. Each of these extracted points was mapped as an epipolar line in all other camera images, as shown e.g. in Fig. 5.19 for camera 2. The two red lines are epipolar lines mapped from the fuselage points of camera 5 and the blue lines represent the detected vortex locations in the image of camera 2. The intersection points between the 2D vortices and the epipolar lines were determined and stored together with the original points from the master camera. These discrete and paired groups of 2D vortex points in two different camera images are the basis for the reconstruction of the corresponding object-space vortex filaments. The point-pairing scheme returned unambiguous connections for the majority of all processed data points. Despite the coding of vortices, however, false pairing of points on non-corresponding vortices could not be prevented for some vortex segments. This problem is illustrated by the upper epipolar line in Fig. 5.19,

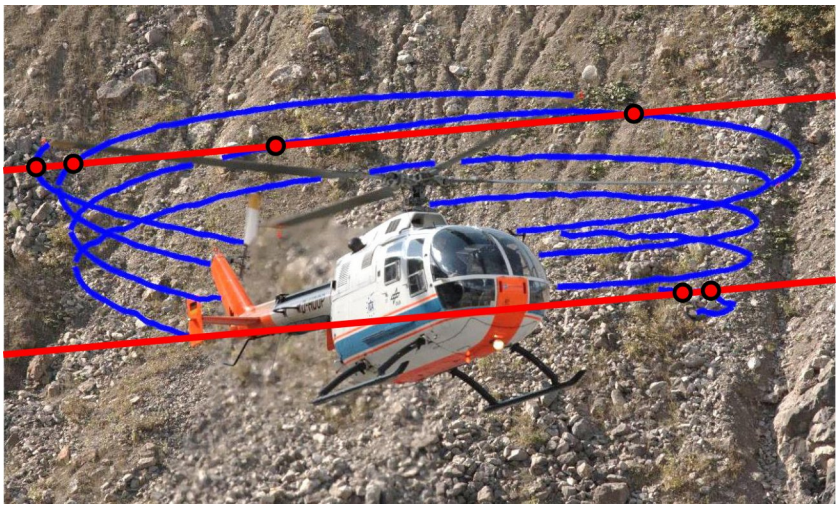

Figure 5.19: Picture of BO 105 from camera 2 with blue vortices, red epipolar lines mapped from camera 5, and multiple intersection points, after Bauknecht et al. (2014d)

which intersects with more than one vortex segment. A second source of error are multiple intersections of epipolar lines with a single curved or wave-shaped vortex. The underlying ambiguity of the epipolar mapping is also illustrated in the principle sketch of Fig. 5.18, where the point X_A is mapped to all points X_i on the epipolar line in the image plane of camera B. Only by intersecting the epipolar line with the correct vortex filament, a valid point pair is generated. For the vortex pairing in the present evaluation, up to four intersection points were found on a single vortex filament, as depicted by the lower epipolar line in Fig. 5.19. Some of the false point pairs were directly removed by detecting skips in a continuous series of 2D points. The remaining false point pairs were filtered out after the reconstruction process, as they resulted in unphysical object-space points outside the rotor tip region.

The present camera setup featured large horizontal and relatively small vertical distances between the cameras due to the layout of the test site. Consequently, epipolar lines with only moderate inclination angles of around 10° were generated, as shown e.g. in Fig. 5.19. Some segments of the blade tip vortices had a comparable orientation, which led to shallow intersection angles, a reduced horizontal accuracy of the corresponding point pairing, and thus an increased uncertainty of the reconstructed position of the object-space point.

5.4.5 3D reconstruction of vortex positions

The 3D reconstruction of the object-space vortices was carried out by a triangulation-based stereo photogrammetry technique. The point-based method necessitated the discretization and pairing of 2D points by the epipolar geometry method, as explained in the previous subsection. Consequently, only discrete points on the 3D vortices were reconstructed instead of continuous curve segments. The previously defined combinations of a master camera with all other cameras were applied again for the reconstruction. As some parts of the vortex system were not captured by a single master camera, two different master cameras (1 and 5) on opposite ends of the camera setup were used to increase the number of reconstructed vortex segments.

For each camera pair, a 3D point cloud was generated that represented discrete points on the 3D vortices. The combination of multiple of these camera-dependent point clouds exhibited scattering due to the previously described false point pairing, multiple intersection locations, and the residual camera calibration error. For each azimuthal position and coded vortex segment, the median center position was computed. Points with a distance greater than 4 $\%R$ or 0.2 m from this median center position were treated as outliers and deleted. A second routine proceeded along groups of contiguous 3D vortex points and filtered out points with a deviation of more than 2 $\%R$ or 0.1 m from a locally fitted polynomial curve. Small discontinuities were caused by the variation of the master camera as different points on the vortex segments were used for the point-pairing process in combination with altered intersection angles of the epipolar lines with the vortices. As a consequence, the horizontal scattering of the reconstructed vortex points was increased in some parts of the wake and decreased in others. Up to six individual vortex point clouds were reconstructed for a single master camera and six paired cameras. The residual point scattering was of the order of $\pm$ 0.4 $\%R$ or $\pm$ 0.02 m around the average vortex positions. By adding the second master camera, the number of camera combinations doubled and the corresponding point scattering increased at some locations, leading to fluctuations of up to $\pm$ 1 $\%R$ or $\pm$ 0.05 m around the average vortex positions.

5.4.6 Numerical comparison

A numerical simulation of the helicopter wake was carried out by Jianping Yin from DLR Braunschweig to enable a qualitative comparison with the experimentally determined 3D vortex positions. For the simulation, the incompressible, unsteady 3D free-wake panel method solver UPM was used, see Yin & Ahmed (2000) and Yin (2012) for details. UPM is a velocity-based, indirect potential formulation that uses a combination of source and dipole distributions on the rotor blades. In the rotor wake, dipole panels and a full-span free-wake model including a tip vortex roll-up formulation are applied for the computation of the vortex system. Rigid blades were assumed for the simulation and adjusted with a force trimming procedure to achieve a rotor thrust of $T = 25$ kN and a vertical rate of climb of 1 m/s. These operational conditions were estimated for the ascending hovering flight test case used for the 3D vortex reconstruction, which is described in the following section.

5.4.7 Concluding remarks about the BOS data analysis

The vortex reconstruction process employed here requires a processing time of the order of 50 hours for a set of 7 camera images. The majority of the involved routines are automated and do not significantly contribute to this duration. The processing time is mainly affected by the iterative camera calibration, semi-automatic vortex detection, and filtering of unphysical vortex positions in the spatial domain. An improvement with respect to both the processing time and accuracy of the results can be achieved by replacing the time-consuming iterative camera calibration with a camera calibration based on automatically detected marker points. In combination with a larger vertical angle between the cameras, this measure would positively affect the number of outliers in the reconstructed object-space domain and reduce the post-processing time of the results.

5.5 Results of the full-scale vortex reconstruction

5.5.1 Multi-camera vortex visualization

A multi-camera visualization of the vortex system of the BO 105 in ascending hovering flight is shown in Fig. 5.20. The graphic depicts seven cropped photographs of the helicopter that were simultaneously acquired by cameras 1 – 7. The corresponding detected 2D vortex filaments are overlaid on the pictures. The curves are color-coded based on the rotor blade from which they originated (red: front, green: right-hand side, blue: rear, yellow: left-hand side; positions are in the helicopter frame of reference). The characteristic helical shape of the vortex system with a decreasing diameter with wake age is visible in all seven camera views, but most clearly in the images of cameras 2, 3, and 5. The vertical convection rate is moderate close to the rotor

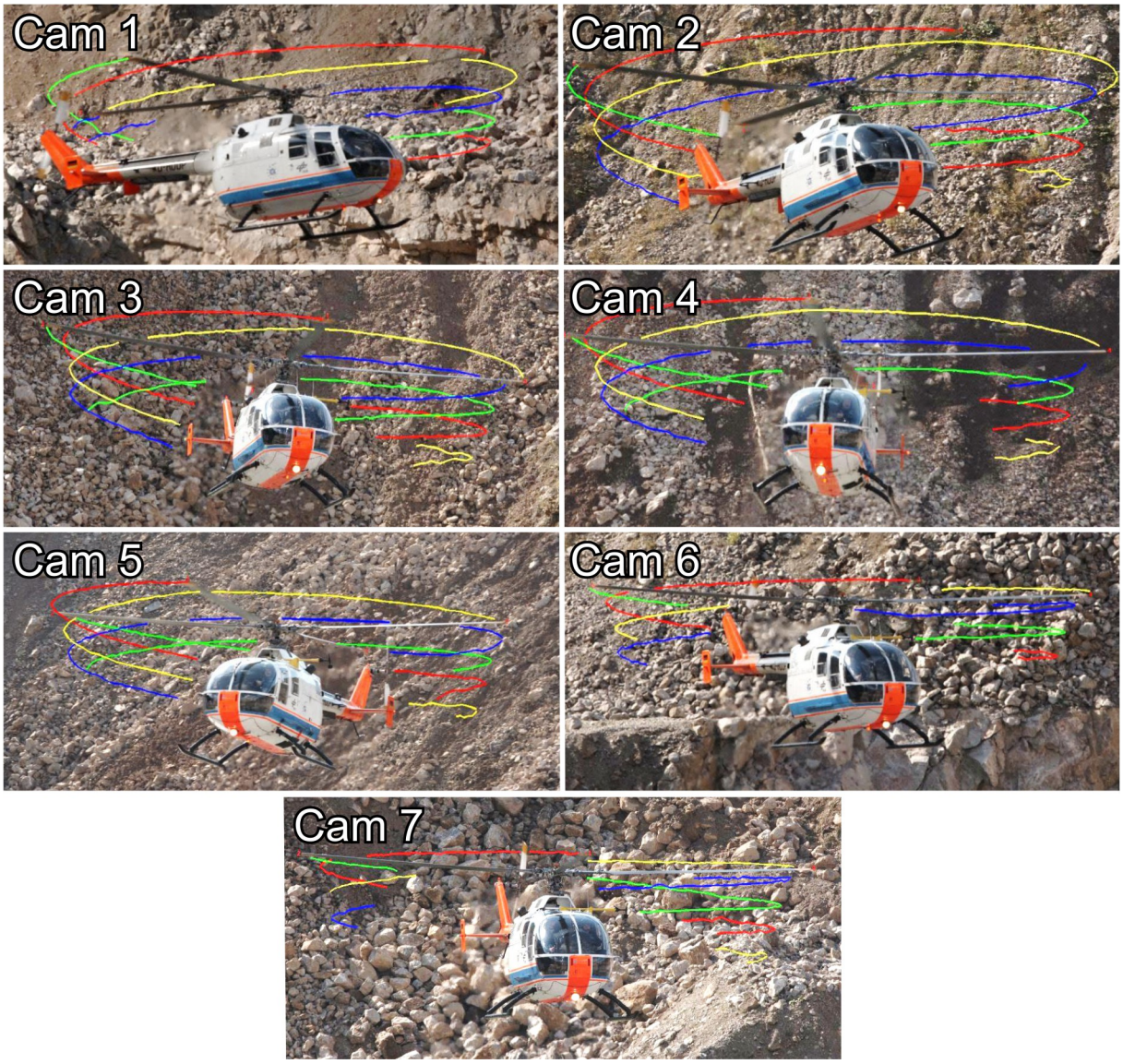

Figure 5.20: Photographs of the BO 105 from cameras 1 – 7 with extracted and grouped 2D tip vortices color-coded by blade, after Bauknecht et al. (2014d)

disk, resulting in small vertical distances between consequent vortex generations, as visible e.g. on the right-hand side of camera image 6 in Fig. 5.20. The vertical convection rate grows with increasing wake age, inducing larger distances between the vortex filaments. Long and largely continuous vortex curves are detected for the lower cameras $1-5$ with maximum visible vortex ages of just above $\psi_v = 360°$. Interruptions of the vortex curves are caused by the helicopter fuselage, the rotor blades, the hot engine exhaust, and the dark, soil-covered, low-contrast areas in the background, see e.g. Fig. 5.20, camera 4. The onset of vortex instability effects is visible for the lower yellow vortex segment around $\psi_v = 360°$. Visibility of this segment, however, is not equally good for all cameras and mainly restricted to a region close to the edge of the rotor wake, which varies with the observation angle. Only a partial 3D reconstruction of this vortex filament is therefore possible. As stated above, the backgrounds for cameras $1-5$ are better suited for the BOS evaluation than the backgrounds of cameras $6-10$. For cameras $8-10$, the increased noise level causes a loss of the vortex signal for large parts of the vortex system. Only at the lateral edges of the rotor disk are some vortices visualized where the increased integration length through the vortex filaments intensifies the displacement signal. As the additional information gained by cameras $8-10$ is limited, only cameras 6 and 7 from the upper group are used for the reconstruction. Despite the limitations due to the imperfect natural background, a large part of the helicopter vortex system is visualized using cameras $1-7$, which is already an improvement compared to a single camera result.

5.5.2 Full-scale vortex reconstruction

Based on the iteratively optimized camera calibration and the 2D data set shown in Fig. 5.20, a 3D reconstruction of the vortex system and the helicopter fuselage was carried out. Multiple views of the reconstructed 3D vortex system are depicted in Fig. 5.21. A new local coordinate system (x, y, z) is defined by translation of its origin to the instantaneous rotor hub center, while keeping the orientation of the previously defined axes (X, Y, Z) constant. The plot axes are normalized with the rotor radius R. The vortices are color-coded according to the blade they trail from, as given in Fig. 5.20. A 3D model of the BO 105 helicopter is added to the plots with its position and orientation determined by the reconstructed calibration points on the helicopter fuselage. In addition, the rotor blades are added based on the reconstructed locations of the blade tips. In comparison with the other reconstructed object-space points, the azimuthal blade tip positions exhibit increased scattering due to motion blurring and the residual camera jitter in combination with the high blade tip velocity. This leads to an increased uncertainty in the azimuthal blade tip positions of around $\pm 0.2c$.

The BO 105 is depicted from perspectives close to camera 5 in Fig. 5.21a and camera 1 in Fig. 5.21b, respectively. The top view of the vortex system is given in Fig. 5.21c. As previously explained, the reconstructed vortex system corresponds to an ascending hover flight state. In more detail, the BO 105 performed a swinging motion along the vertical axis and the images were acquired close to the bottom reverse point of the maneuver, where the vertical acceleration and the blade loads were relatively high. At the moment of the image acquisition, the fuselage of the helicopter had an inclination of 6° and a roll angle of −2°, which is also visible in Fig. 5.21.

A close resemblance between the 2D projections shown in Fig. 5.20 and the 3D vortex curves is observed. The previously described characteristic contraction of the rotor wake is evident in the

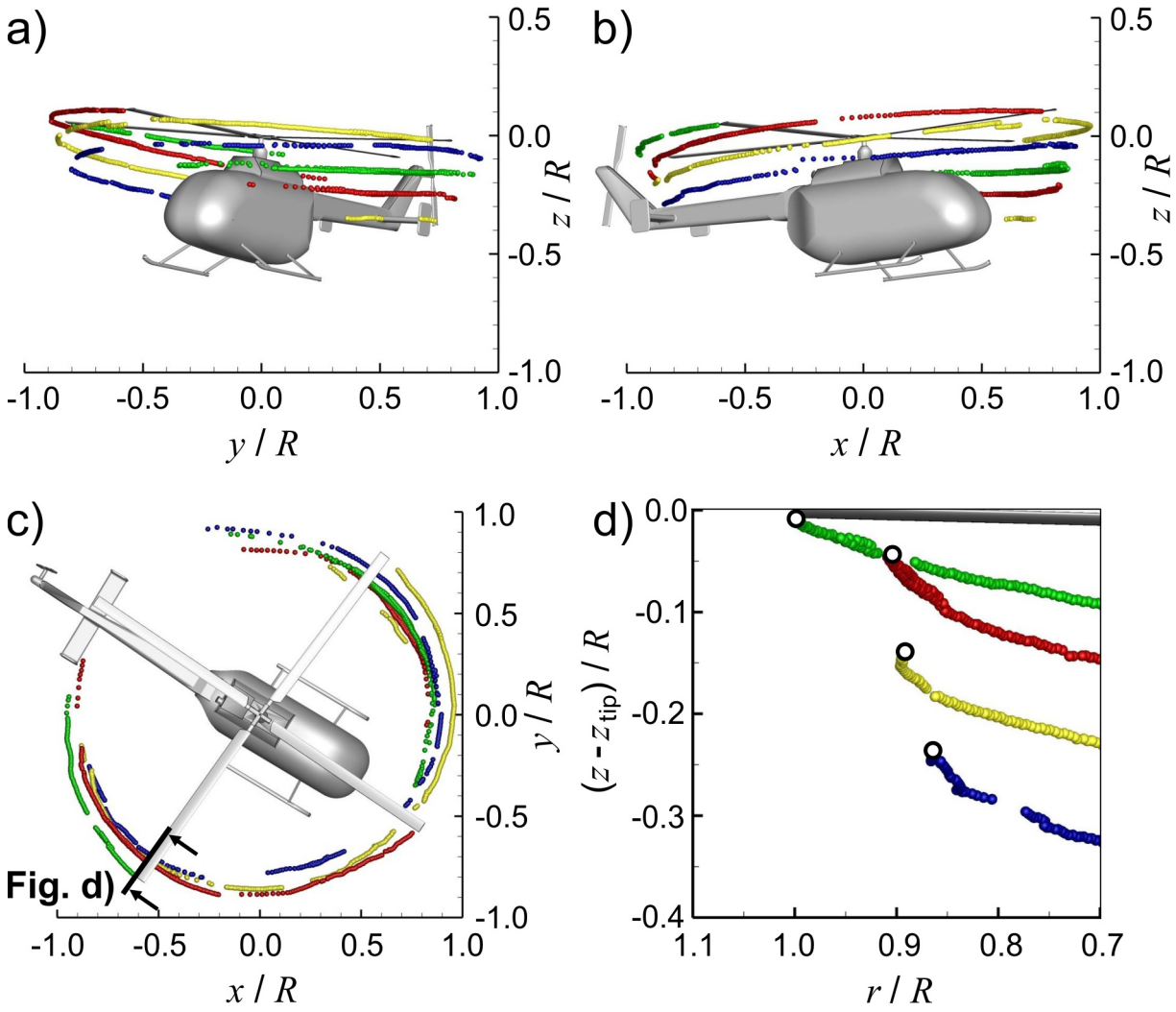

Figure 5.21: Different perspectives **a-c)** of the BO 105 and reconstructed main rotor vortex system, and **d)** radial section at marked position in **c)**, after Bauknecht et al. (2014d)

3D plots as well, especially in the top view (Fig. 5.21c). The large initial radial convection of the young vortices close to the rotor plane can be seen e.g. for the red curve of the vortex shed by the forward facing blade. The strongest radial convection is found directly behind the forward facing blade for a vortex age up to $\psi_v = 20°$. The initial radial contraction is smaller for the other blades, which can potentially be attributed to the unsteady flight condition and the different blade loads due to the control inputs of the pilot to keep the BO 105 within the measurement volume. The azimuthal asymmetry decreases for older vortex ages and the characteristic helical vortex shape develops. Parts of the vortex system are well covered by more than two cameras, which leads to the reconstruction of continuous vortex segments with an azimuthal extent of up to 90°, as can be seen for the yellow vortex curve behind the retreating blade in Fig. 5.21. Due to the outlier filtering – as explained in the previous sections – gaps are generated in the vortex segments. Vortex filaments that are only covered by a single camera cannot be reconstructed, as can be observed for the green vortex segment above and to the left-hand side of the tail boom that is only detected by camera 1 in Fig. 5.20. This monoscopic coverage of parts of the rotor wake is caused by the small horizontal viewing angle of 83° between the outermost cameras and the view obstructions by the helicopter fuselage and the engine exhaust.

An increased scattering of up to $\pm 1\,\%R$ or ± 0.05 m is visible for the green vortex curve in front of the helicopter for vortex ages of between 210° and 260°. This increased scattering corresponds to the shallow intersection angles in the epipolar point-pairing process, which are caused by the mainly horizontal vortex filaments in the lower camera images and missing curve segments in the upper camera images. The vertical camera separation is consequently less effective for this part of the vortex system and reduces the accuracy of the 2D point-pairing.

The onset of macroscopic instability effects is observed for vortex ages close to $\psi_v = 360°$, as depicted for the yellow vortex curve in Fig. 5.21. A complete reconstruction of the corresponding vortex segment was not possible due to missing projections in the images of camera 1 and 6, in combination with limited overlap between the vortex filaments detected by the other cameras. The wave-like shape of the instability zone was therefore only partially captured.

A radial cut through the vortex system at the marked trailing edge position in Fig. 5.21c is plotted in Fig. 5.21d. The radial coordinate r is measured in the rotor frame of reference and normalized with the rotor radius R. The vertical coordinate z is given relative to the blade tip height z_{tip} and also normalized with R. Four different vortex segments from the rear half of the vortex system are shown in the image. Their intersection locations with the sectional plane are marked by black circles, visualizing the outline of the contracting wake. The green vortex segment is generated by the blade depicted in the frame and intersects with the sectional plane just behind the tip of the blade trailing edge. As helicopter rotors operated in hovering flight are generally not prone to BVI effects, the positional information extracted from the present set of reconstructed vortices cannot be used for the analysis of BVI. Nevertheless, the determination of important geometric parameters such as the minimum miss distance between the red vortex and the advancing blade of $0.8c$ at a location of $r/R = 0.905$ with an interaction angle of close to 90° shows the potential of this measurement technique for application to real BVI studies.

A qualitative comparison between corresponding views of the reconstructed experimental vortex system and the result of a 3D free-wake panel code simulation is shown in Fig. 5.22. The simulation was set up with estimated boundary conditions, the details of which are discussed

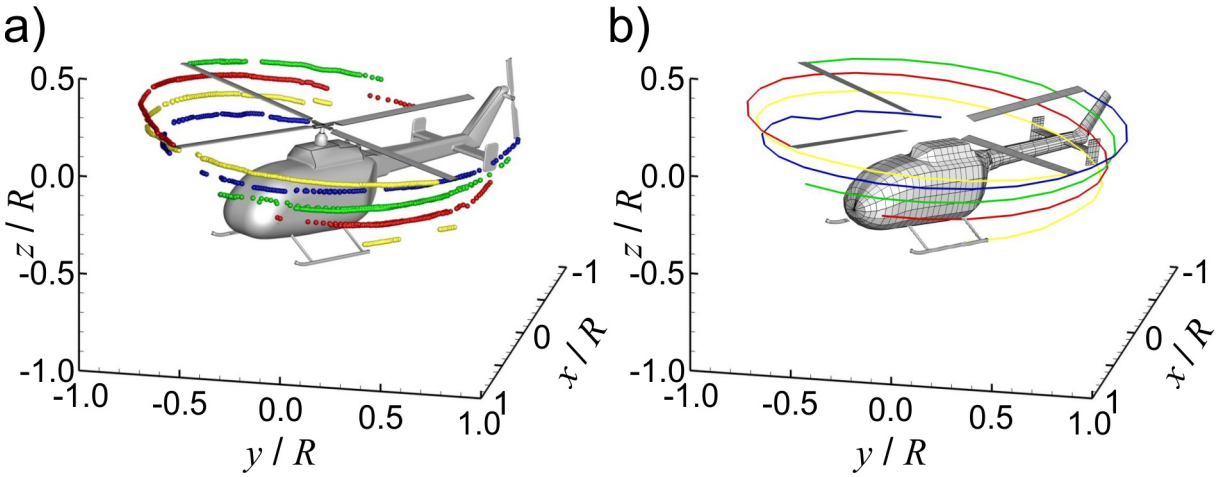

Figure 5.22: Comparison of corresponding views of **a)** the experimental vortex system from Fig. 5.21 and **b)** result from an unsteady 3D free-wake panel code simulation of a similar flight state, after Bauknecht et al. (2014d)

in Subsection 5.4.6. The result of the simulation in Fig. 5.22b also depicts a fuselage model of the BO 105 and the computed blade tip vortices. The maximum visibility of the vortices was matched with the experimental result in Fig. 5.22a. The overall shapes of the two vortex systems exhibit a high qualitative agreement. In detail, some differences in the wake contraction and vortex disturbance levels are observed. This can be attributed to the temporal resolution of the simulation and the estimated experimental boundary conditions, as exact measurements were not available. Despite these differences, the overall agreement between the results shown in Fig. 5.22 underlines the quality and comparability of the experimental data and gives an outlook for potential applications of future 3D BOS results with well-determined boundary conditions.

5.5.3 Summary of the flight tests

The flight test program conducted within this work comprised three preliminary and one main flight tests, which have been discussed within this chapter. The main goal of the preliminary flight tests was the demonstration of the visualization capabilities of the BOS method and the reference-free BOS variant. The vortices of a BO 105 helicopter under hovering and landing flight conditions were visualized with a retro-reflective reference-free BOS setup close to the ground. The unrestricted maneuvering flight of a Cougar helicopter was studied in a mountain environment with a pivoted and versatile reference-free dual camera system and natural backgrounds. Unprecedented vortex visualization results were obtained during high-speed and unsteady maneuvers such as accelerating forward flight and flare, allowing the study of details such as vortex instability effects. As a further demonstration of the capability of the reference-free BOS method to operate under highly unsteady conditions, an airborne dual camera system was used to visualize the vortices of a BO 105 during free maneuvering flight. The moving perspective from above the helicopter allowed for the study of high-speed forward flight and related phenomena such as vortex roll-up and BVI.

The goal of the main flight test was the 3D localization of a full-scale helicopter vortex system. A multi-camera BOS setup with natural backgrounds was utilized to simultaneously acquire BOS measurement images of the BO 105 helicopter under maneuvering flight from various perspectives. A test case of ascending hovering flight was selected for the visualization, detailed analysis, and 3D reconstruction of the main rotor vortex locations. The processing consisted of the visualization of the blade tip vortices, semi-automatic detection of their positions in the camera images, iterative calibration of the camera setup, discretization and pairing of 2D vortex curves with the corresponding vortices in other camera images, and the reconstruction of the 3D locations using a triangulation-based stereo photogrammetry technique. As a final result, the main rotor blade tip vortex system of the BO 105 was localized in object-space with an average accuracy of the point locations of about ± 0.02 m. Gaps in the vortex data originated from a relatively small maximum horizontal viewing angle of 83° between the outermost cameras and obstructions by the fuselage and the exhaust gases from the engines. From the reconstructed vortex system, geometric data was extracted that is important for the assessment of BVI effects. A minimum miss distance between a vortex and the advancing blade of $0.8c$ was determined at a location of $r/R = 0.905$ with an interaction angle of close to 90°. The quality and level of detail of the reconstructed data set shows the potential of the BOS measurement technique for quantitative full-scale measurements of real BVI test cases.

6 Conclusions and outlook

This thesis focuses on two important aspects of *blade-vortex interactions* (BVI): a reduction of the adverse effects of BVI and realizing a full-scale validation of BVI results obtained from sub-scale model rotor tests. The corresponding evaluation is based on experimental results obtained from the hover test of a *smart-twisting active rotor* (STAR) and multiple flight tests on full-scale helicopters. These experiments were conducted to answer the main questions that were formulated in the introduction. The conclusions of this work are correspondingly split into two sections, followed by an outlook on future BVI investigations.

6.1 Active twist investigation on a large-scale model rotor

The first section focuses on the results of the STAR model rotor test under hover conditions. The main research question that motivated this experiment was:

What are the effects of active twist actuation on the shed blade tip vortices?

The experimental investigation of the STAR active twist rotor was conducted and evaluated with respect to this question. The rotor blades were actuated with harmonic frequencies of $1/revolution$ to $5/rev$ over a range of control phase angles with 45° increments. The test was conducted in a hover chamber and comprised simultaneous and time-resolved stereoscopic *particle image velocimetry* (PIV) and *background-oriented schlieren* (BOS) measurements to investigate the velocity and density fields around the tip vortices for wake ages of $\psi_v = 3.56° - 45.74°$. The corresponding velocity and density data were evaluated to determine the strength, extent, and locations of the tip vortices, as well as actuator-induced changes thereon, relative to an unactuated test case. The following conclusions were drawn from the actuated hover test:

1. The recirculation in the hover chamber and geometric variation between the rotor blades both caused similar and significant levels of aperiodicity in the recorded data. These effects were effectively counteracted by performing the vortex analysis in the blade tip frame of reference, and by applying individual averaging based on the mean swirl velocity profile obtained from 72 cuts through the vortex. These measures were found to adequately reduce the influence of random variation in both the positions and shape parameters of the vortices. The actuation-induced effects thus exceeded the random fluctuations, enabling a meaningful analysis of the effects of active twist on the blade tip vortices.

2. The recorded particle images exhibited a characteristic seeding void close to the vortex center, which had to be excluded during the evaluation to prevent the falsification of the velocity information close to the vortex core. The extent of the void was generally

smaller than the detected vortex core radius and thus had little influence on the measured vortex parameters. A direct comparison between results obtained by the PIV and BOS measurement systems exhibited a good correlation for the strength and trajectories of the vortices, and marginally increased values for the BOS-based core radii with an average offset of $0.35\%c$. The reliability of the measured aerodynamic data is thus substantiated by the converging results from two entirely different measurement systems.

3. The swirl velocity profiles across the unactuated vortex compared well with the Vatistas vortex model with a form factor of $n = 2$. The extracted peak swirl and axial velocity components exhibited a similar decay with time as found in previous studies.

4. A deviation from the expected square root development of the core radius was observed up to a vortex age of $\psi_v = 15°$ due to the unfinished roll-up of the vortex. This trend was found for both PIV and BOS data, and for the unactuated and most of the actuated test cases, therefore supporting former observations by Ramasamy et al. (2009b). The comparison of vortex parameters between different rotor experiments was thus found to crucially depend on a completed vortex roll-up. The high temporal resolution of the PIV measurements enabled an analysis of the 3D vortex formation and thus allowed detailed insights into the vortex roll-up process.

5. The present evaluation comprises the first quantitative reconstruction of density across a rotor blade tip vortex based on a laser speckle-illuminated BOS system and a reference experiment with a known density distribution. The approach returned plausible magnitudes and trends for the vortex density that were qualitatively comparable with the peak swirl velocity. The density investigation also enabled the identification of two distinct phases for the temporal development of the core density with different recovery rates. This discovery provides a valuable insight into the mechanisms of vortex decay and illustrates the merits of a density-based vortex investigation.

6. The effect of active twist on the strength and trajectories of the vortices highly depends on the control frequency and phase angle of the actuation. Careful application of the twist control thus enables selective targeting of the BVI-critical vortex segments by modifying their strength during the interaction and increasing the blade-vortex miss distance.

7. No significant alterations of the shape of the vortex trajectories – about $\pm 0.5\,\%R$ around the baseline condition – were observed for the $1/rev$, $4/rev$, and $5/rev$ actuation frequencies. The $1/rev$ actuation had a significant effect on the blade flapping motion, which resulted in a variation of the vertical blade tip position by up to $1.3\,\%R$ above and $-1.01\,\%R$ below the unactuated test case. The largest vertical vortex displacements were found for the $2/rev$ actuation with up to $-1.4\,\%R$ below the baseline case, and for the $3/rev$ actuation with a shift of up to $-2\,\%R$ within the first 35° of wake age. A miss distance of $5\,\%R$ between the vortex and the following rotor blade is extrapolated for the $3/rev$ vortex displacement, illustrating the control authority of the active twist actuation over the vortex trajectories and potentially over the magnitude of BVI.

8. Active twist actuation with frequencies of $1/rev$, $4/rev$, and $5/rev$ only resulted in moderate variations of the initial peak swirl velocity – studied here as a measure of vortex strength – of between $-22\,\%$ and $+12\,\%$ relative to the unactuated reference velocity. The

$2/rev$ and $3/rev$ actuation caused comparably large changes of the initial peak swirl velocity of between $-34\,\%$ and $+31\,\%$ around the unactuated reference velocity. The active twist actuation thus effects an azimuthal redistribution of the vortex strength, and has to be phase-shifted correctly to ensure minimal strength of the trailing vortices that undergo BVI. Overall, the magnitude of the changes in peak swirl velocity demonstrates the large control authority of the active twist actuation over the vortex strength.

In summary, the hover tests demonstrated a high control authority of the active twist actuation on the strength and trajectories of the trailing blade tip vortices. The magnitude of the evoked changes indicates that the active twist actuation constitutes an effective measure for the mitigation of BVI-induced noise on real helicopters.

6.2 Three-dimensional vortex localization on helicopters

The second section of the conclusions focuses on the development of new measurement techniques for full-scale rotor investigations. The main motivation for this part of the investigation was also stated in the introduction:

> *Is it possible to acquire three-dimensional blade tip vortex positions for a full-scale helicopter under free flight conditions?*

To answer this question, three preliminary and one main flight test were conducted with a BO 105 and an AS532UL Cougar helicopter in combination with different BOS setups. The preliminary flight tests aimed to advance the reference-free variant of the BOS technique for full-scale helicopter investigations. This technique was applied in the first preliminary test to study the tip vortices of a hovering helicopter in front of an artificial background. The application of a pivoting reference-free BOS setup with large natural backgrounds in the second flight test enabled a visualization of the entire vortex system of a helicopter during highly dynamic, BVI-relevant flight maneuvers. In the third test, the same camera setup was operated aboard a microlight airplane to capture the vortex system of a helicopter under forward flight conditions. A multi-camera BOS setup consisting of 10 individual cameras and a large natural background was employed during the main flight test to perform a quantitative 3D vortex reconstruction on a maneuvering helicopter. The following conclusions were drawn from the flight tests:

1. High-quality visualization results in highly dynamic, large-scale, and challenging test environments were obtained by the reference-free variant of the BOS technique, where other measurement principles are not practicable. The reference-free BOS technique can be realized with natural backgrounds and enables non-intrusive, full-scale, and whole-field vortex visualizations on free flying helicopters with little to no maneuvering restrictions.

2. Fields and scree-covered slopes were found to provide ideal conditions for outdoor BOS measurements in terms of background structure size, contrast, and two-dimensionality. The temporal consistency of the background has to be considered for standard BOS measurements with a time-displaced acquisition of the undisturbed reference image. Backgrounds covered with vegetation are susceptible to wind gusts, whereas 3D backgrounds

are especially affected by changes of the natural illumination. Based on the present observations, selected natural backgrounds provide highly suitable conditions for outdoor BOS measurements that are even comparable with those of artificial backgrounds.

3. The vertical gradient of the vertical image displacements constitutes a suitable and robust measure for the detection of helicopter tip vortices with a small imaged vortex extent. The quality of this visualization criterion enabled a semi-automatic localization of the imaged vortex segments in the measurement images. A fully automatic vortex detection was hindered by residual background noise and obstructions of the vortices by the fuselage and blades of the helicopter, and the engine exhaust gases.

4. The results of the preliminary flight tests demonstrate the large-scale application of the reference-free BOS technique for the visualization of full-scale helicopter vortices under increasingly realistic flight conditions. The detection of tip vortices up to a vortex age of $\psi_v = 630°$ for a range of hover, high-speed forward flight, and BVI-relevant flare maneuvers constitutes a major advance for full-scale vortex investigations. The high level of detail of the measurements allowed for the analysis of vortex instability and interaction effects, as well as the roll-up of the vortex system on the lateral edge of the rotor disk.

5. The spatial extent of the main flight test setup prevented the usage of a calibration target of known geometry for the calibration of the multi-camera assembly. The presently used, iterative, two-step calibration approach had a suitable accuracy that resulted in a variation of ±0.03 m between reconstructed points from different camera pairs.

6. The test site chosen for the main flight test provided scree-covered natural backgrounds that were large enough for the 3D vortex investigation with a multi-camera BOS system. The layout of the test site and the measurement volume, however, limited the maneuverability of the helicopter and restricted the investigation to low-speed flight states. The high resolution of the cameras, in combination with a small background structure size, enabled a high-quality multi-perspective visualization of the main rotor vortex system up to a vortex age of $\psi_v = 360°$. The 3D reconstruction of the vortices allowed for a detailed and quantitative assessment of the main rotor vortex system under ascending hover flight conditions, including the extraction of BVI-relevant parameters such as a blade-vortex miss distance and interaction angle. The current main flight test therefore enabled the first full-scale reconstruction of a main rotor vortex system of a helicopter in free flight.

In summary, the results of the flight tests illustrate the potential of the BOS and reference-free BOS techniques for full-scale vortex investigations, and prove that the acquisition of 3D blade tip vortex positions is possible for helicopters under free dynamic flight conditions.

6.3 Outlook

Despite the advances that the current collection of studies contribute to the investigation of BVI, future studies have several issues to consider. A realistic assessment of the effects of active twist actuation on BVI can only be made based on wind tunnel tests. A wind tunnel

entry of the STAR model rotor was prevented by endurance issues of the piezoceramic active twist actuators. A DLR-internal follow-up project is currently investigating the sources of the malfunctions and strives to manufacture and test a new set of active twist rotor blades based on advanced piezoelectric actuators. The final goal of this new project is again the realization of a wind tunnel test to investigate the effects of active twist actuation under BVI-relevant flight conditions. Some of the measurement techniques applied within the present work – such as high-speed stereoscopic PIV and a 3D vortex reconstruction base on BOS measurements – are highly suited for the investigation of BVI under these forward flight conditions. An application of these measurement techniques could greatly contribute to improve the understanding of BVI and the exact influence of the active twist actuators thereon.

The reference-free BOS technique has been shown to be a versatile and powerful experimental method for vortex visualization, even under extreme and highly unsteady test conditions. It is particularly suited for large-scale aerodynamic and thermal investigations on rotorcraft and aircraft due to the combination of its high measurement sensitivity, potentially very high measurement resolution, and relatively simple implementation in large-scale outdoor environments. The present implementation of reference-free BOS with a dual-camera setup could be replaced by a single camera with both a high spatial resolution and a short sensor readout time in the future. Larger camera sensor resolutions could improve both regular and reference-free BOS systems and would allow for the acquisition of finer aerodynamic details or an increased field of view, which could e.g. simplify the investigation of helicopter vortices during high-speed flight tests with a fixed camera measurement volume.

A reconstruction of the main rotor vortex system of a free-flying helicopter was successfully carried out in the present work based on a multi-camera BOS system with large-scale natural backgrounds. This full-scale vortex investigation already constitutes a major advance for full-scale helicopter flight testing, but it has not exploited the full potential of the measurement technique yet. The natural backgrounds in the present 3D vortex investigation exhibited inhomogeneous areas, were partially poorly lit due to the low altitude of the sun, and only covered an azimuthal angle of about 80° around the helicopter. Future 3D helicopter vortex investigations should employ homogeneous and adequately illuminated natural backgrounds that further encircle the measurement volume to ensure that each vortex segment is acquired by at least two cameras, despite unpreventable obstructions by the fuselage and engine exhaust. The investigation of BVI on full-scale helicopters further requires the performance of high-speed flight maneuvers, which puts additional demands on the topology of the test site. The measurement volume of a setup that allows for full maneuverability of the helicopter would potentially be located far above the ground. This kind of setup would necessitate a fast, yet accurate, and unconventional concept for the camera calibration, e.g. based on automatically detectable markers attached to a drone flying within the measurement volume and the simultaneous acquisition of calibration images by all cameras.

The final step for future full-scale vortex visualization tests is the generation of comparable and comprehensive experimental data sets by simultaneously acquiring not only the 3D vortex system, but also the helicopter movements and accelerations, the blade tip deformations, the pilot control inputs, and the environmental boundary conditions. Such exhaustive data sets could then be used for the validation of comprehensive rotor codes, sub-scale model tests, and computational investigations.

References

Acheson DJ (1990), *Elementary fluid dynamics*, Clarendon Press, Oxford, Oxford, ISBN: 0-19-859660-X.

Adrian RJ & Westerweel J (2011), *Particle Image Velocimetry*, Cambridge Aerospace Series, Cambridge University Press, Cambridge, UK, ISBN: 9780521440080.

Adrian RJ (1991), "Particle-Imaging Techniques for Experimental Fluid Mechanics", *Annu. Rev. Fluid Mech.* Vol. 23, pp. 261–304.

Adrian RJ & Yao CS (1985), "Pulsed laser technique application to liquid and gaseous flows and the scattering power of seed materials", *Applied Optics*, vol. 24, no. 1, p. 44, DOI: 10.1364/AO.24.000044.

Allongue M, Marze H & Potdevin F (1999), "The Quiet helicopter-from research to reality", *Proc. American Helicopter Society 55th Annual Forum*, Montreal, Canada, May 25–27, 1999.

Anderson JD (2007), *Fundamentals of aerodynamics*, McGraw Hill International, New York.

Bagai A & Leishman JG (1993), "Flow visualization of compressible vortex structures using density gradient techniques", *Experiments in Fluids*, vol. 15, pp. 431–442.

Bagai A & Leishman JG (1995), "Rotor Free-Wake Modeling Using a Pseudo-Implicit Technique - Including Comparisons with Experimental Data", *Journal of the American Helicopter Society*, vol. 40, no. 3, pp. 29–41, DOI: 10.4050/JAHS.40.29.

Bailey SC, Tavoularis S & Lee BH (2006), "Effects of Free-Stream Turbulence on Wing-Tip Vortex Formation and Near Field", *Journal of Aircraft*, vol. 43, no. 5, pp. 1282–1291, ISSN: 0021-8669, DOI: 10.2514/1.19433.

Batchelor GK (1964), "Axial flow in trailing line vortices", *Journal of Fluid Mechanics*, vol. 20, no. 04, pp. 645–658, ISSN: 1469-7645, DOI: 10.1017/S0022112064001446.

Bauknecht A, Merz CB & Raffel M (2014a), "Airborne Application of the Background Oriented Schlieren Technique to a Helicopter in Forward Flight", *Proc. 17th Int Symp on Applications of Laser Techniques to Fluid Mechanics*, Lisbon, Portugal, July 7–10, 2014.

Bauknecht A, Merz CB, Raffel M, Landolt A & Meier AH (2014b), "Blade-Tip Vortex Detection in Maneuvering Flight Using the Background-Oriented Schlieren Technique", *Journal of Aircraft*, vol. 51, no. 6, pp. 2005–2014, ISSN: 0021-8669, DOI: 10.2514/1.C032672.

Bauknecht A, Ewers B, Wolf C, Leopold F & Raffel M (2014c), "Three-dimensional reconstruction of blade tip vortices of a BO 105 using a multi-camera BOS system", *Proc. American Helicopter Society 70th Annual Forum*, Montreal, Canada, May 20–22, 2014.

Bauknecht A, Ewers B, Wolf C, Leopold F, Yin J & Raffel M (2014d), "Three-dimensional reconstruction of helicopter blade-tip vortices using a multi-camera BOS system", *Experiments in Fluids*, vol. 56, no. 1, pp. 1–13, ISSN: 0723-4864, DOI: 10.1007/s00348-014-1866-6.

Bauknecht A, Ewers B, Schneider O & Raffel M (2015), "Aerodynamic results from the STAR hover test: An examination of active twist actuation", *Proc. 41st European Rotorcraft Forum*, Munich, Germany, Sept. 1–4, 2015.

Bebesel M, Polz G & Schoell E (1999), "Aerodynamic and aeroacoustic layout of the ATR(Advanced Technology Rotor)", *Proc. American Helicopter Society 55th Annual Forum*, Montreal, Canada, May 25–27, 1999.

Bendat JS & Piersol AG (1986), *Random data: analysis and measurement procedures*, 2nd, John Wiley & Sons.

Bernhard A & Chopra I (1996), "Development of a smart moving blade tip activated by a piezo-induced bending-torsion coupled beam", *Proc. SPIE Conference on Smart Structures and Integrated Systems*, San Diego, CA, USA, Feb. 25, 1996.

Bhagwat MJ & Leishman JG (2000), "Correlation of helicopter rotor tip vortex measurements", *AIAA Journal*, vol. 38, no. 2, pp. 301–308.

Bhagwat MJ & Leishman JG (1998), "On the Relationship Between Blade Circulation and Tip Vortex Characteristics", *Proc. American Helicopter Society 54th Annual Forum*, Washington D.C., USA, May 20–22, 1998.

Bhagwat MJ & Leishman JG (2002), "Generalized Viscous Vortex Model for Application to Free-Vortex Wake and Aeroacoustic Calculations", *Proc. American Helicopter Society 58th Annual Forum*, Montreal, Canada.

Bhagwat M, Caradonna FX & Field M (2015), "Fundamental Characterization of Spanwise Loading and Trailed Wake Vortices", *Proc. American Helicopter Society 71st Annual Forum*, Virginia Beach, USA, May 5–7, 2015.

Birch DM & Martin N (2013), "Tracer particle momentum effects in vortex flows", *Journal of Fluid Mechanics*, vol. 723, pp. 665–691, ISSN: 00221120, DOI: 10.1017/jfm.2013.82.

Birch D & Lee T (1992), "Rollup and Near-Field Behavior of a Tip Vortex", *Journal of Aircraft*, vol. 40, no. 3, pp. 603–607.

Boatwright DW (1972), *Measurements of velocity components in the wake of a full-scale helicopter rotor in hover*, tech. rep., Mississippi State University.

Boutier A, Lefevre JB & Micheli F (1996), "Analysis of helicopter blade vortex structure by laser velocimetry", *Experiments in Fluids*, vol. 21, pp. 33–42.

Braukmann J (2015), "Untersuchung von Blattspitzenwirbeln an Rotorversuchsständen mittels Hintergrund-orientiertem Schlierenverfahren", Master thesis, RWTH Aachen.

Brocklehurst A & Pike AC (1994), "Reduction of BVI noise using a vane tip", *Proc. American Helicopter Society Aeromechanics Specialists Conference*, San Francisco, CA, USA, Jan. 19–21, 1994.

Brooks TF, Booth ER, Boyd DD, Splettstoesser WR, Schultz KJ, Kube R, Niesl GH & Streby O (1991), "HHC study in the DNW to reduce BVI noise - an analysis", *American Helicopter Society/RAeS International Technical Specialists Meeting - Rotorcraft Acoustics and Fluid Dynamics*, Philadelphia, PA, USA.

Burley CL, Brooks TF, van der Wall BG, Richard H, Raffel M, Beaumier P, Delrieux Y, Lim JW, Yu YH, Tung C, Pengel K & Mercker E (2002), "Rotor wake vortex definition - initial evaluation of 3-C PIV results of the HART-II study", *Proc. 28th European Rotorcraft Forum*, Bristol, England, Sept. 17–20, 2002.

Burley CL, Brooks TF, Rozier KY, van der Wall BG, Richard H, Raffel M, Beaumier P, Delrieux Y, Lim JW, Yu YH, Tung C, Pengel K & Mercker E (2006), "Rotor wake vortex definition-evaluation of 3-C PIV results of the HART-II study", *International Journal of Aeroacoustics*, vol. 5, no. 1, pp. 1–38.

Caradonna FX, Lautenschlager JL & Silva MJ (1988), "An experimental study of rotor-vortex interactions", *Proc. 26th AIAA Aerospace Sciences Meeting*, Reno, NV, USA, Jan. 11–14, 1988.

Chen PC & Chopra I (1997), "Hover Testing of Smart Rotor with Induced-Strain Actuation of Blade Twist", *AIAA Journal*, vol. 35, no. 1, pp. 6–16, ISSN: 0001-1452, DOI: 10.2514/2.74.

Childress OS (1991), "The NASA/AHS noise reduction program - A brief overview", *Proc. NATO-CCMS Symposium on Noise Aspects of Rotary-Wing Aircraft*, Monterey, CA, USA, July 29–Aug. 1, 1991.

Chopra I (2000), "Status of Application of Smart Structures Technology to Rotorcraft Systems", *Journal of the American Helicopter Society*, vol. 45, no. 4, pp. 228–252, DOI: 10.4050/JAHS.45.228.

Coyne A, Bhagwat M & Leishman J (1997), "Investigation into the Rollup and Diffusion of Rotor Tip Vortices using Laser Doppler Velocimetry", *Proc. American Helicopter Society 53rd Annual Forum*, Virginia Beach, VA, Apr. 29–May 1, 1997.

DS 3D calibration plate (2009), Lavision GmbH, Manual No. 1000390, Göttingen, Germany.

Dalziel SB, Hughes GO & Sutherland BR (2000), "Whole-Field Density Measurements by 'Synthetic Schlieren'", *Experiments in Fluids*, vol. 28, pp. 322–335, DOI: 10.1007/s003480050391.

Dalziel S (1998), "Synthetic schlieren", *Proc. 8th Int. Symposium on Flow Visualization*, Sorrento, Italy, Sept. 1–4, 1998, ISBN: 0 9533991 09.

Dancila DS & Vasilescu R (2002), "Development of a wing section with piezoelectrically modulated/vectored blowing", *Proc. 43 rd AIAA/ASME/ASCE/AHS/ASC Structures, Structural Dynamics, and Materials Conference*, Denver, CO.

Debrus S, Francon M, Grover CP, May M & Robin ML (1972), "Ground glass differential interferometer", *Applied Optics*, vol. 11, pp. 853–857, DOI: 10.1364/AO.11.000853.

Devenport WJ, Rife MC, Liapis SI & Follin GJ (1996), "The structure and development of a wing-tip vortex", *Journal of Fluid Mechanics*, vol. 312, no. 1, pp. 67–106, ISSN: 0022-1120, DOI: 10.1017/S0022112096001929.

Felker FF, Maisel MD & Betzina MD (1986), "Full-Scale Tilt-Rotor Hover Performance", *Journal of the American Helicopter Society*, vol. 31, no. 2, pp. 10–18, DOI: 10.4050/JAHS.31.10.

Fischler MA & Bolles RC (1981), "Random sample consensus: a paradigm for model fitting with applications to image analysis and automated cartography", *Communications of the ACM*, vol. 24, no. 6, pp. 381–395.

Fradenburgh EA (1990), *Basic Aerodynamics for Rotor Performance*, tech. rep., AGARD-R-781.

Gelhaar B, Junker B & Wagner W (1993), "DLR Rotor Teststand Measures unsteady Rotor Aerodynamic Data", *Proc. 19th European Rotorcraft Forum*, Cernobbio, Italy, Sept. 14–16, 1993.

George AR (1978), "Helicopter Noise: State-of-the-Art", *Journal of Aircraft*, vol. 15, no. 11, pp. 707–715, ISSN: 0021-8669, DOI: 10.2514/3.58436.

Ghee TA & Elliott JW (1992), "A study of the rotor wake of a small-scale rotor model in forward flight using laser light sheet flow visualization with comparisons to analytical models", *Proc. American Helicopter Society 48th Annual Forum*, Washington D.C., USA, June 3–5, 1992.

Ghee TA & Elliott JW (1995), "The Wake of a Small-Scale Rotor in Forward Flight Using Flow Visualization", *Journal of the American Helicopter Society*, vol. 40, no. 3, pp. 52–65, DOI: 10.4050/JAHS.40.52.

Giuni M & Green R (2013), "Vortex formation on squared and rounded tip", *Aerospace Science and Technology*, vol. 29, no. 1, pp. 191–199, DOI: 10.1016/j.ast.2013.03.004.

Glauert H (1922), *An aerodynamic theory of the airscrew*, British ARC R&M 786.

Grant I (1997), "Particle Image Velocimetry: A Review", *Proc. Institution of Mechanical Engineers*, vol. 211 Part C, pp. 55–76.

Gray RB (1956), *An Aerodynamic Analysis of a Single Bladed Rotor in Hovering and Low Speed Forward Flight as Determined from Smoke Studies of the Vorticity Distribution in the Wake*, tech. rep., Princeton University, Report No 356.

Green SI & Acosta aJ (1991), "Unsteady flow in trailing vortices", *Journal of Fluid Mechanics*, vol. 227, pp. 107–134, ISSN: 0022-1120, DOI: 10.1017/S0022112091000058.

Green SI (1995), *Fluid vortices: fluid mechanics and its applications*, vol. 30, Springer Science & Business Media, Dordrecht, ISBN: 978-94-010-4111-9.

Haller G (2005), "An objective definition of a vortex", *Journal of Fluid Mechanics*, vol. 525, pp. 1–26, ISSN: 0022-1120, DOI: 10.1017/S0022112004002526.

Ham N (1983), "Helicopter Individual-blade-control and its applications", *Proc. American Helicopter Society 39th Annual Forum*, St. Louis, MO, May 9–11, 1983.

Han YO & Leishman JG (2004), "Investigation of Helicopter Rotor-Blade-Tip-Vortex Alleviation Using a Slotted Tip", *AIAA Journal*, vol. 42, no. 3, pp. 524–535.

Han YO, Leishman JG & Coyne AJ (1997), "Measurements of the Velocity and Turbulence Structure of a Rotor Tip Vortex", *AIAA Journal*, vol. 35, no. 3, pp. 477–485.

Hardin JC & Lamkin SL (1986), "Concepts for reduction of blade/vortex interaction noise", *Journal of Aircraft*, vol. 24, no. 2, pp. 120–125.

Hargather MJ & Settles GS (2010), "Natural-background-oriented schlieren imaging", *Experiments in Fluids*, vol. 48, no. 1, pp. 59–68, ISSN: 0723-4864, DOI: 10.1007/s00348-009-0709-3.

Hartley RI (1997), "In defense of the eight-point algorithm", *IEEE Transactions on pattern Analysis and Machine Intelligence*, vol. 19, no. 6, pp. 580–593.

Hartley R & Zisserman A (2003), *Multiple view geometry in computer vision*, Cambridge university press, UK.

Heineck JT, Yamauchi GK, Wadcock AJ, Lorenco L & Abrego A (2000), "Application of three-component PIV to a hovering rotor wake", *Proc. American Helicopter Society 56th Annual Forum*, Virginia Beach, VA, USA, May 2–4, 2000.

Heineck JT, Kushner LK, Schairer ET & Walker LA (2010), "Retroreflective Background Oriented Schlieren (RBOS) as applied to Full-Scale UH-60 Blade Tip Vortices", *Proc. American Helicopter Society Aeromechanics Specialists' Conference*, San Francisco, CA, USA, Jan. 20–22, 2010.

Heineck JT, Kushner LK & Schairer ET (2013), "Measurements of Tip Vortices from a Full-Scale UH-60A Rotor by Retro-Reflective Background Oriented Schlieren and Stereo Photogrammetry", *Proc. American Helicopter Society 69th Annual Forum*, Phoenix, AZ, USA, May 21–23, 2013.

Highspeed controller D80 (2010), Lavision GmbH, Manual No. 1006382, Göttingen, Germany.

Hoad D (1979), *Evaluation of helicopter noise due to blade-vortex interaction for five tip configurations*, tech. rep., NASA TP-1608.

Hoffmann F, Opitz S & Riemenschneider J (2009), "Validation of Active Twist Modeling Based on Whirl Tower Tests", *Proc. American Helicopter Society 65th Annual Forum*, Ft. Worth, TX, USA., May 27–29, 2009.

Hoffmann F, Schneider O, van der Wall BG, Keimer R, Kalow S, Bauknecht A, Ewers B, Pengel K & Feenstra G (2014), "STAR Hovering Test - Proof of Functionality and Representative Results", *Proc. 40th European Rotorcraft Forum*, Southampton, UK, Sept. 2–5, 2014.

Horner MB, Stewart JN & Galbraith R (1994), "An examination of vortex deformation during blade-vortex interaction utilising particle image velocimetry", *Proc. 19th Congress of the International Council of the Aeronautical Sciences*, Anaheim, CA, USA, Sept. 18–23, 1994.

Iversen JD (1976), "Correlation of turbulent trailing vortex decay data", *Journal of Aircraft*, vol. 13, no. 5, pp. 338–342.

Jacklin SA, Haber A, de Simone G, Norman TR, Kitaplioglu C & Shinoda P (2002), "Full-Scale Wind Tunnel Test of an Individual Blade Control System for a UH-60 Helicopter", *Proc. American Helicopter Society 58th Annual Forum*, Montreal, Canada, June 11–13, 2002.

Jeong J & Hussain F (1995), "On the identification of a vortex", *Journal of Visalization*, vol. 285, pp. 69–94.

Johnson B, Ramasamy M & Leishman JG (2010), "Turbulence Measurements inside Blade Tip Vortices Using Dual-Plane Particle Image Velocimetry", *Journal of the American Helicopter Society*, vol. 55, pp. 1–15.

Kato H, Watanabe S, Kondo N & Saito S (2003), "Application of stereoscopic PIV to helicopter rotor blade tip vortices", *Proc. 20th Congress on Instrumentation in Aerospace Simulation Facilities*, Göttingen, Germany, Aug. 25–29, 2003.

Kaufmann W (1962), "Über die Ausbreitung kreiszylindrischer Wirbel in zähen (viskosen) Flüssigkeiten", *Ingenieur-Archiv*, vol. 31, no. 1, pp. 1–9, ISSN: 00201154, DOI: 10.1007/BF00538235.

Keane RD & Adrian RJ (1992), "Theory of cross-correlation analysis of PIV images", *Applied Scientific Research*, vol. 49, pp. 191–215.

Kindler K, Mulleners K, Richard H & Raffel M (2009), "A Full-Scale Particle Image Velocimetry Investigation of "Young" Rotor Blade Tip Vortices", *Proc. American Helicopter Society 65th Annual Forum*, Ft. Worth, TX, USA, May 27–29, 2009.

Kindler K, Goldhahn E, Leopold F & Raffel M (2007), "Recent developments in background oriented Schlieren methods for rotor blade tip vortex measurements", *Experiments in Fluids*, vol. 43, no. 2-3, pp. 233–240, ISSN: 0723-4864, DOI: 10.1007/s00348-007-0328-9.

Kindler K, Mulleners K, van der Wall BG, Richard H & Raffel M (2011), "Aperiodicity in the Near Field of Full-Scale Rotor Blade Tip Vortices", *Experiments in Fluids*, vol. 50, no. 6, pp. 1601–1610.

Klein S, Hoppmann D, Scholz P & Radespiel R (2014), "High-Lift Airfoil Interacting with a Vortical Disturbance: Wind-Tunnel Measurements", *AIAA Journal*, vol. 53, no. 6, pp. 1–12, ISSN: 0001-1452, DOI: 10.2514/1.J053441.

Klinge F, Hecklau M, Raffel M, Kompenhans J & Göhmann U (2006), "Measurement of the position of rotor blade vortices generated by a helicopter in free flight by means of stereoscopic Background Oriented Schlieren Method (BOS)", *Proc. 13th Intl. Symp. on Applications of Laser Techniques to Fluid Mechanics*, Lisbon, Portugal, June 26–29, 2006.

Köpf U (1972), "Application of speckling for measuring the deflection of laser light by phase objects", *Optics Communications*, vol. 5, pp. 347–350, DOI: 10.1016/0030-4018(72)90030-2.

Koratkar NA & Chopra I (2002), "Wind Tunnel Testing of a Smart Rotor Model with Trailing-Edge Flaps", *Journal of the American Helicopter Society*, vol. 47, no. 4, p. 263, ISSN: 00028711, DOI: 10.4050/JAHS.47.263.

Koushik S & Schmitz FH (2014), "Measurements and Computations of Experimentally Simulated Blade-Vortex Interaction Noise", *AIAA Journal*, vol. 52, no. 10, pp. 2241–2250, ISSN: 0001-1452, DOI: 10.2514/1.J052851.

Kube R, Splettstoesser WR, Wagner W, Seelhorst U, Yu YH, Tung C, Beaumier P, Prieur J, Rahier G, Spiegel P, Boutier A, Brooks TF, Burley CL, Boyd DD, Mercker E & Pengel K

(1996), “HHC Aeroacoustic Rotor Tests in the German Dutch Wind Tunnel: Improving Physical Understanding and Prediction Codes”, *Proc. American Helicopter Society 52nd Annual Forum*, Washington D.C., USA, June 4–6, 1996.

Kutz BM, Keßler M & Krämer E (2013), “Experimental and numerical examination of a helicopter hovering in ground effect”, *CEAS Aeronautical Journal*, vol. 4, no. 4, pp. 397–408, ISSN: 1869-5582, DOI: 10.1007/s13272-013-0084-x.

Lamb H (1932), *Hydrodynamics*, 6th, Cambridge University Press, Cambridge, UK, Cambridge, pp. 592–593.

Landgrebe AJ (1971), *An Analytical and Experimental Investigation of Helicopter Rotor Hover Performance and Wake Geometry Characteristics*, tech. rep., USAAMRDL, TR-71-24.

Landgrebe AJ (1972), “The wake geometry of a hovering helicopter rotor an its influence on rotor performance”, *Journal of the American Helicopter Society*, vol. 17, no. 4, pp. 3–15, ISSN: 00028711, DOI: 10.4050/JAHS.17.3.

Lazar E, Deblauw B, Glumac N, Dutton C, Elliott G & Head A (2010), “A Practical Approach to PIV Uncertainty Analysis”, *Proc. 27th AIAA Aerodynamic Measurement Technology and Ground Testing Conference*, Chicago, IL, USA, June 28–July 1, 2010.

Leighty BD, Rhodes DB, Franke JM & Jones SB (1991), *A synchronous strobed laser light sheet for rotor flow visualizations*, tech. rep., NASA TM-4266.

Leishman JG (2006), *Principles of Helicopter Aerodynamics*, Cambridge University Press, New York, NY.

Leishman JG, Baker AM & Coyne AJ (1996), “Measurement of rotor tip vortices using three-component LDV”, *Journal of the American Helicopter Society*, vol. 41, no. 4, pp. 342–353.

Leishman JG (1998), “Measurements of the aperiodic wake of a hovering rotor”, *Experiments in Fluids*, vol. 25, no. 4, pp. 352–361, ISSN: 0723-4864, DOI: 10.1007/s003480050240.

Leopold F (2007), “The application of the colored background oriented Schlieren technique (CBOS) to free-flight and in-flight measuremen”, *Journal of Flow Visalization and Image Processing*, pp. 279–293, DOI: 10.1615/JFlowVisImageProc.v16.i4.10.

Light JS, Frerkin A & Norman TR (1999), “Application of the Wide-Field Shadowgraph Technique to Helicopters in Forward Flight”, *Proc. American Helicopter Society 46th Annual National Forum*, Washington D.C., USA, May 21–23, 1999.

Lim JW & Strawn RC (2008), “Computational modeling of HART II blade-vortex interaction loading and wake system”, *Journal of Aircraft*, vol. 45, no. 3, pp. 923–933.

Lim TT & Cui YD (2005), “On the generation of a spiral-type vortex breakdown in an enclosed cylindrical container”, *Physics of Fluids*, vol. 17, no. 4, ISSN: 10706631, DOI: 10.1063/1.1872072.

Lowson MV (1992), “Progress towards quieter civil helicopters”, *Aeronautical Journal*, vol. 96, pp. 209–223.

Lugt H (1996), *Introduction to vortex theory*, Vortex Flow Press, Potomac, Maryland, USA, ISBN: 0-9657689-0-2.

Mahalingam R & Komerath N (1997), “Measurements of the near wake of a rotor in forward flight”, *AIAA Paper*, pp. 98–0692.

Marcolini MA, Booth ER, Tadghighi H, Hassan AA, Smith CD & Becker LE (1995), “Control of BVI noise using an active trailing edge flap”, *Proc. American Helicopter Society Vertical Lift Aircraft Design Conference*, San Francisco, CA, USA, Jan. 18–20, 1995.

Martin PB & Leishman JG (2002), “Trailing vortex measurements in the wake of a hovering rotor blade with various tip shapes”, *Proc. American Helicopter Society 58th Annual Forum*, Montreal, Canada, June 11–13, 2002.

Martin PB, Pugliese GJ & Leishman JG (2000a), "Laser Doppler Velocimetry uncertainty analysis for rotor blade tip vortex measurements", *Proc. 38th Aerospace Sciences Meeting and Exhibit*, Reno, NV, USA, Jan. 10–13, 2000.

Martin PB, Leishman JG, Pugliese GJ & Anderson SL (2000b), "Stereoscopic PIV Measurements in the Wake of a Hovering Rotor", *Proc. American Helicopter Society 56th Annual Forum*, Virginia Beach, VA, USA, May 2–4, 2000.

Martin PB, Pugliese GJ & Leishman JG (2003), "High Resolution Trailing Vortex Measurements in the Wake of a Hovering Rotor", *Journal of the American Helicopter Society*, vol. 48, no. 1, pp. 39–52.

McAlister KW & Takahashi RK (1991), *NACA 0015 wing pressure and trailing vortex measurements*, tech. rep., NASA, Moffett Field, NASA TP 3151.

McAlister KW, Schuler Ca, Branum L & Wu JC (1995), *3-D Wake Measurements Near a Hovering Rotor for Determining Profile and Induced Drag*, tech. rep., NASA, Moffett Field, NASA TP 3577.

McAlister K, Tung C & Heineck J (2001a), *Devices that Alter the Tip Vortex of a Rotor*, tech. rep., NASA TM-2001-209265.

McAlister KW (2003), "Rotor wake development during the first revolution", *Journal of the American Helicopter Society*, vol. 49, no. 4, pp. 371–390.

McAlister KW, Tung C & Heineck JT (2001b), "Forced Diffusion of Trailing Vorticity from a Hovering Rotor", *Proc. American Helicopter Society 57th Annual Forum*, Washington D.C., USA, May 9–11, 2001.

McCormick BW, Tangler JL & Sherrier HE (1968), "Structure of trailing vortices.", *Journal of Aircraft*, vol. 5, no. 3, pp. 260–267, ISSN: 0021-8669, DOI: 10.2514/3.43936.

Meier AH & Roesgen T (2013), "Improved background oriented schlieren imaging using laser speckle illumination", *Experiments in Fluids*, vol. 54, no. 6, p. 1549, ISSN: 0723-4864, DOI: 10.1007/s00348-013-1549-8.

Meier GEA (2000), "Hintergrund Schlierenmessverfahren", *German Patent, DE 199 42 856 A1*.

Merzkirch W (1981), "Density Sensitive Flow Visualization", *Fluid Dynamics*, vol. 18A, Methods in Experimental Physics, Academic Press, pp. 345–403, DOI: 10.1016/S0076-695X(08)60547-5.

Meyn LA & Bennett MS (1993), "Application of a Two Camera Video Imaging System to Three-Dimensional Vortex Tracking in the 80- by 120-Foot Wind Tunnel", *Proc. AIAA 11th Applied Aerodynamics Conference*, Monterey, CA, Aug. 9–11, 1993.

Mikhail EM, Bethel JS & McGlone JC (2001), *Introduction to modern photogrammetry*, vol. 1, John Wiley & Sons Inc, New York.

Milluzzo J & Leishman JG (2013), "Development of the Turbulent Vortex Sheet in the Wake of a Hovering Rotor", *Proc. American Helicopter Society 69th Annual Forum*, Phoenix, AZ, USA, May 21–23, 2013.

Morbitzer D, Arnold UTP & Müller M (1998), "Vibration and noise reduction through individual blade control experimental and theoretical results", *Proc. 24th European Rotorcraft Forum*, ASSOCIAZIONE ITALIANA DI AERONAUTICA ED ASTRONAUTICA, Marseilles, France, Sept. 15–17, 1998.

Murashige A, Tsuchihashi A, Tsujiuchi T & Yamakawa E (1997), "Blade-tip vortex measurement by PIV", *Proc. 23rd European Rotorcraft Forum*, ASSOCIAZIONE ITALIANA DI AERONAUTICA ED ASTRONAUTICA, Dresden, Germany, Sept. 16–18, 1997.

Norman TR, Shinoda P, Peterson RL & Datta A (2011), "Full-scale wind tunnel test of the UH-60A airloads rotor", *Proc. American Helicopter Society 67th Annual Forum*, Virginia Beach, VA, USA, May 3–5, 2011.

Norman T & Light J (1987), "Rotor tip vortex geometry measurements using the wide-field shadowgraph technique.", *Journal of the American Helicopter Society*, vol. 32, no. 2, pp. 40–50.

Oseen CW (1911), "Über Wirbelbewegung in einer reibenden Flüssigkeit", *Arkiv för matematik, astronomi och fysik*, vol. 7, no. 14, pp. 14–21.

Peng D & Gregory JW (2015), "Vortex dynamics during blade-vortex interactions", *Physics of Fluids*, vol. 27, no. 5, pp. 1–23, ISSN: 1070-6631, DOI: 10.1063/1.4921449.

Percin M, van Oudheusden BW, Eisma HE & Remes BDW (2014), "Three-dimensional vortex wake structure of a flapping-wing micro aerial vehicle in forward flight configuration", *Experiments in Fluids*, vol. 55, no. 9, p. 1806, ISSN: 0723-4864, DOI: 10.1007/s00348-014-1806-5.

Politz C, Lawson NJ, Konrath R, Agocs J & Schröder A (2010), "In-flight flow visualisation using Particle Image Velocimetry", *Proc. 15th int. Symp. on Applications of Laser Techniques to Fluid Mechanics*, Lisbon, Portugal, July 5–8, 2010.

Raffel M & Meier GEA (2000), *Verfahren zur Detektion räumlicher Dichtegradienten*, German patent: DE 100 10 045 C2.

Raffel M, Seelhorst U, Willert C, Vollmers H, Bütefisch K & Kompenhans J (1996), "Measurement of vortical structures on a helicopter rotor model in a wind tunnel by LDV and PIV", *Proc. 8th International Symposium on the Application of Laser Techniques to Fluid Mechanics*, Lisbon, Portugal, July 8–11, 1996.

Raffel M, Seelhorst U & Willert C (1998a), "Vortical flow structures at a helicopter rotor model measured by LDV and PIV", *The Aeronautical Journal*, vol. 102, no. 1014, pp. 221–227.

Raffel M, Tung C, Richard H, Yu Y & Meier GEA (2000a), "Background oriented stereoscopic schlieren (BOSS) for full scale helicopter vortex characterization", *Proc. 9th Int. Symp. on Flow Visualization*, Edinburgh, UK, Aug. 22–25, 2000.

Raffel M, Richard H & Meier GEA (2000b), "On the applicability of background oriented optical tomography for large scale aerodynamic investigations", *Experiments in Fluids*, vol. 28, no. 5, pp. 477–481, ISSN: 0723-4864, DOI: 10.1007/s003480050408.

Raffel M, Richard H, Agocs J, Otter D, Mattner H & Göhmann U (2001), "Experimental aspects of PIV applied to a Bo105 helicopter in hover-flight condition", *Proc. 4th Int. Symp. on Particle Image Velocimetry*, Göttingen, Germany, Sept. 17–19, 2001.

Raffel M, Richard H, Ehrenfried K, van der Wall BG, Burley C, Beaumier P, Alister KM & Pengel K (2004), "Recording and evaluation methods of PIV investigations on a helicopter rotor model", *Experiments in Fluids*, vol. 36, pp. 146–156.

Raffel M, Willert C, Wereley S & Kompenhans J (2007), *Particle image velocimetry, a practical guide*, Springer Berlin Heidelberg, DOI: 10.1007/978-3-540-72308-0.

Raffel M, Heineck JT, Schairer E, Leopold F & Kindler K (2014), "Background-Oriented Schlieren Imaging for Full-Scale and In-Flight Testing", *Journal of the American Helicopter Society*, vol. 59, no. 1, pp. 1–9, DOI: 10.4050/JAHS.59.012002.

Raffel M (2015), *User Manual Aerosol Generator PivPart40-Dry series*, Göttingen.

Raffel M, Willert C, Kompenhans J, Ehrenfried K, Lehmann G & Pengel K (1998b), "Feasibility and capabilities of particle image velocimetry (PIV) for large scale model rotor testing", *Proc. Int. Conference of the American Helicopter Society*, Gifu, Japan, Apr. 21–23, 1998.

Raffel M, Merz CB, Bauknecht A & Schwermer T (2013), "High-Speed PIV, deformation and BOS measurements for rotor aerodynamics", *Proc. AFDAR Workshop on "Application of advanced flow diagnostics to aeronautics"*, Brunswick, Germany, Feb. 6–7, 2013.

Ramasamy M & Leishman JG (2004), "Interdependence of diffusion and straining of helicopter blade tip vortices", *Journal of Aircraft*, vol. 41, no. 5, pp. 1014–1024.

Ramasamy M & Leishman JG (2006a), "A Generalized Model for Transitional Blade Tip Vortices", *Journal of the American Helicopter Society*, vol. 51, no. 1, pp. 92–103.

Ramasamy M, Johnson B, Huismann T & Leishman JG (2009a), "Procedures for measuring the turbulence characteristics of rotor blade tip vortices", *Journal of the American Helicopter Society*, vol. 54, pp. 2201–2206.

Ramasamy M, Paetzel R & Bhagwat MJ (2011), "Aperiodicity correction for rotor tip vortex measurements", *Proc. American Helicopter Society 67th Annual Forum*, Virginia Beach, VA, USA, May 3–5, 2011.

Ramasamy M & Leishman JG (2005), "Reynolds Number Based Blade Tip Vortex Model", *Proc. American Helicopter Society 61st Annual Forum*, Grapevine, TX, USA, June 1–3, 2005.

Ramasamy M & Leishman JG (2006b), "Benchmarking PIV with LDV for Rotor Wake Vortex Flows", *AIAA*, pp. 1–29.

Ramasamy M & Leishman JG (2007), "A Reynolds Number-Based Blade Tip Vortex Model", *Journal of the American Helicopter Society*, vol. 52, p. 214, ISSN: 00028711, DOI: 10.4050/JAHS.52.214.

Ramasamy M, Johnson B, Huismann T & Leishman JG (2009b), "Digital Particle Image Velocimetry Measurements of Tip Vortex Characteristics Using an Improved Aperiodicity Correction", *Journal of the American Helicopter Society*, vol. 54, pp. 1–13.

Ramasamy M, Gold N & Bhagwat M (2010), "Flowfield Measurements to Understand Effect of Wake Behavior on Rotor Performance", *Proc. AIAA 28th Applied Aerodynamics Conference*, Fluid Dynamics and Co-located Conferences, AIAA, Chicago, IL, USA, June 28–July 1, 2010, DOI: doi:10.2514/6.2010-4237.

Ramasamy M, Pete A, Bhagwat MJ & Caradonna FX (2014), "An Experiment to Simulate the Airloads and Wake Typical of a Hovering Rotor", *Proc. American Helicopter Society 5th Decennial Specialists' Meeting on Aeromechanics*, San Francisco, CA, USA, Jan. 22–24, 2014.

Richard H & Raffel M (2001), "Principle and applications of the background oriented schlieren (BOS) method", *Meas. Sci. Technol.* Vol. 12, no. 9, pp. 1576–1585, DOI: 10.1088/0957-0233/12/9/325.

Richard H & Raffel M (2002), "Rotor wake measurements: full-scale and model tests", *Proc. American Helicopter Society 58th Annual Forum*, Montréal, Canada, June 11–13, 2002.

Richard H & van der Wall B (2006), "Detailed investigation of rotor blade tip vortex in hover condition by 2C and 3C-PIV", *Proc. 32nd European Rotorcraft Forum*, Maastricht, the Netherlands, Sept. 12–14, 2006.

Richard H, Raffel M, Rein M, Kompenhans J & Meier GEA (2000), "Demonstration of the Applicability of a Background Oriented Schlieren (BOS) Method", *Proc. 10th int. Symp. on Applications of Laser Techniques to Fluid Mechanics*, Lisbon, Portugal, July 10–13, 2000.

Richard H, Bosbach J, Henning A, Raffel M & van der Wall BG (2006), "2C and 3C PIV measurements on a rotor in hover condition", *Proc. 13th International Symposium on Applications of Laser Techniques to Fluid Mechanics*, Lisbon, Portugal, June 26–29, 2006.

Riemenschneider J, Keimer R & Kalow S (2013), "Experimental Bench Testing of an Active-Twist Rotor", *Proc. 39th European Rotorcraft Forum*, Moscow, Russia, Sept. 3–6, 2013.

Riemenschneider J, Wierach P, Opitz S & Hoffmann F (2007), "Testing and simulation of an active twist rotor blade", *Proc. Adaptronic Congress*, Göttingen, Germany, May 23–24, 2007.

Rival D, Manejev R & Tropea C (2010), "Measurement of parallel blade-vortex interaction at low Reynolds numbers", *Experiments in Fluids*, vol. 49, no. 1, pp. 89–99, ISSN: 07234864, DOI: 10.1007/s00348-009-0796-1.

Robinson SK (1990), "A Review of Vortex Structures and Associated Coherent Motions in Turbulent Boundary Layers", *Structure of Turbulence and Drag Reduction*, Springer Berlin Heidelberg, pp. 23–50, ISBN: 978-3-642-50973-5, DOI: 10.1007/978-3-642-50971-1-2.

Rossow VJ (1999), "Lift-generated vortex wakes of subsonic transport aircraft", *Progress in Aerospace Sciences*, vol. 35, no. 6, pp. 507–660, ISSN: 03760421, DOI: 10.1016/S0376-0421(99)00006-8.

Roussinova V & Balachandar R (2012), *River Flow*, CRC Press, Boca Raton, FL, USA, pp. 171–175, ISBN: 978-0-415-62129-8.

Saripalli K (1995), "Application of Particle Imaging Velocimetry Techniques to Helicopter Rotor Flowfields at McDonnell Douglas Aerospace", *Proc. AIAA 33rd Aerospace Sciences Meeting and Exhibit*, Reno, NV, USA, Jan. 9–12, 1995.

Scarano F & Riethmuller ML (1999), "Iterative multigrid approach in PIV image processing with discrete window offset", *Experiments in Fluids*, vol. 26, no. 6, pp. 513–523, ISSN: 07234864, DOI: 10.1007/s003480050318.

Scheimpflug T (1904), *Improved method and apparatus for the systematic alteration or distortion of plane pictures and images by means of lenses and mirrors for photography and for other purposes*, British Patent No. 1196.

Schimke D, Jänker P, Blaas A, Kube R & Keßler C (1997), "Individual blade control by servo-flap and blade root control a collaborative research and development programme", *Proc. 23rd European Rotorcraft Forum*, Dresden, Germany, Sept. 16–18, 1997.

Schultz KJ, Splettstoesser W, Junker B, Wagner W, Schoell E, Mercker E, Pengel K, Arnaud G & Fertis D (1996), "A parametric windtunnel test on rotorcraft aerodynamics and aeroacoustics (Helishape) – test procedures and representative results", *Aeronautical Journal*, vol. 101, no. 1004, pp. 143–154, ISSN: 0001-9240.

Scully M & Sullivan JP (1972), *Helicopter rotor wake geometry and airloads and development of laser Doppler velocimeter for use in helicopter rotor wakes*, MIT Aerophysics Laboratory.

Settles GS (1999), "Schlieren and shadowgraph imaging in the great outdoors", *Proc. PSFVIP-2 Schlieren and Shadowgraph Techniques; Visualizing Phenomena in Transparent Media*, Honolulu, HI, USA, May 16–19, 1999.

Simons IA, Pacifico RE & Jones JP (1966), "The movement, structure and breakdown of trailing vortices from a rotor blade", *Proc. CAL/USAA AVLABS Symposium*, Buffalo, NY, USA, June 22–24, 1966.

Smith D & Sigl D (1995), "Helicopter Rotor Tip Shapes for Reduced Blade Vortex Interaction - an Experimental Investigation", *Proc. AIAA 33rd Aerospace Sciences Meeting and Exhibit*, Reno, NV, USA, Jan. 9–12, 1995, AlAA 95–0192.

Spalart PR (1998), "Airplane trailing vortices", *Annual Review in Fluid Mechanics*, vol. 30, pp. 107–138.

Spencer RH (1970), "Application of vortex visualization test techniques to rotor noise research", *Proc. American Helicopter Society 26th Annual Forum*, Washington D.C., USA, June 16–18, 1970.

Splettstoesser WR, Schultz KJ, Boxwell DA & Schmitz FH (1984), *Helicopter Model Rotor-Blade Vortex Interaction Impulsive Noise: Scalability and Parametric Variations*, tech. rep., Moffett Field, CA, USA: NASA.

Splettstoesser WR, Niesl G, Cenedese F, Nitti F & Papanikas DG (1995), "Experimental Results of the European HELINOISE Aeroacoustic Rotor Test", *Journal of the American Helicopter Society*, vol. 40, no. 2, pp. 3–14, DOI: 10.4050/JAHS.40.3.

Splettstoesser WR, Kube R, Wagner W, Seelhorst U, Boutier A, Micheli F, Mercker E & Pengel K (1997), "Key results from a higher harmonic control aeroacoustic rotor test (HART)", *Journal of the American Helicopter Society*, vol. 42, no. 1, pp. 58–78.

Squire HB (1965), "The growth of a vortex in turbulent flow", *Aeronautical Quarterly*, vol. 16, pp. 302–306.

Sullivan JP (1973), *An experimental investigation of vortex rings and helicopter rotor wakes using a laser Doppler velocimeter*, tech. rep., MIT Technical Report 183.

Tangler JL (1977), "Schlieren and Noise Studies of Rotors in Forward Flight", *Proc. American Helicopter Society 33rd Annual National Forum*, Washington D.C., USA, May 9–11, 1977.

Thompson TL, Komerath NM & Gray RB (1988), "Visualization and measurement of the tip vortex core of a rotor blade in hover", *Journal of Aircraft*, vol. 25, no. 12, pp. 1113–1121.

Toepler A (1864), *Beobachtungen nach einer neuen optischen Methode*, Max Cohen & Sohn, Bonn, Germany.

Van de Hulst HC (1957), *Light scattering by small particles*, John Wiley & Sons, Inc., New York, NY, USA, (republished 1981 by Dover Publications, New York).

Van der Wall BG (2012), "Extensions of prescribed wake modelling for helicopter rotor BVI noise investigations", *CEAS Aeronautical Journal*, vol. 3, no. 1, pp. 93–115, ISSN: 1869-5582, DOI: 10.1007/s13272-012-0045-9.

Van der Wall BG & Richard H (2006), "Analysis methodology for 3C-PIV data of rotary wing vortices", *Experiments in Fluids*, vol. 40, pp. 798–812.

Van der Wall BG & Richard H (2008), *Hover Tip Vortex Structure Test (HOTIS) - Test Documentation and Representative Results*, tech. rep., Brunswick, Germany: DLR, pp. 1–144.

Van der Wall BG, Burley CL, Yu YH, Pengel K & Beaumier P (2004), "The HART II Test - Measurement of Helicopter Rotor Wakes", *Aerospace Science and Technology*, vol. 8, no. 4.

Van Oord J (1997), *The design of a stereoscopic DPIV-system*, tech. rep. MEAH-161, Delft University of Technology.

Vasilescu R (2004), "Helicopter blade tip vortex modifications in hover using piezoelectrically modulated blowing", PhD thesis, Georgia Institute of Technology.

Vatistas GH, Kozel V & Mih WC (1991), "A simpler model for concentrated vortices", *Experiments in Fluids*, vol. 11, no. 1, pp. 73–76, ISSN: 07234864, DOI: 10.1007/BF00198434.

Venkatakrishnan L & Meier GEA (2004), "Density measurements using the Background Oriented Schlieren technique", *Experiments in Fluids*, vol. 37, no. 2, pp. 237–247, ISSN: 0723-4864, DOI: 10.1007/s00348-004-0807-1.

Vogt A, Baumann P, Kompenhans J & Gharib M (1996), "Investigations of a wing tip vortex in air by means of DPIV", *Advanced Measurement and Ground Testing Conference*, DOI: 10.2514/6.1996-2254.

Wadcock AJ, Yamauchi GK, Solis E & Pete AE (2011), "PIV Measurements in the Wake of a Full-Scale Rotor in Forward Flight", *Proc. AIAA 29th Applied Aerodynamics Conference*, Honolulu, HI, USA, June 27–30, 2011.

Weinstein LM (1994), *An optical technique for examining aircraft shock wave structures in flight*, tech. rep., High-Speed Research: 1994 Sonic Boom Workshop, NASA CP-3279.

Wells V & Glinka A (1997), "The flip tip - A novel method for reducing blade-vortex interaction noise", *Proc. Innovation in rotorcraft technology*, The Royal Aeronautical Society, London, UK, pp. 11.1–11.11.

Wernekinck U & Merzkirch W (1987), "Speckle photography of spatially extended refractive-index fields", *Applied optics*, vol. 26, no. 1, pp. 31–32.

White Jr. RP (1980), "The Status of Rotor Noise Technology", *Journal of the American Helicopter Society*, vol. 25, no. 1, pp. 22–29, DOI: 10.4050/JAHS.25.22.

White Jr. RP, Balcerak JC & Pegg RJ (1975), "Summary of results indicating the beneficial effects of rotor vortex modification", *Proc. National Symposium on Helicopter Aerodynamic Efficiency*, Hartford, CT, USA, Mar. 6–7, 1975.

Wieneke B & Pfeiffer K (2010), "Adaptive PIV with variable interrogation window size and shape", *Proc. 15th int. Symp. on Applications of Laser Techniques to Fluid Mechanics*, Lisbon, Portugal, July 5–8, 2010.

Wierach P, Riemenschneider J, Optiz S & Hoffmann F (2007), "Experimental investigation of an active twist model rotor blade under centrifugal loads", *Proc. 33rd European Rotorcraft Forum*, Kazan, Russia, Sept. 11–13, 2007.

Wilbur ML & Yeager WT (2002), "Further Examination of the Vibratory Loads Reduction Results From the Nasa/Army/MIT Active Twist Rotor Test", *Proc. American Helicopter Society 58th Annual Forum*, Montreal, Canada, June 11–13, 2002.

Wilbur ML, Mirick PH, Yeager WT, Langston CW, Cesnik CES & Shin S (2001), "Vibratory Loads Reduction Testing of the NASA/Army/MIT Active Twist Rotor", *Journal of the American Helicopter Society*, vol. 47, no. 2, p. 123, ISSN: 00028711, DOI: 10.4050/JAHS.47.123.

Yamauchi GK, Burley CL, Mercker E, Pengel K & Janakiran R (1999), "Flow measurements of an isolated model tilt rotor", *Proc. American Helicopter Society 55th Annual Forum*, Montreal, Canada, May 25–27, 1999.

Yamauchi GK, Wadcock aJ, Johnson W & Ramasamy M (2012), "Wind Tunnel Measurements of Full-Scale UH-60A Rotor Tip Vortices", *Proc. American Helicopter Society 68th Annual Forum*, Fort Worth, TX, USA, May 1–3, 2012.

Yin JP & Ahmed SR (2000), "Helicopter Main-Rotor/Tail-Rotor Interaction", *Journal of the American Helicopter Society*, vol. 45, pp. 293–302.

Yin J (2012), "Main Rotor and Tail Rotor Blade Vortex Interaction Noise under the Influence of the Fuselage", *Proc. 38th European Rotorcraft Forum*, Amsterdam, The Netherlands, Sept. 4–7, 2012.

Yu Y, Tung C, Wall BVD & Pausder H (2002), "The HART-II test: Rotor wakes and aeroacoustics with higher-harmonic pitch control (HHC) inputs - The joint german/french/dutch/us project", *Proc. American Helicopter Society 58th Annual Forum*, Montreal, Canada, June 11–13, 2002.

Yu YH (2000), "Rotor blade-vortex interaction noise", *Progress in Aerospace Sciences*, vol. 36, no. 2, pp. 97–115, ISSN: 0376-0421, DOI: 10.1016/S0376-0421(99)00012-3.

Zhou J, Adrian RJ, Balachandar S & Kendall TM (1999), "Mechanisms for generating coherent packets of hairpin vortices in channel flow", *Journal of Fluid Mechanics*, vol. 387, pp. 353–396, ISSN: 00221120, DOI: 10.1017/S002211209900467X.

Curriculum Vitae

Work experience

since 02/2016 **German Aerospace Center (DLR), Göttingen**
Postdoctoral research

11/2011 – 02/2016 **German Aerospace Center (DLR), Göttingen**
Doctoral studies
- Effects of active twist actuation on blade tip vortices
- Optical vortex visualization on full-scale helicopters

01/2012 – 03/2012 **German Aerospace Center (DLR), Brunswick**
Research stay
- Modeling of fuselage-induced flow for comprehensive rotor codes

05/2010 – 11/2010 **California Institute of Technology, Pasadena, USA**
Research stay
- Diploma thesis at the Graduate Aerospace Laboratories "Effects of active boundary-layer control by morphing surfaces on flow over a sphere near the critical Reynolds number"

Education

10/2005 – 10/2011 **University of Stuttgart, Germany**
Studies of aeronautical and aerospace engineering
- Graduate degree (Dipl.-Ing.)
- Majors: Fluid Dynamics, Aircraft Propulsion
- Student research project at the Institute of Aircraft Propulsion "Numerical Simulation of Shock-Flame Interactions"

09/1996 – 06/2005 **Theodor-Heuss-Gymnasium, Pforzheim, Germany**
Abitur
- A-level degree (Abitur)

Scholarships and Awards

2013 AHS International best paper award in the Test & Evaluation sessions
2010 Travel stipend of the German National Academic Foundation
2006 – 2011 Scholarship of the German National Academic Foundation

Languages

German Native speaker
English Fluent
French Basic knowledge